EBC

Energy in Buildings and Communities Programme

Current Updates on the Development and Implementation of Micro-Cogeneration System Models for Building Simulation Programs

Energy in Buildings and Communities Programme

October 2014

A Report of Annex 54 "Integration of Micro-Generation and Related Energy Technologies in Buildings"

Edited by

Ken Darcovich (Research Council of Canada) – Subtask A Leader
Evgueniy Entchev (National Resources Canada, Canada) – Operating Agent
Peter Tzscheutschler (Technische Universität München, Germany) – Operating Agent

On behalf of IEA EBC Annex 54

iea Energy Technology Network

Published by Technische Universität München, Germany, 2014

Citation: K. Darcovich, et.al.: "Current Updates on the Development and Implementation of Micro-Cogeneration System Models for Building Simulation Programs", published by Technische Universität München, Germany, 10/2014

Participating countries in EBC:

Australia, Austria, Belgium, Canada, P.R. China, Czech Republic, Denmark, Finland, France, Germany, Greece, Ireland, Italy, Japan, Republic of Korea, the Netherlands, New Zealand, Norway, Poland, Portugal, Spain, Sweden, Switzerland, Turkey, United Kingdom and the United States of America.

Current Updates on the Development and Implementation of Micro-Cogeneration System Models for Building Simulation Programs

Energy in Buildings and Communities Programme

October 2014

A Report of Annex 54 "Integration of Micro-Generation and Related Energy Technologies in Buildings"

Authored by:

Ken Darcovich	(National Research Council of Canada)
Peter Tzscheutschler	(TU München, Germany)
Evgueniy Entchev, Libing Yang, Mohamed Ghorab	(CanmetENERGY Research Centre, Canada)
Ian Beausoleil-Morrison, Geoff Johnson	(Carleton University, Canada)
Nick Kelly	(University of Strathclyde, UK)
Michael Steck	(FfE, Germany)
Juliana Zapata, William D'haeseleer	(KU Leuven, Belgium)
Bruno Lee	(TU Eindhoven, Netherlands)
Tatsuo Sakonji	(Tokyo Gas, Japan)
Sergio Sibilio, Antonio Rosato	(Seconda Università di Napoli, Italy)
Maurizio Sasso, Giovanni Angrisani, Carlo Roselli, Catarina Brandoni	(Università degli Studi del Sannio, Italy) (Università Politecnica delle Marche, Italy)
Biagio Di Pietra, Giovanni Puglisi, Francesca Bonfà, Fabio Zanghirella	(ENEA, Italy)
Marco Manzan	(Università di Trieste, Italy)
Euy Joon Lee, Maurizio Sasso	(Korea Institute of Energy Research)
Soolyeon Cho	(North Carolina State University)
Shin Woo Chul	(Daejeon University, Korea)

Acknowledgements

This report is the result of an international project performed within Annex 54 of the IEA/EBC programme. We would like to express our great appreciation to the participants of Annex 54 for their contribution as well as for the support given by different national bodies.

The guidance of the EBC Executive Committee is gratefully acknowledged.

Ken Darcovic (Subtask A Leader), Evgueniy Entchev, Peter Tzscheutschler (Operating Agents)

Table of Contents

1 Introduction

The IEA Annex 54 on “Integration of Micro-Generation and Related Energy Technologies in Buildings” is undertaking an in depth analysis of micro-generation and associated other energy technologies. The scope of activities encompasses:

- multi-source micro-cogeneration systems, polygeneration systems (i.e. integrated heating / cooling / power generation systems) and renewable hybrid systems;
- the integration of micro-generation, energy storage and demand side management technologies at a local level (integrated systems);
- customised and optimum control strategies for integrated systems;
- the analysis of integrated and hybrid systems performance when serving single and multiple residences along with small commercial premises; and
- the analysis of the wider impact of micro-generation on the power distribution system. To broaden the impact of the Annex’s output there will be significant effort to disseminate its deliverables to non-technical stakeholders working in related areas such as housing, product commercialisation and regulatory development.

In view of the above outlined activities, a number of expected outcomes were:

- An update on occupant related DHW and electric load profiles.
- Component models and their implementation in building simulation tools.
- Review of best practice in the operation and control of integrated micro-generation systems.
- Predictive control algorithms to maximize the performance and value of micro-generation.
- Experimental data sets for the calibration and validation of device models.
- Performance assessment methodologies.
- Country-specific studies on the performance of a range of micro-generation systems.
- Studies of the viability of micro-generation systems in different operational contexts and of the impacts of micro-generation on the wider community and the potential benefits, in particular for the electricity network.
- An investigation of interactions between technical performance and commercialization/regulatory approaches for micro-generation.
- Compilation of case studies of the introduction of microgeneration technologies.

Annex 54 builds upon the results of Annex 42 "The Simulation of Building-Integrated Fuel Cell and Other Cogeneration Systems", and can be viewed as a continuation, extension, update and refinement of the information, models and findings established there.

Annex 54 has been divided into three Subtasks to facilitate organizing and classifying its constituent activities and outputs. In broad terms, Subtask A was Technical Development, Subtask B was Performance Assessment and Subtask C was Communication and Dissemination. In more detail, Subtask A encompasses electrical and domestic hot water load profiles and system models, methodology for model development, data collection for micro-generation systems, as well as work on predictive controls development and optimization. The present report is focused on model development for microgeneration devices used in residential and small scale applications, microgeneration system design, configuration and optimisation, new models for balance of plant equipment incorporated into systems for energy storage, as well as reporting on some recent advances on control strategies and algorithms for deploying microgeneration systems.

1.1 Subtask A: Technical Development

This Subtask will undertake the model development and data collection activities that will underpin the work of Subtasks B and C, with the emphasis on the optimised operation of micro-generation systems. This will require the development of models of contemporary micro-generation devices and controllers to maximise the energy performance for local and possibly community energy needs in different operational scenarios.

Work will also involve the specification of boundary conditions for the modelling of micro-generation, especially the establishment of appropriate hot water and electrical demand profiles.

Specific objectives for Subtask A are:

- The micro-cogeneration models (SOFC, PEM, ICE and Stirling Engine) developed in Annex 42 will be updated with performance characteristics from more modern devices. Initially this will be done using some of the data emerging from the final tests undertaken on more up-to-date devices.
- Subtask A will also encompass laboratory tests to acquire new performance data using the established testing protocol for relevant microgeneration and energy storage devices. The data emerging from these tests will be used for calibration and validation of existing models.
- New balance of plant models (i.e. Lithium-ion battery storage and a thermally-activated-cooling device) will be developed where necessary. A number of studies were undertaken on the system level, where energy storage has been recognized as a key component.
- To gain a better understanding of the contexts in which microgeneration systems can be energetically and economically viable, Annex 54 aimed to consider models of full residential energy use systems, which can also include energy storage devices, inputs from renewables, bi-directional grid connection and buildings which include, but not limited to single family residences.
- To date, the control applied to micro-cogeneration devices was rudimentary (i.e. on-off heat load following). More advanced controllers tasked with optimising performance for local and energy network needs and reflecting the potential for incorporating demand side management (DSM) will be investigated. The control structures, communications protocols and data inputs that could be used to inform the operation such controllers will be identified through a review of related technologies such as state-of-the-art BEMS, smart metering and DSM. Additionally, a review of

current best practice in micro-generation will be undertaken to identify effective operation and control strategies. Potential control vectors, for instance: variable electricity tariffs and real time energy pricing will also be examined.

- New control algorithms for the optimum operation of single device systems, hybrid (multi-source systems), poly-generation and systems incorporating storage and DSM will be developed. The new algorithms will be expected to optimise performance against both local energy needs and within the context of wider heat and power networks. The dwelling and device models developed in Subtask B will be used as the test-bed for this activity.
- Finally, Annex 54 will measure/collate occupant related electric and hot water demands to assist in defining load profiles for different operational scenarios as well as to provide an up to date data inventory of energy demand data from participating nations. On this point, the scope of Annex 54 allows for more varied building types than simply single family homes, so load profile data from a range of different types of buildings were sought at size scales commensurate with microgeneration.

In view of the objective statements derived from the Annex 54 project proposal, reporting is to be provided on tests which obtained new and/or updated performance data using established testing protocol for the current generation of micro-generation and energy storage devices. The data used for calibration and validation of existing models also should serve to reinforcing the use of IEA protocols, as well as enabling ready comparison and standarised certification criteria

Keeping apace of emerging residential energy use systems, Annex 54 sought to develop new balance of plant models incorporating emerging energy storage devices (i.e. electrical storage withLithium-ion battery storage, thermally-activated-cooling device, desiccant wheel, phase change material tank). By the same token, the development of models for energy from renewables (ie; photovoltaics, wind) was undertaken, especially in view of how such units are supported and/or mandated by policy instruments

Microgeneration prime mover technologies have become relatively well known over the past decade. Aside from simply demonstrating their performance as isolated units, Annex 54 worked towards extending the scope of modeling to consider simulations of complete energy systems and explore various configurational scenarios in order to provide evidence of the techno-economic benefits associated with their uptake and implementation. Much of these benefits must be found in contextual details, and Annex 54 included many projects which developed new algorithms which aimed to optimise performance considering both local energy demands and the wider context of heat and power networks.

Linked to all the above was an understanding that system operation is also a key consideration for the worthiness of microgeneration systems. To this end Annex 54 incorporated new efforts on the development of control strategies for microgeneration equipment and systems.

1.2 Review of Annex 42 Model Format

A primary focus of Subtask B of Annex 42 was the development of cogeneration models for use within existing whole-building simulation programs [1]. The models created by Annex 42 were implemented into existing tools such as ESP-r, TRNSYS, and EnergyPlus. These cogeneration models were used in conjunction with the simulation tools' existing capabilities (for modeling the building envelope, plant components,

electrical systems, etc) to assess the technical, environmental, and economic performance of the residential cogeneration technologies.

The main requirement for the models developed within Annex 42 (from a user's perspective) is to accurately predict the thermal and electrical outputs of the residential cogeneration devices as well as to correctly simulate their interaction with the building's envelope, thermal plant, and electrical systems. Essentially, this meant that the device models had to be able to interact with the other technical domains of the building simulation tool on a time-step basis.

Additionally, the Annex 42 device models needed to be of a form capable of being coupled to models of associated plant components, such as hot-water storage, peak-load boilers and heaters, circulating pumps and fans, radiators and air-handling units, etc. The interconnection of these components was necessary for systems models which were coupled to models that predict the building's thermal and electrical demands.

Typical uses for the component and associated integrated systems models developed include:

- Annual simulations for quantifying energy consumption and associated carbon emissions.
- Seasonal simulations where the objective is to analyse the performance of a building and systems over a particular subset of the year.
- Weekly simulations where the operation of the building and its systems is examined in more detail, analysing performance characteristics such as on/off cycling, overheating and under-heating, response to significant daily variations in climate, and thermal comfort.
- Systems analysis simulations in which the performance of environmental systems is examined in fine detail, perhaps examining the transient performance with different operational settings, different component parameters or component configurations.

Consequently, the Annex 42 cogeneration models had to be capable of being used in simulations with significantly different objectives and operate with time-steps that were on the order of a few seconds to a few minutes and were suitable for conducting simulations over durations ranging from a day up to a year.

The prime movers receiving most treatment traditionally have been reciprocating engines, normally internal combustion engines and stirling engines, as well as fuel cells. Detailed examples of cogeneration models employed for energy use simulations can be found in [2] and [3].

1.3 Modelling Strategy

The energy and mass flows in ICE or SE-based cogeneration devices comprise:

- convective and radiant heat release from combustion of fuel in air;
- convective heat transfer with the flow of reactant and product gases, and coolant;
- energy storage in the engine block and other thermally massive components;
- conductive heat transfer across heat exchangers, and possible latent heat recovery from the combustion gases;
- mechanical shaft power produced by the engine, and used by fluid-handling equipment; and

- electrical power produced by the system's alternator, and used by the system'selectric motors to drive fluid handling equipment.

During the operation of an ICE or SE cogeneration device, energy is converted betweenthermo-chemical, thermo-fluid, mechanical and electrical domains. However for the generalized model topology described in this section, many of the energy exchanges were captured in the performance map, and only those energy exchanges that interact with other balance of plant components were of interest. This modelling approach therefore aggregated the internal energy exchanges into two empirical correlations that describe the system's part-load electrical and thermal efficiencies.

1.3.1 Model Topology

Three control volumes are used to model the cogeneration unit dynamic thermal characteristics:

- the *energy conversion control volume* represents the engine working fluid, combustion gases and engine alternator, this control volume feeds information from the engine unit performance map (in the form of a heat flux) into the thermal model;
- the *thermal mass control volume* represents the aggregated thermal capacitance associated with the engine block and the majority of the heat exchanger shells; and
- the *cooling water control volume* represents the cooling water flowing through the device and the elements of the heat exchanger in immediate thermal contact.

The energy flows between these control volumes are depicted in Fig. 1

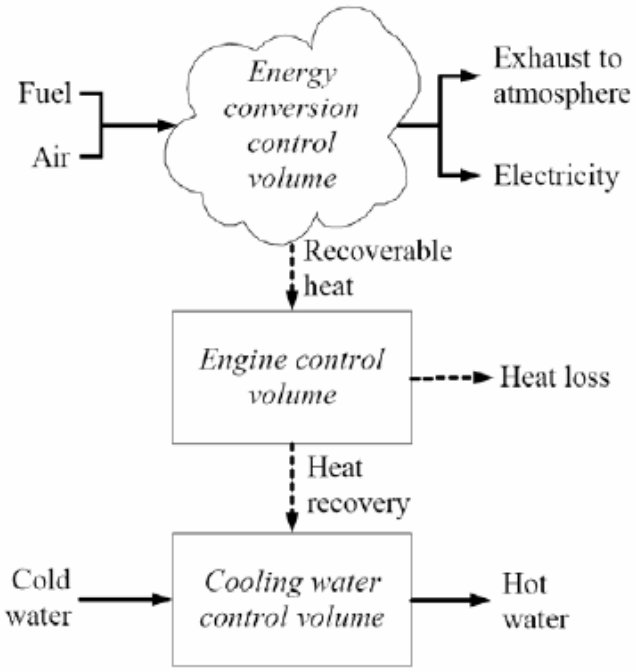

Fig. 1: Combustion cogeneration model control volumes.

1.4 Model Calibration

Two models for simulating the performance of residential-scale cogeneration devices [1] often serve as reference models and serve as a basis for comparisons of units and systems. One of these models treats fuel cell systems while the other treats combustion-based systems (Stirling engines and internal combustion engines).

Previous models for fuel cell systems and combustion-based systems were developed using a "grey box" approach, wherein the structure of the model generally corresponded to the basic underlying physical processes. However, many of the characteristic equations used in the models take the form of parametric equations describing the relationships between key input and output parameters. One of the models also features equations that describe time-varying characteristics such as dynamic heat exchange. Each of these parametric equations requires the input of empirical constants that characterize the performance of subsystems of specific cogeneration devices. The establishment of these empirical constants is known as the process of model *calibration*.

1.4.1 Experimental Work and Calibration

The present Annex 54 will make use of the model formats developed previously [1] in order to provide a common basis for comparison, as well as to facilitate effective and efficient experimental planning. In terms of existing models a total 13 separate investigations were conducted on devices of the following types:

- Solid oxide fuel cell (SOFC);
- Polymer exchange membrane fuel cell (PEMFC);
- Stirling engine (SE);
- Internal combustion engine (ICE);

In some cases these experimental programmes were conducted prior to the establishment of the experimental protocol, but where possible the protocol was adhered to for the purposes of collecting data suitable for model calibration purposes.

The scope of Annex 54 is such that basic built environment type models for balance of plant purposes, or chilling or cooling operations such as with trigeneration have become highly relevant. Consequently, experimental characterization of units or equipment in roles beyond that of the microgeneration prime mover must be modelled in a compatible fashion. Device modules for equipment such as thermal storage tanks, absorption chillers, lithium ion batteries etc are sought so that energy use systems can be simulated with familiar built environment modelling tools such as ESP-r, TRNSYS, Energy Plus, as well as on other computational platforms.

1.5 Report Outline

Subtask A will report on some laboratory tests to acquire new and/or updated performance data using established testing protocol and modelling methods for a number of micro-generation and energy storage devices. The data emerging from these tests will be used for calibration and validation of existing models.

New balance of plant models (i.e. Lithium-ion battery storage and a thermally-activated-cooling device) will be developed where necessary.

New control algorithms for the optimum operation of single device systems, hybrid (multi-source systems), poly-generation and systems incorporating storage and DSM will be developed. The new algorithms will be expected to optimise performance against both local energy needs and within the context of wider heat and power networks. The dwelling and device models developed in Subtask B of Annex 42 will be used as the test-bed for this activity.

It will be readily seen that the set of established prime movers for micro-CHP has not significantly changed in the past few years, so that the updated focus of the present Annex is more directed at auxiliary system components for energy storage, aimed at a more optimal system efficiency, as well as investigations on system configurations and control schemes with a view to overall energy use savings.

This report documents the experimental investigations of residential cogeneration systems conducted within Annex 54, any ensuing calibration of these device models using these data, as well as modelling efforts of expanded scope which consider a diverse number of energy use system configurations, conceived and optimized in view of regional climatic factors, local energy contexts as well as associated impinging policy environments.

2 Model Updates and Technical Progress

What follows is a compilation of material which reports on projects and research undertaken to update and advance the state of the art of micro-cogeneration modeling. The material is organized by class of model, which consist of cogeneration device models encompassing any tests and experiments for model calibration, balance of plant models and complete system models (balance of plant and generator) classified according to generator. A separate section is also included at the end describing work on control systems and logic for microcogeneration systems.

Table 1 below summarizes the various devices which were modelled over the course of Annex 54. What can be seen is that aside from two studies on fuel cells and one on an internal combustion engine, that seven out of these ten studies were focused on auxiliary functions of thermal or electrical storage, dehumidification and a photovoltaic unit. Similarly, balance of plant models were primarily focused on a system with cooling and thermal storage.

Table 1: Summary of Device Models and Balance of Plant Models covered in Annex 54

Devices	Organization
Water – Water Heat Pump	KIER
Fuel Cell	
Photovoltaic Thermal	
Air Source Heat Pump Model	U Strathclyde
PEM Fuel Cell Model	Carleton U
Lithium-ion battery model	NRC
Desiccant wheel	U Sannio
Thermal Storage	
Variable speed ICE	U Marche
Air Source Heat Pump Model	2U Napoli
Balance of Plant	
Solar cooling system coupled to a chiller	E NEA
Tank storage with phase-change material	U Trieste

Table 2 continues the summary of Annex 54 activities, showing a list of complete system models developed, as well as projects where control strategies were investigated for residential energy systems. It can be seen that all manner of systems are being considered as the various conditions which determine their viability such as energy context, local climate, politically based subsidies, housing characteristics and social factors,

all have a real bearing on ultimately what becomes effective as a system. Beyond system design, comes system operation, and with the growing understanding that a fair amount of customization can be expected for residential energy systems incorporating microgeneration, a well thought out control strategy or a detailed control algorithm can be a key feature of an economically viable commercial product.

Table 2: Summary of Complete System Models and System Control Models reported in Annex 54

Complete Systems	**Organization**
Solar Thermal Model	NRCan
Hybrid IC Engine/ HE Furnace uCHP	
Hybrid IC-Furnace	
Hybrid Microgeneration System with Electric Vehicles	
PV system design approach	TU Eindhoven
Microcogenerator based on ICE	U Sannio
Systems - ICE/boiler/solar thermal	TU Munich
Cogeneration system for an Apartment Building based on Distributed Heat storage technology	Japanese Group
Water Heater models for use in city-level energy use simulations	
High solar concentrator model	U Marche
Optimal strategies for hybrid systems made up of HCPV and micro-CCHP devices	
Control Algorithms	
Alternative algorithms for dispatching a virtual power plant	FfE
Control Strategies for Cogeneration systems with Lithium-ion batteries	NRC
Optimal operation of cogeneration devices for Imbalance reduction	KU Leuven

As will be demonstrated in the sections here which follow, the scope of components relevant to modeling micro CHP systems greatly expanded over term of Annex 54, especially when compared to previous endeavors in this sector. This evolution has been in recognition of the requirements for overall energy-use efficiency for residences, and the understanding that variability in climate, political and energy contexts all contribute to the ultimate configuration of systems. Consequently, significant emphasis has been placed on energy storage, as optimizing efficiency with either a thermally-led or electrically-led system naturally leads to situations where the temporal load demands leads to instances where excesses of heat or electricity have to be handled. As such, the interplay and compatibility of devices has become an important

research topic. In view of this, the subsection 2.4 of Section 2 of this report focuses on control logic and systems for micro-cogeneration.

It has also become evident that the scale of the CHP system is critical in determining its economic viability; as such single residence applications may restrict the benefits of a broader implementation of micro-cogeneration. In addressing questions of scale, a number of systems are considered on a community or shared level, and the logistics and control of such systems are introduced in this report with work done by the participating group from Japan

The subject of incorporating micro-cogeneration systems into trading schemes via virtual power plants is also being studied and implemented. Micro-CHP is recognized as a contributor to power grids. In keeping with currently evolving trends towards a more decentralized distribution grid, the flexibility and interconnectability, for purposes of trade, power stability and quality, as well as delivery scheduling are all relevant items associated with microgeneration

The emergence of microgeneration, and its impact on various local electrical and energy environments, is reflected by the accompanying large recent increase in activity in governmental policy instruments being enacted to support adoption of these technologies, as well as to regulate their use in the broader energy context. Extensive up-to-date information on developments in this area can be found in the Annex 54 report from Subtask C : "A Comparative Review of Microgeneration Policy Instruments in OECD Countries".

2.1 Device and Calibration Models

2.1.1 Introduction to Korea Institute of Energy Research (KIER) Models

There are three main components which were observed for separate effect tests. All of them are tested under TRNSYS platform. In this study, the main components employed are Type 668 of water to water heat pump using manufacture data, CanmetENERGY eCOGEN PEMFC, and Type 563 of PVT.

Type 668: Water – Water Heat Pump (KIER, Korea)

General Description

This component models a single-stage heat pump. The heat pump conditions a one liquid stream by rejecting energy to (cooling mode) or absorbing energy from (heating mode) a second. This model is based on user-supplied data files containing catalog data for the capacity and power draw, based on the entering load and source temperatures.

Type668 operates in temperature level control much like an actual heat pump would; when the user defined control signal indicates that the unit should be ON in either heating or cooling mode, it operates at its capacity level until the control signal values changes.

Nomenclature

Table 3: Variable of heat pump model

Variable	Unit	Description
COP	[-]	The heat pump coefficient of performance in either heating or cooling mode
$Cap_{heating}$	[kJ/hr]	Heat pump heating capacity at current conditions.
$Cap_{cooling}$	[kJ/hr]	Heat pump cooling capacity at current conditions.
$\dot{P}_{heating}$	[kJ/hr]	Power drawn by the heat pump in heating mode
$\dot{P}_{cooling}$	[kJ/hr]	Power drawn by the heat pump in cooling mode.
$\dot{Q}_{absorbed}$	[kJ/hr]	Energy absorbed by the heat pump in heating mode.
$\dot{Q}_{rejected}$	[kJ/hr]	Energy rejected by the heat pump in cooling mode
$T_{source,in}$	[ºC]	Temperature of liquid entering the source side of the heat pump.
$T_{source,out}$	[ºC]	Temperature of liquid exiting the source side of the heat pump.
$T_{load,in}$	[ºC]	Temperature of liquid entering the load side of the heat pump.
$T_{load,out}$	[ºC]	Temperature of liquid exiting the load side of the heat pump.
$\dot{m}_{source}$	[kg/h]	Mass flow rate of the liquid on the source side of the heat pump.
Cp_{source}	[kJ/kg.K]	Specific heat of the liquid on the source side of the heat pump.
$\dot{m}_{load}$	[kg/h]	Mass flow rate of the liquid on the load side of the heat pump.
Cp_{load}	[kJ/kg.K]	Specific heat of the liquid on the load side of the heat pump.

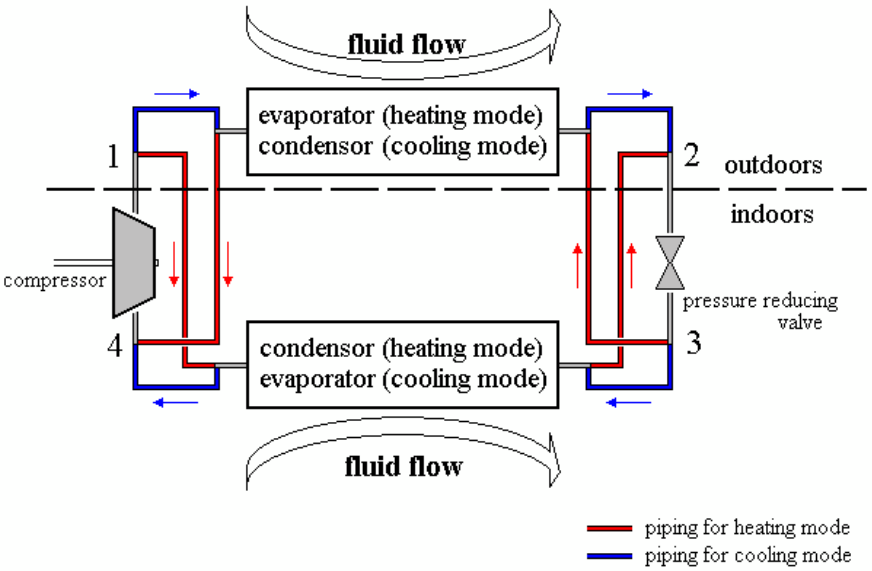

Fig. 2: Heat pump schematic

Detailed Description

A heat pump is a device that transfers energy from a low temperature source to a higher temperature sink. It differs from a pure refrigeration cycle in that the end result of the application could be either to heat or cool depending upon the direction that the refrigerant is currently flowing through the system. [4] Fig. 2 shows a schematic diagram of a heat pump system.

The numbered points on the diagram correspond to the refrigerant states shown on the psychrometric chart in Fig. 3.

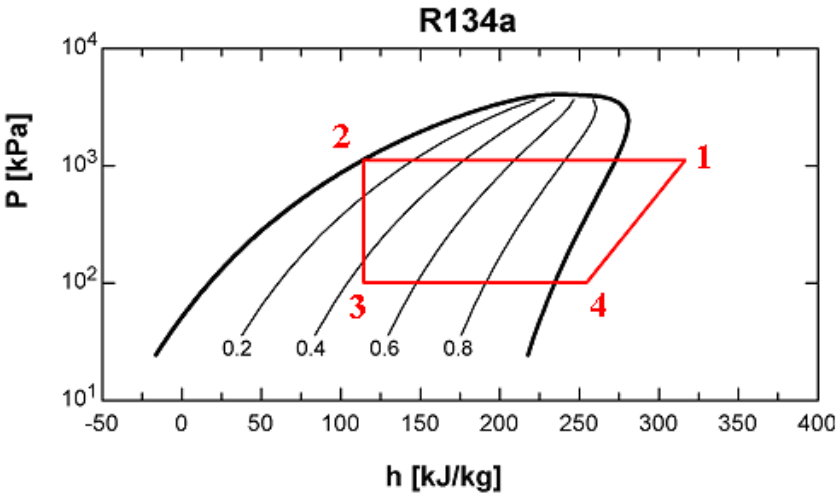

Fig. 3: A generic heat pump cycle

Type668 is not a first principals model but relies instead upon catalog data readily available from heat pump manufacturers. At the heart of the component are two data files: a file containing cooling performance data, and a file containing heating performance data. Both data files provide capacity and

power draw of the heat pump (whether in heating or cooling mode) as functions of entering source fluid temperature and entering load fluid temperature.

Both data files use the standard format for TRNSYS data files as outlined in Section 3.4.2 of Volume 1 of the TRNSYS documentation set. As such, Type668 is able to interpolate data within the range of input values specified in the data files. It is, however, not able to extrapolate beyond the data range and will print a warning in the TRNSYS list file and simulation log if conditions fall outside the data range.

Cooling Performance Data

An example cooling performance data file is provided for use with Type668. The file can be found in \Catalog_Data\WWHPs\Sample\Samp_C.dat. Users creating their own performance data must adhere closely to the syntax of the sample file. The values of entering load temperature must all appear (in ºC) separated by spaces on the first line of the data file. The values of entering source temperature must all appear on the second line of the data file (again in ºC and again space delimited). Users may specify more or fewer values of each of these two independent variables than are shown in the sample file but must also remember to modify the corresponding PARAMETER in the TRNSYS input file. The values of both cooling performance measures (capacity in kW and power drawn in kW) and must then appear, each pair on its own line.

Heating Performance Data

The specification of heating performance data is much the same as for cooling performance data. Two measures of heating performance must be provided in the heating performance data file. These are: total heating capacity (in kW), and power consumed (also in kW). Type668 linearly interpolates between heating performance measures based on the current values of the entering source fluid temperature (in ºC) and the entering load fluid temperature (in ºC).

An example heating performance data file is provided for use with Type668. The file can be found in ..\Catalog_Data\WWHPs\Sample\Samp_H.dat. Users creating their own performance data must again adhere closely to the syntax of the sample file. The values of entering load temperature must all appear (in ºC) separated by spaces on the first line of the data file. The values of entering source temperature must all appear on the second line of the data file (again in ºC and again space delimited). Users may specify more or fewer values of each of these two independent variables than are shown in the sample file but must also remember to modify the corresponding PARAMETER in the TRNSYS input file. The values of both cooling performance measures (capacity in kW and power drawn in kW) and must then appear, each pair on its own line.

Heat Pump Performance

The Type668 heat pump is equipped with two control signals, one for heating and one for cooling. The model does not generate a warning if the user sets both control signals to 1. However, heating mode takes precedence over cooling mode. If the heating and cooling control signals are both ON, the model will ignore the cooling control signal and will operate in heating mode.

If the heat pump is determined to be ON in heating mode (INPUT 6 set to 1), Type668 calls the TRNSYS Data subroutine with the entering source and load fluid. The Data routine accesses the heating performance

data file (specified by the user as a logical unit number in the input file) and returns the machine's heating capacity and power draw. The heat pump's COP in heating is given by equation 1.

$$COP = \frac{Cap_{heating}}{\dot{P}_{heating}} \quad (1)$$

The amount of energy absorbed from the source fluid stream in heating is given by equation 2.

$$\dot{Q}_{absorbed} = Cap_{heating} - \dot{P}_{heating} \quad (2)$$

The amount of energy rejected by the source fluid stream in cooling is given by equation 3 and 4.

$$T_{source,out} = T_{source,in} - \frac{\dot{Q}_{absorbed}}{\dot{m}_{source} Cp_{source}} \quad (3)$$

$$T_{load,out} = T_{load,in} - \frac{Cap_{heating}}{\dot{m}_{load} Cp_{load}} \quad (4)$$

If the heat pump is determined to be ON in cooling mode (INPUT 5 set to 1), Type668 operates in much the same fashion as in heating mode. It calls the TRNSYS Data subroutine with the entering source and load fluid. The Data routine now accesses the cooling performance data file (specified by the user as a logical unit number in the input file) and returns the machine's cooling capacity and power draw. The heat pump's COP in cooling is given by equation 5.

$$COP = \frac{Cap_{cooling}}{\dot{P}_{cooling}} \quad (5)$$

The amount of energy rejected by the source fluid stream in cooling is given by equation 6 and 7.

$$T_{source,out} = T_{source,in} - \frac{\dot{Q}_{rejected}}{\dot{m}_{source} Cp_{source}} \quad (6)$$

$$T_{load,out} = T_{load,in} - \frac{Cap_{cooling}}{\dot{m}_{load} Cp_{load}} \quad (7)$$

Water-to-water Heat Pump Performance Data

In heating mode, the coefficient of performance (COP) of heat pump is affected by several factors such as source temperature, load temperature, and part load ratio, as presented on Table 4 and Fig. 4. COP increases when the source (water inlet) temperature increases, the load temperature decreases, and part load ratio increases.

Table 4: Water to water heat pump performance data in heating mode

Source Temperature (°C)	Load Temperature (°C)	Total Heating Capacity (kW)	Power Consumption (kW)	COP
-3.89	29.44	13.91	4.08	3.41
-1.11	29.44	15.17	4.11	3.69
4.44	29.44	17.45	4.08	4.28
10	29.44	19.79	4.07	4.86
15.56	29.44	22.14	4.19	5.28
21.11	29.44	24.6	4.33	5.68
26.67	29.44	27.32	4.42	6.18
32.22	29.44	30.1	4.51	6.67
-3.89	35	13.53	4.69	2.88
-1.11	35	14.79	4.69	3.15
4.44	35	17.01	4.66	3.65
10	35	19.3	4.65	4.15
15.56	35	21.58	4.78	4.51
21.11	35	23.98	4.95	4.84
26.67	35	26.65	5.05	5.28
32.22	35	29.37	5.15	5.7
-3.89	43.33	13.21	5.8	2.28
-1.11	43.33	14.29	5.64	2.53
4.44	43.33	16.46	5.61	2.93
10	43.33	18.65	5.6	3.33
15.56	43.33	20.85	5.75	3.63
21.11	43.33	23.19	5.95	3.9
26.67	43.33	25.77	6.07	4.25
32.22	43.33	28.37	6.2	4.58

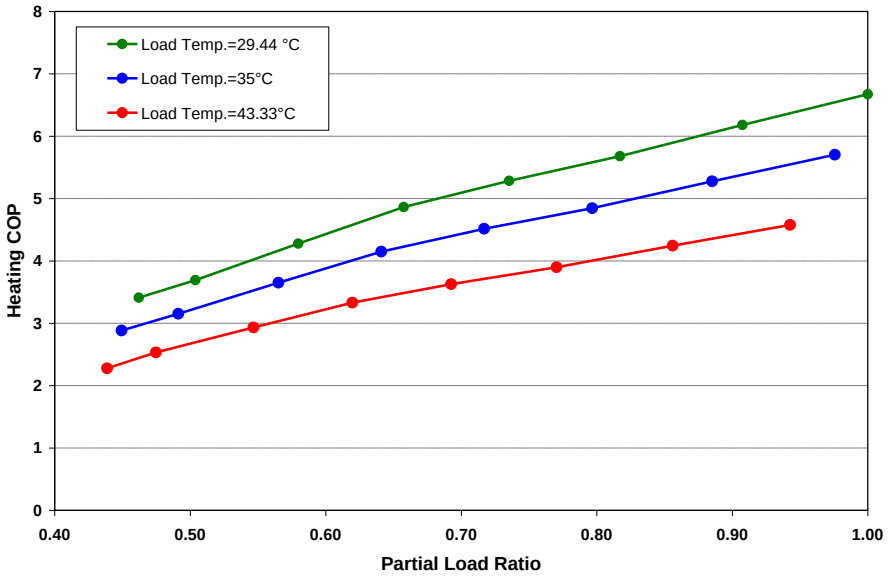

Fig. 4: GSHP performance at partial load in heating mode

Conversely in cooling mode, COP decreases when the source (water inlet) temperature increases, the load temperature decreases, and part load ratio increases, as shown this following Table 5 and Fig. 5.

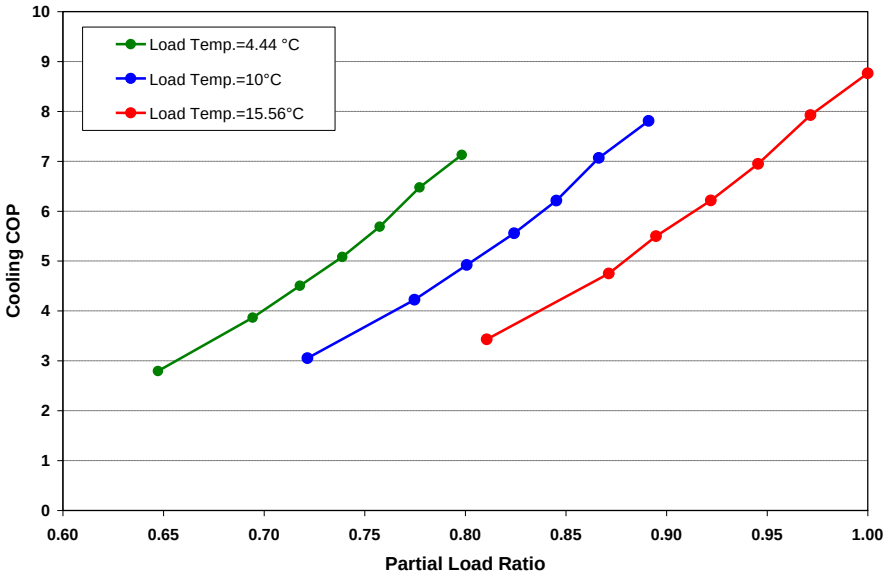

Fig. 5: GSHP performance at partial load in cooling mode

Table 5: Water to water heat pump performance data in cooling mode

Source Temperature	Load Temperature	Total Cooling Capacity	Power Consumption	COP
°C	°C	kW	kW	
4.44	4.44	9.44	1.325	7.13
10	4.44	9.19	1.42	6.47
15.56	4.44	8.96	1.575	5.69
21.11	4.44	8.74	1.72	5.08
26.67	4.44	8.49	1.885	4.5
32.22	4.44	8.21	2.125	3.87
43.33	4.44	7.66	2.74	2.79
4.44	7.22	9.81	1.34	7.32
10	7.22	9.53	1.435	6.64
15.56	7.22	9.3	1.59	5.85
21.11	7.22	9.08	1.74	5.22
26.67	7.22	8.81	1.905	4.63
32.22	7.22	8.52	2.145	3.97
43.33	7.22	7.95	2.765	2.88
4.44	10	10.54	1.35	7.81
10	10	10.25	1.45	7.07
15.56	10	10	1.61	6.21
21.11	10	9.75	1.755	5.56
26.67	10	9.47	1.925	4.92
32.22	10	9.16	2.17	4.22
43.33	10	8.54	2.795	3.05
4.44	12.78	11.2	1.35	8.3
10	12.78	10.95	1.45	7.55
15.56	12.78	10.63	1.61	6.6
21.11	12.78	10.37	1.755	5.91
26.67	12.78	10.07	1.925	5.23
32.22	12.78	9.74	2.17	4.49
43.33	12.78	9.12	2.795	3.26
4.44	15.56	11.83	1.35	8.76
10	15.56	11.49	1.45	7.93
15.56	15.56	11.19	1.61	6.95
21.11	15.56	10.91	1.755	6.21
26.67	15.56	10.59	1.925	5.5
32.22	15.56	10.31	2.17	4.75
43.33	15.56	9.59	2.795	3.43

Fuel Cell (KIER, South Korea)

It is well known that fuel cell performance is directly related to the multi-physic processes taking place within the fuel cell stack. Electrochemical reactions, chemical reactions, mass and charge transport as well as heat transfer occur all at the same time and are tightly coupled. Detailed first-principle based methods are useful, but are fairly complex and time consuming to develop. TRNSYS has a PEMFC (Proton Exchange Membrane Fuel Cell) component model readily available for use. This TRNSYS model is largely mechanistic,

with most terms being derived from theory or including coefficients that have a theoretical basis. However, it does not include a reformer model which can be used to model a FC with natural gas as fuel as the one installed in Canmet test facility. In addition, it requires more than 20 inputs including detailed cell and stack dimensions, hydrogen pressure and flow, heat transfer coefficient for FC stack to ambient, evaporation rate of process water. These inputs and critical processing values are difficult to obtain, as one must disassemble the unit and install instrumentation inside the fuel cell enclosure which may affect the internal control algorithms and operations.

It is due to the above reasons that empirical-based multiple non-linear regression method was chosen to model a fuel cell unit. This approach has the same principle as the "performance map" method described in. Although, the proposed approach relies almost entirely on empirical data, it has significant advantage over the detailed modelling approach due to the simplicity of the model; easy of calibration and reduced data collection burden.During the operation of a fuel cell, energy is converted between thermo-chemical, thermo-fluid, mechanical and electrical domains. However, in this modelling approach, only those energy exchanges that interact with other balance of plant components are of interest. It aggregates the internal energy exchanges into two empirical correlations that describe the system's electrical and thermal efficiencies.

The CanmetENERGY eCOGEN laboratory is well-equipped for measuring electrical/thermal performance and exhaust emissions of micro-CHP devices. A PEMFC (1 kWe and 1.5 kWth) was installed and commissioned at the CanmetENERGY eCOGEN laboratory in Ottawa, Canada [5]. For testing purposes, the fuel cell was instrumented to measure performance and emissions. All instrumentation was installed outside the FC enclosure to ensure that the data collection in no way interfere the FC unit control and operation.

Testing has been divided into three phases, steady-state testing baseline testing, steady state testing under a matrix of varying parameters, and transient state performance testing. Currently, some of the steady-state baseline-testing results are available. The testing covered the operation range of AC power at 500 W, 750 W and 1000 W. Experimental data collected from the system indicate that electrical and thermal efficiencies are a function of FC electrical power generation, cogeneration water inlet temperature and flow rate as shown in Equations 8 and 9.

$$\begin{aligned}\eta_{el} &= f(P_{el}, F_{wtr}, T_{wtr\_in}) \\ &= a0 + a1 \times P_{el} + a2 \times F_{wtr} + a3 \times T_{wtr\_in} \\ &= +a4 \times P_{el}^{2} + a5 \times F_{wtr}^{2} + a6 \times T_{wtr\_in}^{2} + a7 \times F_{wtr} \times T_{wtr\_in}\end{aligned} \quad (8)$$

$$\begin{aligned}\eta_{th} &= f(P_{el}, F_{wtr}, T_{wtr\_in}) \\ &= b0 + b1 \times P_{el} + b2 \times F_{wtr} + b3 \times T_{wtr\_in} \\ &= +b4 \times P_{el}^{2} + b5 \times F_{wtr}^{2} + b6 \times T_{wtr\_in}^{2} + b7 \times F_{wtr} \times T_{wtr\_in}\end{aligned} \quad (9)$$

where:

Pel – Fuel cell DC power set-point, W

Fwtr - Fuel cell co-gen water flow, L/min

Twtr_in - Co-gen water entering fuel cell, °C

Further, for fuel cell with internal control of cooling water flow rate, it can be calculated by:

$$F_{wtr} = f(P_{el}, T_{wtr\_in}) = c0 + c1 \times P_{el} + c3 \times T_{wtr\_in} \quad (10)$$

Once the efficiencies are obtained, the required fuel input energy, fuel flow rate and the co-gen cooling water outlet temperature can be determined by the following equations:

$$Q_{fuel} = \frac{P_{el}}{\eta_{el}} \quad (11)$$

$$F_{fuel} = \frac{P_{el}}{\eta_{el} \times LHV} \quad (12)$$

$$T_{wtr\_out} = T_{wtr\_in} + \frac{Q_{th}}{(F_{wtr} \times \frac{1}{60 \times 1000}) \times \rho \times C_p} \quad (13)$$

And the FC thermal power is calculated by:

$$Q_{th} = \eta_{th} \times Q_{fuel} = \eta_{th} \times \frac{P_{el}}{\eta_{el}} \quad (14)$$

where:

LHV	-	Fuel low heating value, J/m^3
Qth	-	FC thermal power, W
ρ	-	Co-gen water density, kg/m^3
C_p	-	Co-gen water specific capacity, kJ/kg°C

The coefficients obtained by using multiple non-linear regression method are listed in Table 6, and comparison between the measured and calculated values are shown in figures Fig. 6 - Fig. 8. The electrical and thermal efficiencies as a function of cogen water inlet temperature at 1 kWe AC power generation are illustrated in Fig. 9.

It should be noted that, after the preliminary testing, improvement of the testing rig and instrumentation were carried out. Further testing at different output power levels and co-gen water inlet temperatures is currently underway. The fuel cell model will be re-calibrated by the new testing data when it becomes available and will be used in the second round of study. Additionally, constrains introduced by changing of operating points and operation modes, if any, will be examined and considered in the model.

Table 6: Coefficient for fuel cell electrical and thermal efficiencies and co-gen water flow rate

Coefficient	Variables	Electrical Efficiency $0 \le \eta el \le 1$	Thermal Efficiency $0 \le \eta th \le 1$	Co-gen Water Flow (L/min)
a0, b0, c0		0.4039	0.4429	-0.3617
a1,b1, c1	P_{el}	1.736 x 10-4	-4.112 x 10-4	0.00056256
a2, b2	F_{wtr}	-0.2926	2.2681	-
a3, b3, c3	T_{wtr_in}	-0.0035	-0.0034	0.0125
a4, b4	P_{el2}	-4.059 x 10-8	-8.996 x 10-8	-
a5, b5	F_{wtr2}	-0.0468	-0.6021	-
a6, b6	T_{wtr_in2}	6.925 x 10-5	-4.244 x 10-5	-
a7, b7	$F_{wtr} * T_{wtr\_in}$	0.005	-0.0179	-

PEMFC Calibration Results and Performance

Based on the empirical-based multiple non-linear regression method and equations described in previous section , the natural gas flow rate, cogen water outlet temperature and fuel cell thermal power were calculated for the 1 kWe PEMFC. The calculated results were compared to measured data and are shown in the following figures.

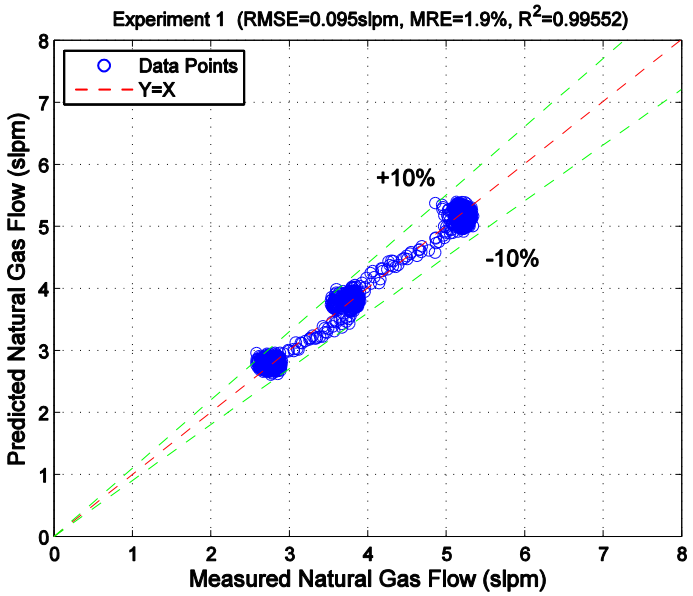

Fig. 6: Predicted versus measured fuel cell natural gas flow

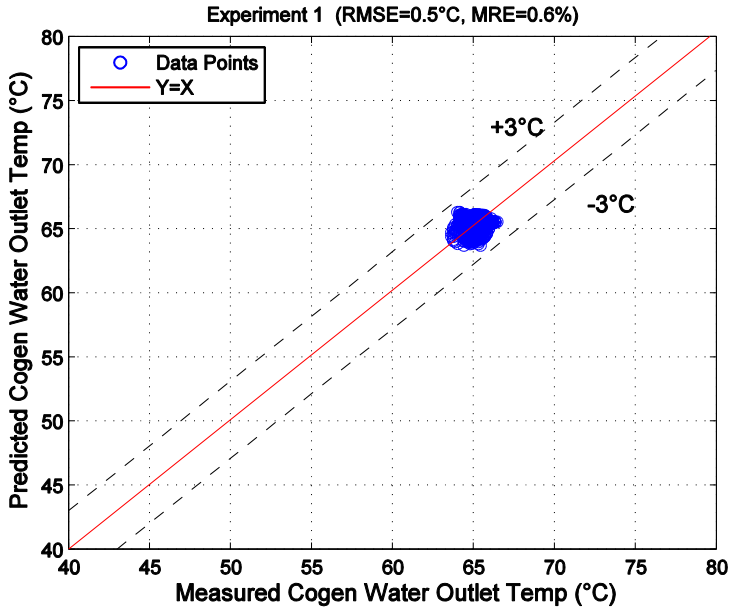

Fig. 7: Predicted versus measured fuel cell cogen water outlet temperature

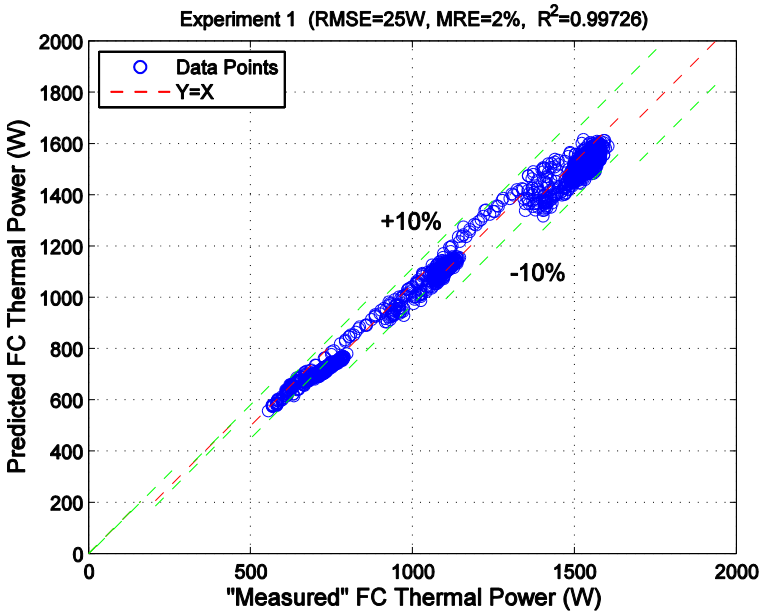

Fig. 8: Predicted versus "measured" fuel cell thermal power (calculated based on cogen water flow and temperatures)

Fig. 9 shows that the efficiency of fuel cell is mainly affected by water inlet temperature. Electrical efficiency slightly decreases in the range of 5°C to 25°C water inlet temperature, whereas in the condition of above 25°C, the electrical efficiency increases up to 40%. On the contrary, thermal efficiency slightly increases up to 62% in 20°C water inlet temperature. On the water inlet temperature of above 20°C, the thermal efficiency will be extremely dropped down to 15%.

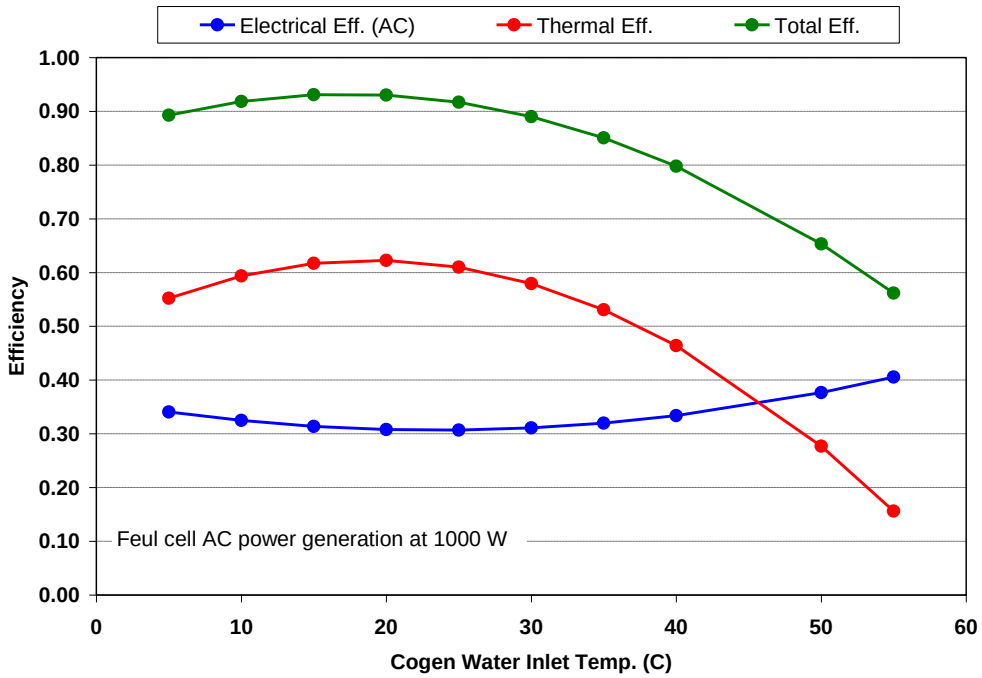

Fig. 9: PEMFC efficiency at 1000 We AC power generation

Photovoltaic Thermal (PVT) (KIER, South Korea)

PVT has two purposes, first generates electrical power from PV cells and secondary provides heat to a fluid passing through tubes located below the absorber plate. Fig. 10 illustrates PVT schematic which consists of PV cells on the top, following by adhesive substrate layer then absorber plate. Underneath the absorber plate, there are installed flow tubes to absorb the heat from the plate and transfer it to fluid. The PV cells are cooled due to the heat transfer to the fluid thus the generated power is increased (and so is the PV electrical efficiency).

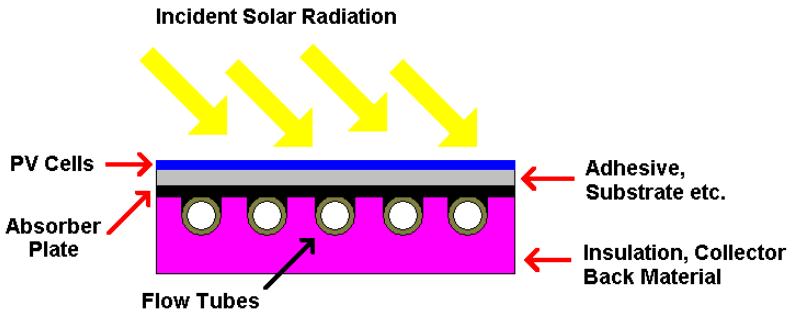

Fig. 10: PVT Schematic

The simplest way to model the PVT panels' electrical and thermal efficiency is to use performance map method. The efficiencies can be described as a function of solar irradiance as well as the temperature difference between fluid inlet and ambient based on experiment tests. Reference [6] reported electric and

thermal performance curves under laboratory test conditions for a PVT module “PVTtwin”. However, the derived thermal efficiency was based on the average fluid temperature through the collector instead of the inlet fluid temperature. Therefore it is difficult to use it directly to develop a performance-map based PVT model, as iterations are required to solve the outlet fluid temperature.

TRNSYS provides three major types of PVT models – Type 50, Type 555 and Type 56(mode). All of these models are largely theoretical based. These TRNSYS PVT models were reviewed under IEA, Solar Heating and Cooling Program, Task 35 [5]. It was reported that Type 50 models contain serious error which limit their usability. Although modified, more reliable generic PVT models have been produced based on Type 50 by IES-SHC Task 35 [5], problems were encountered during attempts in using them in the present study. Type 555 (for air collectors only) and Type 56 (mode) models are updated and more reliable versions of the Type 50 models and they can be adapted for building integrated systems [5].

Based on the above extensive search, it was decided to use Type 563 to model PVT panels in Case 6 in this round of study. The relating efficiency of the PV cell of this model has linear factor with the cell temperature and incident solar radiation. In addition, it assumed that the cells are operated at maximum power condition. As this PV/T collector model (Type 563) can be connected to the multi-zone building model (Type 56) in TRNSYS, the impact of the collector on heating and cooling loads can be evaluated. More information and mathematical description of the PVT model are available in TRNSYS manual [7].

The Type 563 model was validated by manufacturer specification and experiment data obtained from [3]. Detailed validation results are described in Appendix.

PVT TRNSYS Model (Type 563) Validation

The PVT model type 563 is validated based on the measurement test of PV/T model ˝PVTWIN 422˝ provided by Katic [6]. The manufacture collector specification; dimension, maximum electrical and thermal output of PVTWIN 422 collector is presented in Table 7. The electrical and thermal outputs are based on 1000 W/m^2 and 25 $^{\circ}C$ values for irradiance and ambient temperature, respectively. Fig. 11 and Fig. 12 present predicated thermal efficiency and DC electrical power output from TRNSYS model (type 563) based on tested experimental data provided by Katic [6]. The results show a good agreement between simulated results and experimental data for electrical energy output with accuracy more than 90%. Moreover, the output thermal energy performance of TRNSYS model achieves a good agreement with tested data with error less than 10% for $T_{red} > 0.02$. The error increases at low T_{red} value. The main reason for that is due high thermal uncertainty of the experimental data for $T_{red} < 0.02$, especially when the outlet, inlet and ambient temperature are became close and this can be happened early in the morning or after sunset. The dash region in Fig. 11 presents the operating condition during the daytime with high thermal accuracy.

Table 7: Manufacture’s specification of PVTWIN422 collector

Dimensions Collector-box (m)	Aperture (m^2)	Electrical output (W)	Thermal output (W)
1.895*1.895	2.56	295	1535

Table 8 and Table 9 include the simulated and experimental data used to generate Fig. 11 and Fig. 12.

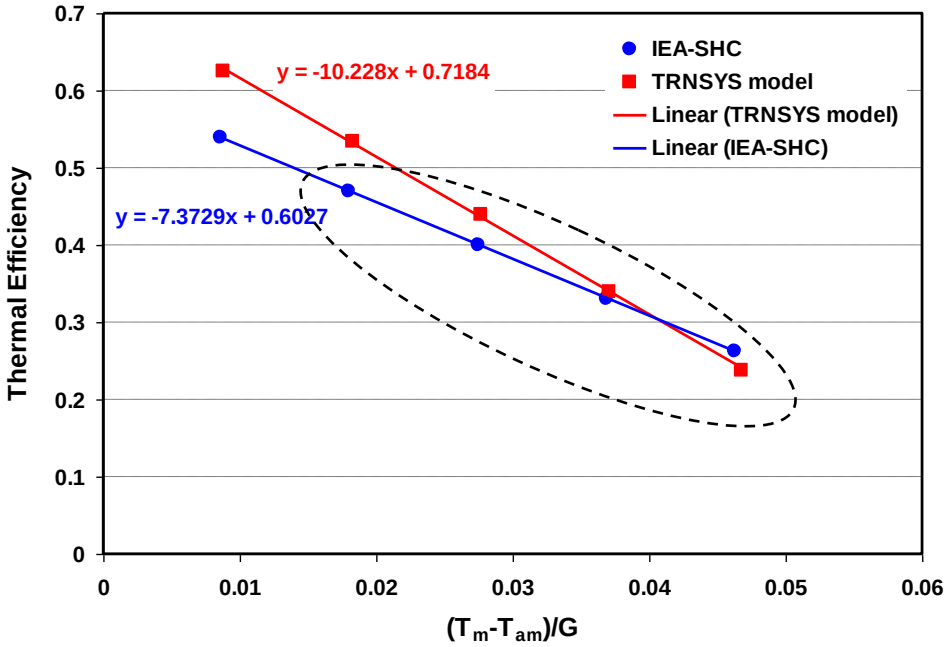

Fig. 11: Validate thermal efficiency of TRNSYS model with measured data (IEA-SHC-Task 35).

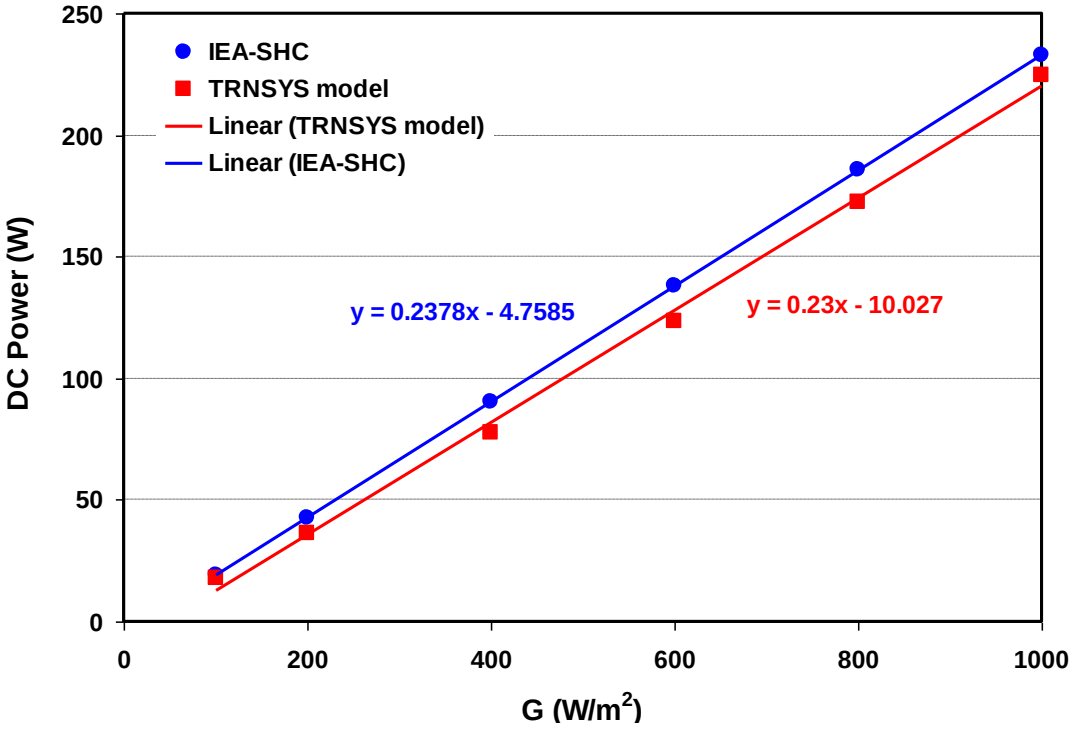

Fig. 12: Validate PVT electrical power of TRNSYS model with measured data (IEA-SHC-Task 35).

Table 7: Manufacture's specification of PVTWIN422 collector

Dimensions Collector-box (m)	Aperture (m^2)	Electrical output (W)	Thermal output (W)
1.895*1.895	2.56	295	1535

Table 8: Simulation and experimental data of thermal efficiency at different inlet temperature

	TRNSYS model		IEA-SHC
T_{in}	T_{red}	Efficiency	Efficiency
30	0.00882	0.625	0.54
40	0.0183	0.534	0.47
50	0.0277	0.439	0.4
60	0.0371	0.34	0.33
70	0.0467	0.237	0.262

Where

$T_{red} = (T_m - T_{am})/G$

T_m is the mean fluid temperature (˚C)

T_{am} is ambient temperature (˚C)

G is irradiance (W/m^2)

T_{in} is inlet fluid temperature (˚C).

Table 9: Simulation and experimental data of DC electrical output power at different irradiance

	Power DC (W)	
G (W/m^2)	TRNSYS model	IEA-SHC
100	17.6	19
200	36.5	42.8
400	77.8	90.4
600	123	138
800	173	185
1000	225	233

TRNSYS Model (Type 563) Input/ Output Parameter

Table 10 - Table 11: TRNSYS model (type 563) input

Parameter	Value	Unit
Inlet flow rate	3*60/row	kg/hr
Incidence angle	45	degrees
Collector slope	45	degrees
Top loss convection coefficient	26	kJ/hr.m^2.K
Fluid heat transfer coefficient	1800	-

Table 12 show different input/output parameter values used in TRNSYS model (type 563) for validation study based on provided experimental data by Katic.

Table 10: TRNSYS model (type 563) parameter

Parameter	Value	Unit
Collector length	1.6	M
Collector width	1.6	M
Absorber plate thickness	0.001	M
Thermal conductivity of the absorber	1400	kJ/hr.m.K
Number of tubes	26	-
Tube diameter	0.0254	M
Bond width	0.01	M
Bond thickness	0.001	M
Bond thermal conductivity	1386	kJ/hr.m.K
Resistance of substrate material	0.0003	$h.m^2.K/kJ$
Resistance of back material	5	$h.m^2.K/kJ$
U-value of roof material	0.95	$kJ/hr.m^2.K$
Fluid specific heat	4.19	kJ/kg.K
Reflectance	0.03	Percentage
Emissivity	0.7	Percentage
1st order IAM	0.1	-
PV cell reference temperature	25	C
PV cell reference radiation	3600	$kJ/hr.m^2$
PV efficiency at reference condition	0.12	Percentage
Efficiency modifier - temperature	-0.02	1/C
Efficiency modifier - radiation	0.0001	$h.m^2/kJ$

Table 11: TRNSYS model (type 563) input

Parameter	Value	Unit
Inlet flow rate	3*60/row	kg/hr
Incidence angle	45	degrees
Collector slope	45	degrees
Top loss convection coefficient	26	$kJ/hr.m^2.K$
Fluid heat transfer coefficient	1800	-

Table 12: TRNSYS model (type 563) output

Temperature at outlet	Unit
Flow rate at outlet	kg/hr
Useful energy gain	kJ/hr
PV power	kJ/hr
PV efficiency	Percentage
Thermal efficiency	Percentage
Collector FR	-
Mean PV temperature	C
Mean fluid temperature	C
Incidence angle modifier	-
Collector top losses - convective	kJ/hr
Collector top losses - radiative	kJ/hr
Collector back losses	kJ/hr
Absorbed solar radiation	kJ/hr
Overall heat loss coefficient	kJ/hr.m^{2}K
FRTAN	-
FRUL (Heat Transfer Coeff.)	kJ/hr.m2K

PVT Helios Type I3A235P Modeling Using TRNSYS Type 94a

PVT Helios Type I3A235P was modeled by using TRNSYS Type 94a to verify the manufacture data on its brochure, as shown at Fig. 13. It was done under the testing conditions as presented in Table 13.

Table 13: Testing conditions of PVT Helios Type I3A235P Using TRNSYS

Parameter	Value
Air Mass	A.M 1.5
Irradiance	STC(1000W/㎡), NOCT(800W/㎡)
Ambient Temp	STC(25℃), NOCT(20℃)

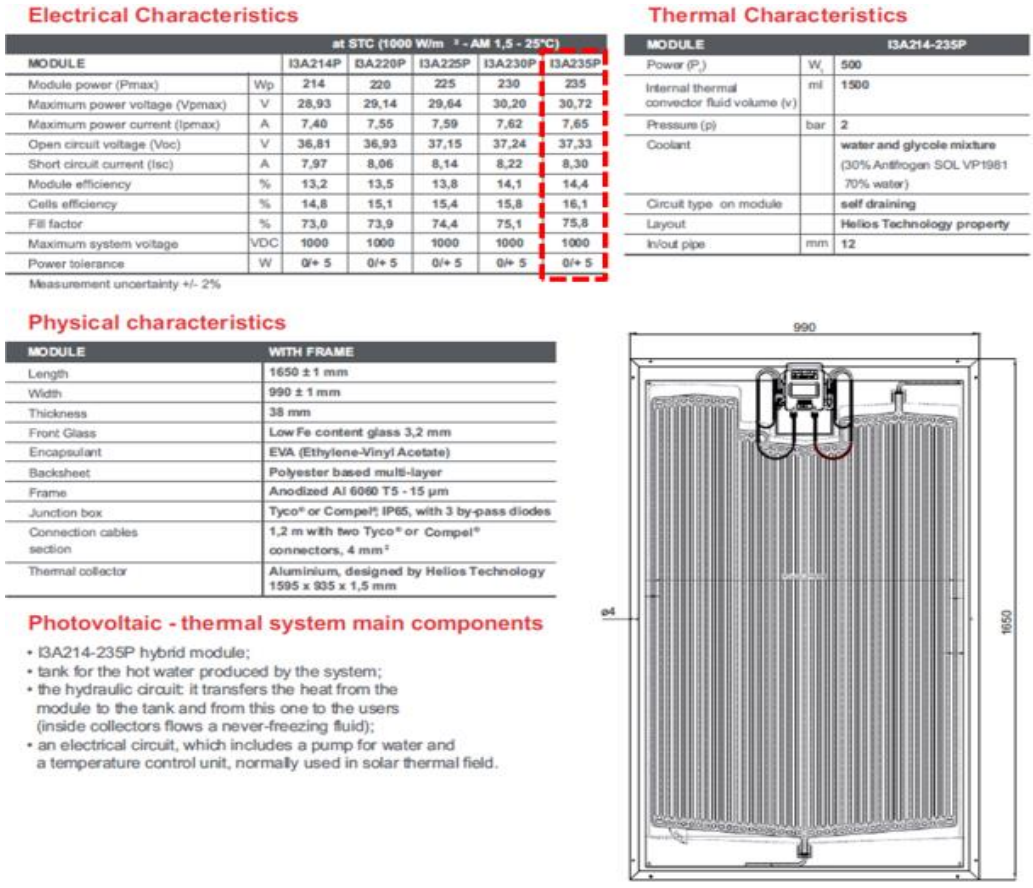

Electrical Characteristics

at STC (1000 W/m ² - AM 1,5 - 25°C)						
MODULE		I3A214P	I3A220P	I3A225P	I3A230P	I3A235P
Module power (Pmax)	Wp	214	220	225	230	235
Maximum power voltage (Vpmax)	V	28,93	29,14	29,64	30,20	30,72
Maximum power current (Ipmax)	A	7,40	7,55	7,59	7,62	7,65
Open circuit voltage (Voc)	V	36,81	36,93	37,15	37,24	37,33
Short circuit current (Isc)	A	7,97	8,06	8,14	8,22	8,30
Module efficiency	%	13,2	13,5	13,8	14,1	14,4
Cells efficiency	%	14,8	15,1	15,4	15,8	16,1
Fill factor	%	73,0	73,9	74,4	75,1	75,8
Maximum system voltage	VDC	1000	1000	1000	1000	1000
Power tolerance	W	0/+ 5	0/+ 5	0/+ 5	0/+ 5	0/+ 5

Measurement uncertainty +/- 2%

Thermal Characteristics

MODULE		I3A214-235P
Power (P_n)	W_n	500
Internal thermal convector fluid volume (v)	ml	1500
Pressure (p)	bar	2
Coolant		water and glycole mixture (30% Antifrogen SOL VP1981 70% water)
Circuit type on module		self draining
Layout		Helios Technology property
In/out pipe	mm	12

Physical characteristics

MODULE	WITH FRAME
Length	1650 ± 1 mm
Width	990 ± 1 mm
Thickness	38 mm
Front Glass	Low Fe content glass 3,2 mm
Encapsulant	EVA (Ethylene-Vinyl Acetate)
Backsheet	Polyester based multi-layer
Frame	Anodized Al 6060 T5 - 15 µm
Junction box	Tyco® or Compel®, IP65, with 3 by-pass diodes
Connection cables section	1,2 m with two Tyco® or Compel® connectors, 4 mm²
Thermal collector	Aluminium, designed by Helios Technology 1595 x 935 x 1,5 mm

Photovoltaic - thermal system main components

- I3A214-235P hybrid module;
- tank for the hot water produced by the system;
- the hydraulic circuit: it transfers the heat from the module to the tank and from this one to the users (inside collectors flows a never-freezing fluid);
- an electrical circuit, which includes a pump for water and a temperature control unit, normally used in solar thermal field.

Fig. 13: PVT Helios Manufacture Data

The simulation testing was done for one panel to observe the effect of voltage to the PV power. The voltage given was in the range of 1 V to 33 V. The PV power was linearly increased as the voltage was increased up to 27 V. At that point, it reached the peak power which was 235.5 Watt as shown in the Fig. 14. On the other hand, as written on the brochure, the maximum power should be 235.1 Watt on the standard testing condition (STC) of 25^{o}C. Therefore, there was 0.4 Watt error or 0.17%.

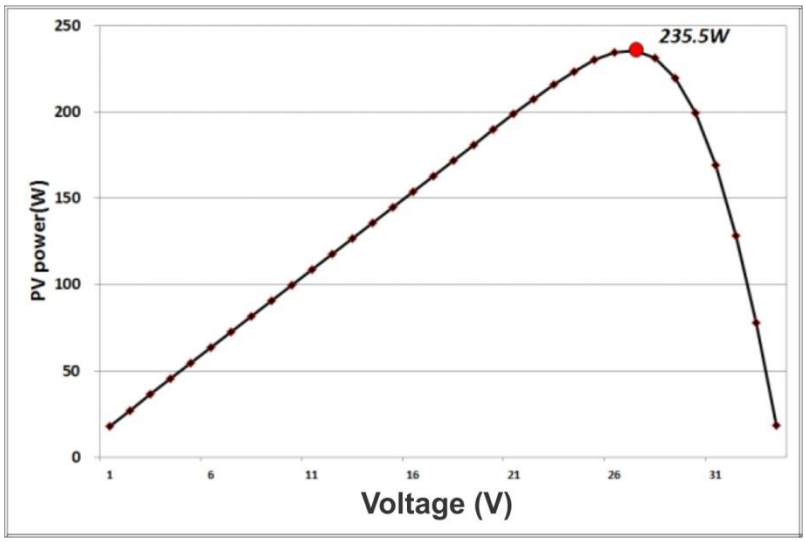

Fig. 14: PVT Helios Characteristics

PVT Efficiency Behavior Testing Using TRNSYS

PVT efficiency behavior was tested using TRNSYS. The PVT chosen was type 560, it was integrated with the other equipments such as heat exchanger, hot water tank, and additional heater as can be seen in the following block diagram on Fig. 15.

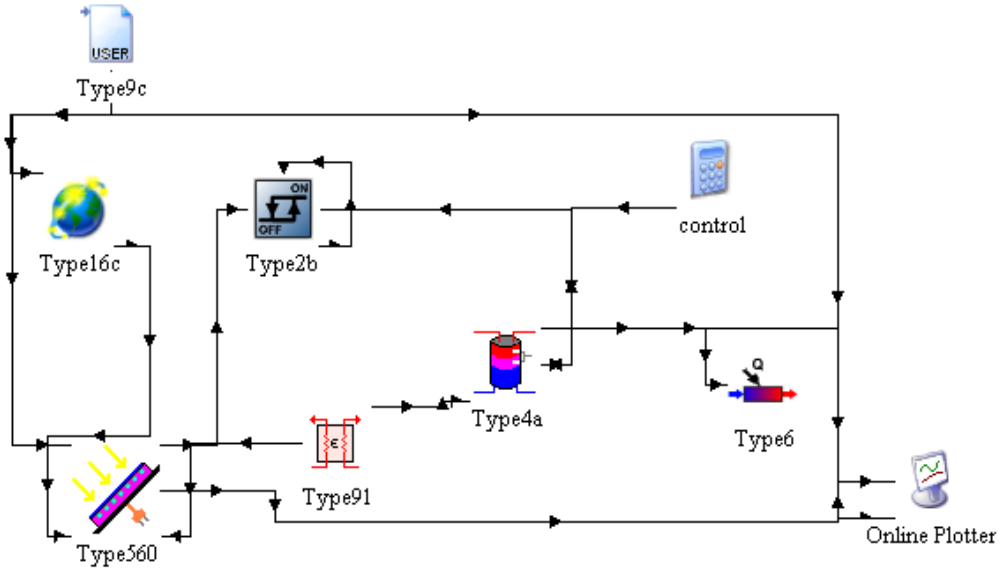

Fig. 15: The TRNSYS block diagram of PVT System

The characteristics of PVT were divided into two types which were thermal collector efficiency and PV power generated affected by inlet water temperature, as shown in the Fig. 16 and Fig. 17 respectively. Fig. 16 shows that the thermal efficiency has the linear trend which is -10.431x + 0.4445 in terms of (Ti-Ta)/It, where Ti is the inlet water temperature, Ta is the ambient temperature, and It is the solar radiance.

From the first curve, it can be concluded that in the same capacity, PVT generates the lower electricity than the PV. However, PVT has the higher the total efficiency because it also produces the thermal energy. Moreover, the second curve indicates that if the decrement of inlet temperature causes the power increment and conversely, the inlet temperature increases as the power decreases.

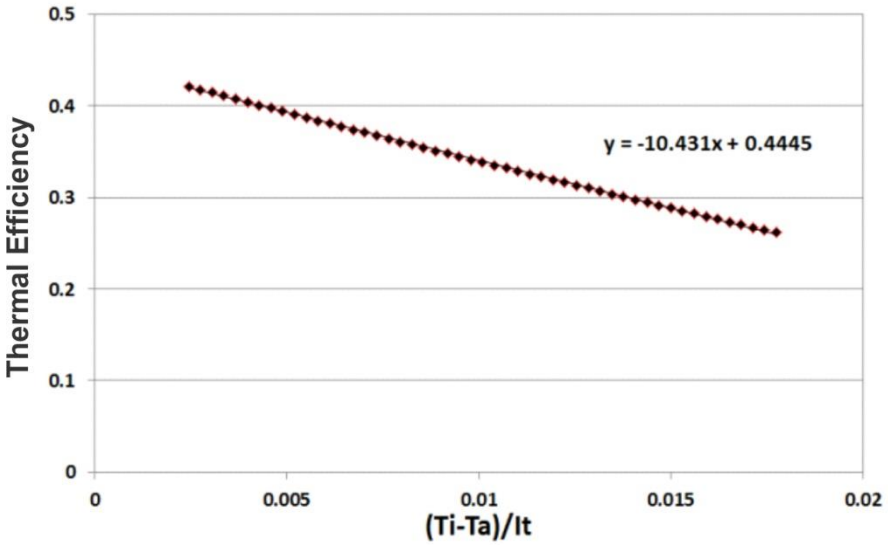

Fig. 16: Thermal collector Efficiency Characteristics

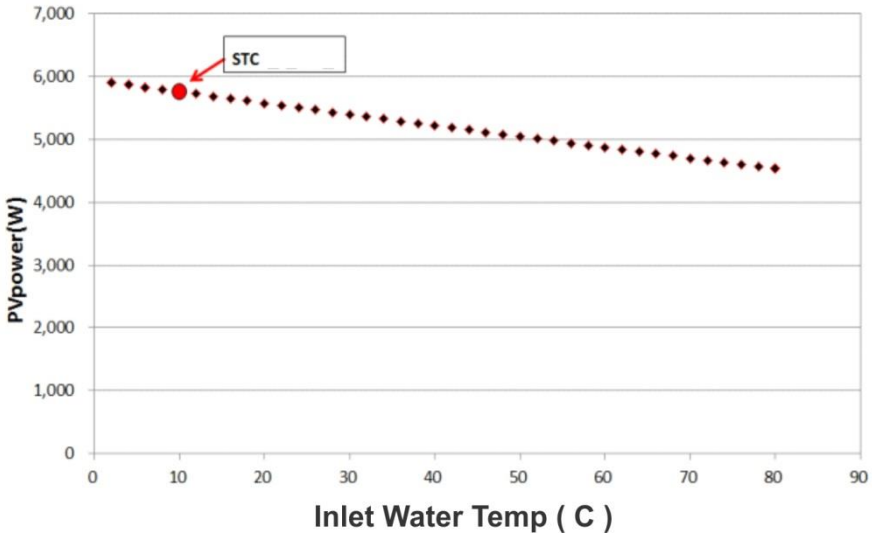

Fig. 17: PV Power Generated vs Inlet Water Temperature Curve

The observation of power generation, thermal generation, and total efficiency of PVT is presented in the Table 14 and Fig. 18 below. Both of them explain that in standard testing condition (STC) if inlet temperature is low, the performance of either thermal or electricity are higher.

Table 14: The characteristics of PVT Efficiency

Inlet Temp (℃)	Power Generation (kW)	Thermal Generation (kW)	Total Efficiency
4	5.9	25.8	0.85
8	5.8	24.8	0.81
12	5.7	23.7	0.78
16	5.6	22.6	0.75
20	5.6	21.5	0.72
24	5.5	20.4	0.69
28	5.4	19.2	0.66
32	5.4	18.1	0.63
36	5.3	17	0.59
40	5.2	15.8	0.56
44	5.1	14.6	0.53
48	5.1	13.5	0.49
52	5	12.3	0.46
56	4.9	11.1	0.43

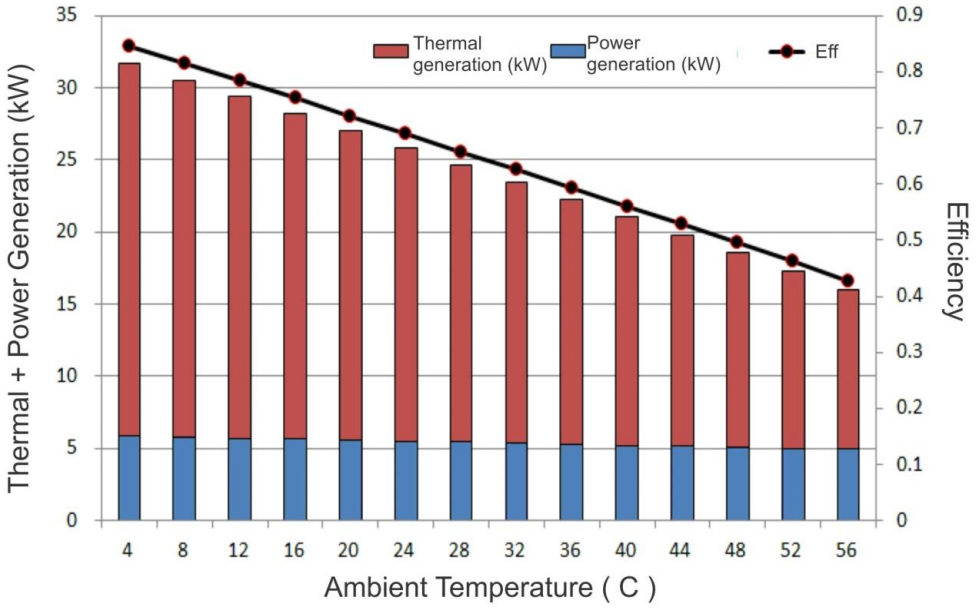

Fig. 18: The characteristics of PVT Efficiency

Temporary Results of KIER Photovoltaic – Thermal System Testing

The PVT installed in KIER laboratory is PVT Helios Type I3A235P . The PVT testing in KIER were divided into three steps called pre-testing, testing, and post-testing. Pre-testing was to test the photovoltaic-thermal system in real experiment by inputting two kinds of inlet water temperature (shown in Table 14), then observing which other parameters are affected, and finally generating the equations of PVT, as shown in the Fig. 19 and Fig. 20.

The testing step was to validate the equations generated in pre-testing step with manufacture data. If this validation has the small error, then the next step, post-testing can be done. The post-testing was to use the validated equations to generate the results without doing the real experiment (Table 15).

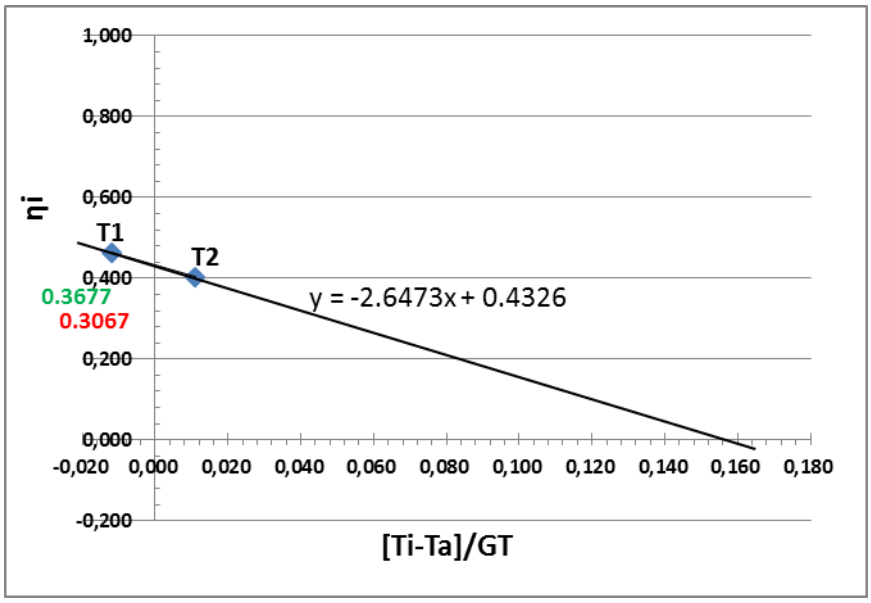

Fig. 19: The efficiency characteristics of solar collector

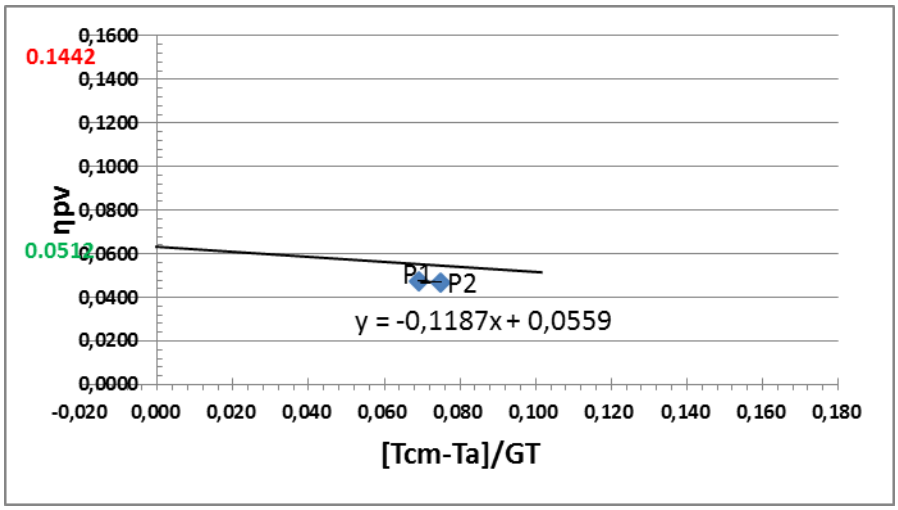

Fig. 20: The efficiency characteristics of PV

Table 15: Test results of KIER PVT

Unit	Pre -Testing 1	Pre-Testing 2	Manufacture Data	Post-Testing
G_T [W/㎡]	500	500	1000	1000
A_C [㎡]	1.63	1.63	1.63	1.63
T_i [°C]	16.8	26.3	49.5	49.5
T_a [°C]	22.5	20.8	25	25
T_{cm} [°C]	57.1	58.3	65	65
$(T_i-T_a)/G_T$ [㎡°C/W]	-0.0114	0.011	0.0245	0.0245
$(T_{cm}-T_a)/G_T$ [㎡°C/W]	0.0692	0.0750	0.0400	0.0400
Q_e [W]	39	38	235	83
η_{pv}	0.0477	0.0470	0.1442	0.0512
Q_t [W]	377	329	500	599
η_i	0.4628	0.4035	0.3067	0.3677

Additional data can be found in the appendix

2.1.2 The Development And Calibration Of An Air Source Heat Pump Model (University of Strathclyde, UK)

Introduction

In the UK, gas boilers are the predominant energy source for heating in housing, due primarily to the ready availability of natural gas. The take-up of heat pumps has lagged far behind Europe and North America. However, with the development of standards for low and zero-carbon housing, gas price rises and the depletion of the UK's natural gas reserves, interest in heat pump technology is growing. Heat pumps, particularly air source heat pumps (ASHP), have the potential to be a direct, low-carbon replacement for gas boiler systems in housing.

In this paper, a model of an ASHP for building a simulation tools is described along with a comparison of the model's predictions against field trial data, indicating that it provided a suitable test bed for energy performance assessment.

The work outlined here makes a number of contributions: develops an air source heat pump model; outlines a straightforward calibration process (based on Annex 42 work); and compares the model's predictions with field trial data.

The model is described in more detail in [8].

Scope of Model

An ASHP device model was developed that could be fully integrated into a larger building and plant model (described later). From a performance analysis perspective, the main requirement for this model was to accurately predict the time-varying electrical demand and thermal output of the device and its explicit interaction the building's envelope, thermal plant, and control systems. The model had to be capable of predicting the key variables that couple the ASHP device to the other constituents of a building simulation model, specifically the hot water output temperature and flow rate. Other outputs of interest included the device's operational status (e.g. on/off cycling, defrost status, temperature compensation, etc.), performance efficiencies, fuel consumption and resulting carbon emissions.

[9] describes a model that fulfilled similar criteria, but that was employed in the modelling of micro-cogeneration devices; this model was adapted for the purposes of this study. The model is best described as 'grey-box', where the structure reflects the underlying physical features of the device; however, its key performance characteristics are approximated using empirically-derived expressions.

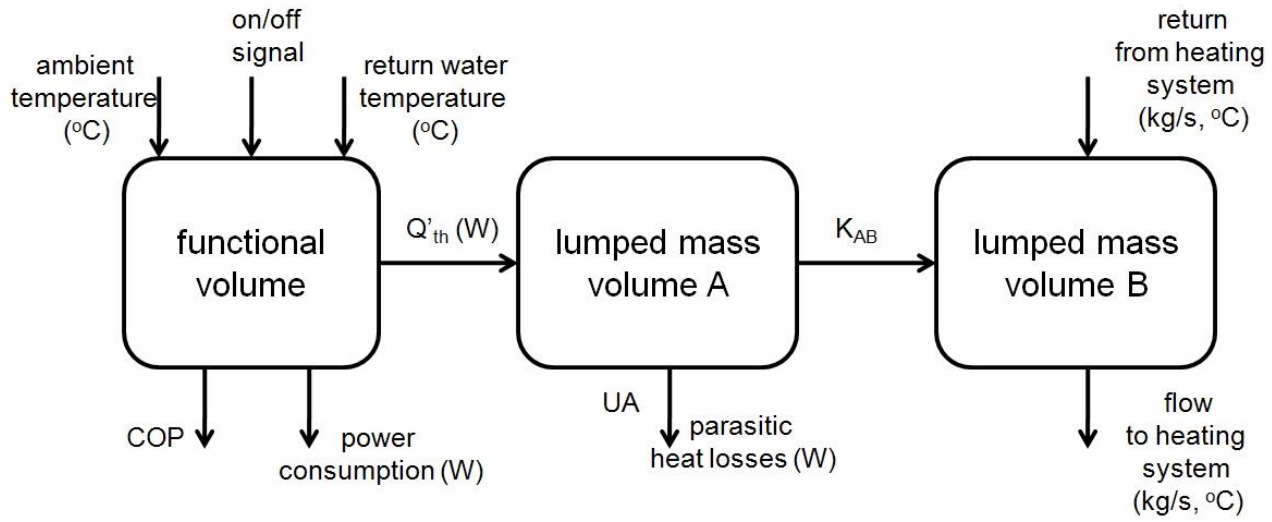

Fig. 21: Diagrammatic representation of the ASHP model.

The model structure comprises three control volumes as shown in Fig. 21. The first (functional) volume is employed to calculate the performance of the refrigerant circuit and auxiliary components. The algorithm underpinning the volume calculates the time-varying COP and the nominal heat output ($\dot{Q}'_{th}$) from the refrigeration cycle using 2nd-order polynomial functions of the heating system return water temperature and the external ambient temperature difference (ΔT) (Equations 15 and 16).

$$COP\ (t) = f_1(\Delta T) \tag{15}$$

$$\dot{Q}'_{th}(t) = f_2(\Delta T) \tag{16}$$

Where:

$$\Delta T = T_{return}\ (t) - T_{\infty}(t) \tag{17}$$

and

$$Q'_{th}(t) = Q_{th}(t) + UA\,[T_A(t) - T_{\infty}(t)] \tag{18}$$

With $\dot{Q}_{th}$ is the heat supplied (W) to the water in the heating circuit; T_{return} is the temperature of the water flowing into volume B; T_A is the temperature (^{o}C) of volume A; UA is the heat loss coefficient (W/K) to the environmental temperature (T_{∞}).

The total instantaneous electrical demand of the device compressor, $\dot{Q}_e$ (W) is calculated as follows:

$$\dot{Q}_e(t) = \frac{\dot{Q}_{th}(t)}{COP\ (t)} \tag{19}$$

The performance map equations were augmented (15)-(19) with algorithms to calculate the defrost status of the device and to modulate the return water temperature set point based on outside temperature.

The heat output from equation (16) is passed to a lumped-capacitance volume (volume A) that essentially represents the thermal capacitance of the device on the refrigerant-side of the condenser. Heat is transferred between this volume and volume B representing the water-side of the condenser. Volume B is also the connecting point to the heating system. Together, these lumped mass volumes enable the transient thermal response of the device to be encapsulated in the model output. The general form of the energy balance for these volumes A and B is as follows

For volume A:

$$M_A c_A \frac{dT\ (t)_A}{dt} = \dot{Q}'_{th}(t) - UA\,[T_A(t) - T_{\infty}(t)] - K_{AB}\,[T_A(t) - T_B(t)] \tag{20}$$

For volume B:

$$M_B c_B \frac{dT\ (t)_B}{dt} = \dot{Q}'_{th}(t) - UA\,[T_B(t) - T_{\infty}(t)] - K_{AB}\,[T_B(t) - T_A(t)] \tag{21}$$

Where M_i is the mass (kg) of volume A or B; T_B is the temperature (^{o}C) of volume B; K_{AB} is the heat exchange coefficient (W/K) between the volumes A and B; and $\dot{m}$ is the flow rate of coolant (kg/s) to volume B; and c is the specific heat of water (J/kgK).

The parameters for the polynomials used in equations 1 and 2 were calibrated using data from laboratory performance tests conducted on the ASHP; these calibrated equations enable the performance

characteristics of the device to be simulated over the range of ambient and flow temperatures experienced during normal operation. The parameters of the capacitance volumes A and B were calibrated using an iterative parametric identification technique described by [9] using high resolution start-up data from the field trial data.

A comparison of the predictions of COP from the calibrated model are shown against measured data (independent of the calibration data set) in Fig. 22.

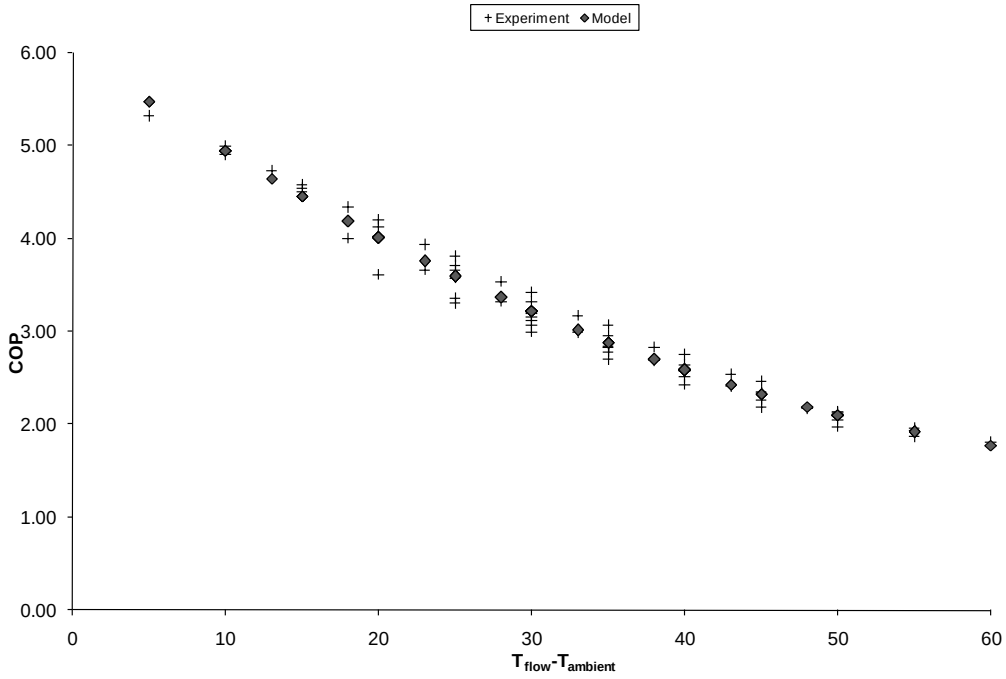

Fig. 22: Calibrated COP characteristics of the ASHP device.

Verification

The ASHP device model was integrated into a larger building and systems model of one of the test houses developed on the ESP-r building simulation tool [10]. The model comprised a detailed representation of the dwelling, the heat pump and heating distribution system. Each individual room was explicitly represented in the model and the constructions used were identical to those in the actual building. The building model was also augmented with a zonal airflow model; this calculated air-exchange between the different spaces within the building and between the building and the exterior according to prevailing wind-driven pressure differences and temperature differences. The model was calibrated to give the same external air leakage rate as that was determined from a blower door test of the actual building (approximately 0.5 air changes per hour).

The heating system was modelled in detail, where all of the heating system's components (radiators, piping, valves, etc.) and their inter-connections are modelled explicitly. A comprehensive description of the basic heating system component models used in this work is given by [10].

The heating system operating 07:00-09:00 and 17:00-22:00 during weekdays and 08:00-23:00 at weekends. The assumption was made that the system was switched off at night rather than reverting to a set back-

temperature (this is common practice in the UK). For the purposes of the heating system comparison, the dwelling's heat gain profiles were normalized to be consistent with the sensible internal heat gains employed in the UK's standard assessment procedure (SAP [DECC, n.d.]) of some 55.7kWh/week.

The integrated ASHP/dwelling model was simulated at a time resolution of 1-minute intervals; this fine temporal resolution was employed to adequately capture the action of control on the operation of the ASHP (e.g. on/off cycling) and other pertinent operations such as defrost and any overheat shutdowns. This temporal resolution has been employed by other researchers, notably [11] who indicated that high resolution modelling was required in order to adequately characterise performance. Finally, as no long-term climate data existed for the Westfield site, the simulations were run with an equivalent Scottish climate data set that was representative of the field trial location.

The model's predictions for heat pump performance were compared to the data collected from the field trials.

Fig. 23 shows the model's predictions of the coefficient of performance (COP) vs. ambient air temperature against averaged COP data from the field trials; this average relationship was derived from the measured COP values from the 8 monitored houses and represents typical ASHP performance under varying conditions of occupancy, climate and internal conditions. As the climate and assumed occupancy for the simulation differed from the exact conditions experienced during the field trials (this data was not captured in the monitoring data) a temporal comparison of simulation and monitored results would not be appropriate. Instead, the comparison looks at whether the range and trend of the COP emerging from the simulations is similar to the averaged trend from the actual houses: this would indicate that the simulation is providing as a suitable test bed for the device in that the operating conditions and resulting performance are similar to those encountered in reality.

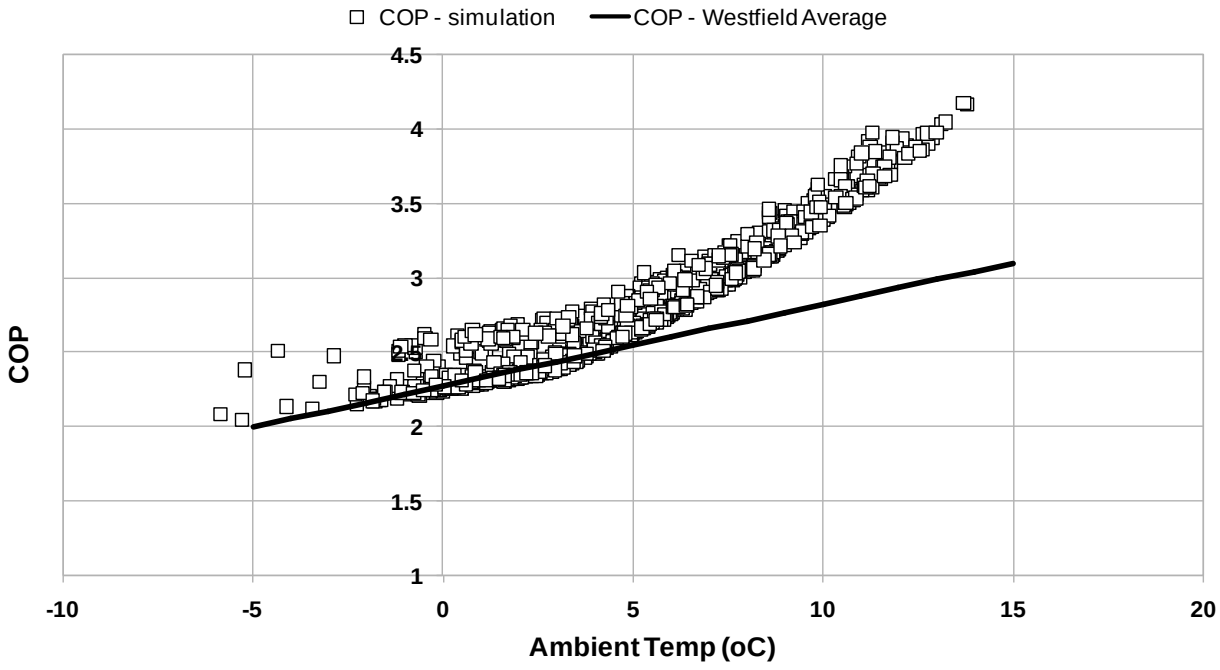

Fig. 23: Ppredicted COP vs Westfield average COP.

The initial simulation results clearly diverged from the monitored data at higher ambient air temperatures (Fig. 23). Closer investigation revealed that the temperature compensation facility on the heat pumps used in the Westfield houses had not been enabled due to an installer error. Consequently, a further simulation was conducted with the temperature compensation disabled in the model. Fig. 24 shows the results from this simulation. It is evident that the low-density scatter in the ASHP model output is predominantly above the average COP line: these points are indicative of the dynamic nature of the model and represent periods when the heating system and building are warming up and where the resulting low heating system flow and return temperatures produce a temporarily high COP. However, the highest density of points is close to the average performance line; corresponding with periods in which the heat pump was operating with the return water temperature close to the set point (45°C); this demonstrates that the ASHP device in the ESP-r model is operating in under similar conditions to those experienced in the actual houses.

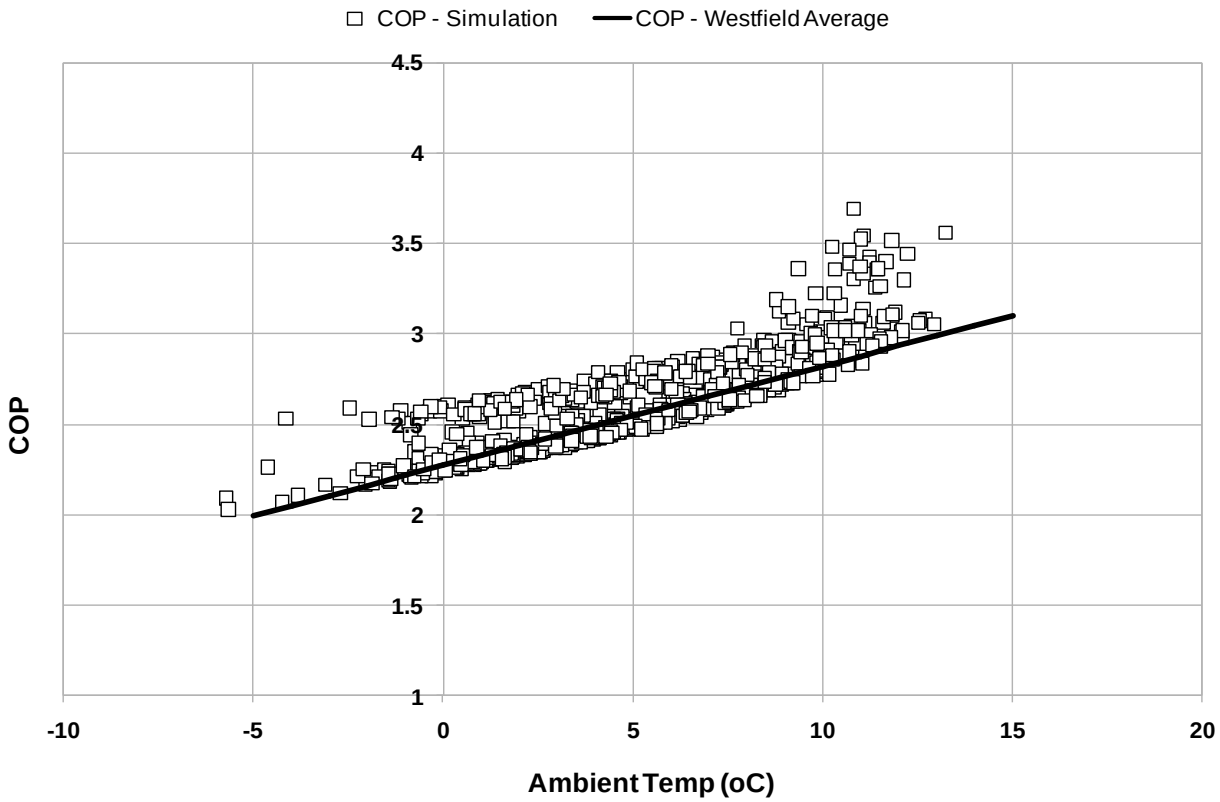

Fig. 24: Predicted COP (no temperature compensation) vs Westfield average COP.

Conclusions

A combination of simulation and field trial data has been used to assess the annual performance of a domestic ASHP heating system when retro-fitted into social housing in Westfield, Scotland.

A detailed ASHP device model has been developed on the ESP-r platform, based on the work of [9]. The model was calibrated using laboratory data and then integrated into a larger whole-building model of one of the Westfield dwellings.

The predictions of COP from the model were compared to data emerging from the Westfield field trial; these initially indicated a divergence between monitored and simulated values. Investigation revealed

some shortcomings in the ASHP installation at Westfield, where outside air temperature compensation was not enabled on the installed units. Adjusting the simulation model to account for this flaw and re-simulating indicated that the model suitably replicated the ASHP operating conditions observed in the field trial.

2.1.3 PEM Fuel Cell Model (Carleton University, Canada)

Prior to this research a fuel-cell micro-cogeneration model was developed by Annex 42 members for whole-building performance simulation [13]. The thermodynamic and chemical processes within a fuel-cell are not explicitly represented by this model, rather, the model relies on calibration to experimental data. This model was calibrated with experimentally gathered performance data from a 2.8 kW_{AC} SOFC by [14] after its development. Although the Annex 42 model was developed to also treat PEMFC devices, it was not calibrated to represent the performance of a PEMFC micro-cogeneration device within the context of Annex 42.

In this research, documented in [12], initially attempted to calibrate the Annex 42 fuel-cell model with new experimentally gathered performance data from a 1kW_{AC} PEMFC. Due to the limitations of the performance data that were gathered and to adequately model the processes specific to the PEMFC that was studiedi was not possible to calibrate the Annex 42 fuel-cell model without adapting it first. The various components of this new model adapted from the Annex 42 fuel-cell model are illustrated in Fig. 25.

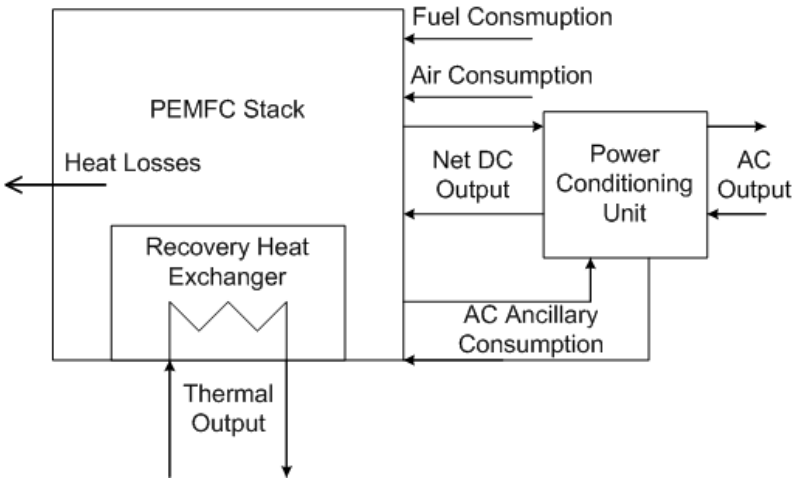

Fig. 25: PEMFC model derived from Annex 42 model by [12]

Experimental data were gathered to characterize all the of the components shown in Fig. 25 over the range of boundary conditions that could be independently controlled (the water temperature entering the recovery heat exchanger and the AC output). A performance map of data was gathered that spanned water temperatures of approximately 15°C to 60°C (at 5°C intervals) and AC outputs of 25%, 50%, 75% and 100% of the maximum electrical output (1 kW_{AC}) to calibrate the model. An adaptation of the performance map given in [12] is shown in Fig. 26 to help illustrate the model calibration procedure and the range of boundary conditions for which data were gathered.

The experimentally gathered data illustrated in Fig. 26 were used to calibrate the thermal output component of the PEMFC model. Each marker from the "data gathered from experiments" set represents a time averaged value from a steady-state experiment that was conducted for approximately 30 (min) where data were sampled every 6 (s). For the calibration procedure, a function of mixed polynomial and exponential form was fit to the data gathered from experiments.

The end result of calibration was the derivation of the coefficients and exponents of this function. These coefficients and exponents are given in [12].

The thermal output values that were calculated by using this calibrated function are plotted on Fig. 26 as well. By inspection it can be seen that these values calculated from the adapted model fit the data gathered from experiments well.

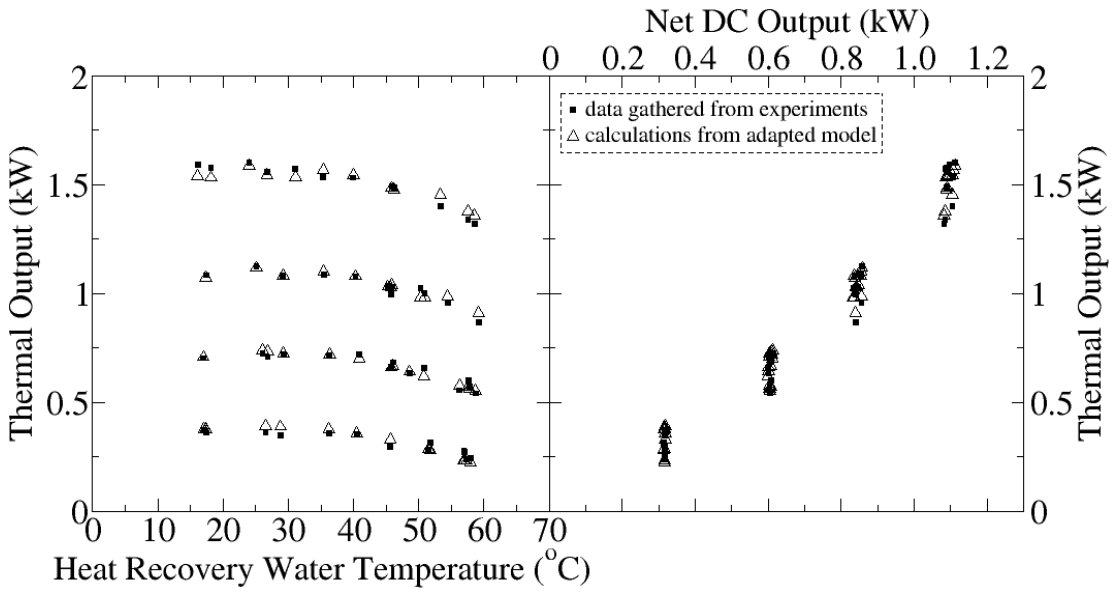

Fig. 26: PEMFC heat recovery data and model predictions adapted from Johnson et al. (2013)

In a procedure analogous to the calibration of the thermal output equation, model equations for the power conditioning unit efficiency, DC electrical efficiency (relative to the LHV of the fuel), AC ancillary power consumption, air consumption, and heat losses were calibrated as well. [12] also found that the maximum rate the DC output could be modulated by was 0.6 (Ws^{-1}). All of these calibrated model equations together constitute a PEMFC model that is suitable for use with whole-building performance simulation. The modified form of the Annex 42 model as described in this work has been implemented into the ESP-r simulation program to make this work accessible to other researchers.

2.1.4 Lithium-Ion Battery Model (National Rresearch Council, Canada)

Introduction – Battery Basics

There are several different approaches to battery modeling, each having their own benefits and limitations. The finite difference approach is the highest level of resolution.

This approach involves the discretization of the anode, cathode and electrolyte of a Li-ion cell. By applying the laws of conservation of mass, momentum and energy, the diffusion of lithium ions through these discretized nodes, driven by the chemical potential gradient between the anode and cathode, is modelled. The model can be specified in all spatial coordinates and unsteady temporal frames. This approach is closely based on Fick's law of diffusion [15]:

$$\frac{\dot{m}_A}{A} = -\vec{D} \cdot C_A \tag{22}$$

where $\frac{\dot{m}_A}{A}$ is the mass flow rate with respect to time per area, D is a proportionality diffusion coefficient in area per time, and C_A is a mass concentration per volume.

The largest advantage to this approach is the ability to accurately capture the true behaviour of a battery's internal resistance, essentially its efficiency, by applying different boundary conditions. This includes the relationship of resistance with current and temperature, other phenomena such as impurities in the manufacturing process, which may lead to ion concentrations on the electrode surfaces, and realistic long-term battery degradation. Limitations to this approach are the same experienced in conventional computational fluid dynamics. These include the truncation of higher order terms in Taylor series expansion, etc. Another limitation is the lack of empirical data, specifically in terms of life cycle degradation, to apply realistic boundary conditions to the model. A drawback limiting an implementation of such a model in this work is the integration of this solver with the rest of a whole building simulation program such as ESP-r [16]. Examples of this modelling approach include that of Darcovich [17] and the VRFB work by Ribberink and Wang [18].

Equivalent Resistive Network Approach

The equivalent resistive network approach is the next level of resolution for battery modelling. This model uses a lumped capacitance approach with state parameters such as DOD and OCV. It characterizes the internal resistance of a battery which, neglecting manufacturing impurities, is a function of current and temperature. Typically, this results in the use of a resistor-capacitor (RC) network to capture the real internal resistance component, from constant current draw, and the imaginary impedance component, from changes in current rates with respect to time, of a battery (see Fig. 27).

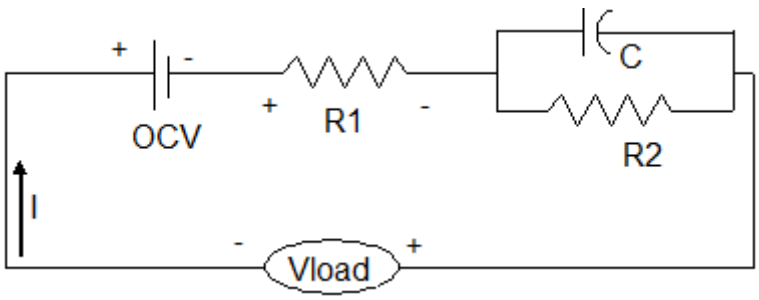

Fig. 27: RC network schematic used in lumped capacitance modeling of Li-ion battery.

This relationship between resistance, current and temperature, while non-linear, has been approached in several ways. Some use polynomial fits to empirical data of charge and discharge curves [19]. This method

tends to neglect the complexity of the resistance and still requires significant data and effort to extract the polynomial coefficients. Others attempt to quantify the value of the equivalent RC network using Nyquist plots [20, 21]. The limitations to the equivalent resistive network model is the lumped capacitance assumption. This assumption does not capture realistic occurrences such as battery degradation due to ion concentrations from impurities in the manufacturing process, and long-term reduction in battery capacity from cycling; although work has been done to include this phenomena as well [18]. Its advantage in the context of this work is that its use of state functions can be integrated within ESP-r's power flow network with ease.

Gao Approach

Recent work by Gao et al. [22], has introduced a new approach based on a lumped capacitance assumption and state variables. This approach uses a reference curve, based on a polynomial curve fit to empirical data, to determine the battery's DOD as a function of OCV. Rather than attempting to derive relationships between current and internal resistance, and temperature and internal resistance, this approach simply scales the reference curve by factors depending on the battery's current and temperature. These factors are measured empirically and are unique to each battery, making this approach potentially general to all battery types. Validation by Gao et al. [22] has shown adequate accuracy using this technique; however, verification and calibration would be necessary in the implementation of such a model.

In analyzing the different battery modelling approaches above, the approach by Gao et al. [22] seems most suitable for an application within ESP-r. The finite difference approach may be the most realistic in capturing true battery behaviour; however, it would require the definition of several quantities and boundary conditions on the electrochemical level. A model using this approach for a VRFB has been somewhat implemented in ESP-r [18].

The second approach of lumped capacitance parameters is the basis of the approach used by Gao et al. [22]. Where the Gao approach differs is in capturing the relationship between internal resistance, current and temperature. In the lumped capacitance approach, the internal resistance and battery capacity is calculated using long empirically-fit polynomials, with coefficients relating to both current and temperature. Extracting the coefficients to properly calibrate a battery would be difficult. Calibrating a model using the Gao approach would only require a set of charge/discharge curves at various currents and temperatures. By this argument, the Gao approach will be used for this work's development of a Li-ion battery model.

The model chosen for this work is based on a lumped-capacitance approach to evaluate the true voltage of the battery, given an applied electric load based on the current and temperature. This approach involves the use of an RC network as shown in Fig. 27.

In an RC network, a portion of the OCV is dropped across a real resistor (labeled R1 in Fig. 27), and a complex resistor/capacitor (labeled R2 and C in Fig. 27) before arriving at the load. The OCV as a function of DOD is expressed as a 5th order polynomial fit to measured data, at a reference temperature:

$$\mathrm{OCV(DOD)} = \sum_{i=1}^{5} E_i \, DOD_i \qquad (23)$$

The real resistor accounts for the resistance due to the magnitude of current and increases linearly with current. The voltage during discharging is then:

$$V\,(t,\mathrm{DOD},I(t)) \;=\; \mathrm{OCV}(\mathrm{DOD}) \;-\; I(t)R_{\mathrm{int}}(\mathrm{DOD}) \qquad (24)$$

where the OCV is measured in Volts, I(t) is the current in Ampere and R_{int} is the internal resistance in ohms. This results in a vertical shift of the voltage as a function of DOD curve, equal to the internal resistance multiplied by the current, as illustrated in Fig. 28.

An RC network is able to capture the impedance of any device, real or complex, by equating the device's real impedance into a resistive load and its complex impedance into a resistor/capacitor load. The resistor/capacitor impedance accounts for internal resistances due to changes in current with respect to time. In general, this impedance captures losses in batteries in a continuous time frame from highly transient currents imposed. This is significant in electric vehicle applications, for example, where "pulse" current or power might be required from the battery on the magnitude of seconds or less. Simulations in ESP-r occur at discrete time-steps in a quasi-steady-state fashion within the time interval. The battery current during the time-step is considered uniform and steps instantly with respect to the next time-step. Although, in reality this is not strictly true since the load is continuously changing. As such, the impedance term in Fig. 27 is removed in this model formulation. Future work should include exploration into the complex impedance contribution from a Li-ion battery under changing current with respect to time, if any exists.

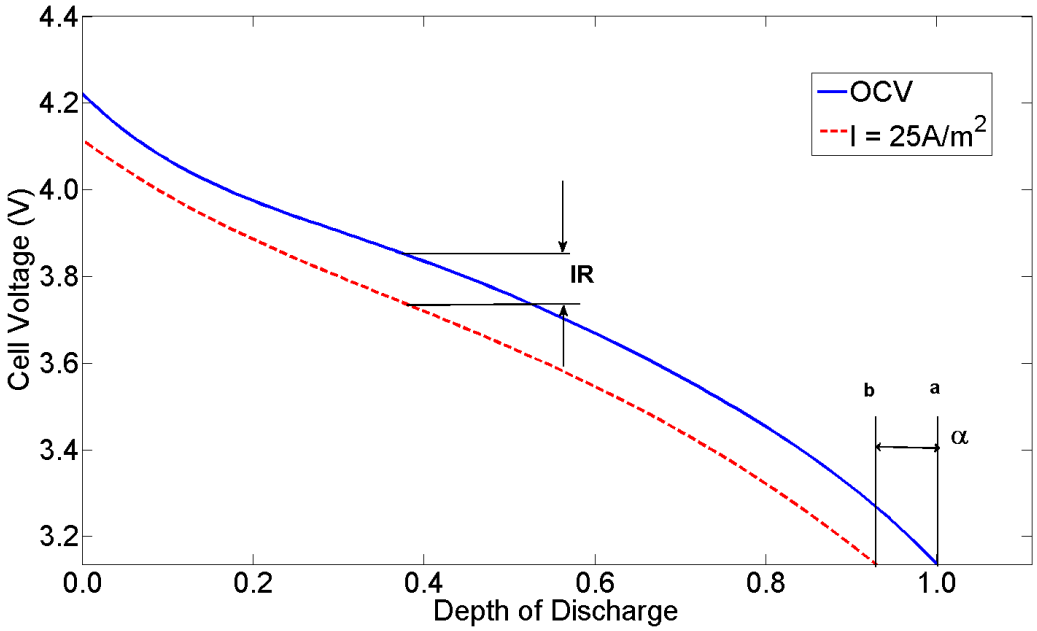

Fig. 28: Transformation of voltage as a function of DOD curve due to an imposed current.

Battery capacity also decreases with increasing current. Where other approaches try to capture this capacity change using another polynomial fit, Gao et al. [22] treats this by measuring the difference in battery capacity between the OCV curve and the voltage curve representing the desired current. This is done at the same reference temperature and is illustrated in Fig. 28. The OCV battery capacity, labelled "a"

in Fig. 28, is the reference capacity, in Ah (if the voltage is assumed to be nominal over the entire discharge). The capacity for the curve at the higher current is labeled “b”. Gao et al. [22] defines a current factor, α, as the ratio of these values.

$$\alpha = \frac{b}{a} \tag{25}$$

Battery temperature plays a similar role as current in the transformation of OCV with respect to DOD. For a charge or discharge at a battery temperature different than the reference, the voltage at the load will be different than the OCV. Gao et al. [8] defines this simply as a V (T) (see Fig. 29).

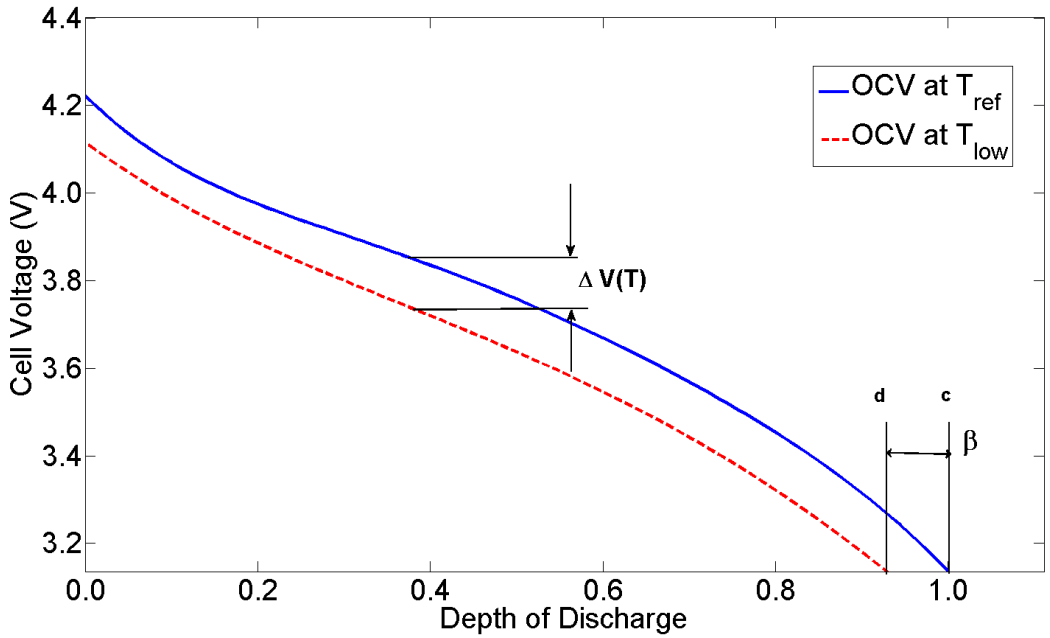

Fig. 29: Transformation of voltage as a function of DOD curve due to a change in temperature.

$$V(t,T) = \text{OCV}(\text{DOD}) + V(T) \tag{26}$$

The battery capacity also increases or decreases with increasing or decreasing temperature from the reference temperature, respectively. Gao et al. [22] defines this as a temperature factor, β, which is the ratio of the battery capacity at its reference temperature, “c”, and the capacity at the battery’s actual temperature, “d”.

$$\beta = \frac{d}{c} \tag{27}$$

The change in DOD of a cell is the change, in percentage, of its capacity. Thus, the DOD at the end of a time-step of a cell discharging at constant current, taking into account effects of current and temperature is then:

$$\mathrm{DOD_{end}} = \mathrm{DOD_{initial}} - \frac{It}{\alpha\beta \mathrm{Cap_{ref}}} \quad (28)$$

where $\mathrm{Cap_{ref}}$ is the reference capacity of a single cell in $\mathrm{A_s}$, I is the discharge current in Ampere, and t is the time-step in s. In charging mode, the second term on the right side of equation 28 would be positive. The cell's capacity, $\mathrm{Cap_{ref}}$ will also vary with the amount of cycles the cell has undergone, as previously discussed. At the end of every time-step, the model will take the absolute value of the change in DOD, DOD and add this to the number of cycles already spent. This will be elaborated further.

Implementation in ESP-r Battery Subroutine

As mentioned, an electric storage model existed in ESP-r prior to the current work. It was developed in a subroutine that is capable of having additional storage models appended to it. A PbA model, using a lumped-capacitance RC approach, and a VRFB, using a basic finite difference approach, exists in this subroutine [18]. The Li-ion battery model developed in this work, using the approach by Gao et al. [22], is appended to this subroutine. At each time-step, the subroutine must calculate if the Li-ion battery will inject or draw electricity into the electrical network node where it is defined, or remain idle.

To determine the battery's contribution, the subroutine begins the simulation by initializing monitoring flags to zero and retrieving the battery's initial state values. The monitoring flags developed in this work for the Li-ion model are over/under voltage flags and over/under temperature flags. These flags are part of the Li-ion BMS to ensure that the voltages and temperatures of the battery remain within safe limits. The initial state values for the Li-ion model are the battery's temperature and DOD. At subsequent time-steps, the monitoring flags are re-assessed. If the temperature and/or voltage is higher or lower than the allowed operating range, the appropriate monitoring flag is turned on. These flags are revisited later in the subroutine. Next, the subroutine retrieves the power demanded from the battery, assigned from outside the subroutine. If this value is positive, by convention, power is required from the battery, and it is placed in discharge mode. If the power demanded is negative or zero, the battery is placed in charge or idle mode, respectively. In charge mode, the power demanded is made positive for the remainder of the subroutine.

The maximum current that the battery can deliver or receive over the next timestep is then calculated. This uses an existing subroutine in ESP-r [18]. This current is limited by the minimum allowable DOD (or voltage) in charge mode, and the maximum allowable DOD (or voltage) in discharge mode. The subroutine calculates the current that would reach these charge/discharge limits using the following:

$$V_{\mathrm{max}} = V_{\mathrm{end}} + (R_{\mathrm{int}} I) \quad (29)$$

$$V_{\mathrm{max}} = V_{\mathrm{end}} + (R_{\mathrm{int}} I)\, V_{\mathrm{min}} = V_{\mathrm{end}} - (R_{\mathrm{int}} I) \quad (30)$$

where V_{max} and V_{min} are the upper and lower cutoff voltages of the battery and V_{end} is the final voltage of the battery at the end of the time-step. The end voltages and internal resistance of the battery are dependent on the current and the final DOD at the end of the time-step. These values for the PbA and VRFB models are calculated using specific approaches in existing subroutines. New subroutines, calculating these

values using the approach by Gao et al. [22] explained above, have been added to include the function of a Li-ion battery.

The maximum current subroutine uses an iteration technique to converge to a final solution. After the maximum current for this time step is determined, the corresponding maximum power is found. Again this takes into account internal resistance and temperature effects in its calculations. The maximum current and power are limits on the battery's capabilities for the time-step. The interested reader is referred to the paper by Ribberink and Wang [18] on how this occurs in more detail.

The Li-ion model then enters its BMS subroutine, developed in this work, to control the battery, and revisit its flags. Given the present state of the battery (i.e., DOD and temperature), the external power demanded or received, and the maximum power/current available, the BMS assesses the appropriate action to take over the next time-step. This is explained in the BMS flowchart show in Fig. 30. If the over/under voltage flags were set, the model calculates the amount of power, in Watts, needed to be discharged/charged in the next time-step in order to return the battery into a safe range using the following equation:

$$\text{Power}_{\text{LOAD}} = \Delta\text{DOD}\,\frac{\text{Cap}\,V_{\text{avg}}}{\Delta t} \tag{31}$$

where ΔDOD is the change in DOD that the battery must go through to return to safe limits. The battery capacity (accounting for current and temperature), Cap in A_s, and the voltage over the time-step, V_{avg}, is a function of current which is initially unknown. Thus, the current is initialized to zero and the process iterates until convergence.

Once the power needed to discharge/charge the battery back to its safe limits has been found, the BMS subroutine decides from where it will come. From Fig. 30, if the battery mode coincides with what is necessary to return to its safe limits, e.g., if the battery is already in discharge mode and an over voltage flag is set, the routine will see if the demanded power can be met. For example, if 100 W is demanded from the battery, and it needs to discharge 50 W to return within a safe range, it can easily do both. If it cannot still satisfy the demand, excess electricity will be needed for this time-step. Any surplus or deficit of electricity needed over a time-step will be met by the electric grid.

If the battery mode does not coincide with what is necessary to return the battery to safe limits, e.g., if the battery is already in discharge mode and an under voltage flag is set, the battery mode is changed from discharge to charge. In this case, the maximum current and power requirements are re-assessed for charging the battery over the next time-step rather than discharge. The battery will be assigned, in this case, to charge at the necessary power without exceeding the maximum current and power limits. This case will always result in an unbalance between the battery power demanded and the battery power delivered, ultimately relying on the grid to return to safe limits.

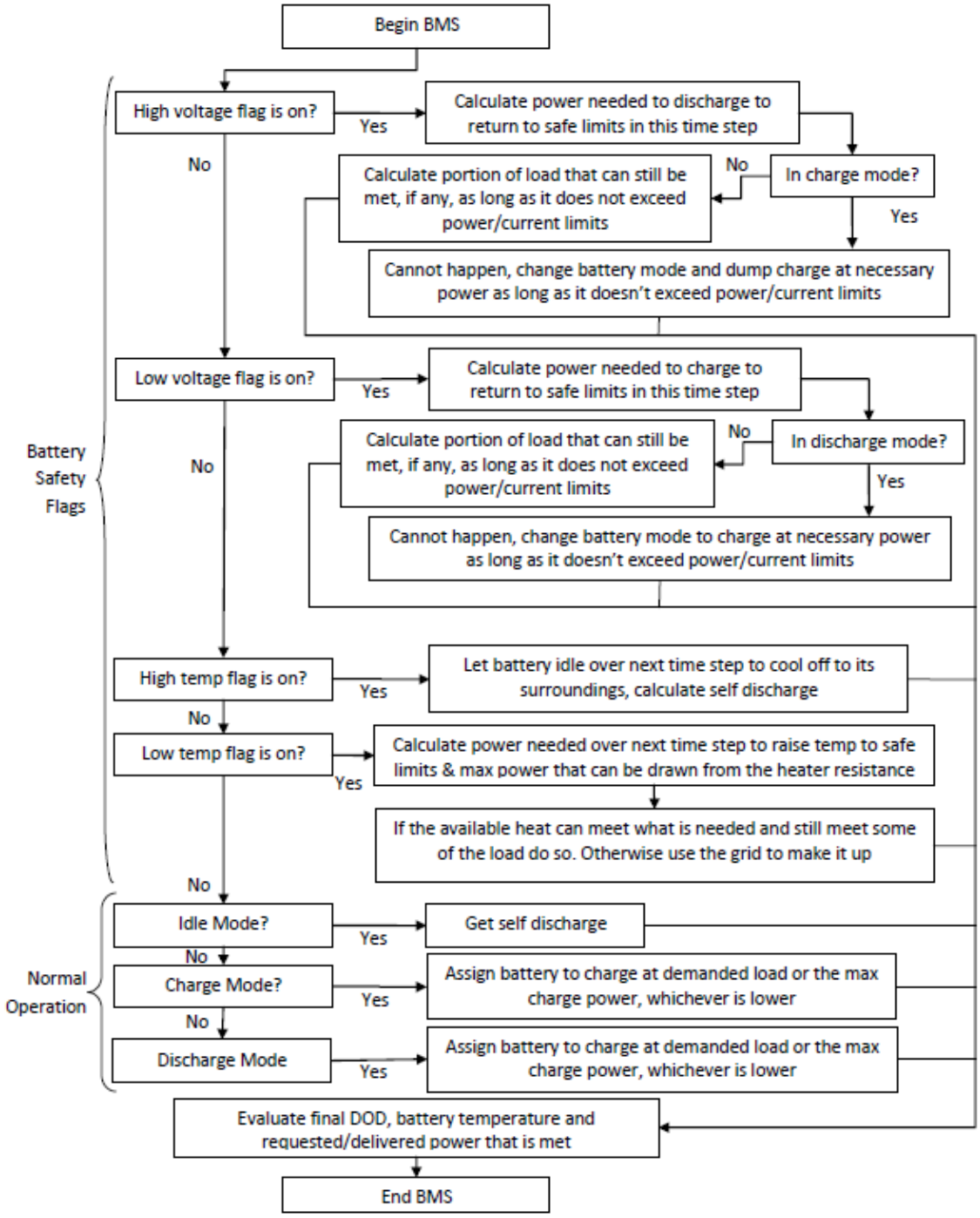

Fig. 30: Battery management system used in Li-ion battery subroutine.

Implementation of ESP-r Battery Model for High Capacity Chemistries

Micro-cogeneration systems are making inroads for electricity generation at the residential level. The devices which provide both heat and power, known as the prime mover of the system, include internal combustion engines, solid oxide fuel cells, proton exchange membrane fuel cells, or Stirling engines (SEs). They typically generate less than 15kW of electricity and are located within the household. When producing electricity alone, micro-cogeneration devices yield poor efficiencies, however when configured in systems which recover thermal energy generated in the electrical conversion process, the efficiency can rise to over 80%, referenced to the higher heating value of the fuel. [23]

Annex 42 of the International Energy Agency's Programme on Energy Conservationin Building and Community Systems (IEA/ECBCS) was focussed on reducing residential electric demand using micro-cogeneration devices through study with whole-building computer simulation software. [24] Among its conclusions were that engine start-up times, high operating temperatures, large thermal inertia, and internal controls preventing high thermal stresses, all contributed to sub-optimal response of micro-cogeneration systems to transient electrical loading. Accommodating these conditions would assist the transient performance of residential micro-cogeneration systems at times when electricity demand fluctuates rapidly. Forecasting into the future with high penetration rates of micro-cogeneration devices in households, it was concluded that the grid could no longer be viewed as an infinite power storage source. Thus, power storage technologies will become essential for residential micro-cogeneration applications.

The succeeding current IEA Annex 54 (www.iea-annex54.org) is expanding the scopeof micro-cogeneration systems to also consider components contributing renewable electricity for the building. The temporal character of power generation from transient sources does not coincide with that for power consumption, thus electrical storage capacity is highly necessary for obtaining maximal energy use benefits and the best economy from these micro-cogeneration systems. Storing electricity in a rechargeable battery facilitates a quick transient response to a varying imposed electric load. Thus as a good solution for small-scale power generation, and the prospects are promising for scenarios with a large degree of market penetration.

Rechargeable large-scale lithium ion batteries with good capacity and cyclability are among the most promising choices for RES applications. Lithium ion batteries have many characteristics which make them highly suitable for being the electrical storage components of choice. These characteristics include very high energy density, good power output, good cycle life with a broad cycling range, high coulombic efficiencies and comparatively low heat output [25]. For prolonged intensive use, such as a in a micro-cogeneration system, proper control and management of a lithium-ion battery is crucial to ensure high capacity retention, as well as to operate the unit in a safe manner.

Current understanding suggests that lithium ion batteries at ratings around a 2 kW/6 kWh level are of a size suitable for development for residential power supply and storage. It has been shown that they can provide economic benefit under time-of-use pricing structures, as storing energy can reduce peak power demands as well as offset costly infrastructure upgrades to electrical power grid networks. [3] By simulating lithium ion battery physics and chemistry, the aim is to help identify microstructural properties and materials which will respond well to real imposed current loads which have been obtained from recent electrical profile measurements. [26] This approach can also help demonstrate a battery materials parameter set as a target for accompanying material development research to satisfy realistic operating requirements.

At present some large-scale commercial battery energy storage systems (BESS) have been built and installed. [27, 28] For now, at the beginning stages of the adoption of these technologies, economies of scale have not been achieved. Under present conditions, larger BESS systems are more economically viable, as the associated control equipment represents a significant fraction of the unit cost, and it does not increase in proportion with battery size. The battery management electronics for smaller storage systems contributes to their current high cost.

An avenue being pursued to rectify the high cost of BESSs is that of higher capacity battery materials. The quest for higher energy/power density lithium batteries has led to research on higher voltage cathode materials to replace the commonly used LiMO2 (M = Co and Ni) and LiMn2O4 or even LiMPO4 olivines (M = Fe and Mn). Substituted spinels of the family $LiMn_{2-x}M_xO4$ (M = Cr, Ni, Cu, Co, and Fe) exhibit a significant capacity above 4.5 V.

Laboratories at the National Research Council of Canada have had success in developing several of these kinds of materials, two of which are explored as examples of how improved battery materials can enhance RES units integrated into micro-cogeneration systems. First among these materials is LiMn1.5Ni0.5O4 or LiNMO, which has a relatively high theoretical capacity of 146.7 mAh/g, almost all of which is around 4.7 V, and good cycling capability. [29]

The second material, lithium nickel cobalt aluminum oxide (LiNi0.8Co0.15Al0.05O2 or LiNCA) is a leading candidate for lithium-ion batteries due to its high capacity and durability. The nominal voltage is 3.7 V, and the material capacity is in the 150 to 180 mAh/g range. [30] NCA is less commonly used in the consumer market. Its great potential as a cathode material has caught the attention of the automotive industry, despite safety and cost being current research issues.

Table 16 presents some cost figures related to materials costs for the three cathode materials considered here. [31] The LiNCA material is significantly more costly on a weight basis compared to the other two materials, owing to the high cost of its cobalt component. The cost per unit of current output however is still higher, but still more or less in line with the other two materials, since the cathode represents only one part of the total cell cost.

Table 16: Comparison of material costs for the three cathode formulations. [31]

material	capacity [mAh/g]	$/kg	$/A
$LiMn_2O_4$	110	16	0.145
LiNCA	180	40	0.222
LiNMO	147	25	0.170

Residential energy use studies typically employ whole building simulation tools such as ESP-r to explore operational scenarios and system configurations in order to provide informed comment and recommendations for the suitability of their implementation. [32]

The main theme of this present work is to present some analysis of the performance of a micro-cogeneration system consisting of a Stirling engine as the combined heat and power (CHP) prime mover, along with a large Li-ion battery for energy storage and provision, according to the varying temporal demands of an annual electrical load profile. The inclusion of the battery in the system allows for less overall draw from the grid, as well as the storage of any temporary excess of electricity for use at a later time. A further theme is to show that by demonstrating improved battery performance through simulating discharge properties of novel higher-capacity cathode materials, the prospects for the viability of such CHP systems with batteries are much enhanced.

A novel contribution of the present work is to incorporate and scale-up the measured fundamental electrochemical behaviour of a Li-ion cell, to produce a new Li-ion battery pack component module for use with the ESP-r software. This new ESP-r module then made it possible to simulate the performance of a Li-ion battery in a micro-cogeneration system with a SE as prime mover. Cases were explored and evaluated for two new high-capacity battery chemistries, and compared with the performance of the same system using the conventional LiMn2O4 battery chemistry.

The objectives of this present research can be stated as follows. First, charge-discharge curves for LiMNO and LiNCA batteries for a range of currents up to 1C (ie; a current that would discharge the battery in one hour) were to be determined experimentally. Parameter estimates could be then made for some of the electroceramic properties of LiNMO and LiNCA to allow transport based electrochemical discharge simulations of these batteries to be run at a broader range of currents required to be representative of real residential electrical power loads. These electrochemical simulations provide anextended set of charge-discharge curves, which will serve as the basis for creating an ESP-r battery module representing each of these two novel types of Li-ion battery.

The above framework serves to prepare the required inputs for the comparison of the annual energy performance of a micro-cogeneration system consisting of a SE with a Li-ion battery for electrical storage, with respect to measured electrical demand profiles, for three cases. The first, is the reference case which has a Li-ion battery with a LiMn2O4 cathode material, and it is then compared to two prospective cases where the Li-ion battery is made with either LiNMO or LiNCA high capacity cathode materials.

Dual Model Overview

Two different modeling procedures were employed in this project. The first was a fundamentals based electrochemical transport model of discharge in a single Li-ion cell. [17] Output from a range of currents from this basic model was collected and condensed into an engineering type empirical model to represent the function of a Li-ion battery pack operating as a RES unit in a residential micro-cogeneration system. The engineering-level model is based on an equivalent circuit representation of a battery, and is presented in Sec. 3.2 (above) in this report. This equivalent circuit model can be used for simulating battery packs of consisting of multiple cells, and can be interfaced with residential energy use simulations.

The Gao model, described above, was used to model the battery pack. The required battery pack was constructed of small basic cells with a capacity of 1.80 Ah. These would be in line with LiMn2O4 18650 cells. [33]. In terms of battery architecture, the requirement for a pack of 6 kWh at 120 V called for a configuration of 35 in-series sets of 34 cells in parallel, a total of 1190 individual cells.

Table 17: Depth of discharge potential range for the cathode materials.

cathode	$\phi_{\mathrm{DOD}=0}$ (V)	$\phi_{\mathrm{DOD}=1}$ (V)
$LiMn_2O_4$	4.22	3.15
LiNCA	4.15	2.77
LiNMO	4.72	3.43

To demonstrate the performance of Li-ion batteries for residential storage considered in this work, a model of a house was created in ESP-r for an annual simulation. The layout of the house was basic: a single-zone, rectangular house located in Ottawa, Canada. The model used typical constructions to represent the houses walls, ceiling and floor. It had a floor space of 132 m^2 and a volume of 528 m^3. These values were chosen to represent a typical Canadian single family detached dwelling [34].

A SE (Whisper Tech Ltd. WhisperGen Stirling engine, fuelled by natural gas), represented in a model developed by Ferguson, was used as the micro-cogeneration device in the simulation. [35] Weather data taken for the year 2008 in Ottawa, Ontario, plant configuration used in the simulation is shown in Fig. 31. The SE was configured to constantly produce 900 W of electricity for the house throughout the year. The useful heat recovered by the engine was circulated via a pump to an air-to-water heat exchanger. The air-to- water heat exchanger, driven by a fan, supplied warm air to the household. The pump and the fan consumed 50 W and 25 W of electricity, respectively.

The household electrical demands were input as combined non-HVAC and space cooling loads on a five-minute basis. Data from a medium-level energy use house from a Carleton University field data collection project served as the power use profile. [26] The battery was inserted into the system to buffer energy demand and improve efficiency. Under the battery management logic devised for the simulations, if the combined electricity demand from the household, pump and fan was less than the production from the stirling engine, the battery would charge with the excess electricity produced. If the SE and battery could not meet the combined electric demand, electricity would be imported from the grid. Likewise, if electricity production from the stirling engine was greater than the combined electric demand and the battery was fully charged, the excess electricity was exported to the grid. Finally, if the thermal demands of the household exceeded the heat produced by the SE, an auxiliary natural gas burner, not shown in Fig. 31 provided the necessary heat.

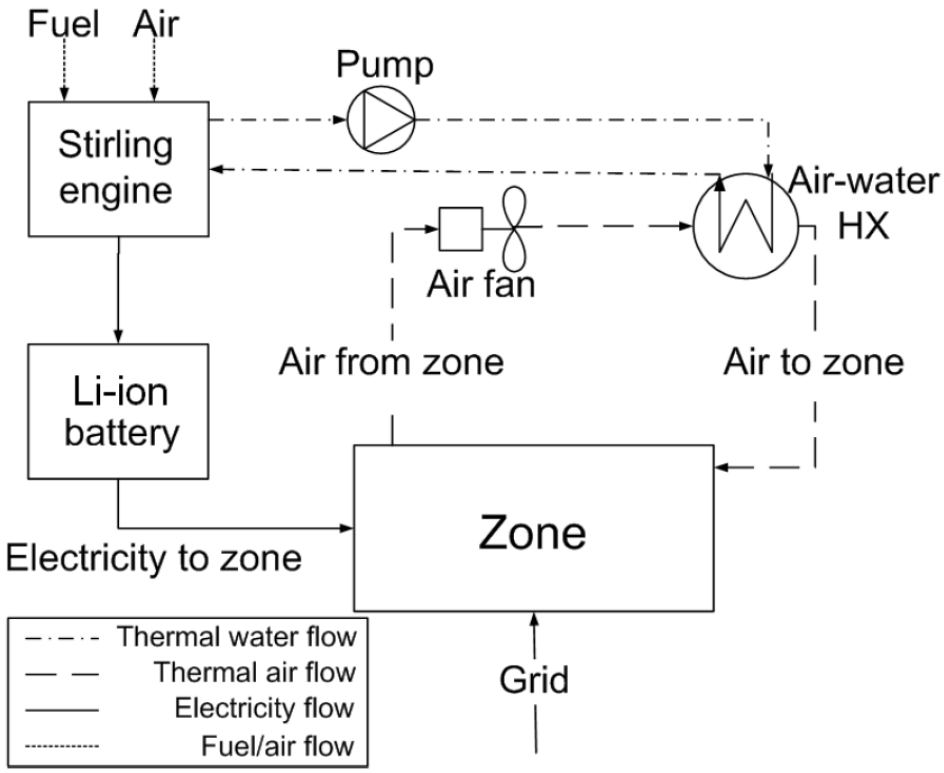

Fig. 31: Plant system schematic for application demonstration.

Results and Discussion

A number of scenarios have been explored using the integrated model outlined above [36]. A number of beneficial effects resulted from the inclusion of a lithium ion battery in a micro-cogeneration configuration. The first example considers the integrated system with the conventional LiMn2O4 cathode material. In this case, the house electrical demand and battery load over two summer days as depicted in Fig. 32, shows that the production of the SE during overnight periods was able to satisfy the household power demand and charge the battery with its excess electricity production. Over the daytime, the household electricity demand increased above the production of the SE and the battery began to discharge to help manage the power load and reduce power draw from the grid. The inclusion of a RES in a micro-cogeneration system reduced the extent of grid interactions with the home.

A similar scenario as presented in Fig. 32 was next simulated with battery packs of the same size made with the novel LiNCA and the LiMNO cathode materials. It would be expected that the benefits of battery use with micro-cogeneration would improve in proportion to the pack capacity. Note that while Fig. 32 was shown as an example of the system behavior, different dates were chosen for Fig. 33 and Fig. 34 where the demand peaks were shorter and broader, and better illustrate the differences and benefits of the batteries with the higher-capacity cathode materials and some of the design corrections taken to improve the performance.

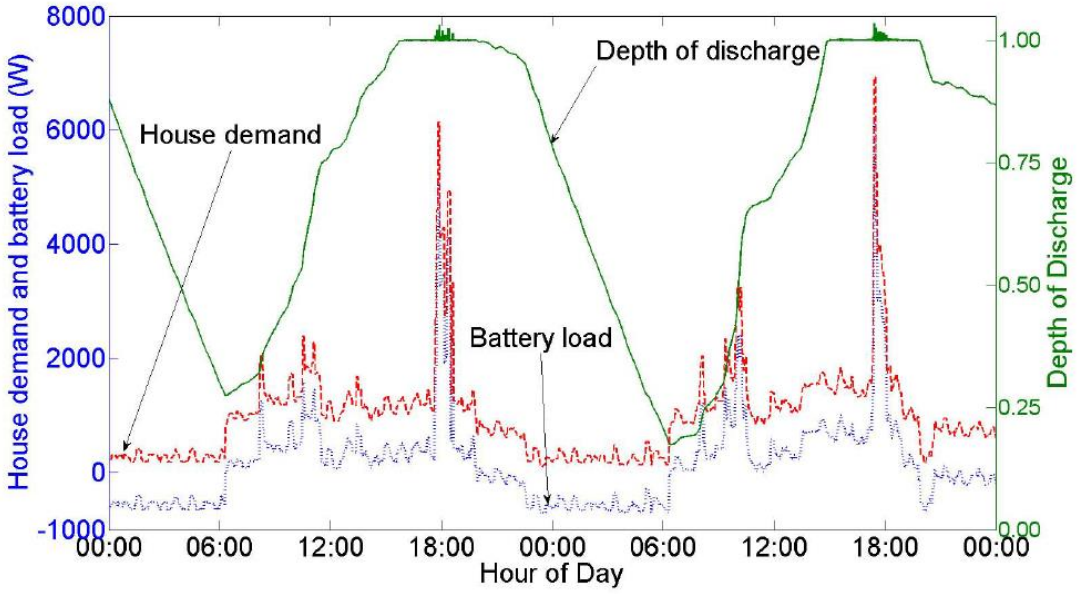

Fig. 32: Household electricity demand, LiMn2O4 battery load and battery DOD over two days of simulation beginning August 4th, 2008.

Fig. 33 compares the micro-cogeneration performance of same size batteries with the three different cathode materials. What can be seen here in this initial instance is that the increased capacities of the LiNCA and LiNMO batteries do not seem to show appreciable benefits in this scenario.

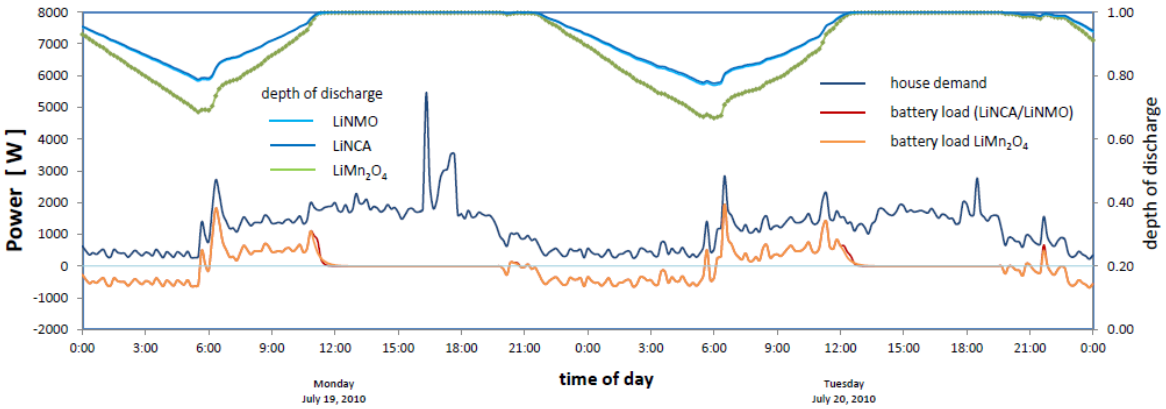

Fig. 33: Comparison of household electricity demand, LiMn2O4, LiNCA and LiMNO battery load and battery DOD over two days of simulation beginning August 4th, 2008.

Fig. 33reveals that an integrated design of all the equipment in the configuration must be undertaken in order to attain a more optimal performance with the micro-cogeneration system. The shortcomings shown in Fig. 7 arise from a mismatch between the power output from the SE and the battery capacity. A 900W SE cannot fully recharge the conventional battery nor the higher capacity batteries during the off-peak charging periods under the battery management system as provided. The battery load for the two higher capacity batteries is essentially identical to that of the conventional battery with a LiMn2O4 cathode. There is still a minor benefit from the higher capacity materials, in that they do not cycle as deeply, and will thus show a longer service life under the scenario of Fig. 33.

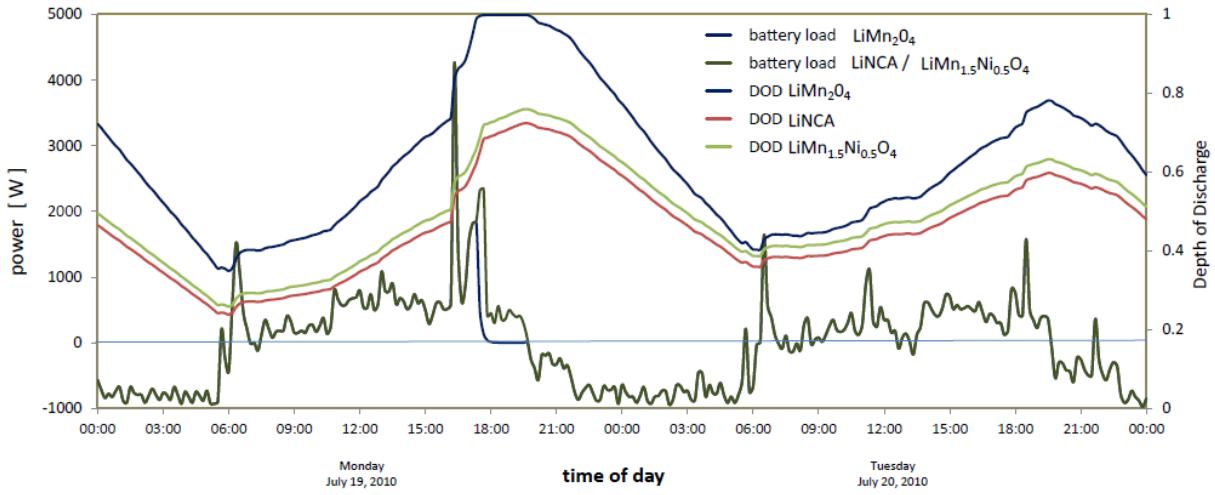

Fig. 34: Comparison of household electricity demand, LiMn2O4, LiNCA and LiMNO battery load and battery DOD over two days of simulation beginning July 19, 2008. In this case the SE capacity is 1200 W.

A possible adjustment to improve the system performance would be to decrease the size of the battery, such that the LiMn2O4 battery could be properly charged during the off-peak periods. In preliminary tests with smaller capacity cells where this does occur, it was still found that the reduced battery pack size leads to a very rapid battery discharge, including when simulated with the LiNCA and LiMNO batteries, despite their higher capacity.

A number of simple preliminary simulations confirmed that the electrical load required of the battery was simply too great to be provided by cells ranging from 1.2 kWh up to 6 kWh capacity in the existing micro-cogeneration configuration. In a sense, this was an obvious consequence, but the point of the exercise was to check if the higher capacity batteries could offer any advantage in this situation. They did not.

Another approach with the same logic of decreasing the battery capacity ratio to SE power output was taken for exploring a two day scenario. Here, the system was modified by enlarging the SE. From the year-long data set, the two consecutive days beginning July 19, 2008, were found where the discharge was near complete at the start of the cycle. Starting from a near fully discharged state puts the battery capabilities in higher relief for demonstrating their performances.

A power output of 1200 W was selected for the simulation. This larger SE is capable of providing suffcient charge to the higher capacity LiNCA and LiMNO batteries, such that some of the peak periods of the daily demands can be met without reaching a full dept of discharge. Fig. 35 shows this simulated scenario. The other benefit of this configuration is that the higher capacity batteries cycle through a smaller part of their capacity range, thereby putting less net stress on the battery materials which will serve to extend the useful lifetime of these batteries. Fig. 34 shows a month long simulation for the system shown in Fig. 34, where the depth of discharge is recorded as well as a total number of battery cycles. For the cases of incomplete cycles, one cycle was calculated on current-based stoichiometric equivalents of the full battery capacity.

It was not the intention of the present project to exhaustively explore a large number of micro-cogeneration scenarios in order to identify the conditions where the present combination of components can be operated optimally. The point to be made is that with the present trend of improvements in battery materials, the prospects for Li-ion technology to be used in a RES context are indeed promising. From the

results of the simulations that are partially depicted in Fig. 35 the LiMn2O4 battery used approximately 800 cycles over the year. If the long-term industry goal of a 10,000 cycle life span can be realized this would equate to a service lifetime of more than 12 years. [37] For the LiMNO and LiNCA battery chemistries, the expected service life would be 17 and 18 years respectively.

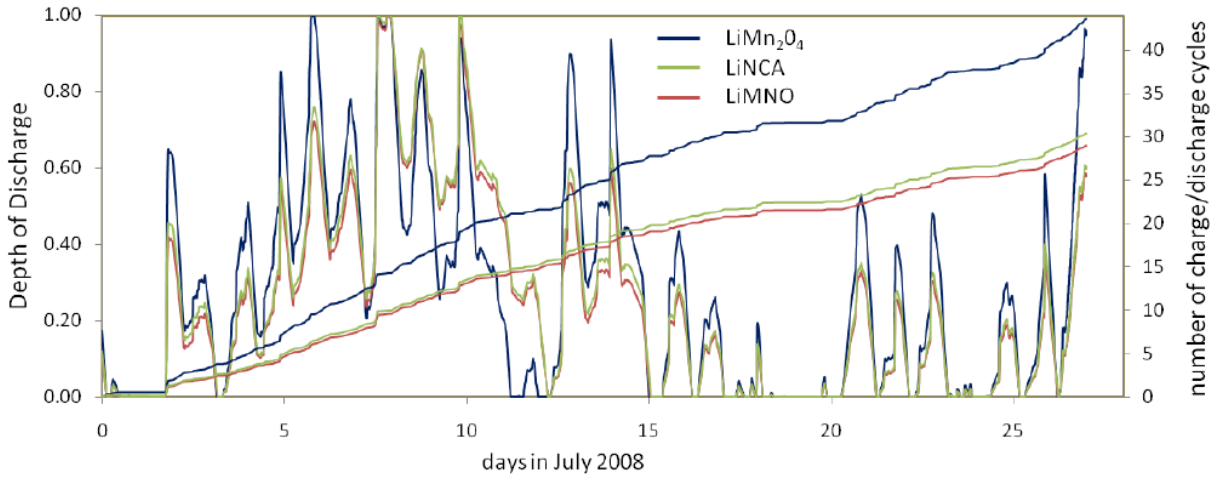

Fig. 35: Battery pack depth of discharge profiles and cumulative total of discharge cycles over the month of July 2008, based on micro-cogeneration system with 1200 W Stirling Engine and 1190 cell battery pack.

In a best case scenario, where the all the heat energy provided by the Stirling engine could be used, micro-cogeneration with a lithium ion battery under the conditions outlined in [3] can reduce daily power consumption from the electrical grid by 30% from 61 kWh to 43 kWh, at a cost savings of about $CAD440/year. Annual cost savings with the same sized batteries under this use scenario with the LiNCA and LiMNO cathodes would be about $CAD750/year and $CAD690/year respectively.

Conclusions

A fundamental transport based model of the function of a lithium ion battery has been used to provide the necessary inputs to create a battery module based on the Gao equivalent circuit model in ESP-r for residential energy storage. The purpose of this battery simulation module was for the performance assessment of large scale storage batteries operating in a micro-cogeneration system, and to show that making batteries using from novel advanced high-capacity battery cathode materials significantly enhance the economic viability of such systems.

The present study evaluated annual residential energy use for a typical Canadian home connected to the electrical grid, equipped with a micro-cogeneration system consisting of a Stirling engine for supplying heat and power, coupled with a nominal 2 kW/6 kWh lithium ion battery. The energy performance of two novel battery cathode chemistries,one a new Li-NCA material, the other a high voltage Ni-doped lithium manganate, were compared in the residential micro-cogeneration context with a system equipped with the presently conventional LiMn2O4 spinel-type battery. It was found that the complex nature of a multi-piece micro-cogeneration system benefits to a great extent from usage scenario simulations due to the specific capacities and outputs of the components. Since the sizes and performance of the components are not continuously scalable, energy use simulation was shown to be an effective means to recommend the details of system configurations for specific cases. It was also found that the prospects for Li-ion technology

for residential energy storage are positive, stemming from novel of battery materials advances. Higher capacity cathode materials such as LiMNO and LiNCA will extend battery pack service lives upwards of 30%, and will be a key factor in their eventual commercial viability.

Analysis of using large batteries in building environment simulations clearly demonstrate how expected demands on large-scale batteries for residential energy storage assist in sizing and configuring components for optimal use in micro-cogeneration systems. Continued materials research and engineering know-how derived from this work will serve to enable the realization of cost-effective large-scale lithium ion batteries for residential energy storage.

2.1.5 Desiccant Wheel Model (University of Sannio, Italy)

Desiccant-based Air Handling Units, thermally activated by solar collectors or cogenerators, are without any doubt an interesting alternative for solving problems of electrical over-consumption in traditional vapour compression air conditioning. They have several advantages compared to conventional cooling dehumidification systems. Their use for tertiary and residential buildings is also spreading, especially when the regeneration of the desiccant can be obtained by using available thermal wastes.

The main component of Desiccant-based Air Handling Units is the desiccant wheel (DW). It is a rotor, filled with desiccant material, used to dehumidify the process air, exploiting the difference in water vapour pressure between the incoming humid air and the surface of the desiccant material.

In order to ensure a continuous operation of the system, the DW has to be regenerated by means of a regeneration air flow, heated up to a suitable temperature (from 60 °C up to 140 °C, depending on the adsorbent material and the desired humidity ratio reduction).

At “Università degli Studi del Sannio”, in Benevento (Southern Italy), a desiccant-based Air Handling Unit coupled to a natural gas-fired reciprocating internal combustion engine microcogenerator, an electric chiller and a natural gas-fired boiler, is installed.

The DW is filled with silica gel, a desiccant material that can be effectively regenerated at temperatures as low as 60-70 °C. These values are obtainable with the thermal recovery from the MCHP and, only when necessary, the natural gas boiler. The rotor matrix is composed by alternate layers (smooth and wavy) of silica gel sheets and metallic silicate, chemically bound into an inorganic fibre frame (Fig. 36).

Fig. 33reveals that an integrated design of all the equipment in the configuration must be undertaken in order to attain a more optimal performance with the micro-cogeneration system. The shortcomings shown in Fig. 7 arise from a mismatch between the power output from the SE and the battery capacity. A 900W SE cannot fully recharge the conventional battery nor the higher capacity batteries during the off-peak charging periods under the battery management system as provided. The battery load for the two higher capacity batteries is essentially identical to that of the conventional battery with a LiMn2O4 cathode. There is still a minor benefit from the higher capacity materials, in that they do not cycle as deeply, and will thus show a longer service life under the scenario of Fig. 33.

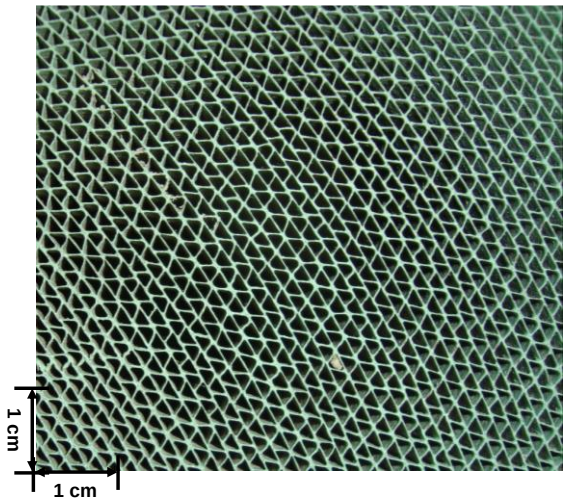

Fig. 36: The silica-gel desiccant wheel.

The development of a simple and reliable model for the analysis of a desiccant-based AHU and of its main components can lead to useful conclusions as regards the effect of the various operating parameters, namely, regeneration temperature, outdoor air temperature and humidity ratio. Moreover, such simple models can be used, e.g., in whole-building simulation software, in order to estimate annual energy and environmental performance of desiccant-based AHU, thermally activated by different energy sources (solar energy, thermal wastes).

In particular, the development of a reliable and accurate model for the main component of these systems – the desiccant wheel – is a complex task, due to the combined processes of heat and mass transfer, as well as to the high number of independent variables affecting its performance, such as temperature, humidity, flow rates, rotational velocity, desiccant material and so on.

Model I

Experimental data collected during several tests [38 - 40] were used to correlate thermal and dehumidification performances of the wheel, temperature, flow rate and humidity ratio of both inlet process and outlet regeneration air flows, and regeneration temperature. Experimental results were further worked out to develop a simple descriptive model, based on practical and reliable correlations readily applicable for the analysis or the simulation of the silica gel desiccant wheel, to provide a mechanistic framework for the interpretation of the results [41].

To evaluate the performance of the desiccant wheel, the following performance parameter – SER (Sensible Energy Ratio) – has been analyzed:

$$SER = \frac{\dot{m}_{proc}\, c_p \left(t_2 - t_1\right)}{\dot{m}_{reg}\, c_p \left(t_3 - t_1\right)} = \frac{V_{proc}\left(t_2 - t_1\right)}{V_{reg}\left(t_3 - t_1\right)} \qquad (32)$$

SER is the ratio between the thermal power due to the process air heating through the wheel and the regeneration thermal power. $\dot{m}_{proc}$ and $\dot{m}_{reg}$ are mass flow rates of process and regeneration air, V_{reg} and V_{proc} are the corresponding volumetric flow rates, c_p is specific heat at constant pressure, t_1 and t_2 are

process air temperature upstream and downstream the DW, t_3 is regeneration air temperature entering the desiccant rotor.

High values of SER are unfavorable, as it means a higher increase of the process air temperature through the wheel and therefore a higher cooling load on the cooling device.

Experimental observations suggest that SER experimental data could be related to a "new" operating variable, namely the product of the volumetric flow rates ratio and the regeneration temperature, according to the following equation:

$$SER = \frac{k_1 k_2}{k_2 + \left(t_{reg} \, V_{reg} / V_{proc} \right)} \tag{33}$$

where $t_{reg} = t_3$ is the regeneration temperature

Experimental data has been fitted to the previous equation (Fig. 37), solving the weighted least squares problem of minimizing the weighted sum of squares of the residuals to find the best-fit parameters by means of a modified Levenberg–Marquardt algorithm, and an excellent agreement with the results has been obtained, as shown in Fig. 37. Values of k_1 and k_2, as well as coefficients standard errors and coefficient of determination R^2, are reported in Table 18.

Table 18: Values of k_1 and k_2, standard error coefficients and coefficient of determination R^2

	Value	Standard error
k1	3.7804	0.1641
k2	13.2044	0.7116
R2	0.9397	

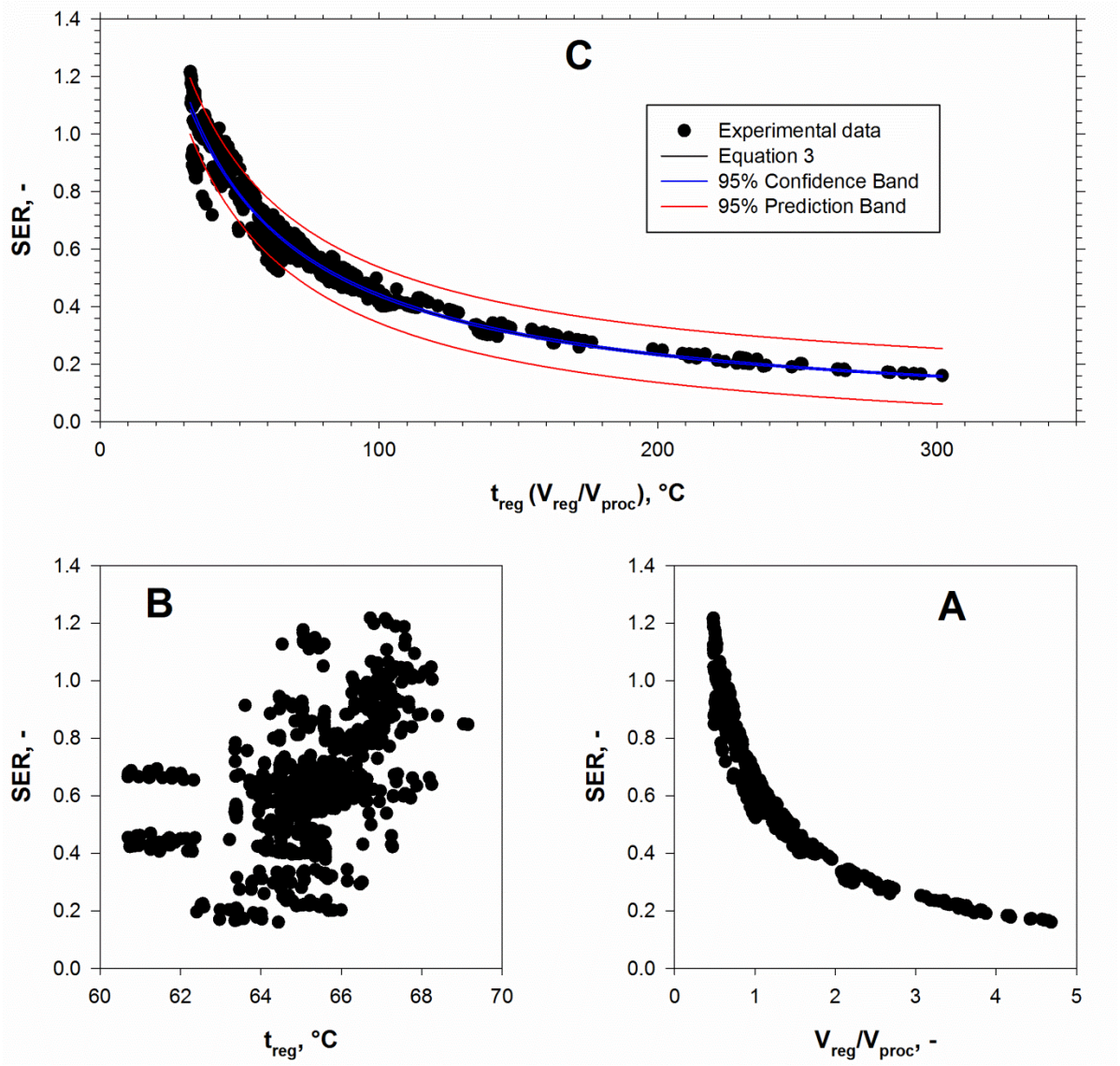

Fig. 37: SER as a function of Vreg/Vproc (A), treg (B) and treg Vreg/Vproc (C).

Model II

Theoretical existing models for the operation of the main subsystems of a desiccant air-conditioning system were experimentally calibrated and validated through a wide number of measurements in the typical summer operating range for these systems [42]. The operation of each subsystem is described by a specific efficiency factor. In particular, the validity of the assumption for efficiency factors presenting constant values is experimentally investigated. For each subsystem, the average value of the selected efficiency factor and standard deviations are calculated. The validity of the assumed models has been confirmed by the evaluation of the Root Mean Standard Error (RMSE) that compares experimental and simulated values for each subsystem.

As regards the desiccant wheel, the simplified approach of Maclaine-Cross and Banks has been used. This approach models the dehumidification process, a combined heat and mass transfer process, in analogy with a simple heat transfer process. Equations for coupled heat and mass transfer are reduced to two

uncoupled differential equations of two independent variables called characteristic potentials, F_1 and F_2. The discussion about the nature of these potentials is quite difficult and it is out of the scope of this section, but it can be stated that constant F_1 lines coincide with constant enthalpy lines, while constant F_2 lines coincide with constant relative humidity lines on the psychrometric chart.

The potential functions depend on thermohygrometric properties of air and on the thermo-physical properties of the wheel, especially the desiccant material. The relations have been expressed for the working pair air-silica gel, defining the model presented below:

$$F_{1,i} = \frac{-2865}{(t_i + 273.15)^{1.49}} + 4.344\left(\omega_i / 1000\right)^{0.8624} \tag{34}$$

$$F_{2,i} = \frac{(t_i + 273.15)^{1.49}}{6360} - 1.127\left(\omega_i /1000\right)^{0.07969} \tag{35}$$

The intersection of constant potential lines gives the outlet conditions of process air in the ideal case, i.e. assuming that both the adsorption and the desorption process are isenthalpical. Then actual outlet conditions are estimated using two effectiveness indices of the wheel, η_{F_1} and η_{F_2}, calculated in analogy to the efficiency of a heat exchanger:

$$\eta_{F_1} = \frac{F_{1,2} - F_{1,1}}{F_{1,6} - F_{1,1}} \tag{36}$$

$$\eta_{F_2} = \frac{F_{2,2} - F_{2,1}}{F_{2,6} - F_{2,1}} \tag{37}$$

In particular, η_{F_1} represents the degree to which the process approximates the adiabatic one, while η_{F_2} represents the degree of dehumidification. If η_{F_1} = 0 and η_{F_2} = 1, the dehumidification process is ideal, i.e. it is adiabatic and there is a maximum dehumidification level for assigned geometry and flow conditions. If the values of η_{F_1} and η_{F_2} are known, then temperature and humidity ratio of the processed air exiting the wheel can be evaluated.

Intense laboratory activities provided over 200 hours of experimental data necessary to calibrate and validate the model presented above. To this aim, the whole data set has been divided in two equal subsets: the former has been used for the calibration, the latter for the validation of the models.

The present section experimentally investigates the assumption of constant efficiency factors for the above described models within the range of operating conditions that cover the available experimental data.

In the model calibration effort, the average value of the selected efficiency factor is calculated, for each test included in the calibration data subset. The following average values of efficiency were obtained: $\eta_{F_1} = 0.207$ and $\eta_{F_2} = 0.717$, with standard deviation equal to 0.0460 and 0.0478, respectively. The

values of standard deviations are rather low, suggesting the plausibility of the constant efficiency hypothesis.

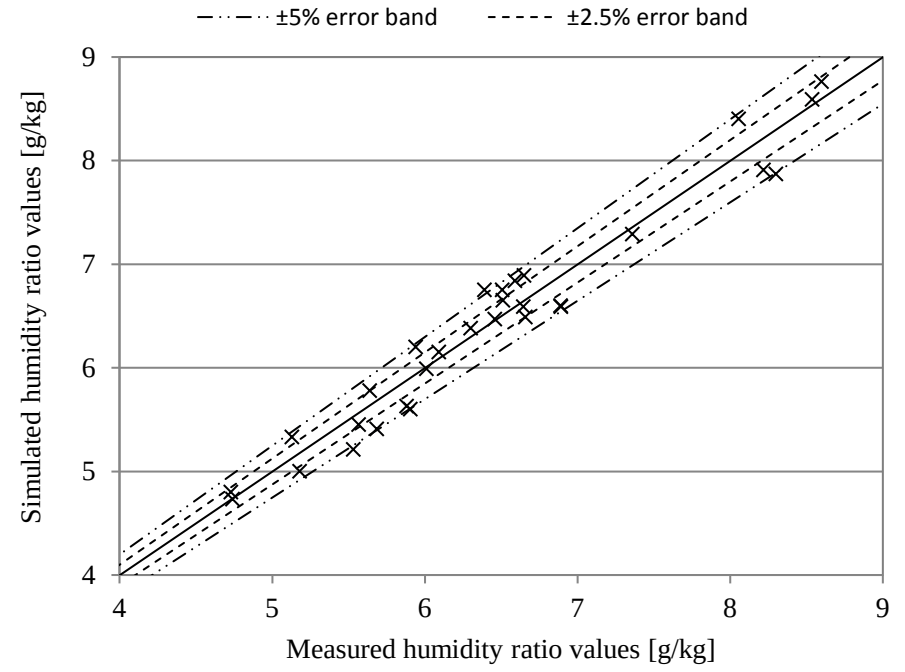

(a)

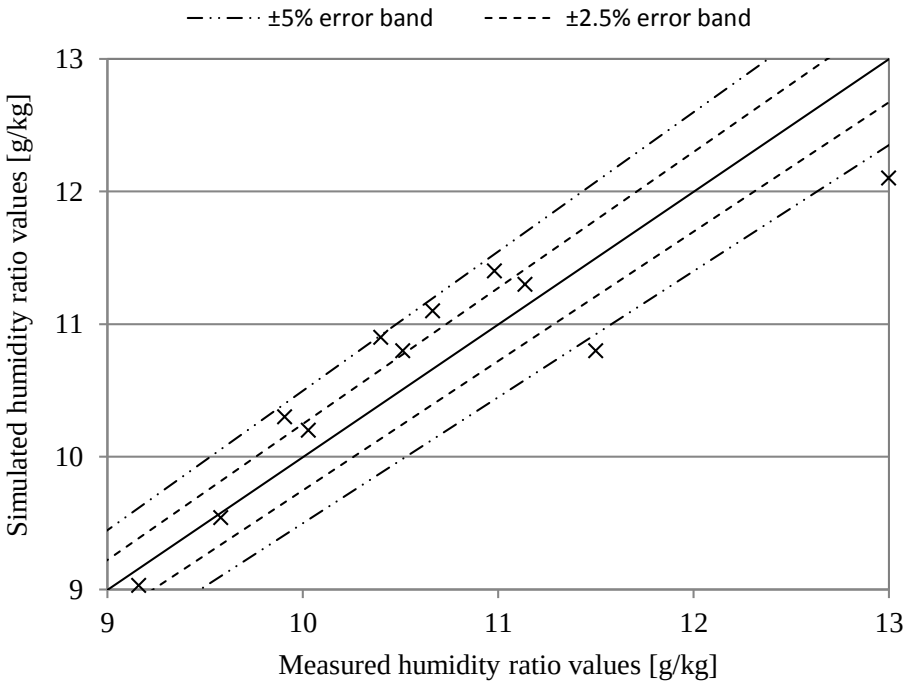

(b)

Fig. 38: Measured and simulated values of process air humidity ratio at the outlet of the desiccant wheel.

In other papers, the constant efficiency model for a DW is experimentally validated. The obtained values of effectiveness indices are in agreement with the ones obtained by the authors.

Validation of the model has been carried out by comparing the measured air thermal-hygrometric properties at the outlet of the component with the corresponding values calculated by the model, while the remaining thermal-hygrometric properties that are contained in the model equation are treated as inputs to the model itself. In fact, according to the efficiency factors determined, the temperature and the absolute humidity at the outlet of the desiccant wheel can be simulated, under the operating conditions of the measurements included in the validation data subset. Thus, N pairs of measured and simulated values of temperature and/or absolute humidity are available, where N denotes the number of these measurements. The validity of the assumed models can be confirmed by the evaluation of the Root Mean Standard Error (RMSE).

The following values of RMSE were obtained: 1.28 °C and 0.301 g/kg, for temperature and humidity ratio of process air at the outlet of the desiccant wheel. Also in this case, the obtained values are in agreement with those found in literature. Considering the uncertainties of the measuring instruments, it can be stated that the above results demonstrate the adequacy of the constant efficiency models. The previous analysis is confirmed by Fig. 38. The measured and simulated values for process air humidity ratio exiting the desiccant wheel are shown, together with the ±2.5% and ±5% error bands. In particular Fig. 38 has been divided in Fig. 38a and b in order to improve its readability. In the former, outlet humidity ranges from 4 to 9 g/kg, in the latter from 9 to 13 g/kg. Only few values are outside the ±5% error band. The agreement between measured and simulated values is quite good for both cases.

2.1.6 Thermal Storage Model (University of Sannio, Italy)

At University of Sannio, a thermal storage system is installed and experimentally tested (Fig. 39). The buffer is made of carbon steel, with a capacity of 1000 liters and a net storage volume of 855 liters. It has three heat exchangers: two of them, placed in the lower and upper part of the storage, are carbon steel heat exchangers that can interact with external energy conversion device; the third one, that extends along the entire height of the storage, is a stainless steel corrugated coil heat exchanger for domestic hot water “production”. A third energy conversion device can directly interacts in open circuit with the fluid stored in the tank. [43, 44]

The tank is insulated with a layer of polyurethane with a thickness of 100 mm and a thermal conductivity equal to 0.038 W/mK.

The model used to simulate the described storage tank is "*type 60*", which represents the most detailed model available in TRNSYS to simulate a stratified thermal storage. The thermal performance of a water-filled sensible energy storage tank, subject to thermal stratification, is modeled by assuming that the tank consists of N fully-mixed equal volume segments, for each of them a uniform temperature is considered. The degree of stratification is determined by the value of N. If N is equal to 1, the storage tank is modeled as a fully-mixed tank and no stratification effects are possible.

Options of fixed or variable inlets, unequal size nodes, temperature dead band on heater thermostats, incremental loss coefficients, internal submersed heat exchangers, non-circular tanks, horizontal tanks, and losses to the flue of a gas auxiliary heater are all available.

By means of experimental analysis conducted in the test facility of University of Sannio, it was possible to experimentally calibrate and validate the tank model.

The model parameters have been set to take into account the three internal heat exchangers, as well as two inlets and two outlets of the stored fluid. 50 nodes were considered to model thermal stratification.

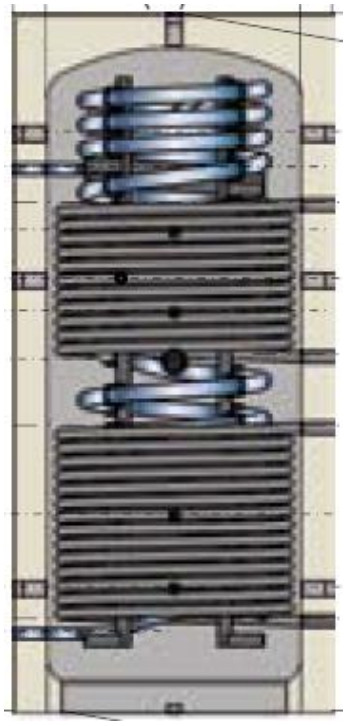

Fig. 39: the layout of the thermal storage

The energy balance for the generic node of the storage (Fig. 40), neglecting optional internal gas (flue in Fig. 40) and electric (aux in Fig. 40) heaters, can be written as:

$$\begin{aligned}\left(M_i c_p\right)\frac{dT_i}{dt} = {} & \frac{\left(k+\Delta k\right)A_{c,i}}{\Delta x_{i+1\to i}}\left(T_{i+1}-T_i\right)+ \\ & + \frac{\left(k+\Delta k\right)A_{c,i}}{\Delta x_{i-1\to i}}\left(T_{i-1}-T_i\right)+\left(U_{\tan k}+\Delta U_i\right)A_{s,i}\left(T_{env}-T_i\right)+ \\ & + \dot{m}_{down}\,c_p T_{i-1}-\dot{m}_{up}\,c_p T_i-\dot{m}_{down}\,c_p T_i-\dot{m}_{up}\,c_p T_{i+1} \\ & + UA_{hx1}\,lmtd_1+UA_{hx2}\,lmtd_2 \\ & + UA_{hx3}\,lmtd_3+\dot{m}_{1in}\,c_p T_{1in}-\dot{m}_{1out}\,c_p T_i+\dot{m}_{2in}\,c_p T_{2in} \\ & - \dot{m}_{2out}\,c_p T_i\end{aligned} \tag{38}$$

where:

k is the tank fluid thermal conductivity [W/mK]

Δk is the de-stratification conductivity [W/mK]

$A_{C,i}$ is the cross-sectional area of node "i" [m^2]

$A_{S,i}$ is the surface area of node "i" [m^2]

c_p is the tank fluid specific heat [kJ/kgK]

M_i is the mass of node "i" [kg]

t is the time [s]

$\Delta x_{i+1 \to i}$ is the center-to-center distance between node "i" and the node "i+1" below it [m]

$\Delta x_{i-1 \to i}$ is the center-to-center distance between node "i" and the node "i-1" above it [m]

T_i is the temperature of node "i" [K]

T_{i+1} is the temperature of node "i+1" [K]

T_{i-1} is the temperature of node "i-1" [K]

U_{tank} is the loss coefficient per unit area of the storage tank [W/m^2K]

ΔU_i is the additional loss coefficient for node "i" [W/m^2K]

T_{env} is the ambient temperature [K]

$\dot{m}_{down}$ is the fluid flow rate down the tank [kg/s]

$\dot{m}_{up}$ is the fluid flow rate up the tank [kg/s]

UA_{hx} is the overall heat transfer coefficient of the heat exchanger [W/K]

$Imtd$ is the logarithmic mean temperature difference of the heat exchanger [K]

$\dot{m}_{1in}$ is the mass flow rate entering at inlet 1 [kg/s]

T_{1in} is the temperature at inlet 1 [K]

$\dot{m}_{2in}$ is the mass flow rate entering at inlet 2 [kg/s]

T_{2in} is the temperature at inlet 2 [K]

$\dot{m}_{1out}$ is the mass flow rate leaving at outlet 1 [kg/s]

$\dot{m}_{2out}$ is the mass flow rate leaving at outlet 2 [kg/s]

To model de-stratification due to mixing at node interfaces and conduction along the tank wall, the user may enter an additional conductivity parameter *Δk*. This additional conductivity term is added to the conductivity of the tank fluid and is applied to all nodes.

Furthermore, in many circumstances, the tank may not be uniformly insulated. It is possible to incrementally insulate certain nodes of stratified storage tanks by the specification of the additional loss coefficient for node "i" (ΔU_i).

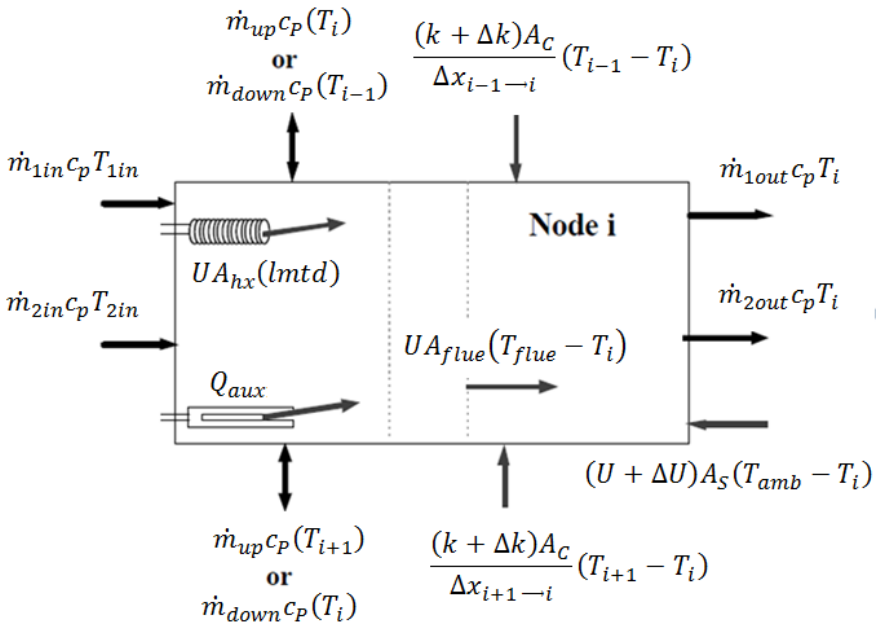

Fig. 40: Energy flows for the generic node of the thermal storage

In Table 19, the main parameters used to model the storage tank are listed.

The parameters related to height of flow inlet and outlet in the storage tank and the heat exchangers do not refer to the height above ground, but to the height above the bottom of the tank, that have a basis of 0.0375 m. Furthermore, it has been assumed that the fluid in the lower heat exchanger (HX-1) is water, as it interacts with a MCHP system, while the fluid in the upper heat exchanger (HX-2) is a water-Propylene Glycol mixture, as it interacts with solar collectors

Experimental data acquired with different plant configurations, in terms of energy conversion devices supplying thermal energy to the storage tank and thermal users drawing thermal energy from the storage tank, were compared with the data resulting from the corresponding simulation. The comparison is carried out between the temperatures measured by the seven immersion sensors installed in the tank, and the temperatures of the nodes of the model located at the same height of the sensors.

Table 19: Parameters for the type 60

Parameter	Value	Units	Description
Tank volume	855	l	The actual volume of the storage tank.
Tank height	2.04	m	The height of the storage tank.
Height of flow inlet 1	1.33	m	The height of the first inlet above the bottom of the tank.
Height of flow outlet 1	2.04	m	The height of the first outlet from the storage tank above the bottom of the tank.
Height of flow inlet 2	1.76	m	The height of the second inlet to the staorage tank above the bottom of the tank.
Height of flow outlet 2	0.36	m	The height of the 2nd outlet from the storage tank above the bottom of the tank.
Fluid specific heat	4.19	kJ/kgK	The specific heat of the fluid contained in the storage tank.
Fluid density	1000	kg/m^3	The density of the fluid contained in the storage tank.
Tank loss coefficient	0.405	W/m^2K	The average tank loss coefficient per unit area.
Fluid thermal conductivity	0.580	W/mK	The thermal conductivity of the fluid contained in the storage tank.
De-stratification conductivity	0.285	W/mK	To model de-stratification due to mixing at node interfaces and conduction along the tank wall, the user may enter this additional conductivity parameter.
Boiling temperature	127	°C	The boiling point temperature of the fluid contained in the storage tank.
Number of internal heat exchangers	3	-	The number of internal heat exchangers that are contained within the storage tank.
HX Fluid indicator-1	1	-	The fluid contained in the first internal heat exchanger: 1=Water; 2=Propylene Glycol; 3=Ethylene Glycol.
Fraction of glycol-1	0	-	The fraction of glycol contained in the internal heat exchanger fluid by volume.
Heat exchanger inside diameter-1	0.029	m	The inside diameter of the pipe comprising the internal heat exchanger.
Heat exchanger outside diameter-1	0.032	m	The outside diameter of the pipe comprising the internal heat exchanger.
Heat exchanger fin diameter-1	0.032	m	The diameter of the fins on the outside pipe surface of the internal heat exchanger.

Table 20: Parameters for the type 60

Parameter	Value	Units	Description
Total surface area of heat exchanger-1	3.1	m^2	The total outside surface area of the internal heat exchanger.
Heat exchanger length-1	30.85	m	The total length of internal heat exchanger pipe immersed within the storage tank fluid.
Heat exchanger wall conductivity-1	45	W/mK	The conductivity of the heat exchanger wall including any applicable contact resistance.
Heat exchanger material conductivity-1	45	W/mK	The thermal conductivity of the material which comprises the internal heat exchanger.
Height of heat exchanger inlet-1	0.85	m	The height above the bottom of the storage tank of the inlet of the internal heat exchanger.
Height of heat exchanger outlet-1	0.25	m	The height of the outlet of the internal heat exchanger from the tank above the bottom of the storage tank.
HX Fluid indicator -2	2	-	The fluid contained in the first internal heat exchanger: 1=Water; 2=Propylene Glycol; 3=Ethylene Glycol.
Fraction of glycol-2	0.33	-	The fraction of glycol contained in the internal heat exchanger fluid by volume.
Heat exchanger inside diameter-2	0.029	m	The inside diameter of the pipe comprising the internal heat exchanger.
Heat exchanger outside diameter-2	0.032	m	The outside diameter of the pipe comprising the internal heat exchanger.
Heat exchanger fin diameter -2	0.032	m	The diameter of the fins on the outside pipe surface of the internal heat exchanger.
Total surface area of heat exchanger-2	2.5	m^2	The total outside surface area of the internal heat exchanger.
Heat exchanger lenght-2	24.88	m	The total length of internal heat exchanger pipe immersed within the storage tank fluid.
Heat exchanger wall conducitivity-2	45	W/mK	The conductivity of the heat exchanger wall including any applicable contact resistance.
Heat exchanger material conductivity-2	45	W/mK	The thermal conductivity of the material which comprises the internal heat exchanger.
Height of heat exchanger inlet-2	1.54	m	The height above the bottom of the storage tank of the inlet of the internal heat exchanger.

Table 21: Parameters for the type 60

Parameter	Value	Units	Description
Height of heat exchanger outlet-2	1.08	m	The height of the outlet of the internal heat exchanger from the tank above the bottom of the storage tank.
HX Fluid indicator -3	1	-	The fluid contained in the first internal heat exchanger: 1=Water; 2=Propylene Glycol; 3=Ethylene Glycol.
Fraction of glycol-3	0	-	The fraction of glycol contained in the internal heat exchanger fluid by volume.
Heat exchanger inside diameter-3	0.0254	m	The inside diameter of the pipe comprising the internal heat exchanger.
Heat exchanger outside diameter-3	0.0381	m	The outside diameter of the pipe comprising the internal heat exchanger.
Heat exchanger fin diameter -3	0.0381	m	The diameter of the fins on the outside pipe surface of the internal heat exchanger.
Total surface area of heat exchanger-3	7.8	m^2	The total outside surface area of the internal heat exchanger.
Heat exchanger lenght-3	61	m	The total length of internal heat exchanger pipe immersed within the storage tank fluid.
Heat exchanger wall conducitivity-3	16	W/mK	The conductivity of the heat exchanger wall including any applicable contact resistance.
Heat exchanger material conductivity-3	16	W/mK	The thermal conductivity of the material which comprises the internal heat exchanger.
Height of heat exchanger inlet-3	0.15	m	The height above the bottom of the storage tank of the inlet of the internal heat exchanger.
Height of heat exchanger outlet-3	1.6	m	The height of the outlet of the internal heat exchanger from the tank above the bottom of the storage tank.
Height of each node	0.0408	m	The height of the node.

Table 22 shows the RMSE and the maximum values of the absolute and relative error for the seven sensors installed.

Table 22: Values of RMSE and the maximum absolute and relative error

	Sensor 1	Sensor 2	Sensor 3	Sensor 4	Sensor 5	Sensor 6	Sensor 7
RMSE [°C]	2.81	2.60	2.58	0.372	2.06	1.92	0.746
Max relative error [%]	8.72	7.36	6.81	2.11	5.90	5.19	2.74
Max absolute error [°C]	3.96	3.37	3.11	1.01	2.73	2.41	1.30

To reduce the errors shown in Tab. 2, the TRNSYS optimization tool GenOpt has been used. The selected variables to be varied in order to minimize the objective function are the actual tank volume (*V*) and the Nusselt constant (*C*) for the lower heat exchanger. The latter is an input of the model, not a parameter, therefore it has not been listed in Table 19. For the results of Table 22, the default value of *C* has been used.

The optimization process provide as results:

C = 0.359

V = 974 l.

The validation of the tank storage model has been repeated with these new values of the selected variables. The results are shown in Table 23.

Table 23: Values of RMSE and the maximum absolute and relative error after the optimization process

	Sensor 1	Sensor 2	Sensor 3	Sensor 4	Sensor 5	Sensor 6	Sensor 7
RMSE [°C]	0.628	0.513	0.404	2.04	0.284	0.446	1.65
Max relative error [%]	4.72	2.97	2.16	0.64	1.12	1.18	0.26
Max absolute error [°C]	2.29	1.44	1.05	0.325	0.548	0.581	0.131

As seen, an overall reduction of the errors has been achieved and now the results can be considered acceptable to implement the model in whole-building simulation software.

2.1.7 Model of Variable Speed Internal Combustion Engine (Università Politecnica delle Marche, Italy)

The ICE has been simulated in Matlab/Simulink environment by describing all the subsystems which compose the ICE, such as the engine shaft, the engine and the heat exchangers (Fig. 41). [45]

The key assumption was that the thermo-fluid-dynamic processes of the engine are much faster than the change rate in thermodynamic boundary conditions. Thus the ICE has been modelled as a quasi-stationary machine and the ICE performances are simulated on the basis of two look-up tables defined according to the engine performance maps provided by the manufacturer.

A 28 kW_{el} ICE has been modelled, whose main technical parameters are shown in Table 24.

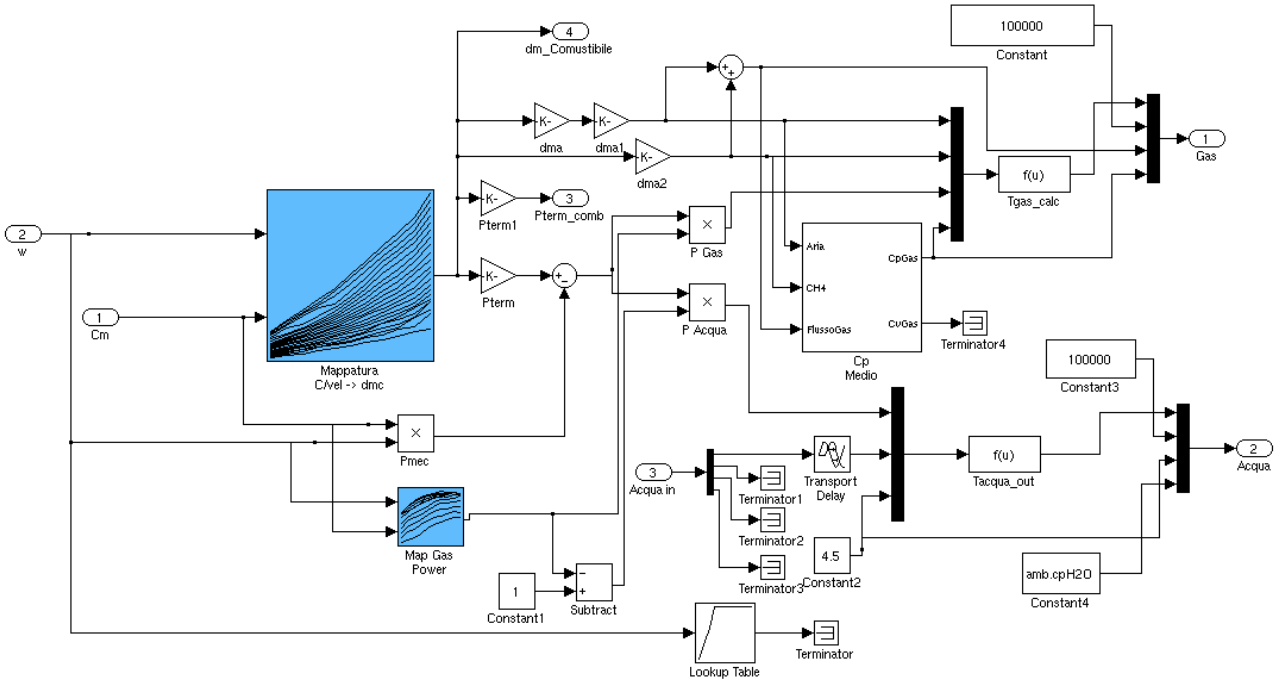

Fig. 41: Engine sub-system

Table 24: Technical parameters of ICE under analysis

Parameter	VALUE
Maximum rated electric output	28 kW_{el}
Maximum rated power output	58 kW_{th}
Minimum electric power	6 kW_{el}
Minimum thermal power	18 kW_{th}
Electrical efficiency	28.5 %

A control model was developed for both thermal and electrical priority mode. In the electric priority mode a speed regulator provides for the desired electric power output by the system. The regulator is based on an optimization table that, for any given power, helps the system choose the speed ensuring the greatest electric efficiency. Examples of the effect of speed optimization on electric efficiency are shown in Table 25. Electric efficiency gains can be obtained with the variable speed unit (compared with the constant speed machine at 3000 rpm), the lower the electric power setting the greater the gain.

Table 25: Effect of speed optimization on electric efficiency

Electric Power [kW]	Electric efficiency [%]		Percent variation [%]
	Constant speed operation (3000 rpm)	Variable speed operation	
28	0.285	0.285	0.0
26	0.280	0.286	2.1
24	0.273	0.286	4.8
22	0.269	0.281	4.5
20	0.261	0.279	6.9
18	0.253	0.273	7.9
16	0.239	0.272	13.8
14	0.227	0.268	18.1
12	0.211	0.258	22.3
10	0.198	0.256	29.3
8	0.171	0.241	40.9
6	0.147	0.217	47.6

Typical applications, a 10-flat apartment building for the residential sector, and an office and a hotel for the service sector, were chosen as test cases and the results discussed in terms of energy performances and of profitability. The technical–economic analysis showed that good energy and economic performances compared with a separate generation system can be achieved both in household and in hotel applications, especially with variable speed operation. In contrast, any office application would be scarcely profitable, since savings would be achieved only in the winter and would be too low to allow an economic return on the investment in a reasonable time. The possibility of regulating the rotational speed of the engine enhances energy performances, and although it entails a higher initial investment, the variable speed concept shortens the payback period and increases profits.

2.1.8 Empirical Calibration and Validation of the Annex 42 Combustion Cogeneration Model (Seconda Università degli Studi di Napoli, Italy)

Introduction

The current section treats the empirical calibration and validation of the Annex 42 combustion cogeneration model [46, 47] based on the experiments performed at the Built Environment Control Laboratory of the Seconda Università degli studi di Napoli (Italy). The experimental programme documented in [48, 49] consisted of a series of experiments with varied and controlled boundary conditions.

The tests were performed on a reciprocating internal combustion engine-based micro-cogeneration device commercialized by AISIN SEIKI company [50], fuelled by natural gas, and characterized by 6.0 kW as the nominal electrical output and 11.7 kW as the nominal thermal output.

The experiments yielded data that were used to calibrate the model to represent the performance of this specific device. Simulations results produced with the TRNSYS [51] implementation of the model using the calibrated inputs were compared with the measurements taken during the empirical validation tests.

The combustion cogeneration model was calibrated and validated using these experimental data during Annex 54's working phase.

Experimental set-up

A schematic diagram of the test apparatus of the Built Environment Control Laboratory detailing instrumentation components is shown in Fig. 42. The experimental set up is located in Frignano, a municipality in the Province of Caserta (about 20 km far from Naples). Additional details about the test apparatus can be found in [48, 49, 52].

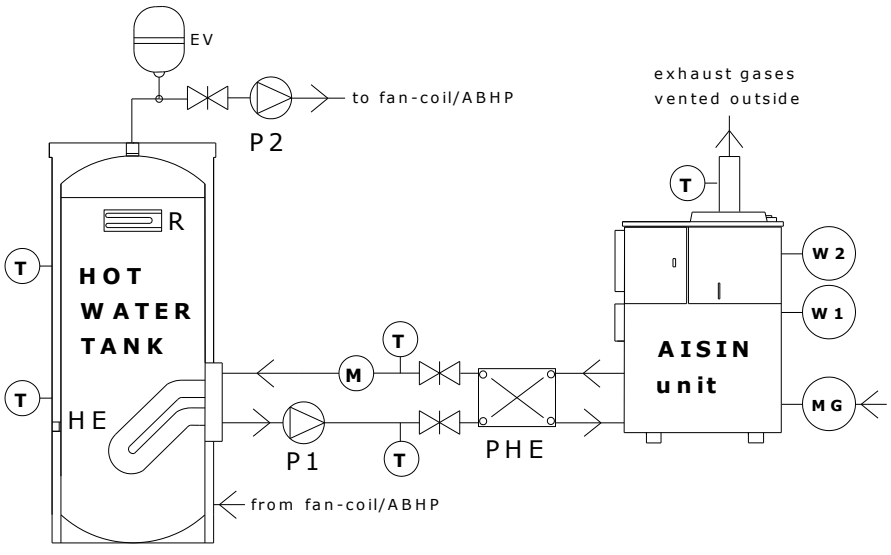

Fig. 42: Scheme of experimental apparatus

The micro-cogeneration under investigation is the model GECC60A2 NR/P commercialized by the AISIN SEIKI company [50]. This model is based on a reciprocating internal combustion engine that can be fuelled by natural gas or Liquified Petroleum Gas (LPG). The prime mover has three cylinders, with four strokes, and a total displacement of 952 cm^3. The endothermic engine drives a synchronous generator that can supply up to a nominal electric power of 6.0 kW; at the same time, its modern technology allows recovering the heat otherwise dissipated by the engine with a nominal power of 11.7 kW. The main characteristics of unit specified by the manufacturer [50] are reported in **Fehler! Ungültiger Eigenverweis auf Textmarke.**.

Table 26: Main characteristics of the model GECC60A2 (NR-P) produced by AISIN SEIKI unit [50].

Model	GECC60A2 (NR-P)
Engine type	water cooled, 4 cycles, 3 cylinders
Displacement (cm3)	952
Speed revolution (rpm)	1600÷1800
Fuel	Natural gas, LPG
Generator type	Permanent - magnet type, synchronous generator 16 poles
Rated electric output (kW)	0.3÷6
Heat recovery rate (kW)	11.7
Operating sound at 1.0 m distance and 1.5 m height (dB)	54
Electric efficiency at maximum load (%)	28.8
Thermal efficiency at maximum load (%)	56.2

The MCHP unit can operate under electric load-following logic or under thermal load-following control mode:

a) in the case of electric load-following operation, the cogeneration system produces electricity by modulating the power supplied through the inverter on the basis of the electric demand. The unit is turned off when electric energy is not required. Heat is also available during unit operation, but its level depends on the system electric output;

b) in the case of thermal load-following operation, the system operates according to the external temperature signal coming from a thermostat placed on the tank: when this temperature is lower than the set-point value, the unit operates providing its maximum electric and thermal outputs; when the water temperature in the storage exceeds the set-point value, the unit is turned off. Any unused excess of electricity that is not self-used is sent to the power line.

At the Built Environment Control Laboratory of the Seconda Università degli studi di Napoli the electric demand profile can be varied by managing eight halogen lamps characterized by different electric consumtpion; each lamp is equipped with a timer by means of which it is possible to schedule the lamps

operation. As alternative, the micro-cogeneration device can operate in order to follow the electric needs of the building associated to the operation of lighting appliances, PCs, printers, plotters, etc.

The thermal recovery during the MCHP unit operation is obtained from the exhaust gases and the engine jacket of the micro-cogenerator by using a water-glycol mixture as coolant. The heat recovered is transferred to the cooling water flowing through a high efficiency plate heat exchanger located inside the unit. The cooling water is circulated by the wet rotor pump P1 and its mass flow rate can be modified by varying the pump revolution speed: three different values can be manually set. The recovered thermal power is stored by means of a 1000 liters tank equipped with an internal heat exchanger; the hot water storage is insulated with 50 mm flexible polyurethane layer. During the winter the thermal energy stored within the tank is used for heating the laboratory.

The experimental plant is well instrumented in order to measure directly the following parameters: (1) water temperature in the key-points of the plant, (2) ambient temperature, (3) water mass flow rate in the key-points of the plant, (4) natural gas mass flow rate entering the micro-cogenerator, (5) electric power required by the lamps, (6) electric power supplied by the micro-cogenerator to the end-user.

Water and ambient temperatures are measured by using resistance thermometers Pt100; water mass flow rate is obtained by using an ultrasonic mass flow sensor, while a thermal mass flow meter is installed to evaluate the natural gas volumetric flow rate; two watt-meters measure the electric power supplied by micro-cogenerator and the electric power requested to the MCHP system. Two resistance thermometers were constructed to measure a temperature profile within the hot water tank.

The quantities directly measured during the experiments and the instrumentation employed are provided in Table 27. The instrumentation bias errors associated with each measurement are also given in this table.

Table 27: Main characteristics of the plant instrumentation.

Parameter	Instrument	Operating range	Uncertainty
Temperature	Resistance thermometer Pt100	-50÷100 °C	±0.2 °C
Cooling water volumetric flow rate	Ultrasonic volumetric flow meter	0÷50 l/min	±2.5% of full scale
Fuel volumetric flow rate	Thermal volumetric flow meter	0÷5.0 Nm3/h	±0.8% of reading ±0.2% of full scale
Electric output of the MCHP unit	Wattmeter	0÷6 kW	0.2% of full scale
Electric load	Wattmeter	0÷10 kW	0.2% of full scale

Model calibration

The Annex 42 model [46, 47] requires as inputs 103 empirically derived coefficients; therefore the model must be calibrated using empirical data and each set of model inputs is applicable to only one engine type, capacity, and fuel type; five input parameters defining the control method (input #1), the control signal

(input #2), the ambient temperature (input #3), the coolant inlet temperature (input #4) as well as the coolant mass flow rate (input #5) are also required by the model.

Additional details about the list of both the 103 calibration parameters and the 5 input parameters can be found in [46, 47].

In this work a two-stage calibration process was adopted.

Firstly, the equations describing the steady-state electrical and thermal efficiencies were formulated using data from testing the unit at different steady-state operating conditions.

Secondly, the dynamic characteristics of the model were calibrated using data from the device in thermally transient modes of operation. Because the experiments did not include sufficient measurements to directly calibrate all of the inputs required by the model, an iterative parameter identification approach was adopted. This approach used an optimization tool to determine the set of input parameters providing the closest agreement to the experimental data.

In 2004 Annex 42 participants defined an experimental protocol for testing cogeneration equipment [53]: this protocol guided Annex 42 testing programs to ensure the resulting data were suitable for calibration and validation of the model. The experiments conducted for calibrating the AISIN SEIKI unit [50] were performed trying to follow as closely as the physical constraints of the test bench permitted the guidelines suggested by the protocol [53]. However the test facility installed at the Built Environment Control Laboratory of Seconda Università degli Studi di Napoli was designed to replicate real-world conditions inside a residential application and therefore this study did not fully adhere to the Annex 42 experimental protocol [53].

Static model calibration

In this paragraph the calibration procedures followed to determine the calibration parameters #1-21, #26-30, #37-103 are described in detail. Additional information about the model calibration can be found in [48].

Calibration of the parameter #1

The calibration parameter #1 represents the maximum electric power that can be provided by the MCHP unit. A specific test was carried in order to identify this parameter: the model's maximum power generation parameter was set to 5596.2 W based on the results of this experiment.

Calibration of the parameter #2

The value of the calibration parameter #2 depends on the value of the input #1. In this study the input #1 was set to the value 2 (electrical control interface is used) and, therefore, the calibration parameter #2 was the minimum electric output of the unit. In this work the calibration parameter #2 was set to 0.

Calibration of the parameter #3

The calibration parameter #3 defines the maximum cooling water outlet temperature: the model shuts down the unit in case of the cooling water temperature at the outlet of the system exceeds the value set for the calibration parameter 3. Taking into consideration that the AISIN SEIKI cogeneration device [50] is

not deactivated in any case, the control associated to the calibration parameter #3 was disabled in this study.

Calibration of the parameters #4-19

Calibration parameter #4 identifies the fuel type (liquid or gaseous). In case of a liquid fuel is used, the model requires the specification of an empirically derived lower heating value (calibration parameter #5) and the liquid fuel CO_2 emission factor (calibration parameter #6). The AISIN SEIKI unit [50] is fuelled by natural gas; in the case of a gaseous fuel type is used, the model requires only the composition of the fuel by setting the calibration parameters #7-19.

The facility was not equipped to measure the composition or the calorific heating value of the natural gas used to fuel the AISIN SEIKI cogeneration device. As a consequence, the composition reported in Table 28 [54] representing the average Italian natural gas composition was assumed for the Annex 42 model calibration work. According to this composition, the model calculated the lower heating value: the composition reported in Table 28 provides a lower heating value of 49599 kJ/kg.

Table 28: Assumed natural gas composition [9].

Compound	Molar mass (g/mol)	Mole fraction (%)
Hydrogen	2.016	0
Methane	16.043	99.461
Ethane	30.07	0.063
Propane	44.097	0.009
Butane	58.123	0.008
Pentane	72.15	0
Hexane	86.18	0.01
Methanol	32.042	0
Ethanol	46.07	0
Carbon monoxide	28.01	0
Carbon dioxide	44.01	0.03
Nitrogen	28.014	0.419
Oxygen	15.999	0

Calibration of the parameters 37-90

The calibration parameters #37-90 are the empirically derived coefficients (a_0-a_{26} and b_0-b_{26}) that characterize the influence of cooling water mass flow rate $\dot{m}_{cw}$, cooling water inlet temperature $T_{cw,i}$, and net electrical power output at steady-state $P_{net,ss}$ on the steady-state electric (η_e) and thermal (η_q) efficiencies:

$$\eta_e = a_0 + a_1 P_{net,ss}^2 + a_2 P_{net,ss} + a_3 \dot{m}_{cw}^2 + a_4 \dot{m}_{cw} + a_5 T_{cw,i}^2 + a_6 T_{cw,i} + a_7 P_{net,ss}^2 \dot{m}_{cw}^2 + a_8 P_{net,ss} \dot{m}_{cw} + a_9 P_{net,ss} \dot{m}_{cw}^2 + a_{10} P_{net,ss}^2 \dot{m}_{cw} + a_{11} P_{net,ss}^2 T_{cw,i}^2 + a_{12} P_{net,ss} T_{cw,i} + a_{13} P_{net,ss} T_{cw,i}^2 + a_{14} P_{net,ss}^2 T_{cw,i} + a_{15} \dot{m}_{cw}^2 T_{cw,i}^2 + a_{16} \dot{m}_{cw} T_{cw,i} + a_{17} \dot{m}_{cw} T_{cw,i}^2 + a_{18} \dot{m}_{cw}^2 T_{cw,i} + a_{19} P_{net,ss}^2 \dot{m}_{cw}^2 T_{cw,i}^2 + a_{20} P_{net,ss}^2 \dot{m}_{cw}^2 T_{cw,i} + a_{21} P_{net,ss} \dot{m}_{cw}^2 T_{cw,i}^2 + a_{22} P_{net,ss}^2 \dot{m}_{cw} T_{cw,i}^2 + a_{23} P_{net,ss}^2 \dot{m}_{cw} T_{cw,i} + a_{24} P_{net,ss} \dot{m}_{cw}^2 T_{cw,i} + a_{25} P_{net,ss} \dot{m}_{cw} T_{cw,i}^2 + a_{26} P_{net,ss} \dot{m}_{cw} T_{cw,i} \quad (38)$$

$$\eta_q = b_0 + b_1 P_{net,ss}^2 + b_2 P_{net,ss} + b_3 \dot{m}_{cw}^2 + b_4 \dot{m}_{cw} + b_5 T_{cw,i}^2 + b_6 T_{cw,i} + b_7 P_{net,ss}^2 \dot{m}_{cw}^2 + b_8 P_{net,ss} \dot{m}_{cw} + b_9 P_{net,ss} \dot{m}_{cw}^2 + b_{10} P_{net,ss}^2 \dot{m}_{cw} + b_{11} P_{net,ss}^2 T_{cw,i}^2 + b_{12} P_{net,ss} T_{cw,i} + b_{13} P_{net,ss} T_{cw,i}^2 + b_{14} P_{net,ss}^2 T_{cw,i} + b_{15} \dot{m}_{cw}^2 T_{cw,i}^2 + b_{16} \dot{m}_{cw} T_{cw,i} + b_{17} \dot{m}_{cw} T_{cw,i}^2 + b_{18} \dot{m}_{cw}^2 T_{cw,i} + b_{19} P_{net,ss}^2 \dot{m}_{cw}^2 T_{cw,i}^2 + b_{20} P_{net,ss}^2 \dot{m}_{cw}^2 T_{cw,i} + b_{21} P_{net,ss} \dot{m}_{cw}^2 T_{cw,i}^2 + b_{22} P_{net,ss}^2 \dot{m}_{cw} T_{cw,i}^2 + b_{23} P_{net,ss}^2 \dot{m}_{cw} T_{cw,i} + b_{24} P_{net,ss} \dot{m}_{cw}^2 T_{cw,i} + b_{25} P_{net,ss} \dot{m}_{cw} T_{cw,i}^2 + b_{26} P_{net,ss} \dot{m}_{cw} T_{cw,i} \quad (39)$$

In Table 29 the operating conditions experimentally investigated at the Built Environment Control Laboratory in order to determine the parameters a_0-a_{26} and b_0-b_{26} were summarized: the date, the steady-state electric output, the cooling water flow rate, the minimum cooling water inlet temperature and the maximum cooling water inlet temperature were specified for each test.

Table 29: Operating conditions investigated for determining the calibration parameters #37-90.

Test number	Date (day/month/year)	$P_{net,ss}$ (kW)	$\dot{m}_{cw}$ (l/s)	$T_{cw,i,min}$ (°C)	$T_{cw,i,max}$ (°C)
1	02/11/2011	5.58	0.29	24.2	62.0
2	11/11/2011	3.15	0.29	27.6	64.5
3	07/12/2011	0.60	0.29	21.0	56.0
4	08/11/2011	5.60	0.18	26.0	57.7
5	21/11/2011	3.13	0.18	22.9	61.7
6	25/11/2011	0.58	0.18	25.4	67.1

In order to determine the calibration parameters #37-90, the protocol [53] suggests to operate the cogeneration device with both a constant electrical output and a constant cooling mass flow rate, while the temperature of the water supplied by the experimental facility to the cogeneration device's heat exchanger is varied over the range that can be achieved given the constraints of the experimental set-up and the operational requirements of the cogeneration device in approximately 5 °C steps; according to the protocol, the above test sequence should be repeated at other constant electrical outputs and then

repeated one more time at other constant cooling water mass flow rates. However the test facility was not designed to impose steady-state conditions on the combustion cogeneration unit. Therefore all of the experiments were dynamic tests in which the temperature of the cooling water varied continuously according to conditions in the water tank. As suggested by the protocol, the system was operated with three different electric outputs levels: ≈5.6 kW, ≈3.1 kW and ≈0.6 kW; tests number 1-3 were performed with a cooling water flow rate of 0.29 l/s, while the remaining experiments were carried by using a lower flow rate of the coolant equal to 0.18 l/s.

The set of six experiments provided a "performance map" of cogeneration device over the full range of system outputs and thermal boundary conditions and it was carried out with the main aim to characterize the influence of the following parameters on both electric and thermal efficiencies:

- electrical power output;
- flow rate of water entering the micro-cogeneration device for thermal load extraction;
- temperature of water entering the micro-cogeneration device for thermal load extraction.

The unit was maintained switched off at least 72 hours between two consecutively tests in order to evaluate the system efficiency in case of cold start-up.

Fig. 43 and Fig. 44 allow to analyse the influence of the temperature of the water entering the micro-cogeneration device, the electrical power output and the flow rate of cooling water on both electrical efficiency (η_e) and thermal efficiency (η_q).

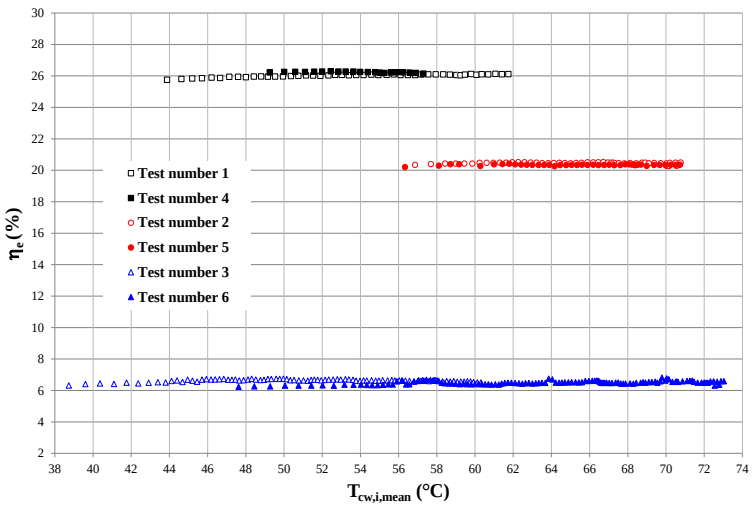

Fig. 43: Experimental values of η_e measured during tests #1-6.

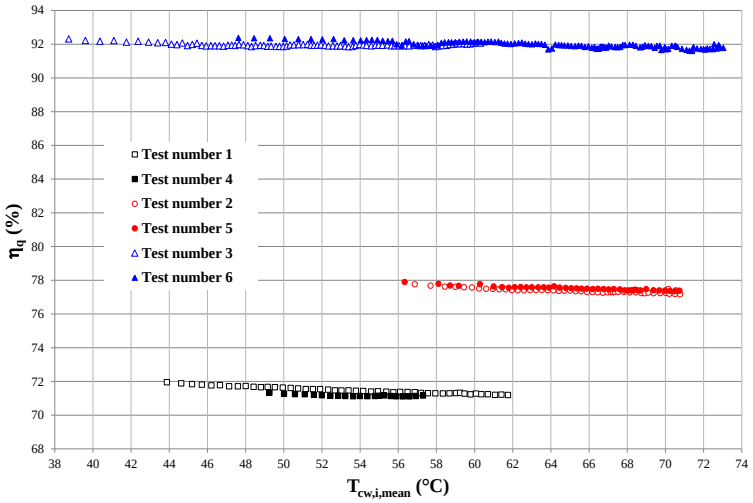

Fig. 44: Experimental values of η_q measured during tests #1-6.

The figures of η_e and η_q were obtained by directly measuring the net electric output at steady-state $P_{net,ss}$, while the evaluation of both the gross heat input into the system q_{gross} and the rate of heat generation within the engine $q_{gen,ss}$ was indirect. In particular, the primary power and the recoverable heat were calculated as follows:

$$q_{gross} = \dot{V}_{fuel} \cdot \rho_{fuel} \cdot LHV_{fuel} \tag{40}$$

$$q_{gen,ss} = q_{gross} - P_{net} - q_{exh} \tag{41}$$

where q_{exh} is the thermal power dissipated by the exhaust gases.

In the equation (3) the fuel volumetric flow rate was directly measured, the fuel density was assumed equal to 0.719 kg/m^3, the lower heating value of the fuel (49599 kJ/kg) was provided by the model accordingly with the fuel composition specified in Table 28. The thermal power dispersed by the exhaust gases was calculated by using the following formula:

$$q_{exh} = \dot{m}_{exh} \cdot c_{p,exh} \cdot (T_{exh} - T_{room}) \tag{42}$$

where $\dot{m}_{exh}$, $c_{p,exh}$ and T_{exh} were, respectively, the mass flow rate, the specific heat at constant pressure and the temperature of the exhaust gases and T_{room} was the ambient temperature. Both T_{exh} and T_{room} were directly measured; taking into consideration that the Built Environment Control Laboratory of the Seconda Università degli studi di Napoli was not equipped for measuring the exhaust gases mass flow rate and composition, the values of both $\dot{m}_{exh}$ and $c_{p,exh}$ were determined by assuming the following stoichiometric methane combustion:

$$CH_4 + 2 \cdot O_2 + 7.52 \cdot N_2 \rightarrow CO_2 + 2 \cdot H_2O + 7.52 \cdot N_2 \tag{43}$$

This reaction assumes that AISIN SEIKI unit is fuelled by methane instead of natural gas; however, since natural gas is mostly methane, we neglected the presence of the other compounds specified in Table 28.

The values reported in these figures are referred to the system operation in “normal mode” and represent the average values over three minutes long time intervals where the coolant inlet temperature is characterized by a maximum variation of 0.3 °C.

In Fig. 43 and Fig. 44 the experimental points characterized by the same electric output, but different cooling water flow rate were highlighted by same color of the symbols, but with a different replenishment: empty symbols characterize the experiments performed with $\dot{V}_{CW}$ = 0.29 l/s (tests number 1-3), while the data measured while $\dot{V}_{CW}$ was equal to 0.18 l/s (tests number 4-6) were identified by using solid symbols.

The analysis of the data reported in Fig. 43 and Fig. 44 indicates that there is a negligible influence of the coolant temperature or flow rate on either the electrical or thermal efficiencies. As a consequence, the coefficients a_3-a_{26} and b_3 -b_{26} were set to zero. From both Fig. 43 and Fig. 44 it can be derived that both electrical and thermal efficiencies are affected only by the electrical power output: in particular, the experimental results showed that, whatever the cooling fluid temperature and flow rate are, η_e rises with increasing the electrical power, while η_q increases at decreasing the electric output.

In Fig. 45 the average values of η_e and η_q corresponding to each value of the net electrical output experimentally investigated (≈5.6 kW, ≈3.1 kW, ≈0.6 kW) are plotted as a function of the net electrical output itself.

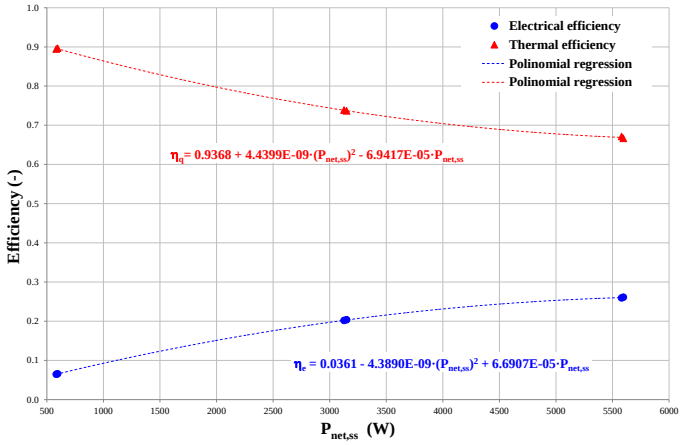

Fig. 45: Average values of $\eta_{e,mean}$ and $\eta_{q,mean}$ as a function of $P_{net,ss}$.

According to the values reported in Fig. 45, the following values were identified for the remaining coefficients of the model’s electrical and thermal efficiency equations by means of a second order polynomial regression of the experimental results:

- a_0 = 0.0361
- a_1 = -4.3890exp-9
- a_2 = 6.6907exp-5
- b_0 = 0.9368
- b_1 = 4.4399exp-9
- b_2 = -6.9417exp-5

Calibration of the parameter #30

When inactive, the AISIN SEIKI cogeneration unit consumes some electricity. The electrical consumption during stand-by operation was measured during the experiments described in Table 29. At any case it was observed that the stand-by power consumption was constant and equal to 90.0 W. Therefore, the model's net stand-by power generation (calibration parameter #30) was set to -90.0 W.

Calibration of the parameters #27-29

The AISIN SEIKI cogeneration model can be reactivate during cool-down operation: as consequence, calibration parameter #28 was set to the value 2. In order to characterize cool-down operation, the Annex 42 model requires to identify also the cool-down period duration (calibration parameter #27) and the electric output during cool-down (calibration parameter #29). Additional experiments were carried out in order to identify these two parameters: a cool-down duration of 331 s and an electric consumption during cool-down equal to 190.0 W were measured.

Some discrepancies were highlighted in relation to the cool-down mode by comparing the Annex 42 model specification and the real operation of AISIN SEIKI cogeneration device. In fact the model assumes that during cool-down the engine consumes no fuel and generates no heat; these assumptions are in contrast with the experimental behaviour of the AISIN SEIKI system.

In addition it can be highlighted that in the case of the end-user requires the unit activation during cool-down, the Annex 42 switches from cool-down mode to warm-up mode and, then, to normal mode. Differently from the model assumption, the AISI SEIKI unit switches directly from cool-down mode to normal mode (avoiding the warm-up mode) in the case of an electric load higher than about 300 W is required during cool-down operation.

Calibration of the parameter #26

In order to identify the duration of warm-up period (calibration parameter #26), tests #1-6 described in Table 29 were analysed and warm-up durations were measured: the results of these measurements were reported in Table 30.

Table 30: Warm-up durations.

Test number	Warm-up duration (s)	Comments
1	91	Cold start-up
1	62	Warm start-up
2	101	Cold start-up
3	121	Cold start-up
4	118	Cold start-up
5	129	Cold start-up
6	107	Cold start-up

These data indicated that warm-up duration is significantly affected by the engine temperature that in turn depends on both ambient temperature and unit operation before the starting. However in the Annex 42 model the start-up characteristics of internal combustion engines are considered not sensitive to the engine temperature. Therefore the highest warm-up duration experimentally determined (129 s) was used for setting the calibration parameter #26.

Calibration of the parameters #20-21

A specific test was performed in order to identify the values of both parameters #20 (maximum rate of change permitted in the system fuel flow $d\dot{m}_{fuel}/dt$) and #21 (maximum rate of change permitted in the system electric output dP_{net}/dt). The values of both $d\dot{m}_{fuel}/dt$ (black dotted line) and dP_{net}/dt (blue solid line) associated to the unit operation after a cold start-up are depicted in Fig. 46.

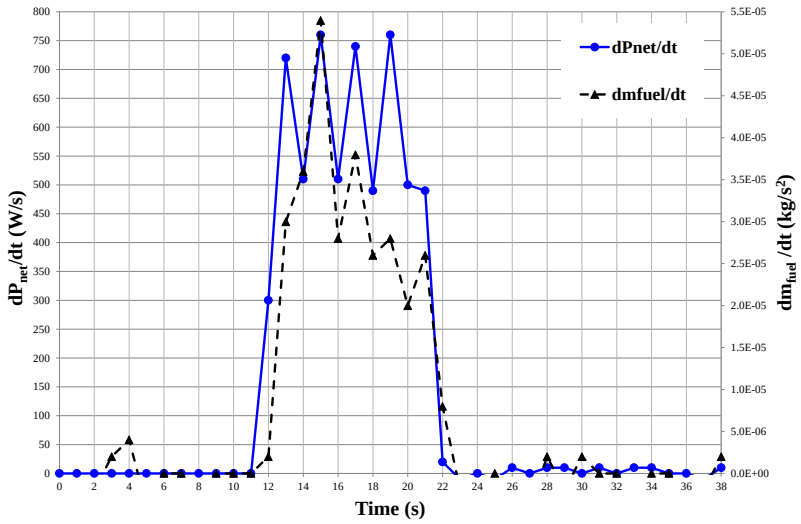

Fig. 46: dP_{net}/dt and dm'_{fuel}/dt as a function of time.

Based on the data reported in this figure, the following values of calibration parameters #20 and #21 were assumed:

$$d\dot{m}_{fuel}/dt\Big|_{max} = 5.4\text{exp-}5 \text{ kg/s}^2 \quad (44)$$

$$dP_{net}/dt\Big|_{max} = 760.0 \text{ W/s} \quad (45)$$

Calibration of the parameters #91-100

Calibration parameter #91 defines the cooling loop configuration. The AISIN SEIKI unit is not capable of regulating the flow rate of water-glycol mixture: therefore, the cooling loop configuration was set to external pump. In this configuration, the water-glycol mixture flow correlation coefficients described in the model specification (calibration parameters #92-100) are superfluous.

Calibration of the parameters #101-103

In the micro-cogeneration systems the air stoichiometry is regulated to manage the combined heat and power unit's combustion efficiency: in the Annex 42 model the air flow rate is calculated using a second order polynomial function based on the fuel mass flow rate. The experiments conducted at the Built Environment Control Laboratory did not include measurement of supply air flow rate. Without these data, calibration of the model's air flow correlations was impossible. As a consequence, the combustion air flow correlation coefficients (calibration parameters #101-103) were set to zero.

Dynamic calibration

The second stage of the calibration process was to tune the characteristics of the dynamic thermal model (calibration parameters #22-25) using data from dynamic tests on the MCHP unit. Additional details about dynamic calibration can be found in [48]. Because the equipment did not include sufficient measurements to directly calibrate all of the inputs required by the model, an iterative dynamic parameter identification approach was adopted. This approach used the GenOpt software tool [55] and a simplex-search-based approach to determine the set of the model's dynamic parameters providing the closest agreement with the experimental data. GenOpt drove the simulation software incorporating the cogeneration device model (in this case TRNSYS [6]) over multiple simulations. In these simulations:

1) the model was subjected to the same cooling water temperature, cooling water flow rate, electric power generation and ambient temperature as the AISIN SEIKI unit experimental tests performed at the Built Environment Control Laboratory;
2) a set of tentative values was chosen for the calibration parameters #22-25;
3) the optimization utility invoked the building simulation program, which performed a simulation using the above-reported parameters and the boundary conditions derived from the experiments;
4) at the end of each simulation, the model's predicted outlet temperature $T_{cw,o,pred}$ was extracted from the simulation and compared with the experimental value $T_{cw,o,exp}$. The objective of this process was to minimise the mean square error between these two values over the N time steps of the simulation:

$$\varepsilon = \sum_N \left(T_{cw,o,pred} - T_{cw,o,exp} \right)^2 \Big/ N \qquad (46)$$

5) The coolant outlet temperature was used as the target for the optimisation as it is the principle, coupling variable between the generic cogeneration model and the systems model into which it would be integrated; the values assigned to the parameters #22-25 were adjusted based on the results of the simulation according to the selected optimization algorithm and steps 2–4 were repeated until the best-possible agreement between model outputs and empirical data was achieved.

GenOpt automates steps 2–4 of the parameter identification process, and can perform thousands of simulations while searching for the optimal input set.

The dataset used in the calibration process was derived from the test #1 described in Table 29, with measurements taken at a frequency of 1 second. The data used in the dynamic calibration included both the warm-up of the engine and the steady-state operation.

The parameter values derived during dynamic calibration of the Annex 42 combustion cogeneration model are reported in the following:

- UA_{loss} = 58.0 W/K
- UA_{HX} = 3493.0 W/K
- $[MC]_{cw}$ = 7955.0 J/K
- $[MC]_{eng}$ = 82845.0 J/K

Model Validation

After the calibration activity, an empirical validation was then used to assess the validity of the mathematical model to simulate the performance of the cogeneration device through the comparison of simulation results with measurements taken in laboratory from an experimental test completely different from the tests used to calibrate the Annex 42 model. Additional detail about the validation activities can be found in [48, 49].

The data used to validate the model were measured by operating the system under electric load-following logic. The daily electric demand profile reported in Fig. 47 was applied; this profile represents the electricity requirements of a 5-dwellings Multi Family House (MFH) derived from a report of the Politecnico of Milano based on measurements onsite of the electric consumptions in the Italian residential sector within the SAVE EURECO and MICENE projects [56].

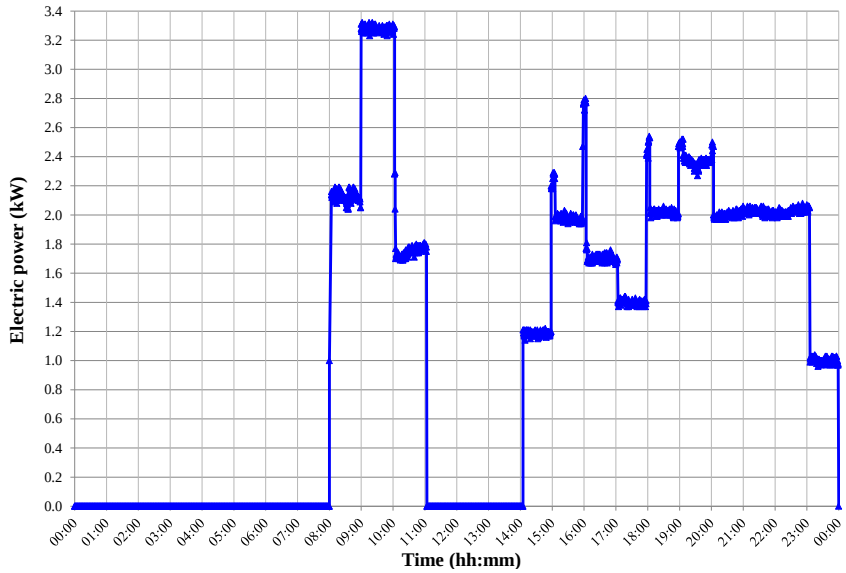

Fig. 47: Daily electric load profile considered for model validation.

This experiment was simulated by means of the Annex 42 model by using the measured values of ambient temperature, cooling water inlet temperature and cooling water mass flow rate as inputs.

The accuracy of the calibration was validated by using the following metrics quantifying both the instantaneous and cumulative difference in the model predictions:

- the average error $\bar{\varepsilon}$;
- the average absolute error $|\bar{\varepsilon}|$;
- the root mean square error ε_{RMS};
- the cumulative error in the energy prediction ε_E.

These parameters were defined as follows:

$$\varepsilon_i = g_{pred,i} - g_{exp,i} \tag{47}$$

$$\bar{\varepsilon} = \sum_{i=1}^{N} \varepsilon_i \Big/ N \tag{48}$$

$$|\bar{\varepsilon}| = \sum_{i=1}^{N} |\varepsilon_i| \Big/ N \tag{49}$$

$$\varepsilon_{RMS} = \sqrt{\sum_{i=1}^{N} (\varepsilon_i - \bar{\varepsilon})^2 \Big/ N} \tag{50}$$

$$\varepsilon_E = \left(E_{pred} - E_{exp} \right) \Big/ E_{pred} \tag{51}$$

where:

- $g_{pred,i}$ is the measured value at time step i;
- $g_{exp,i}$ is the predicted value. at time step i;
- N is the number of measurements.

The statistical comparison among experimental and predicted results was performed not only in relation to the entire database, but also by segregating the data by system mode operation (stand-by mode, cool-down mode, warm-up mode, steady-state mode were considered) with the aim to highlight both strong points and the faults of the model.

The whole database consists of 2875 points; the most part (1548) of the experimental values were measured during steady-state operation; only few points have been recorded during cool-down and warm-up operation.

Table 31 summarizes the errors between the model predictions and observations from the calibration data set.

Table 31: Comparison of model predictions with experimental data.

	Number of experimental points	Parameter	$\overline{\varepsilon}$ (W)	$\overline{\lvert\varepsilon\rvert}$ (W)	ε_{RMS} (W)	ε_E (%)
WHOLE DATABASE	2875	q_{HX}	-41.4	116.8	424.6	-
		q_{gross}	-423.5	442.3	700.1	-
		P_{net}	-1.8	2.4	55.0	-
		E_{HX}	-	-	-	-1.0
		E_{gross}	-	-	-	-6.1
		E_{net}	-	-	-	-0.2
STANDBY MODE	1309	q_{HX}	0.0	0.0	0.0	-
		q_{gross}	0.0	0.0	0.0	-
		P_{net}	-0.4	0.4	6.2	-
COOL-DOWN MODE	11	q_{HX}	-5361.5	5361.5	5396.4	-
		q_{gross}	-8402.1	8402.1	7979.8	-
		P_{net}	0	0	1.8	-
WARM-UP MODE	7	q_{HX}	295.2	309.1	709.3	-
		q_{gross}	733.7	4436.1	5538.4	-
		P_{net}	-712.9	875.7	1108.3	-
STEADY-STATE	1548	q_{HX}	-40.2	177.3	352.4	-
		q_{gross}	-730.1	741.7	409.1	-
		P_{net}	0.1	0.1	5.2	-

With reference to the whole database, it can be noticed that the predicted electric output agreed very well with experimental observations; the Annex 42 model underpredicted both heat recovery and primary power consumption, even if the prediction of q_{gross} exhibited more variation between measurements and predicted values. However, the predicted cumulative heat recovery differed from their measured values by 1.0%, while the cumulative gross input was predicted with a percentage error equal to 6.1%.

As it can be derived from Table 31, the main deviations between the measured and predicted results were associated to the cool-down period of the unit and indicated that the Annex 42 model significantly underpredicted both the primary power consumption (Annex 42 model assumes no fuel consumption during cool-down, while 2772.7 kJ were measured as primary energy consumption during cool-down) and the thermal recovery (Annex 42 model assumes no heat generation during cool-down, while 2039.5 kJ were derived from the experimental data as thermal energy provided during cool-down). The differences between the measured and predicted values can be also explained by taking into account the wrong estimation of warm-up duration by Annex 42 model due to the fact that Annex 42 model does not allow to consider the influence of the engine temperature. No significant discrepancies can be highlighted between

the experiment and the simulation by considering the data recorded during stand-by operation. The reasons for the discrepancy in the heat recovery also reflected the Annex 42 assumption of heat transfer characteristics of the heat exchangers constant over the operating temperature range of the unit.

Even if in the future it would be desirable to extend this work to consider other operating scenarios and despite some problems identified mainly during cool-down and start-up, the results of the empirical validation allowed to conclude that the model is able to predict the thermal and electric behaviour of the AISIN SEIKI unit and, therefore, a detailed performance assessment can be performed using this calibrated model to examine the applicability of this device for supplying building electrical and thermal energy requirements.

Conclusions

In this study, the Annex 42 combustion-based cogeneration model was experimentally calibrated and validated using data collected from an AISIN SEIKI cogeneration unit at Seconda Università degli studi di Napoli (Italy).

The experimental procedures that were employed to calibrate the Annex 42 model were described in detail and the results of this calibration approach were presented. During the calibration activity, some discrepancies between the structure of the model and the experimental behaviour of the micro-cogeneration unit were highlighted and, therefore, some modifications to the mathematical form of the Annex 42 were suggested.

The calibrated inputs derived in the current study were used in an empirical validation effort. In order to empirically validate the model, an additional experiment (disjunct from the tests used to calibrate the model) was conducted and the results of the validation activity was reported. The calibrated model exhibits reasonable agreement when compared with the validation data set: the predicted fuel use, electric output and heat recovery over the duration of the data set all differed from observed values by -6.1%, -0.2% and -1.0%, respectively. As a consequence, despite some discrepancies between the predictions and the experimental results mainly during cool-down and warm-up operation, it was concluded that the model gives an accurate representation of the unit's dynamic and steady-state performance.

2.2 Balance of Plant Models

2.2.1 A Mathematical Model of a Solar Cooling System (ENEA, Italy)

Introduction

The solar cooling model described below is based on one of the most common solar cooling configuration plants. It consists of the following main components: *compound parabolic concentrator* (CPC), *backup boiler*, *ACS boiler*, *H_2O- LiBr absorbtion chiller*, hot *thermal storage, cold thermal storage*, *ACS storage*. [57 – 61]

The model is developed in Matlab-Simulink and is shown in Fig. 48: two main blocks can be seen, one for winter and one for summer operation.

Although some components (boiler, distribution system and emission, storages) are used both for heating and for cooling, some of them have been duplicated with the purpose to optimize the management model.

Starting from the configuration described above, a simulation model of the building-plant system has been developed . The analysis carried out by means of the model aim to identify the optimum operation of the plant integrated with the building, both in winter and summer, and in relation to the user's characteristics.

Model description

The solar field receives weather data from a Weather Generator, which provides, as a function of the geographical data (latitude, etc.), the local temperature and the solar radiation. The produced power feeds the hot tank in order to keep its temperature within the temperature target range required by the emission system (radiators, fan coils, radiant panels, etc.) in winter and by the absorption chiller in summer. The hot tank receives also the energy produced by a backup boiler, which integrates the solar field when its power production is absent or limited.. The *Hot Thermal Tank* contains hot water and it supplies, in winter, the emissions systems of the distribution system, while in summer it supplies the chiller, a typical H2O- LiBr absorption cooling machine. Moreover, it is present a *cold tank* containing cold water and feeding the summer emission system (fan coils). The model has also an electric heat pump to integrate cooling demand of the building in case the absorption chiller isn't able to supply the whole cooling demand.

The power produced by the solar field is usually routed into the storage system; it is dissipated in case exceed the maximum temperature of the tank or when it reaches the maximum operating temperature of the solar collectors to avoid the achievement of the stagnation temperature (that could impair their functionality).

The whole model is operated by a control system based on the logic of maximizing the solar production both in summer and in winter season.

Scope of Model

This section describes the mathematical model of the two most important components of the solar cooling model: the solar collector and the absorption chiller.

Compound Parabolic Concentrator Model

The model, based on the Hottel-Whillier equation, defines the efficiency (η) of a collector as composed by the optical efficiency and by the heat losses:

$$\eta = a_0 - a_1 \frac{(T_i - T_a)}{I_T} - r_1 r_2 a_2 \frac{(T_i - T_a)^2}{I_T} \qquad (52)$$

where a_0 is the optical efficiency, a_1 is the heat loss coefficient [$Wm^{-2}K^{-1}$] , a_2 is a second heat loss coefficient [$Wm^{-2}K^{-2}$], r_1 is a correction factor for differences between the actual and the reference flow in the inner collector, r_2 is a correction factor due to collector in series, T_i is the temperature inside the collector and T_a is the outdoor air temperature.

When the difference between the output temperature and the test temperature is<5%, the solar plant output power is supplied with an iterative loop implemented in the model.

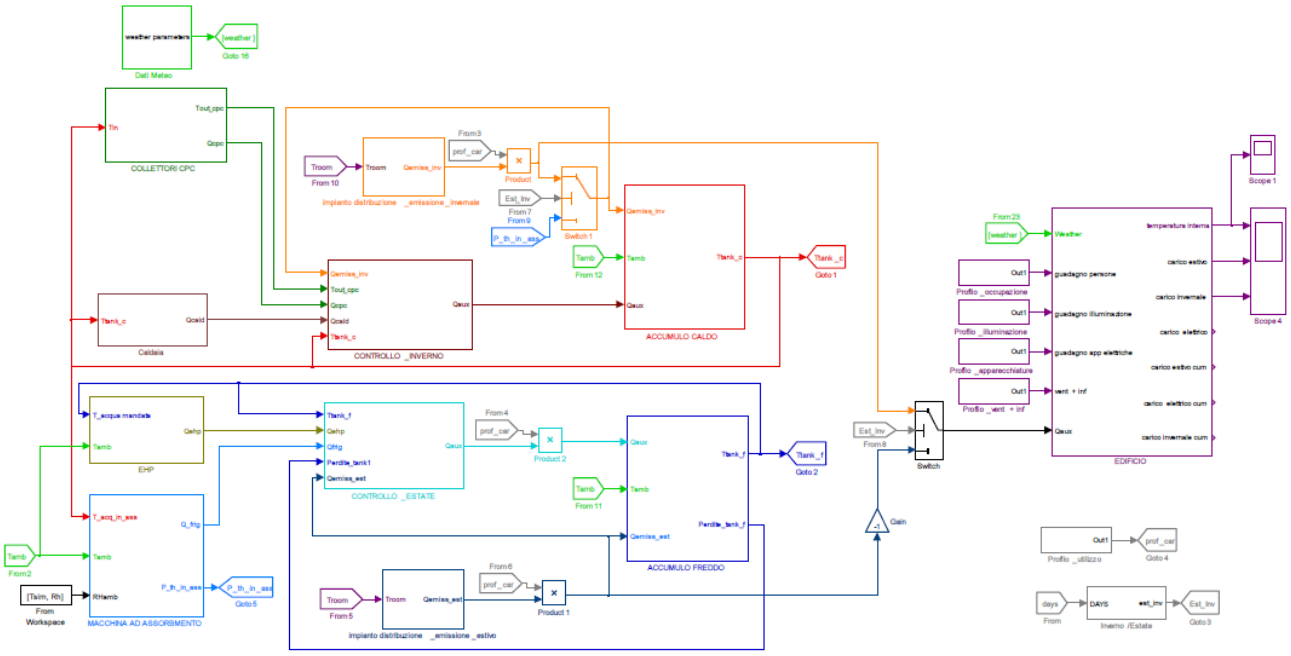

Fig. 48: Layout in Simulink of the solar cooling system.

Model of the H_2O- LiBr Chiller

The model, developed in the Matlab/Simulink platform, calculates the cooling power produced by the absorber, in function of the temperature of the inlet hot water, of the outdoor conditions, and of the nominal heat input to the absorber. The model also estimates the air flow of the cooling tower.

The H2O-LiBr Chiller model has been validated by means of the experimental data provided, in graphs or maps, by the unit manufacturer for the models Yazaki WFC-SC10, -SC20, -SC30.

These maps are parameterized in function of the cooling temperature of the absorber and show the cooling capacity produced by the chiller (P_c) or the thermal power absorbed by the chiller (P_{th}) as a function of the temperature of the hot water at the inlet ($T_{in,\,hot}$). The cooling is supplied by means of water from a cooling tower. The following temperatures of the cooling tower water (T_{tW}) have been used: 27°C, 29.5°C, 31°C and 32°C.

From the maps provided by the manufacturer dimensionless curves, normalized with respect to the nominal operating conditions specified by the manufacturer, have been obtained. The nominal operating conditions are identified by the following temperature values: $T_{in,hot}$ = 88.6 °C and T_{tw} = 31 °C.

In Fig. 49 the experimental dimensionless maps for Yazaki WFC-SC10 chiller are shown.

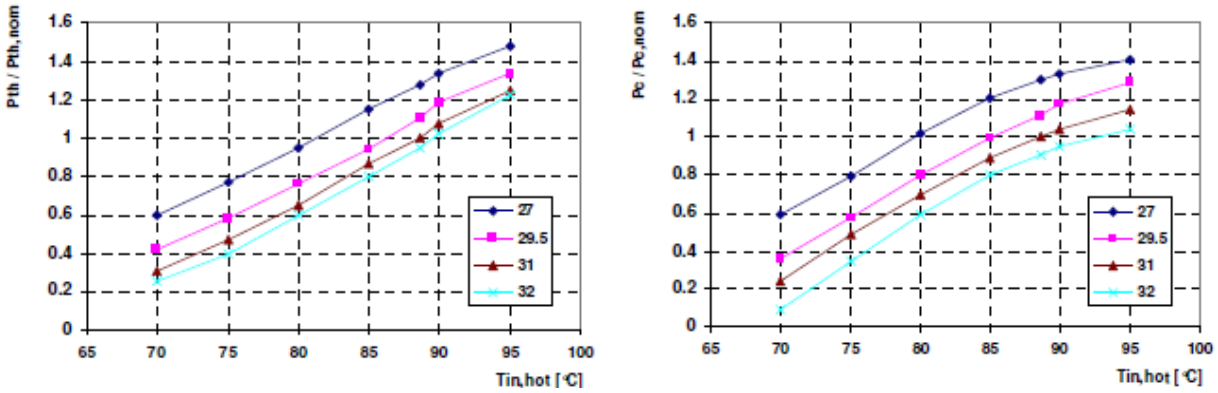

Fig. 49: Experimental dimensionless maps for Yazaki WFC-SC10 Chiller. (a) Thermal power (b) Cooling power.

A mean dimensionless map, valid regardless to the chiller used, can be obtained calculating the average dimensionless thermal power in correspondence of each value of the temperature of the hot water at the inlet and of each temperature of the cooling tower water. The mean dimensionless map of the thermal power absorbed by a generic chiller is shown in Fig. 50.

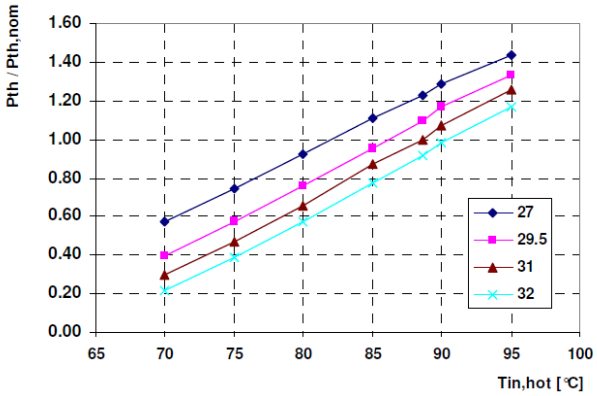

Fig. 50: Dimensionless thermal power absorbed by a generic chiller, parameterized in function of the temperature of the cooling tower water.

Further, for each chiller, the COP, as the ratio between the cooling capacity produced and thermal power absorbed by the chiller, has been calculated for each temperature of the hot water at the inlet and for each temperature of the cooling tower water. These COP values, as a function of the temperature, are shown in Fig. 51a.

Calculating the average value of the COP in correspondence of each value of the temperature of the hot water at the inlet, the medium COP curve (shown in Fig. 51b) can be obtained.

This medium COP curve can be considered valid for each size of the chiller and for each temperature of the cooling tower water and is only a function of the temperature of the hot water at the inlet of the absorber.

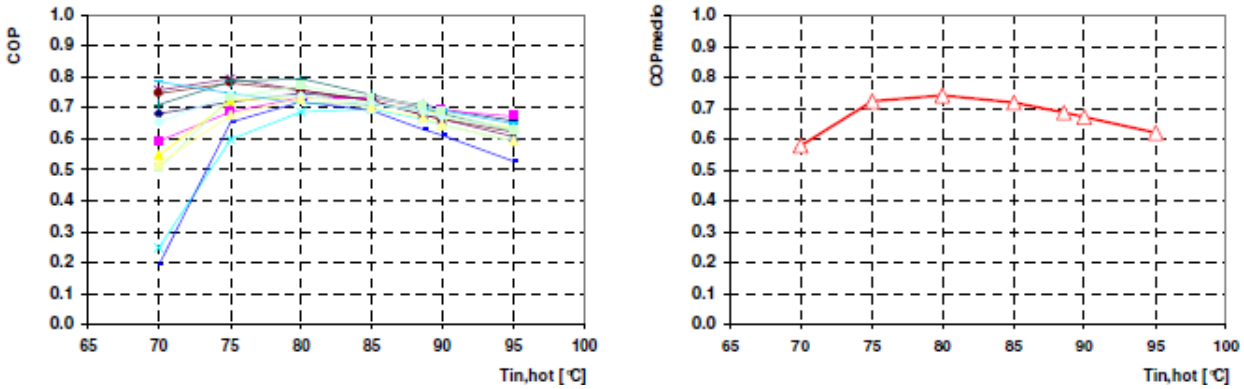

Fig. 51: (a) COP (b) COP - Medium Value

These maps are used in the Simulink model to build a lookup table. The model simulates therefore the operation both of the chiller and of the cooling tower, whose function is to dissipate the thermal power generated by the chiller.

The wet bulb temperature of the air is calculated by means of Jeevananda Reddy equation:

$$T_{wb,amb} = T_{db,amb} \cdot \left(0.45 + 0.006 \cdot RH \cdot \sqrt{\frac{p_{amb}}{1060}}\right) \qquad (2) \qquad (53)$$

The cooling water at the entrance of the chiller (that is the cooling tower water) is calculated adding $T_{wb,amb}$ and $\Delta T_{out,tw/db,amb}$., where $\Delta T_{out,tw/db,amb}$.is an input value.

The two values ($T_{out,tw}$ and $T_{in,hot}$) are then used as input parameters in the maps of the dimensionless thermal power and of the COP.

Multiplying the nominal thermal power and the dimensionless thermal power (map in Fig. 50), we obtain the actual power absorbed by the chiller, which, multiplied for the COP (map in Fig. 51a), gives the power produced by the chiller.

Applying the energy balance to the solar cooling system, we obtain:

$$P_{tW} = P_{th} + P_c \qquad (54)$$

where:

- P_{th} : thermal power supplied by the solar plant;
- P_c : cooling capacity provided by the chiller;
- P_{tw} : thermal power dissipated by the cooling tower.

The model calculates the thermal power dissipated by the cooling tower, once P_c and P_{th} are known.

The P_{tw} can be written as:

$$P_{tW} = \dot{m}_{tW} \cdot c_p \cdot \left(T_{in,tW} - T_{out,tW}\right) = \dot{m}_{tW} \cdot c_p \cdot \Delta T_{in,tW/out,tW} \qquad (55)$$

where $\dot{m}_{tW}$ is the tower water flow; c_p is the water specific heat at constant pressure; $T_{in,tw}$ is the temperature of the water at the inlet if the tower; $T_{out,tw}$ is the temperature of the water at the outlet to the tower.

The model calculates the water flow of the cooling tower and the corresponding air flow $\dot{m}_{air,tW}$ as:

$$\dot{m}_{air,tW} = \frac{\dot{m}_{tW}}{2} \qquad (5) \qquad (56)$$

The Fig. 52 shows the temperature trend of the indoor air of an office building supplied by a modeled solar cooling plant.

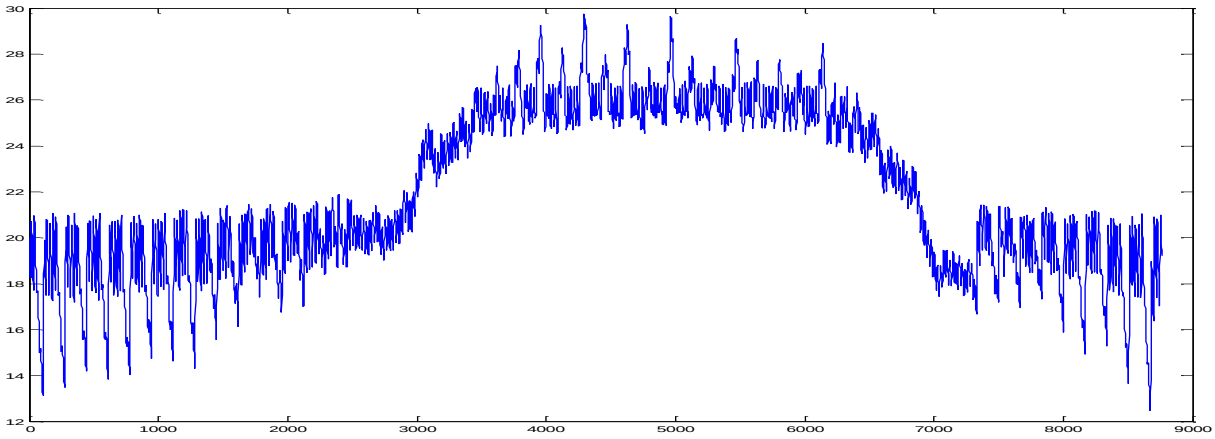

Fig. 52: Office internal temperature

The trend shows that the model is able to manage the power supplied by the various components to maintain the target temperature.

Model inputs and outputs

The input and output parameters used in each main component of the model are listed below.

Solar collector: solar module area [m^2], number of modules, maximum operation temperature [°C], percentage of glycol in solution [%], optical efficiency a_0 [$Wm^{-2}K^{-1}$] , heat loss coefficient a_1 [$Wm^{-2}K^{-1}$], heat loss coefficient a_2 [$Wm^{-2}K^{-2}$]

Thermal hot tank and Cold tank: volume [m^3], limit operating temperature [°C], total transmittance [$Wm^{-2}K^{-1}$], form factor [1/m].

Absorption chiller system : rated cooling capacity [kW].

Emission system: type (fancoil, etc), power of each emission unit [kW], elements number, maximum operation temperature [°C], minimum operation temperature [°C].

Gas Boiler: maximum heating capacity [kW].

Compression chiller system: rated cooling capacity [kW]; Energy Efficiency Ratio [EER].

Conclusions and further developments

A mathematical model of a solar cooling plant, developed in the Matlab/Simulink environment, has been presented and analyzed. The good accuracy and the easy integration of the model with other components described in the other section allow its use in a software platform for dynamic simulation of the whole building-HVAC system and energy demands of small block of buildings developed by ENEA [57]. The results of the integration will be shown in the Subtask B report, where an evaluation of the effective economical and energy convenience of solar cooling plant will be presented.

Nomenclature

- a_0 is the optical efficiency,
- a_1 the heat loss coefficient [$Wm^{-2}K^{-1}$],
- a_2 heat loss coefficient [$Wm^{-2}K^{-2}$],
- $r_1$correction factor for inner collector flow different from test vlue,
- r_2 correction factor due to collector in series,
- T_i the collector inner temperature [°C]
- T_a ambient temperature [°C]
- P_c cooling capacity produced by the chiller [kW]
- P_{th} thermal power [kW]
- $T_{in,\,hot}$ temperature of the hot inlet water [°C]
- T_{tW} temperatures of the cooling tower water [°C]
- P_{tw} thermal power[kW]
- $\dot{m}_{tW}$ tower water flow [kg/s]
- c_p water specific heat at constant pressure [kJ/kg K]
- $T_{in,tw}$ input water temperature to the tower [°C]
- $T_{out,tw}$ outlet water temperature to the tower [°C]
- $\dot{m}_{air,tW}$ air flow [kg/s].

2.2.2 Tank Storage Component Model with Embedded Phase Change Material (University of Trieste, Italy)

Introduction

One of the main problems facing a designer in dealing with cogeneration plants is the requirement of sufficient thermal storage to account for the different times in which energy is generated respect the times when it is needed, this is particularly important when the plant system features different system in order to provide warm water to the final users. This is especially true if renewable energy sources are present, such as solar systems, cogenerative systems, heat pumps and so on.

In an attempt to improve the available thermal storage, the water sensible heat storage of common tanks can be improved using phase change materials wich can absorb and release a substantial quantity of latent energy .during the phase change. Different kinds of PCM are available, such as paraffin or salt hydrates,

with different characteristics and problems. In order to take into account the possible improvements to be obtained using latent storage a tank model used by the building code ESP-r has been modified in order to allow the insertion of cylindrical modules filled with PCM.

The original tank model [62] comprises one or two heat exchangers and it are plant components 104 “Stratified storage tank with 2 immersed HX” and plant component n° 103 “Stratified storage tank with 1 immersed HX”

The new model considers the presence of cylindrical PCM modules as presented in Fig. 53. Fig. 53a) represents the original model with the tank divided in vertical layers to account for stratification, while Fig. 53b) represents the new model with PCM modules. The PCM modules are discretized using a finite volume grid which is independent from the discretization of the tank.

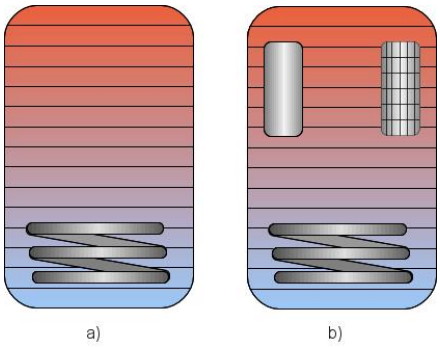

Fig. 53: Tank with internal heat exchanger a) tank with PCM modules b)

Phase Change modeling

Different strategies are implemented in literature to deal with Phase Change problems. The main problem arise from the moving boundary between liquid and solid phases and a different set of equations for the liquid, the solid zones and interface, this is referred as a Stefan problem. To avoid the difficulties of tracking the interface an enthalpy formulation has been adopted as described by Voller in [63]. In this formulation the energy equations for liquid and solid phases are replaced by the following single equation

$$\rho \frac{\partial h}{\partial t} = \nabla \cdot (k \nabla \theta) \tag{57}$$

$$h = \begin{cases} c_s \theta; & \theta < \theta_{pc} \\ c_l \theta + (c_s - c_l)\theta_{pc} + L; & \theta \geq \theta_{pc} \end{cases} \tag{58}$$

valid for both liquid and solid phases and implicitly satisfying the Stefan heat balance condition at the interface. Eqns. (57) and (58) can be solved using an explicit or an implicit formulation, in the former case the computational burden is reduced per time step but a stability limit must be satisfied.

If an explicit formulation is been used to solve Eq. (58) the time step is accordingly short to avoid stability problems, however also the original ESP-r tank model uses a sub stepping technique to deal with the internal heat exchangers

Explicit formulation

Temperature and enthalpy relation can be written as:

$$\theta_P = \begin{cases} \dfrac{h_P}{c_s} & h_P < c_s\theta_{pc} \\ \theta_{pc} & c_s\theta_{pc} \le h_P < c_s\theta_{pc} + L \\ \dfrac{h_P - (c_s - c_l)\theta_{pc} - L}{c_l} & h_P \ge c_s\theta_{pc} + L \end{cases} \tag{59}$$

Eq. (57) can be discretized over a finite volume grid obtaining the general finite volume form

$$\rho a_P^0 h_P^n = \rho a_P^0 h_P^0 + \sum (a_{nb}\theta_{nb}^0 - a_P\theta_P^0) \tag{60}$$

For stability, the time and space steps need to be chosen such that:

$$\Delta t \le \frac{\rho\, c\, V}{\left(\dfrac{k\, A_W}{\Delta r} + \dfrac{2\, k\, A_N}{\Delta l_{PN}}\right)} \tag{61}$$

Eq. (60) can be solved at each time step obtaining the nodal enthalpy field, the computation is completed by obtaining the temperature nodal field using Eq. (59)

PCM module discretization

The cylindrical PCM modules have been discretized using a finite volume approach obtaining the coefficients of Eqn. (60). A two dimensional axisymmetric formulation has been employed. The module discretization In axial and radial direction are defined by the user. In axial direction the grid is uniform while in radial direction the generic finite control volume is a ring with inner radius (R_E+R_P)/2 and outer radius (R_W+R_P)/2 as presented in Fig. 54a).

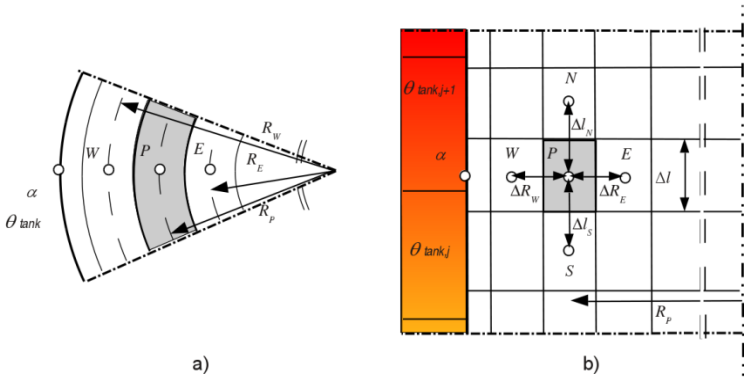

Fig. 54: PCM module discretization

The convective boundary condition for the solution of PCM modules uses the temperature of tank layers obtained at previous time step, the heat transfer coefficients are obtained using a mixed convection

formulation that takes into account the temperature difference among PCM module surface and water temperature and the possible mass flow between inlet and outlet of the water tank crossing a discretized tank layer.

By integration of Eqn. (57) on the generic finite volume represented in Fig. 54 the following balance equation can be written for each internal cell

$$\begin{aligned}\frac{\rho V_P}{\Delta t} h_P^{n+1} &= \frac{\rho V_P}{\Delta t} h_P^n + \frac{k_E A_E}{\Delta R_{PE}} \theta_E^n + \frac{k_W A_W}{\Delta R_{PW}} \theta_W^n \\ &+ \frac{k_N A_N}{\Delta l_{PN}} \theta_N^n + \frac{k_S A_S}{\Delta l_{PS}} \theta_S^n \\ &- \left(\frac{k_E A_E}{\Delta R_{PE}} + \frac{k_W A_W}{\Delta R_{PW}} + \frac{k_N A_N}{\Delta l_{PN}} + \frac{k_S A_S}{\Delta l_{PS}} \right) \theta_P^n \end{aligned} \tag{62}$$

where A_E = 2 (R_E+R_P)/2 π l_j is the East surface of the volume, while A_W =2 (R_W+R_P)/2 π l_j is the west surface area and l_j represents the height of the corresponding layer.

Different equations are obtained for the element on the cylinder axis and for the element situated at the boundary. In the former case the contribution of the east node is neglected, while for the latter the west contribution is replaced with a convective coupling term with the corresponding fluid tank water layer as shown in Fig. 54b) :

$$\begin{aligned}\frac{\rho V_P}{\Delta t} h_P^{n+1} &= \frac{\rho V_P}{\Delta t} h_P^n + \frac{k_E A_E}{\Delta R_{PE}} \theta_E^n \\ &+ \frac{k_N A_N}{\Delta l_{PN}} \theta_N^n + \frac{k_S A_S}{\Delta l_{PS}} \theta_S^n + \alpha \cdot A_{ext} \cdot \theta_{BC} \\ &- \left(\alpha \cdot A_W + \frac{k_E A_E}{\Delta R_{PE}} + \frac{k_N A_N}{\Delta l_{PN}} + \frac{k_S A_S}{\Delta l_{PS}} \right) \theta_P^n \end{aligned} \tag{63}$$

Where A_{ext} is the cell area considering the external radius of module, while θ_{BC} is the boundary condition temperature for each module layer computed as a mean value between the temperatures of the corresponding tank layers, as presented in Fig. 55

$$\theta_{BC,i} = \frac{A_{j,i} \cdot \theta_{tank,j} + A_{j+1,i} \cdot \theta_{tank,j+1}}{A_{j,i} + A_{j+1,i}} \tag{64}$$

When the surface temperature of the module is known, the heat flux contribution of each module layer to the corresponding tank layers can be computed as :

$$\phi_{j,i} = \alpha \cdot A_{j,i}\left(\theta_{1,i} - \theta_{tank\ ,j}\right) \tag{65}$$

Eq. (65) is then used for computing the convection heat flux pertaining to each tank layer

$$\phi_j = \sum_{i=1,nml} \phi_{j,i} \tag{66}$$

where *nml* is the number of module layers in contact with each tank layer.

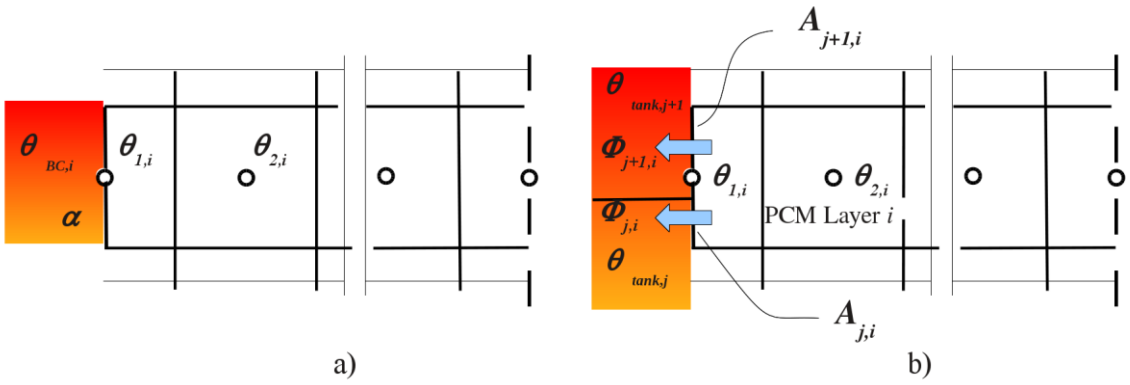

Fig. 55: a) boundary condition b) PCM module layer in contact with two tank layers

Solar Domestic Hot Water Simulation

The PCM enhanced tank component has been used for the simulation of a solar domestic hot water system as presented in Fig. 56a it features a water tank with two immersed heat exchanges, a boiler and a solar panel. A similar problem has been presented by the authors in reference [65], the present case differs from the former case by a different control system of the solar collector pump and from the boiler which in this case is an high performance condensing boiler. The solar collector pump is activated only when the temperature in the collector is higher than the one at the mid height of the tank, while the boiler pump is activated when temperature of the layer with the exit section of the tank falls below 45 °C and it is deactivated when the temperature rises over 50 °C , a tree way valve has been added to the plant and deviates water from the makeup water in order to maintain the supply water at a value of 40 °C. The boiler is component n°17, a gas fired boiler which provides water at a constant temperature of 60 °C, the solar collector is component n°84 with a total area of 4.72 m^2, while daily DHW hourly draw profile is obtained using component n°88. Makeup water is provided to the plant at a constant temperature of 15°C .

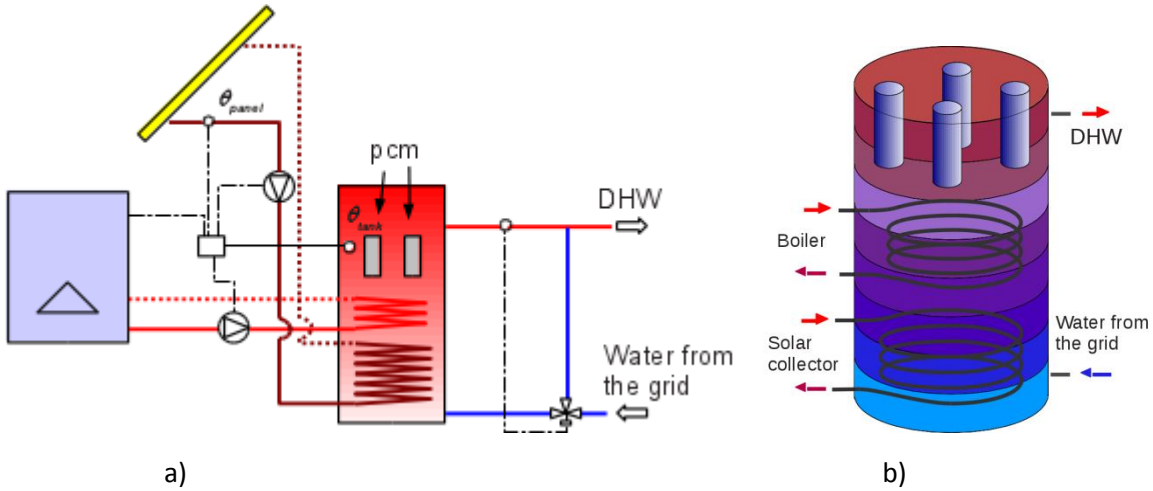

Fig. 56: SDHW system a), PCM enhanced tank b)

The domestic hot water demand, that may be referred to a family of 4 people (approximately 240 liters per day), is modeled through the flow rates shown in Fig. 57.

The fractional thermal energy savings parameter [63] has been computed, it represents a measure of the percentage of non solar energy input for heating that can be reduced by the solar system.

$$f_{sav,\,therm} = 1 - \frac{Q_{pri}}{Q_{pri,\,ref}} \qquad (67)$$

at the denominator of Eq. (11) appears the primary energy consumption without solar system, while the numerator represents the primary energy consumption in presence of the solar system.

Table 32 reports the data used for the simulation of the tank, while Table 33 reports the term $f_{sav,term}$ for two Italian climatic conditions: Rome in center and Trieste in north-east .

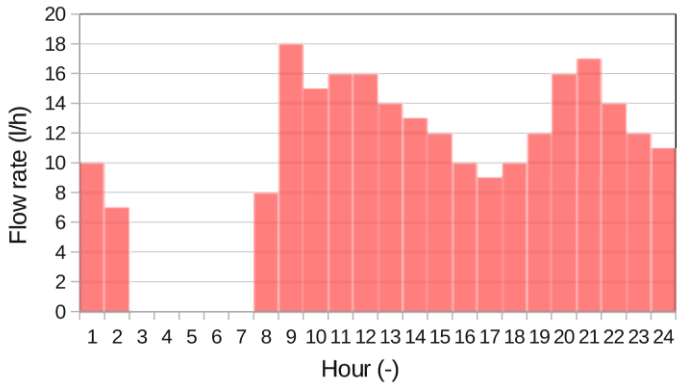

Fig. 57: Water draw profile

Table 32: parameters added to tank component for PCM discretization

parameter	unit	value
Number of PCM modules	-	8
Cylinder height	m	0.2466
Cylinder diameter	m	0.088
Cylinder bottom position	m	0.75
n. of cells in radial direction	-	10
n. of cells in axial direction	-	10
Density of PCM solid	kg/m^3	1350.0
Density of PCM liquid	kg/m^3	1350.0
Specific heat solid		2500.0
Specific heat liquid		2500.0
Latent heat	(J/kg)	0.180E6
Solid conductivity	W/(m K)	2.0
Liquid conductivity	W/(m K)	2.0
Phase change temperature	°C	55.0
Time integration 1=explicit 2 implicit		1
Phase change range (implicit only)	K	2

Table 33: fractional thermal energy savings for the simulated cases

Volume (litres)	Cases	Trieste	Rome
147	No PCM	0.308	0.502
	PCM 55	0.321	0.518
	PCM 60	0.302	0.507

Results

From Table 33 is evident that no consistent improvement is obtained since the $f_{sav,term}$ with PCM is only marginally higher than the one without PCM. Furthermore the results with a different phase change temperature are not sensibly different, the results differ from the ones obtained in [65] since a more efficient boiler has been used with a reduction of the required energy.

The cause of this poor performance is that in a SDHW system the temperatures inside the tank varied too much therefore the latent effect, visible only around the phase change temperature, is not efficiently

exploited. In addition the results refer to a case with only 12 liter of PCM which lead to a fraction of less than 9% of the occupied. The low amount is due to the poor space available in the tanks not occupied by heat exchangers, better results should be obtained increasing the amount of PCM using with tanks especially designed.

Conclusions

The developed component is useful to simulate hot water systems that require a thermal storage system. The modified component for ESP-r allows for the insertion of PCM modules and the characteristics are input by the user using the normal interface of the code.

The numerical solution of the Stefan problem implemented allows to insert the modules inside the tank at different levels modifying the distribution of stratification inside the tank.

2.3 Complete System models

2.3.1 Solar Thermal Model (CANMet, National Resources Canada)

Introduction

A conceptual study is described into the hybridization of Stirling engine based residential cogeneration systems with solar thermal systems [66]. Simulation results of 4 hybrid system configurations applied in various locations in Canada are presented and compared to base case systems without solar input. Additional optimization cases are discussed. Adding solar collectors to a residential cogeneration system has a clear potential to reduce natural gas consumption and GHG emissions. The simulated cases showed a 10 – 15% decrease in the consumption of natural gas, which corresponds to a GHG emission reduction of approximately 700 – 1200 kg per house per year (depending on configuration and location).

Scope of Model

A Stirling engine (SE) based micro-cogeneration system forms the heart of the Base case system (see Fig. 58). The SE provides heat to a 284-litre DHW storage tank through an immersed heat exchanger. A second heat exchanger in the tank allows heat to be extracted for space heating through a hot water-fed air handler. The storage tank is equipped with a back-up heater to provide additional heat in case the SE is not able to keep the DHW water at the desired temperature level.

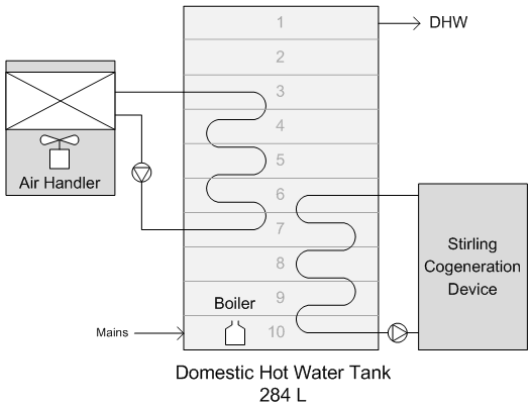

Fig. 58: Base case configuration. DHW: domestic hot water.

Model inputs

Solar heat is used in four variants of a hybrid renewable – microgeneration energy system to replace fossil energy for space heating and DHW production. In Case 1 and 2 (see Fig. 59 and Fig. 60), solar heat is only used to heat DHW; in Cases 3 (see Fig. 61) the output of the solar collectors is used for both DHW and space heating. In the latter systems, space heating is provided, similarly as in the base case system, through an air handler fed by water heated in a heat exchanger in the DHW tank.

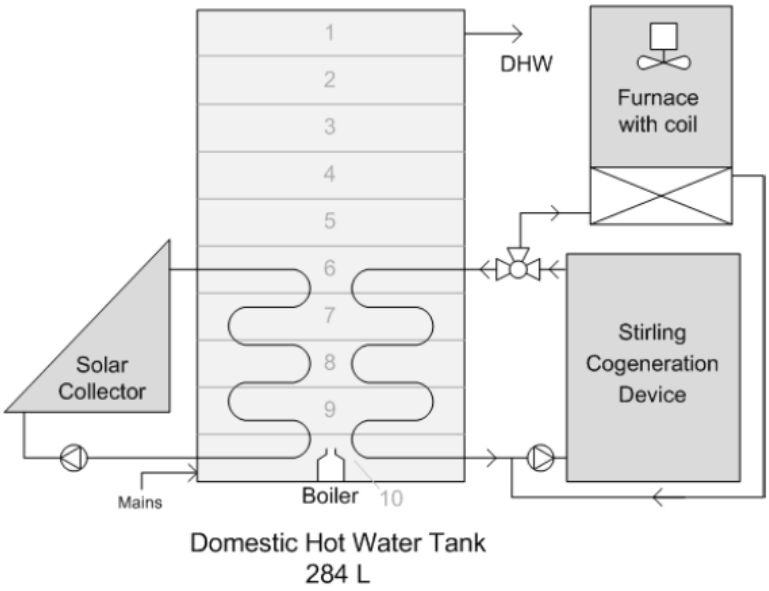

Fig. 59: Configuration for Case 1

In Cases 1 and 2, the SE provides heat either directly to the air handler coil or to the DHW tank. A back-up furnace is installed for additional heat in case the capacity of the SE is insufficient. A Stirling system design similar to Case 1, but with no solar input or back-up DHW heating, was recently installed and tested with acceptable performance at the Canadian Centre for Housing Technology (CCHT) [67]. That study showed the configuration as a cost effective integration pathway for micro-cogeneration in a Canadian home.

The DHW tank in all system variants is equipped with a back-up burner. Systems 1 features a pre-heat tank aimed at enhancing the solar yield. A low-flow pump will transport hot water from the preheat tank to the DHW tank when it is hotter than the water at the bottom of the DHW tank.

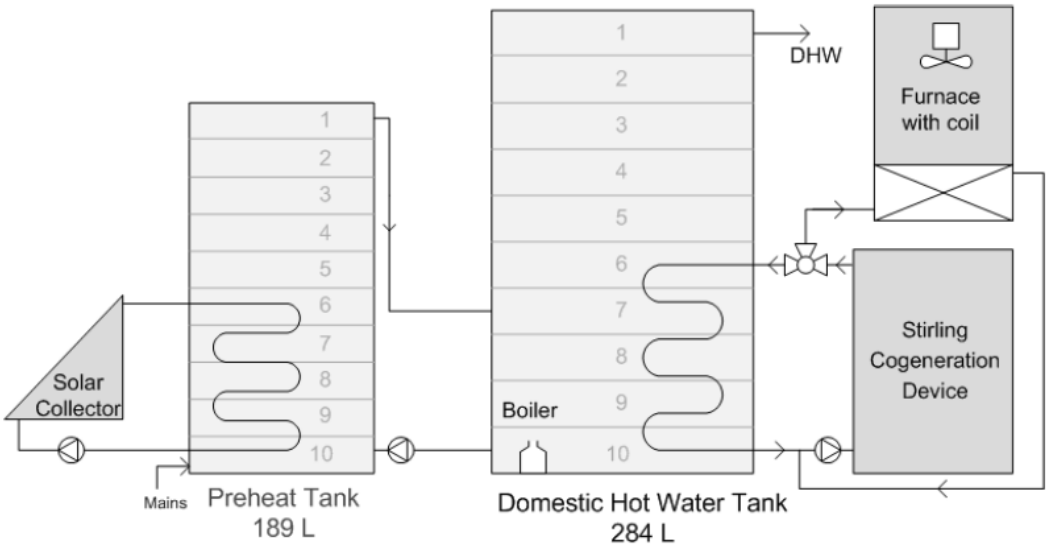

Fig. 60: Configuration for Case 2

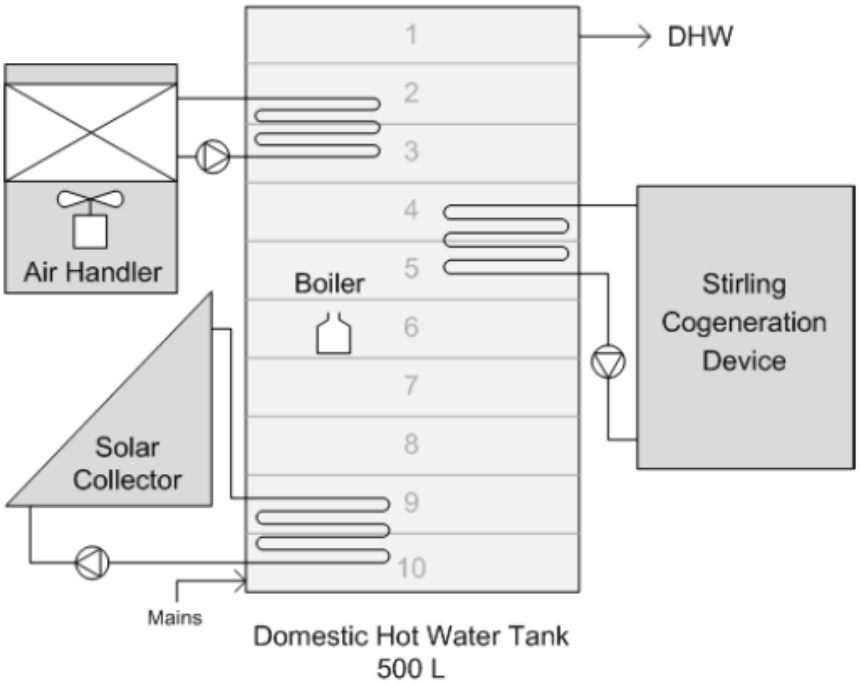

Fig. 61: Configuration for Case 3

Results

A study is presented into the hybridization of residential cogeneration systems and solar thermal technology for providing space heating and domestic hot water to a residence with an average heating load. Hybrid systems displaying various configurations and parameter settings were simulated in TRNSYS and their results compared to a Base Case without solar input. The results of a first round of parameter variation cases were used in a second round of simulation aimed at improved system design and performance. From this study, it can be concluded that:

- Adding solar collectors to a residential cogeneration system has a clear potential to reduce natural gas consumptions and GHG emissions. Simulated cases showed a reduction in annual natural gas consumption of 10 – 15%, which corresponds to a reduction of approximately 700 – 1200 kg GHG per house per year (depending on configuration and location).
- Providing low heat-exchange temperatures for both the Stirling engine and the solar thermal system is crucial for high systems efficiencies. It is also important to provide sufficient storage capacity for the collected solar heat.
- Parameter variation cases showed an increase in systems performance with solar collector area, but with a rapid decrease in marginal improvement.
- The solar panels angle has a limited impact on the overall system performance.
- The hybrid renewable – fossil energy systems are complex and highly integrated systems. Their performance has shown to be influenced by a large number of interrelated parameters, like temperature dependent efficiencies of Stirling engine and solar collectors, heat storage tanks that integrate multiple functions, control strategies that have a much larger influence on the operation of the system than on the controlled variable alone, and varying climatologic conditions that results in completely different operating conditions for various seasons of the year. In this study, only a limited optimization effort could therefore be performed, resulting in several quite different system configurations achieving a similar high natural gas reduction percentage compared to the base case. This indicates that further optimization to even larger GHG emission reductions is likely possible.
- The hybrid systems show similar operation and performance when applied in four cities across Canada with a broad range of heat demands.
- The simulated performance of the residential cogeneration system was based on measured data from a non-optimized early generation unit. The results of this study are therefore not suited to evaluate the potential of this technology.

Conclusions

It is recommended to continue the research into optimal configuration and operation of these hybrid renewable – fossil energy systems by:

- Pursuing optimal system efficiency through a configuration in which the Stirling engine is directly coupled to the air handler of the space heating system or alternatively to the heat storage of a low-

temperature heating system, and the solar heat capture is maximized by low heat storage temperatures that match the temperature requirements of the space heating system;

- Improving the overall control strategy by implementing seasonably adjusted heat storage temperatures to increase solar heat capture and reduce standby losses;
- Further optimization of the solar panel configuration (in series, in parallel, mixed) with optimized variable glycol flow rate;
- Optimizing the heat storage to provide ample storage capacity for solar heat allowing long Stirling engine operating cycles, without excessive heat losses to the environment;
- Investigating a more optimal placement of the various heat exchangers in the heat storage tank(s);
- Using a Stirling engine micro-cogeneration system with improved performance (comparable to or better than that of the auxiliary heat devices);
- Expanding the simulation model to produce DHW with a constant outlet temperature;
- Including an economic analysis of the Base Case and the various system configurations.

2.3.2 ANFIS Modelling of a Hybrid IC Engine/ HE Furnace Micro-Cogeneration System (CANMet National Resources Canada)

Introduction

This study applies adaptive neuro-fuzzy inference system (ANFIS) technique to predict performance parameters of a hybrid micro-cogeneration system [68]. The hybrid system consists of an internal combustion (IC) engine (1kW$_e$ and 3.25 kW$_{th}$) integrated with a high efficiency condensing furnace (16.5 kW$_{th}$). The system was installed in the Experimental House at the Canadian Centre for Housing Technology (CCHT) and system performance data were collected during winter/spring heating season. ANFIS models were developed and trained with CCHT data sets. The study revealed that the trained ANFIS models were able to predict selective hybrid system performance parameters with high degree of accuracy over variety of system operational conditions. It demonstrated that utilizing ANFIS modeling technique micro-cogeneration system's performance could be modelled with high degree of confidence and minimum time demand.

Scope of Model

The hybrid IC/HE furnace system operates on natural gas and consists of an IC engine (1kWe and 3.25 kWth) integrated with a high efficiency condensing furnace (16.5 kWth. The system schematic is shown in Fig. 62. The hybrid system is designed to act as a two stage furnace where the first stage utilizes the heat generated by the engine via an additional heat exchanger (HEX) installed in the furnace compartment. The second stage is the furnace itself supplying additional heat for fast recovery as per the household thermostat request. The hybrid system controller makes intelligent decisions for system operational modes based on information collected from a number of external/internal sensors. The hybrid system was installed at the CCHT Experimental house and connected in parallel to the grid. It was intensively monitored

for four consecutive weeks and performance data were collected. After a preliminary analysis a set of parameters was selected for the ANFIS modeling purposes.

Model inputs

ANFIS models were developed to predict the system power generation and furnace supply air temperature.

ANFIS model for predicting engine electrical power generation

Pre-modelling analysis defined the following input parameters that relate to the engine power generation (Pe):

- M_1: Engine natural gas consumption (L/min)
- T_{11}: Engine combustion air temperature, (°C)
- T_1: Engine coolant temperature, (°C)
- M_3: Engine coolant flow rate (L/min)

The function "genfis1" was used to generate a fuzzy inference system (FIS) structure from experimental data without data clustering. The parameters associated with initial membership functions (MF) are then tuned through the learning "anfis" process by applying a combination of the least squares method and the back propagation gradient decent method. Two membership functions were defined for each input and output. Various input variables and types of MF: generalized bell, triangular, trapezoidal, Gaussian, Pi-shaped curve and product of two sigmoid, were tested in the modeling study and different number of epochs were used to verify the model performance.

Three data sets - training, checking and testing data - were randomly selected from more than 33,000 data points obtained from the experiments. There are 10,080 data points in each data set with no repetition of same data point. It should be noted that these data sets are representative for most operational conditions: engine running alone, engine and furnace running together and both units in a standby mode.

The model was trained with the training data set. The checking data set was used for testing the generalization capability of the fuzzy inference system at each epoch to control the potential for model over fitting the training data. The model was finally validated by the testing data set which has not been used during the training. The FIS structure whose parameters are set according to a minimum checking error criterion was applied to calculate the model output with checking and testing input data.

Model for predicting furnace ANFIS supply air temperature

Two models were developed for predicting the furnace house supply air temperature. The first one considers the furnace and the heat exchanger together as a single black box and the second one is to consider the furnace alone.

The input parameters that have been considered to have an impact on the first model (furnace and heat exchanger) are:

- T_2: Coolant temperature from engine, (°C)
- M_3: Engine coolant flow rate (L/min)
- M_2: Furnace natural gas consumption (L)
- P_f: Furnace electrical power (W)

- T_{10}: Furnace combustion air temperature, (°C)
- T_4: House return air temperature (°C)
- M_4: Furnace air flow (L/s)
- T_7 Room temperature (°C)

As the hybrid system was located inside the house in basement, it is expected that the room temperature has an impact on the supply air temperature mainly when both the engine and the furnace were in standby mode. It should be noted that the furnace fan was running continuously, at either low or high speed, throughout the day. The impact of the room temperature on the model's performance was tested in the study.

Input parameters that have an impact on the second model (furnace alone) are:

- M_2: Furnace natural gas consumption (L)
- P_f: Furnace electrical power (W)
- T_{10}: Furnace combustion air temperature, (°C)
- T_6: Preheated air temperature (°C)
- M_4: Furnace air flow (L/s)
- T_7 Room temperature (°C)

In the second model, preheated air temperature was considered as an input of the model as this temperature is not difficult to measure in practice.

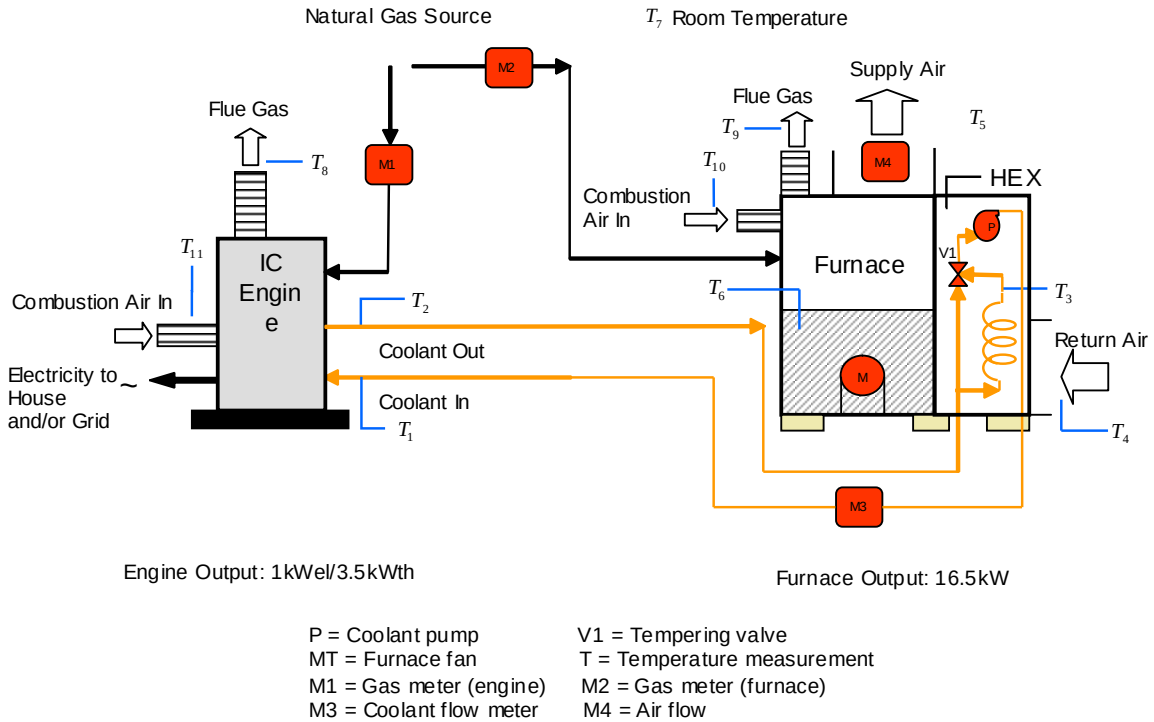

Fig. 62: Hybrid microgeneration system schematic.

As there are many input parameters, subtractive clustering method was used in these two models to identify natural groupings of data from the large data set to produce a concise representation of the

system's behaviour. This reduces the problem of combinatorial explosion of rules when the input data has a high dimension. The cluster information can be used to generate a Sugeno-type fuzzy inference system that models the data behaviour best by using a minimum number of rules. The FIS generation was accomplished by using the function "genfis2". The parameters associated with initial membership functions are then tuned (adjusted) through the learning "anfis" process by applying a combination of the least squares method and the back propagation gradient decent method (hybrid method).

Results

Simulation results of engine electrical power generation

Various input parameters and types of membership functions, generalized bell, triangular, trapezoidal, Gaussian, Pi-shaped curve and product of two sigmoid, were tested in the modeling study. The model performance was evaluated by the mean root square error, RMSE and the evaluation results are summarized in Table 34.

The results in Table 34 show that most models predict well engine electrical power output. However, the model with 3 inputs and with generalized bell MF for each input and output resulted in minimum training and validation errors. The RSME of this model is less than 2.5 W for all data (training, checking and testing) sets.

Different number of epochs, 50, 100, 200, 300, 400 and 500, were tried to test the model performance. The results shown in Table 35 indicate that there was no further improvement on the model performance by increasing the number of training epochs beyond 300.

Table 34: RMSE values of engine power generation model with various input parameters and membership functions.

Inputs	Number of inputs	Data Sets	Membership Function					
			gbellmf	gaussmf	trimf	trapmf	pimf	psigmf
M_1, T_{11}, T_1, M_3	4	Training	2.47	2.48	2.54	2.52	2.54	2.52
		Checking	2.92	2.51	2.74	3.22	4.47	3.36
		Testing	6.69	2.65	3.36	4.60	81.78	41.93
M_1, T_{11}, T_1	3	Training	***2.44***	2.48	2.54	2.53	2.54	2.52
		Checking	***2.44***	2.54	2.58	2.63	2.96	2.50
		Testing	***2.40***	2.53	2.65	2.55	2.86	2.47
M_1, T_{11}	2	Training	2.54	2.53	2.61	2.55	2.56	2.55
		Checking	2.52	2.51	2.63	2.54	2.56	2.53
		Testing	2.54	2.53	2.73	2.57	2.58	2.55

Notes: M_1: engine natural gas consumption, T_{11}: engine combustion air temperature; T_1: coolant temperature into engine; M_3: engine coolant flow rate. 300 epochs were used in the simulations.

Table 35: RMSE values of engine power generation model with various training epochs.

Inputs	Number of inputs	Data Sets	Number of epochs					
			50	100	200	300	400	500
M_1, T_{11}, T_1	3	Training	2.55	2.47	2.44	2.44	2.43	***2.43***
		Checking	2.55	2.45	2.45	***2.44***	2.44	2.44
		Testing	2.53	2.41	2.41	***2.40***	2.40	2.40
Notes: M1: engine natural gas consumption; T11: engine combustion air temperature; T1: coolant temperature into engine; M3: engine coolant flow rate. Membership function: gbellmf.								

Simulation results of furnace supply air temperature

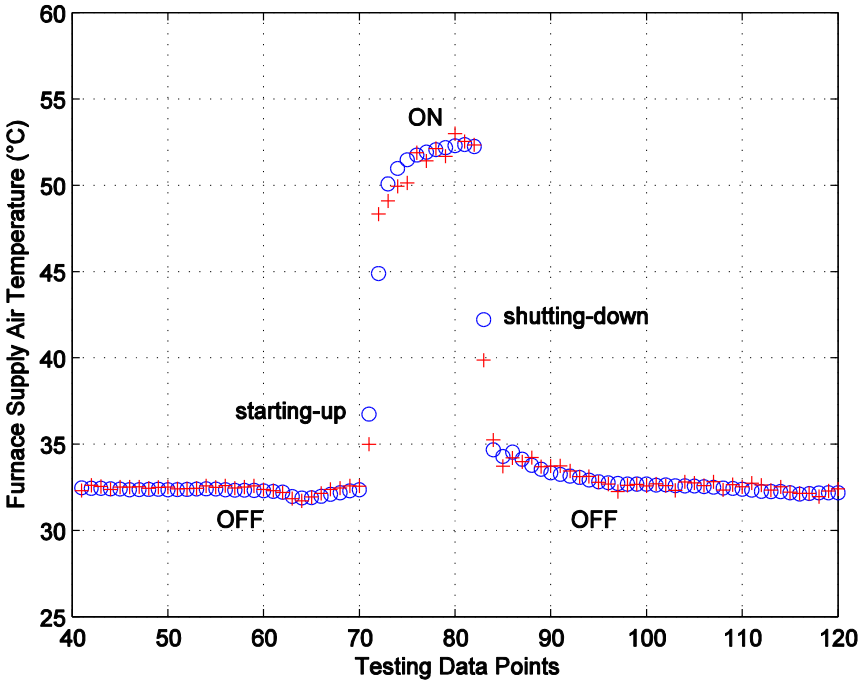

Fig. 63: Comparison of measured and predicted furnace supply air temperature during furnace starting-up and shutting down periods.

Two models have been developed for predicting the furnace supply air temperature. One is to consider the furnace and the heat exchanger together as a black box (Model A) and the other is to consider the furnace alone (Model B. The results show that all models can give prediction of furnace supply air temperature with acceptable accuracy. The RMSE is smaller than 0.6°C. However Model B, which modeled the furnace alone, had a better performance than the model which considered the furnace and heat exchanger together as a black box (Model A). Various "radii" values required by the "genfis2" function were tested in the modeling study. The "radii" values were set to 0.15, 0.2, 0.3, 0.4 and 0.5 for all data dimensions in each model respectively. It was found that the model gave good prediction by specifying a small radius (radii=0.15 or

0.2). Since the results obtained from Model A1 with 8 input parameters and A2 with 6 input parameters are already satisfactory with one “radii” value for all data dimensions, the models were not further tuned with different “radii” values for different input/output parameters.

The results show that vast majority of predicted temperatures are within ±3°C compared to the measured ones. The temperature differences greater than 3°C mainly occurred occasionally during the furnace starting-up or shutting down periods when temperature change gradient was great (see Fig. 63). However, it should be noted that, in most instances, the model can give good prediction of the supply air temperature (difference less than 3°C) in these periods.

Conclusions

Adaptive Neuro-Fuzzy Inference System (ANFIS) technique was applied to predict performance parameters of a hybrid IC engine/ high efficiency furnace micro-cogeneration system in a residential application.

ANFIS models were developed and trained with real life data. The results indicate that the developed models were able to predict system performance with a very good accuracy over a range of operational conditions. The RMSE value obtained from the model with best performance was within 2.5 W for the engine electrical power and within 0.6 °C for the furnace supply air temperature.

2.3.3 Hybrid IC-Furnace system tests at CCHT (National Resources Canada)

Introduction

Results from a field trial are presented with a hybrid micro-cogeneration system applied to satisfy both thermal and power needs of a typical Canadian detached house [69]. The hybrid system consists of an internal combustion engine integrated with a high efficiency furnace. It was installed, integrated with the rest of the mechanical systems and demonstrated at the Canadian Centre for Housing Technology (CCHT). Cost analysis was performed to examine the economics of such systems in relation to different price structures imposed by the electric utilities. The study revealed that the hybrid micro-cogeneration system performed reliably and generated both heat and power with high efficiency during the heating season and was able to satisfy the heating demand under very cold weather conditions. The power generated by the system was first directed to the house satisfying 50% of the electric load with the other 50% being exported to the grid. The project demonstrated that micro-cogeneration systems when sized to meet the base electric load and design thermal load of the residence are a valuable alternative to the central power generation plants and are able to reliably satisfy the house thermal/power demand even under extreme cold conditions.

Scope of Model

The hybrid micro-cogeneration system operates on natural gas and consists of an internal combustion engine and a high efficiency condensing furnace. The internal combustion engine is the smallest known natural gas IC engine (1kWel, 3.25kWth) developed for stationary residential applications. Due to the house higher space heating load the engine has been integrated with the high efficiency condensing furnace with

total system output of 1kWel and 3.25/18kWth. The hybrid system is designed to act as a two stage furnace where the first stage utilizes the rejected heat by the engine and supply it as a low velocity warm air to the house and second stage when the furnace supplements additional heat for fast recovery managed by the thermostat temperature differential. The system control makes intelligent decisions for the system operational modes based on information collected from a number of external/internal sensors. In order to provide long uninterrupted operation of the engine, the integration between the IC engine and HE furnace is done through an interface module mounted on the return air side of the furnace.

Results

The results show that both electrical and thermal efficiencies varied slightly during the test period. The electrical efficiency was between 18.2% and 18.7%, and the thermal efficiency was between 55.1% and 57.3%. The overall efficiency varied between 73.4% and 76.0% with an average value of 74.6%.

The engine daily running time during the testing period ranged from 739 minutes (12.31 hours) to 1437 minutes (23.95 hours). The analysis showed that the engine operation was strongly dependent on outside conditions (both the outdoor temperature and solar radiation). For six days, that were the coldest and with little solar gains, the engine ran close to 24 hr/day continuously with only one break of 3 to 6 minutes.

During the test period, the engine generated 12.5kWh to 24.2 kWh of electricity daily with average generation of 19.4 kWh per day. The breakdown of generated power in percentage is shown in Fig. 64.

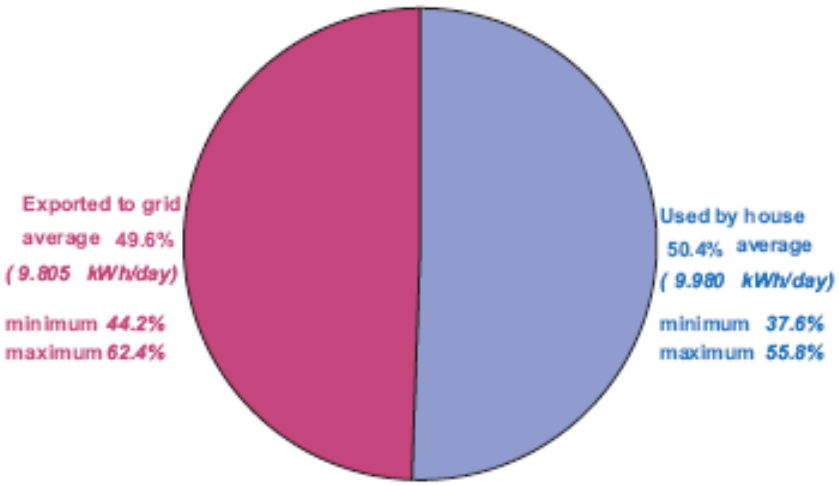

Fig. 64: Breakdown of average daily engine generated electricity.

On average, 50.4% of the generated by the engine electricity was used in the house and 49.6% was exported to the grid. The house utilized 37.6% to 55.8% of the generated electricity during the test period as the house power consumption was strongly dependent on the outside conditions. In general, on cold days, the house consumed a significant percentage of generated electricity and exported less to the grid. It was vise versa for the warmer days.

The house daily electricity consumption varied between 14.3 and 16.9 $kWh_{e.}$ As shown in Fig. 65, on average, 65.5% of the house electricity consumption was supplied by the engine and another 34.5% was

supplemented by the grid. The engine supplied more than 75% of the house electricity needs on those days when engine was running continuously for almost 24 hours. On warm and sunny days when the engine was running less time, it was able to meet at least 39% of the house daily electricity load.

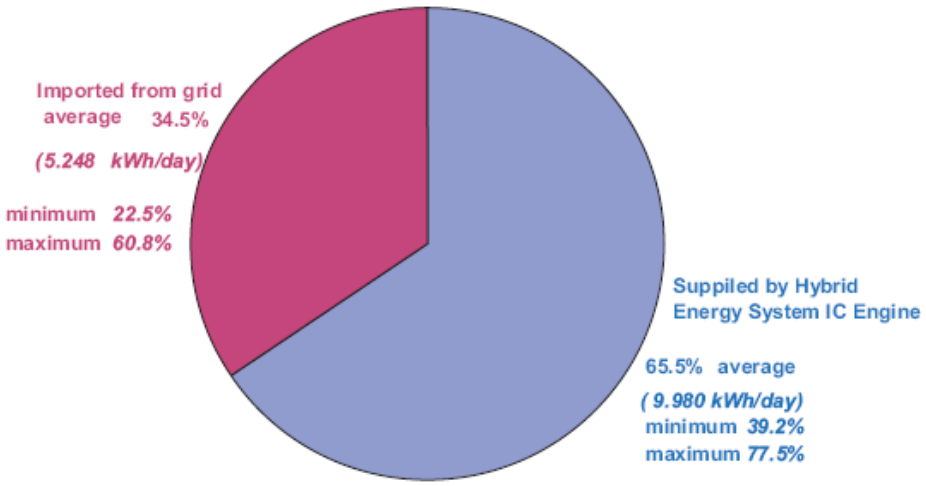

Fig. 65: Breakdown of average daily house electricity supply.

The overall efficiency of the hybrid energy system is defined as the total energy outputs (electrical and thermal energy) divided by the total energy inputs (fuel and auxiliary energy). The average system overall efficiency in the test period was 73.0% as it varies between 69% to 78%.

Conclusions

The results obtained from testing of the hybrid micro-cogeneration system at the Canadian research test facility showed the applicability of such systems to supply heat and power to a residence. The hybrid system operated extremely reliably supplying heat and power to the house without any interruptions or faults during the testing period. The performance comparison between the hybrid system and the high efficiency furnace revealed that for most of the testing period the Experimental House heating demands, even at -26^{o}C outdoor temperature, was satisfied predominantly by the first stage of the hybrid system (IC engine). The second stage of the system (engine and furnace) was in operation occasionally which led to a significant reduction in furnace cycles and on-time operation in comparison to the furnace system in the Reference house.

2.3.4 Hybrid Microgeneration System with Electric Vehicles (CANMet, National Resources Canada)

Introduction

The economic viability of micro-cogeneration (micro-CHP) systems strongly depends on the value of the co-produced electricity. In case electricity produced by the micro-CHP is used inside the house ('behind the meter'), the electricity has the same value as the price otherwise paid to the utility. If the electricity cannot be used inside the house and needs to be exported to the grid, it generally has a much lower value. For

jurisdictions that do not have an active support for micro-CHP, this value could range from zero to at most the whole-sale market price.

The primary function of most micro-CHP systems applied in residences is to provide heat for space heating and in some cases also for domestic hot water. The micro-CHP system generally operates under a heat-load following control strategy, which causes the system to run more in winter and during the night. A large fraction of the electricity is thus produced at times when the electric load of the house is low, requiring substantial amounts of electricity to be exported with low or zero revenues.

Electric vehicles (EVs) consume considerable amounts of electricity. EVs are mostly driven at day and charged at home during the night. The recharging of EVs could thus be a way to drastically increase the own use of electricity produced by the micro-CHP and to boost the profitability of the system. A study was performed into the synergy between electric vehicles and micro-CHP systems by combining the results of the whole building simulation program TRNSYS and NRCan's Plug-in Electric Vehicle – Charge Impact Model (PEV-CIM). Detailed measured profiles of residential electricity consumption were used to determine the economics of a micro-CHP system applied in a single detached house in Ottawa, Ontario, Canada. Subsequently, the potential improvement of the profitability of the micro-CHP system was evaluated for scenarios with recharging of electric vehicles with different driving and charging characteristics.

Scope of Model

A simulation study was performed to investigate the potential synergy between electric vehicles and micro-CHP systems [70]. In this study, results of the whole building simulation program TRNSYS [71] regarding the operation of a micro-generation system applied in a single detached house in Ottawa, Ontario, Canada were combined with results for electric vehicle charging from the Plug-in Electric Vehicle – Charge Impact Model (PEV-CIM) [72] developed by Natural Resources Canada. Detailed measured profiles of residential electricity consumption [73] were used to determine the baseline economics of the micro-CHP system. Subsequently, the potential improvement of the profitability of the micro-CHP system was evaluated for scenarios in which it was also providing (part of the) power required to recharge electric vehicles with different driving and charging characteristics.

An ICE with an electrical capacity of 2 kWe and a thermal output of 5.4 kWth was selected for the micro-CHP system, because the thermal output of the ICE would be a good match for the total heat demand for SH and DHW. The storage tank in the system would allow the ICE to run for extended periods, thus maximizing performance by reducing cycle losses. In IEA/ECBCS Annex 42, a model for a combustion-based micro-cogeneration device was developed and implemented in several whole building simulation programs [74]. The model was recently calibrated against data of a 6 kWe ICE system [75]. However, no calibration for a 2 kWe device could be found in the literature. As the micro-CHP system was configured to run in long operating cycles, the dynamic behaviour of the system would be less important than its steady state performance. It was therefore deemed acceptable to create a 2 kWe model by adjusting the parameter set of the 6 kWe device to give steady state results conform the values presented in Table 36, while keeping the dynamic behaviour similar to that of the 6 kWe unit. PEV-CIM was used to create a set of EV charging profiles representing scenarios in which electric vehicles would drive certain daily distances (20 km, 40 km, 60 km, 80 km, 100 km), would be charged at different power levels (Level 1 or Level 2, see Table 37) and would have their charging session start at different times of the day (5 pm, 8 pm, 10 pm, 12 am).

Table 36: Characteristics of the micro-CHP device and the back-up burner.

	Fuel	Capacity (kW) or efficiency (%HHV)
Micro-CHP (ICE)	Natural gas	
Electric power		2.0 kW
Electrical efficiency		23%
Thermal power		5.4 kW
Thermal efficiency		62%
Back-up burner	Natural gas	
Thermal power		29 kW
Thermal efficiency		85%

Table 37: Characteristics of electric vehicle charge levels. 'Efficiency' (last column) is defined as the DC power usage of the EV divided by the AC power consumption of the charging station.

	Voltage	Power	Efficiency
Level 1 charging	110 V	1.2 kW	79%
Level 2 charging	240 V	3.3 kW	86%

In the EV simulations, it was assumed that all vehicles must be fully recharged by 7 am. This requirement could result in the exclusion of certain combinations of daily driving distance, charge power level, and start time of recharging, as the total recharge duration would be too long to have the vehicle ready by 7 am.

Results

An annual simulation was performed to determine the usage of the micro-CHP system for meeting the demand for space heating and DHW of a detached house in Ottawa. Over the full year, the ICE unit operated for 4,174 hours. It provided 78% of the total heat load for space heating and DHW, the remainder was supplied by the back-up burner. The ICE operated in long cycles with an average duration of 5 hours and 16 minutes. The cycle length varied over the year with an average length in winter of more than 12 hours. During the summer months, supplying heat for DHW only still resulted in an average cycle length of 81 minutes.

The 2 kWe ICE unit of the micro-CHP system produced over 8,000 kWh of electricity. Some of the electricity was used for the internal power consumption of the HVAC system (circulation fan, air handler pump). Over 7,000 kWh were available to cover the 6,510 kWh of annual non-HVAC power consumption. Although more power was available than the total annual consumption for non-HVAC purposes, only 2,088 kWh (32%) of this load could be supplied by the micro-CHP system. Over 60% of the micro-CHP power production (5,005 kWh) could not be used in the house and needed to be exported.

The charge durations were then used to calculate when the daily charging sessions would end assuming various start times For operational reasons, the electric vehicles must be fully charged at 7 am. The

combinations of charge level, daily driving distance and start time of charging that did not result in a full battery by 7 am have been identified. it can be seen that for daily driving distances over 60 kilometres, only Level 2 charging will suffice. A total of 8 scenarios for Level 1 charging and 19 scenarios for Level 2 charging were used for the evaluation of the benefits of combining micro-CHP with electric vehicles.

When trying to utilize the excess power production from the micro-CHP system for EV charging, similar mismatches in timing and power level occur as with covering the non-HVAC electricity consumption. the profiles of electrical production and consumption from 12 am to 3 am on January 1 for the scenario of an electric vehicle driving 40 kilometres per day and being recharged using Level 1 charging starting at 5 pm..

it can be seen that the EV charging session lasts only part o being utilized during the rest of the day. Besides, there is sometimes more excess power available than the EV charger can use (see for instance the period from 1 am to the end of the charging session and around 6 pm). For the same scenario of a 40 km daily driving distance and Level 1 charging starting at 5 pm, profiles of daily averages of electricity production and consumption over the year.

Conclusions

The impact of electric vehicle charging on the economics of a 2 kWe ICE-based micro-CHP system applied in a detached house in Ottawa, Ontario, Canada, was investigated in a simulation study involving detailed analysis of micro-CHP operation, of measured non-HVAC electricity usage patterns, and of electric vehicle charging characteristics.

Providing the majority of heat for space heating and DHW, the micro-CHP system co-produced 8,146 kWh of electricity during the 1-year simulation period. Part of the power generated by the micro-CHP (1,053 kWh) was used for covering HVAC loads (circulation fan, air handler pump), while 2,088 kWh was utilized to meet non-HVAC electricity consumption. Only 32% of the annual non-HVAC electricity consumption was met by power from the micro-CHP system due to the intermittent operation of the micro-CHP and a mismatch between micro-CHP power production (mainly at night) and non-HVAC electricity consumption (mainly during the day). Over 60% of the micro-CHP power production (5,005 kWh) could not be used inside the house and would need to be exported.

Most electric vehicles are driven at day and recharged during the night. EV charging could therefore be a suitable load for excess micro-CHP power in regions without a micro-CHP feed-in tariff. 27 scenarios reflecting various daily driving distances, start times of charging sessions, and level of charge power were evaluated to determine their impact on micro-CHP economics. EV charging significantly reduced electricity exports by up to 54% and created substantial additional micro-CHP revenues of $200 - $300 per year when Level 1 charging was employed. The benefits of Level 2 charging were at best half of those for Level 1 charging.

Most excess power was available after large DHW draws. Excess power during the night (12 am – 6 am) was about twice the power available in the early evening hours (5 pm – 10 pm). Maximum benefits were therefore found for scenarios with EV charging starting at 10 pm, because these scenarios were able to benefit from both the peak in micro-CHP operation to reheat the DHW storage tank after a large draw and the higher level of excess power available at night.

Using EV charging to improve micro-CHP economics is a very realist opportunity, as maximum benefits are found for daily driving distances similar to the average daily distance of vehicles in Canada.

2.3.5 Photovoltaic (PV) System Design Approach (Eindhoven University of Technology - Netherlands)

PV system is one of the most commonly deployed renewable energy generation technologies. However, under conventional design practice, PV systems might not have harnessed the full potential of the available solar energy nor have optimized for the limited available space in which the PV arrays are installed. In fact, conventional design approach is based on rule of thumb design principle that has not considered the hour-by-hour variation of solar irradiation.

Industrial buildings are the case in point. Industrial buildings with large and flat rooftop are mainly situated in sparsely populated areas with open fields in which the performance of PV systems is not hampered by shading of surrounding buildings. Therefore, grid-connected PV systems could be the technology of choice.

Conventional design approach

According to the conventional design approach, the sizing of PV systems is usually based on rated characteristics of the equipment. For example, watt peak (W_P), the nominal value used for sizing of PV systems, is the nameplate power that a PV module can generate under the Standard Test Conditions (STC) of 1,000 W/m^2 irradiance and 25°C cell temperature [76]. In reality, the irradiation peaks at different values according to installation locations and varies hour-by-hour throughout the year. In most cases, sizing of PV systems is based on either the annual average or the worst month average irradiance values at the installation location. Therefore, the actual performance of PV systems might not match nor even come close to their designed performance.

In order to capture the maximum amount of energy, the PV arrays could be tilted to a certain fixed angle that is related to the earth latitude at the installation location. As a rule of thumb, PV systems that have to satisfy a rather constant load could have the arrays tilted to the angle of latitude in order to maximize the annual performance. If PV systems have to satisfy a winter-dominant load, a tilt angle of latitude plus 15° is suggested; on the other hand, if PV systems have to satisfy a summer-dominant load, a tilt angle of latitude minus 15° is recommended [77].

For PV systems with multiple rows, the PV array of the row in front will cast a shadow on the array of the row behind, and thus reduce the overall generation yield, the issue is more apparent for higher latitude countries. The conventional practice tries to avoid shading between 9AM and 3PM by imposing a minimum required spacing between rows of PV arrays [77]. The spacing is commonly expressed in terms of a separation factor, which is the ratio of the spacing and height (H, see Fig. 66).

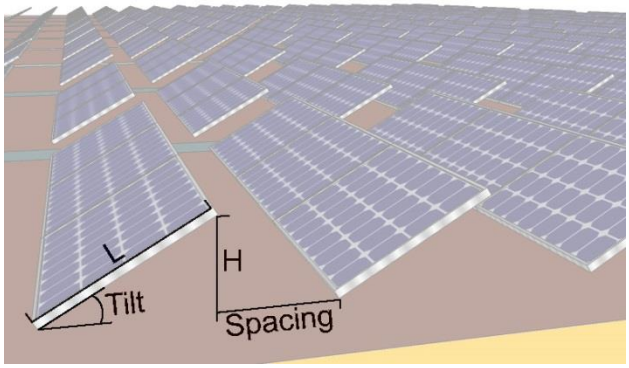

Fig. 66: Configuration of PV system

For Amsterdam, at latitude of 52.4°N, a separation factor of 10 is necessary to avoid shading between 9AM and 3 PM. That is, for a limited space, only few rows of PV arrays can be installed according to the conventional design practice.

PV systems design considerations

PV systems are commonly deployed on a horizontal surface such as that depicted in Fig. 66, with multiple rows of PV arrays tilted at an angle and separated by spacing. Rooftop is a common choice, particularly for factories, warehouses, big-box retailers with a large (and yet finite amount of) space on the rooftop that is not utilized for other purposes. Such type of buildings are usually of similar height that are spaced apart in a suburban setting in which the performance of PV systems is not hampered by shading of the surrounding buildings. The main design limitation during the design phase will be the aforementioned shading effect of the tilted PV arrays.

Effect of shading and bypass diodes

As mentioned, based on the conventional design approach, the design generation capacity of the PV system will be limited by the number of rows that can be installed due to the rather high separation factor in higher latitude countries where the PV arrays are recommended to be tilted at the angle of latitude. And if the PV system is installed with a tighter than recommended spacing, the performance will be hampered drastically due to shading.

To complicate the issue further, the reduction in energy generation due to shading is not in direct proportion to the area being shaded. In large PV systems, like those deployed on rooftop of industrial buildings, PV modules are connected in series or parallel to achieve the desire voltage and current output. If an individual module is partially shaded, or some of the connected modules are shaded while others are not, then a mismatch will occur between those shaded and non-shaded portions, and hot spots will be developed due to current flowing from the non-shaded cells / modules to the shaded ones. The exact effect depends on the configuration of the PV modules and how they are connected.

To prevent the damaging effect of hot spots due to unavoidable shading in many situations, bypass diodes are installed to divert the flow away from shaded portions. PV modules are commonly available in rectangular shape, with groups of PV cells being connected in series and served by bypass diodes. Each bypass diode usually serves around 30 to 40 cells depending on manufacturers. Those groups of PV cells are typically arranged along the short side of the module. Since the shading due to adjacent rows of PV is first

casted from the bottom then to the top, PV modules are commonly deployed with their long side attached to the ground so that sequence of bypass diodes could respond to the shaded area from the bottom up.

Design objectives

By altering the tilt angle, the length (L) of the PV array, and the spacing between rows of PV arrays (as defined in Fig. 66), annual energy generation capability can be evaluated through computational simulation with local weather information. In fact, for a less inclined tilt angle and a tighter spacing, higher generation capability per unit area of rooftop or per design capacity could be obtained.

From an investment point of view, tilt angle or separation factor are not parameters of interest since they do not indicate the worthiness of the investment of PV systems. In reality, energy generation capability (in kWh, the potential annual energy generation of the PV system) determines how much return the PV system can yield, while energy generation capacity (in kW_P, the design capacity at peak) of the PV system defines the amount of capital investment. Therefore, there could be two design objectives for PV systems:

1) to maximize the generation yield; that is, to maximize the energy generation capability (kWh) per energy generation capacity (kW_P). This objective helps promote higher return for the same amount of capital investment.

2) to maximize the generation density; that is, to maximize the energy generation capability per unit space available for installation. The rooftop (or any installation space) is a limiting factor on how much PV could be installed. Depending on the financial resources and the economic benefits, this objective helps fit the maximum amount of PV within the limited available space. In the context of buildings, the energy being generated is most likely prioritized for local consumption. Sustainable building design goals, such as net zero energy building, can be achieved by matching the energy generation density (kWh/m^2 of the available space for PV installation) with the energy consumption (kWh/m^2 of floor area. If a PV system is installed on the rooftop of a single floor structure, as in many warehouses, the area ratio between the rooftop and floor area is 1:1)

The objectives could be achieved with a computational simulation design approach that is described in subsequent sections.

Computational simulation design approach

Computational simulation can be deployed to evaluate the energy generation capability of any combination of the tilt angle, the length (L) of the PV array, and the spacing between rows of PV arrays (as shown in Fig. 66). In order to achieve the above two objectives, a multi-objective optimization can be performed.

In practice, for PV systems with multiple rows, the fact that having no shading for the first row has minimal impact on the overall performance of the PV system as the number of rows increases since the advantage is marginal. Therefore, instead of performing an optimization on a case-by-case basis, it is also possible to evaluate all configurations through a comprehensive design space evaluation (defined by the ranges of tilt angles, lengths, and spacing), such that optimized configurations can be identified and appropriate configurations can be selected according to each project requirement.

A case study (for Amsterdam, the Netherlands)

Amsterdam, is located at a latitude of 52.4°, therefore, a design range from 0° (that is, lay flat on the horizontal surface) to 56° is being investigated. PV modules are commonly available in limited choices of sizes, lengths (the short side of modules) of nominal value of 0.4m, 0.6m, 0.8m, and 1.0m, based on commercially available modules, are being investigated. The investigation is being applied on a hypothetical rooftop in the dimension of 100m (south facing) x 40m. For servicing purpose, a minimum spacing of 0.5m between rows is imposed. Therefore, for a PV length of 0.4m, a maximum of 40 rows could be installed on a rooftop of a depth of 40m. The parameters of investigation are summarized in Table 38.

Table 38: Parameters of investigation

Parameters	Range	Notes
Tilt angle	0° to 56°	in increment of 2°
Length of PV model	0.4m, 0.6m, 0.8m, 1.0m	nominal length for commercially available PV modules
Number of rows (spacing)	max. 40 rows (max. 39.6m)	for a hypothetical rooftop of 40m depth, and to accommodate a minimum spacing of 0.5m (for an installation of one row of PV array of 0.4m length)

In fact, the spacing is a derived quantity in this case study (based on the number of rows). However, the results gathered from this case study can be generally applied and scalable for other applications as a database driven query, which will be demonstrated in the next section.

The simulation is carried out in TRNSYS simulation environment. Type 194 Photovoltaic Array is applied together with Type 30a Collector Array Shading. The default setting assumes a PV cell efficiency of 15.7%, which is quite typical among commonly available flat-plate monocrystalline PV array. The energy generation results can be scaled to different efficiencies.

Three bypass diodes per PV module are assumed. In other words, each bypass diode is serving a third of the PV surface area from bottom up. Depending on the configuration of the PV array, and thus the heat accumulation of the hot spots, bypass diodes might respond differently. Correspondence with practitioners indicates that the bypass diode will have full effect (thus completely disable the connected PV cells) if the corresponding area is more than 55% shaded. Such bypass diode – shading effect is taken into account in the simulation model.

There are many thousands possible configurations of tilt angles, lengths of PV, and number of rows. The results of the comprehensive design space evaluation are presented in Fig. 67. The orange dots indicate all studied configurations, while the red dots indicate the pareto solutions. Pareto solutions are those where there are no alternative that could perform better according to the defined objectives.

The objectives in this study are defined in previous section. For example, at a generation density of 40kWh/m^2, the most efficient configuration of PV system generates 757kWh/kW$_P$, whereas the least

efficient configuration generates only 669kWh/kW$_P$. The simulation results help differentiate one configuration from another by identifying the highest return configuration for the same capital investment.

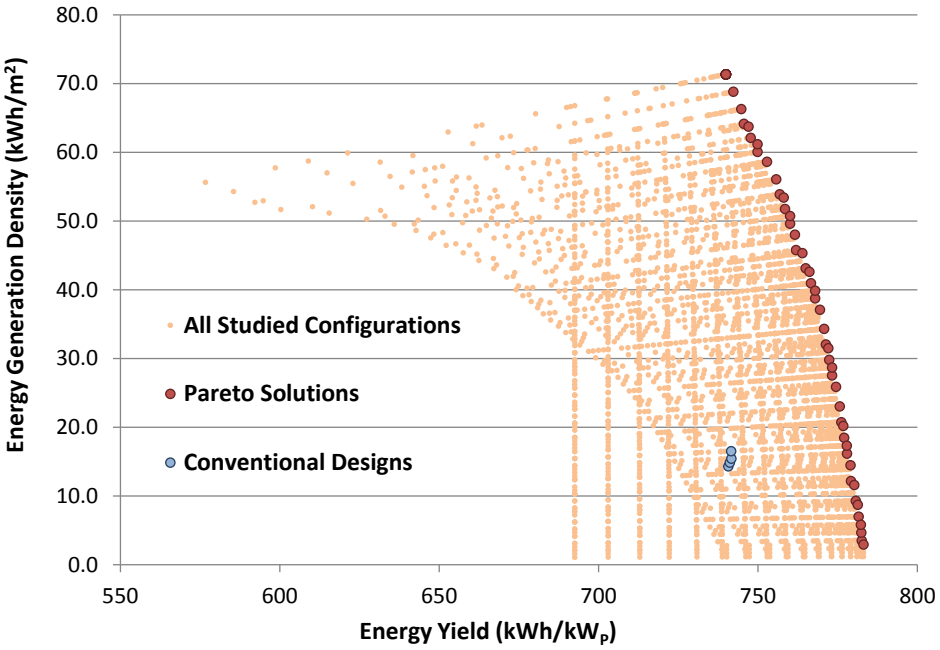

Fig. 67: Energy generation density and yield of all studied configurations of PV systems

Database query

The simulation results will be published in form of an online database query. TU/e has been working on other projects that study energy demand of industrial buildings; results of such have also been developed into database that has been published online by industrial partners.

As mentioned, one of the objectives in deploying PV system could be to achieve the goal of making the building net zero energy. In such case, the design criterion will be to match the energy generation density to the energy consumption (from measured or simulated data). Fig. 68B depicts such input into a mocked-up online database query (inputs in black). The query will return the pareto solution (outputs in red)

A)

PV System : select based on desired system capacity	
Amount of daylighting (0, 5 ,10, 15%)	0
desired system capacity (W_p/m^2), *(max. 113 at 0% daylightin*	24
PV System (possible solution)	
design system capacity (kW_p)	24
PV tilt angle (degree from horizontal)	30
PV length (m)	1.6
spacing between rows of PV (m)	12
predicted energy generation (kWh/m^2-yr)	18

B)

PV System : select based on desired amount of energy generation	
Amount of daylighting (0, 5 ,10, 15%)	0
desired amount of energy generation (kWh/m^2-yr)	83
(max. 83 kWh/m^2-yr at 0% daylighting)	
PV System (possible solution)	
possible system, energy generation (kWh/m^2-yr)	83
PV tilt angle (degree from horizontal)	16
PV length (m)	1.6
spacing between rows of PV (m)	0.8
design system capacity (kW_p)	113

Fig. 68: Database query that returns the pareto solution according to design criterion

Table 39 presents a comparison between results obtained from conventional design approach and computational simulation design approach. In this example, PV array of 1.6m length is installed. With the

conventional design approach, a tilt angle of 52° is assigned and a spacing of 13m between rows of PV arrays is recommended. This configuration will return a predicted energy generation density of 17.4 kWh/m^2-yr at a generation yield of 733 kWh/kW_P annually (recommendations based on conventional design approach are shown as blue dots in Fig. 67. Two pareto solutions generated by the database query are also presented, according to two different design objectives.

Table 39: Comparison between conventional and computational simulation design approach

	Length (m)	Tilt Angle (°)	Spacing (m)	Design Capacity Density (W_P/m^2)	Energy Generation Yield (kWh/kW_P)	Energy Generation Density (kWh/m^2-yr)
conventional design approach						
	1.6	**52**	**13**	24	733	17.4
computational simulation design approach						
same kW_P	1.6	30	12	**24**	772	18.3
max. density	1.6	16	0.8	113	733	**82.6**

The recommended configuration according to the conventional design approach never fully utilizes the available rooftop space, nor generates energy at the highest yield. Therefore, the first objective is trying to find a better alternative for the same design generation capacity of 24 kW_P/m^2 (that is, for the same investment). The database query (Fig. 68A) returns an pareto solution that can generate energy at an yield of 772 kWh/kW_P, which is 5% more efficient than the conventional design approach. On the other hand, if a known energy generation density is desired, the database query can search for the most efficient configuration at the desired density. In the Netherlands, a maximum generation density of 113W_P/m^2 can be efficiently packed into the available space. As shown in Table 39, even at such high density, the optimized pareto solution operates at exactly the same yield (733kWh/kW_P) as the recommended configuration according to the conventional design approach, and at the same time, generates almost five times the amount of energy.

Summary

The computational simulation design approach for PV systems offers two main advantages over conventional design approach; by first, providing time-varying evaluated solutions (vs rule of thumb recommendations), and second, addressing practical considerations, regarding generation yield, space limitation, and net-zero energy design goal, which could not be evaluated with conventional design approach. From the results, it can be observed that designs recommended according to the conventional design approach are neither efficient nor fully utilizing the available space. The computational simulation design approach that could be deputed as database query, provides a convenient and yet objective means to evaluate PV system design.

2.3.6 System Model of Microcogenerator based on ICE (University of Sannio, Italy)

The use of Micro-Combined Heat and Power (MCHP) systems for distributed residential power generation and other polygeneration applications is an interesting alternative to traditional power plants due to their higher overall efficiency.

MCHP has been dealt by several researchers for its potential savings, particularly in distributed energy systems, especially to determine suitable applications and evaluate the financial feasibilities of such devices in comparison with other generation options.

Therefore, several techniques for modelling the performance of both CHP and MCHP technologies have been developed, based on a variety of basic modelling aims. Modelling methods range from simple calculations using thermal and electric energy demand (several computer design tools are commercially available), to multiple-objective optimization approaches. In particular with reference to building-integrated MCHP systems, there are a wide range of levels in modelling detail and temporal resolution.

The analysis of MCHP utilization in buildings is complicated by the strong matching between the cogeneration unit, other HVAC components, and the user's thermal and electrical demands.

The literature is rich with examples of ICE models developed for general analysis of combustion-based stationary engines, but with few exceptions, these models focus on engine phenomena occurring over very short time-scales, which are several orders of magnitude smaller than the time scales used in building simulation.

This issue leads to the development of models for whole-building simulation programs, to facilitate the analysis of residential application. Therefore in the following, a simplified MCHP model, suited for whole-building simulation software, is described, calibrated and validated [78,79] by means of the available experimental data on an ICE-based AISIN Toyota MCHP (Tab. 38).

To simulate the microcogenerator operation, the TRNSYS RIC (Reciprocating Internal Combustion) engine model has been used, by using the Type 907 TESS component. It uses a table of performance data to determine the outputs of the engine, given a set of input conditions. Generally speaking, thermal power can be recovered from the oil cooler, the exhaust gas heat exchanger, the after-cooler and the engine jacket.

The model relies on an external data file which contains efficiency (both mechanical and electrical), air flow rate (fraction of rated flow rate) and heat transfer data (fraction of total thermal power recovered from the generator, the oil cooler, the exhaust gas heat exchanger and the engine jacket and the fraction dissipated to the environment) as a function of the intake temperature and the part load ratio (PLR – actual power over rated power).

The tested microcogenerator is not equipped with invasive temperature and flow rate sensors to separately measure the thermal power recovered from the exhaust gas and the engine jacket; hence it has been assumed that, in the TRNSYS engine model, all the thermal power is recovered by the engine jacket. Moreover, it is not possible to measure the mechanical power transferred from the engine to the electric generator; therefore, a constant value of 0.95 has been assumed for the electrical efficiency of the generator.

Table 40: MCHP manufacturer data.

Power [kW]	Input	20.8
	Electric	6.0
	Thermal	11.7
Efficiencies [%]	Electric	28.8
	Thermal	56.2
	PER	85.0
Fuel		Natural gas
Weight [kg]		465
Size [mm]	Height	1500
	Width	1100
	Depth	660
Engine	Displacement [cm3]	952
	Rotational speed [rpm]	1600-1800
Generator	Permanent magnet, 16 pole synchronous generator	
Sound level [dBA]		54

The external data that contains the performance of the engine as a function of the PLR is reported in Table 41.

The MHCP is modeled by three components, as shown in Fig. 69, that are the RIC engine, a plate heat exchanger, used to transfer the recovered thermal power to a secondary fluid (i.e. water), and a three-way valve. The latter mixes the part of solution flow rate that passes through the plate heat exchanger and the one that is bypassed toward the engine. A control system that manages the thermal recovery circuit of the microcogenerator is also modeled.

Table 41: Values of the parameters used as input data in TRNSYS Type 907.

PLR [-]	Electrical rate [kW] A	Primary energy rate [kW] B	Total waste heat rate [kW] C=B-A	Waste heat recovered rate [kW] D	Electrical Efficiency [-] E=A/B	Mechanical Efficiency [-] F=A/0.95/B	Fraction waste heat recovery [-] G=D/C	Fraction waste heat to environment [-] H=1-G
1.70E-01	1.02E+00	9.49E+00	8.48E+00	7.22E+00	1.07E-01	1.13E-01	8.52E-01	1.48E-01
3.42E-01	2.05E+00	1.22E+01	1.01E+01	7.94E+00	1.69E-01	1.77E-01	7.84E-01	2.16E-01
5.12E-01	3.07E+00	1.46E+01	1.15E+01	8.38E+00	2.11E-01	2.22E-01	7.29E-01	2.71E-01
6.76E-01	4.06E+00	1.69E+01	1.28E+01	9.21E+00	2.40E-01	2.53E-01	7.18E-01	2.82E-01
8.40E-01	5.04E+00	1.91E+01	1.41E+01	9.62E+00	2.64E-01	2.78E-01	6.85E-01	3.15E-01
9.99E-01	5.99E+00	2.12E+01	1.52E+01	1.01E+01	2.83E-01	2.98E-01	6.63E-01	3.37E-01

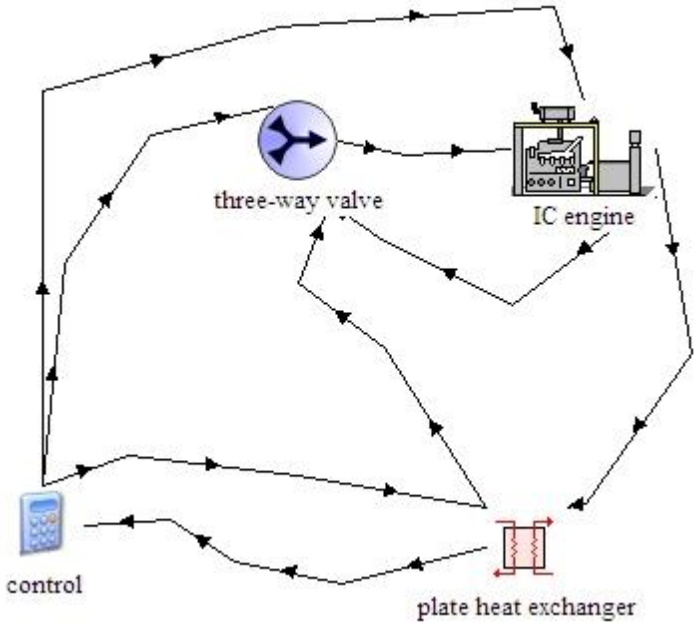

Fig. 69: The MCHP model in TRNSYS

Some tests were carried out to evaluate the mass flow rate of solution that indeed crosses the plate heat exchanger, $\dot{m}_{sol,pl}$, as a function of its temperature at the outlet of the heat exchanger itself, $t_{sol,out,pl}$ (Fig. 70). Results show that $\dot{m}_{sol,pl}$ increases with a 2nd order curve when $t_{sol,out,pl}$ is lower than 55 °C (the equation is shown in Fig. 70); for higher outlet temperatures, a constant mass flow rate of solution (about 0.30 kg/s) passes through the plate heat exchanger.

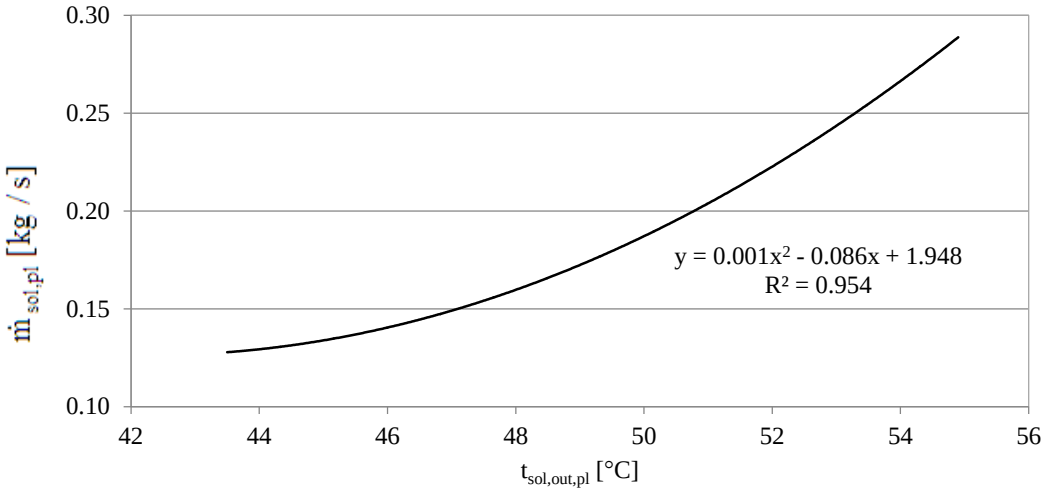

Fig. 70: Solution mass flow rate passing through the plate heat exchanger as a function of its outlet temperature

Concerning the parameters of the RIC engine, only the specific heat of jacket water fluid (3.72 kJ/kgK) and maximum power output (5.73 kW, considering an average consumption of MCHP auxiliaries of 270 W, with radiator fan off) are effectively used, while the other parameters (specific heat of oil cooler fluid, exhaust air, after-cooler fluid and rated exhaust air flow rate) are not used.

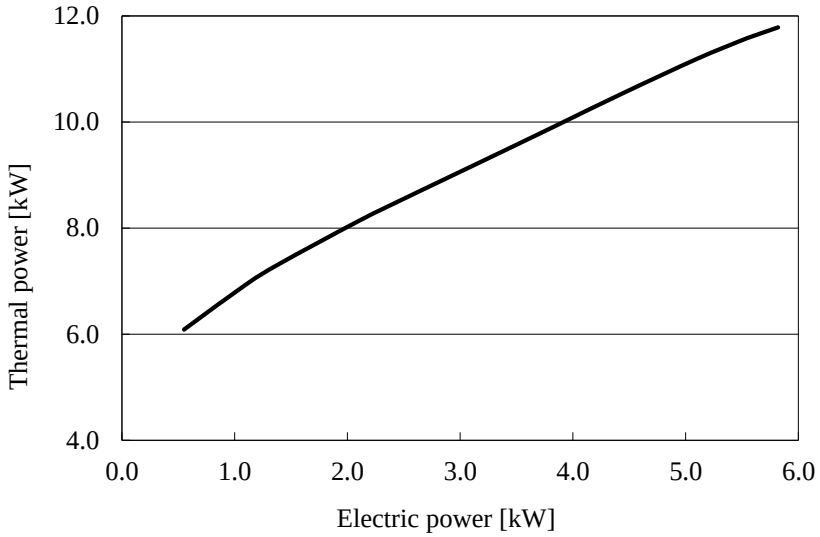

Fig. 71: Thermal power as a function of electric power for the AISIN MCHP

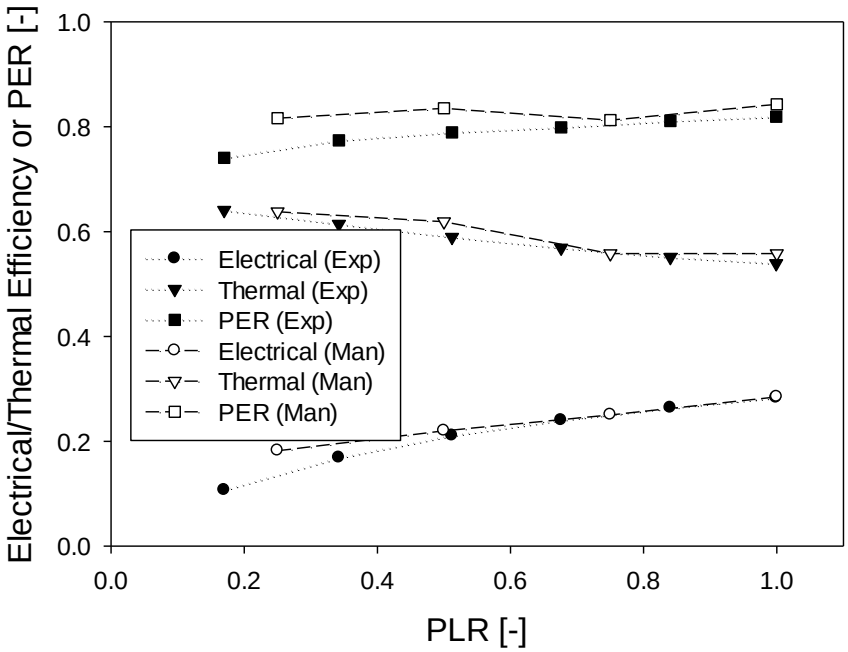

Fig. 72: η_{el}, η_{th} and PER of the AISIN as a function of PLR

The desired output, that is an input of the model, is converted to a part load ratio value and then used to refer to a performance map which contains information on efficiency, exhaust flow and heat distribution. From this performance map, the fuel use and thermal output can be derived.

Regarding the characterization of the MCHP performance, the recovered thermal power as a function of electric power supplied by the MCHP is shown in Fig. 71.

In Fig. 72, electric, thermal and overall efficiency (*PER* – Primary Energy Ratio) of AISIN MCHP as a function of *PLR* are shown, considering both the experimental (Exp) and manufacturer (Man) announced data. Experimental tests established that electric efficiency increases with *PLR*, as expected. Small differences were found for PER, electric and thermal efficiencies curves over all range of PLR.

Even if thermal power increases with PLR (see Fig. 71), thermal efficiency reduces as the primary power input increases more than thermal power itself. Finally, the increase in η_{el} prevails over the reduction in η_{th}; hence *PER* rises with *PLR*.

For the description of the operation of the plate heat exchanger, the NTU-effectiveness method, applied to a counter flow heat exchanger, has been used:

$$\varepsilon_{pl} = \frac{1 - \exp\left[-\frac{UA}{C_{min}}\left(1 - \frac{C_{min}}{C_{max}}\right)\right]}{1 - \frac{C_{min}}{C_{max}}\exp\left[-\frac{UA}{C_{min}}\left(1 - \frac{C_{min}}{C_{max}}\right)\right]} \quad (67)$$

where C_{min} = min(C_{sol}; C_w) and C_{max} = max(C_{sol}; C_w), where C_{sol} is the capacity rate of the glycol-ethylene mixture through the heat exchanger and *UA* is its overall heat transfer coefficient.

Experimental data were used to evaluate the overall heat transfer coefficient as a function of $\dot{m}_{sol,pl}$ (Fig. 73); the 2-nd order equation shown in the figure is used to model the plate heat exchanger.

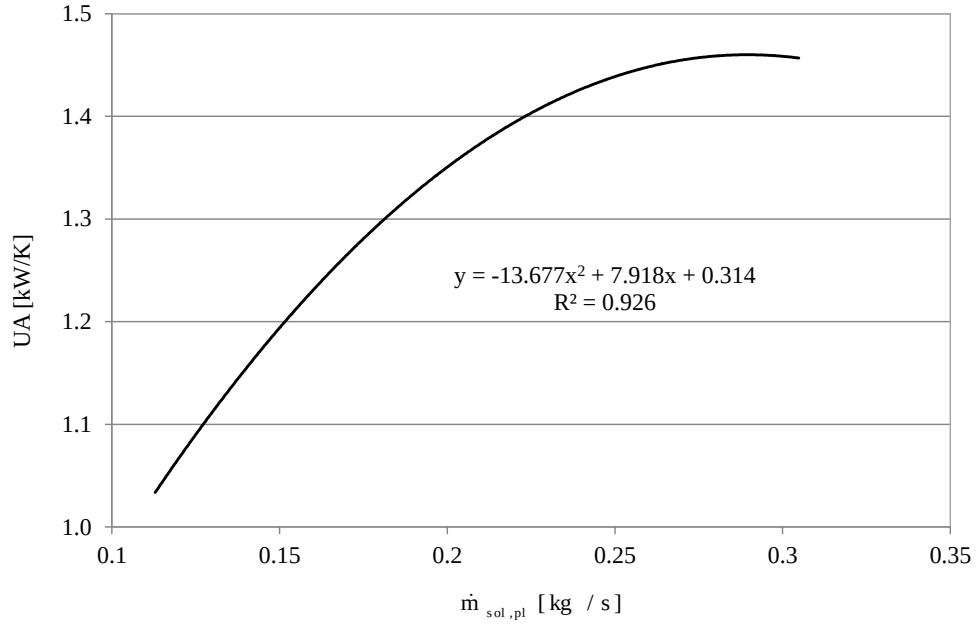

Fig. 73: UA of the plate heat exchanger as a function of the solution mass flow rate passing through it

To validate the MCHP model, a comparison between measured and experimental values of water temperature at the outlet of the heat exchanger (secondary circuit – cold side) was performed, Fig. 74.

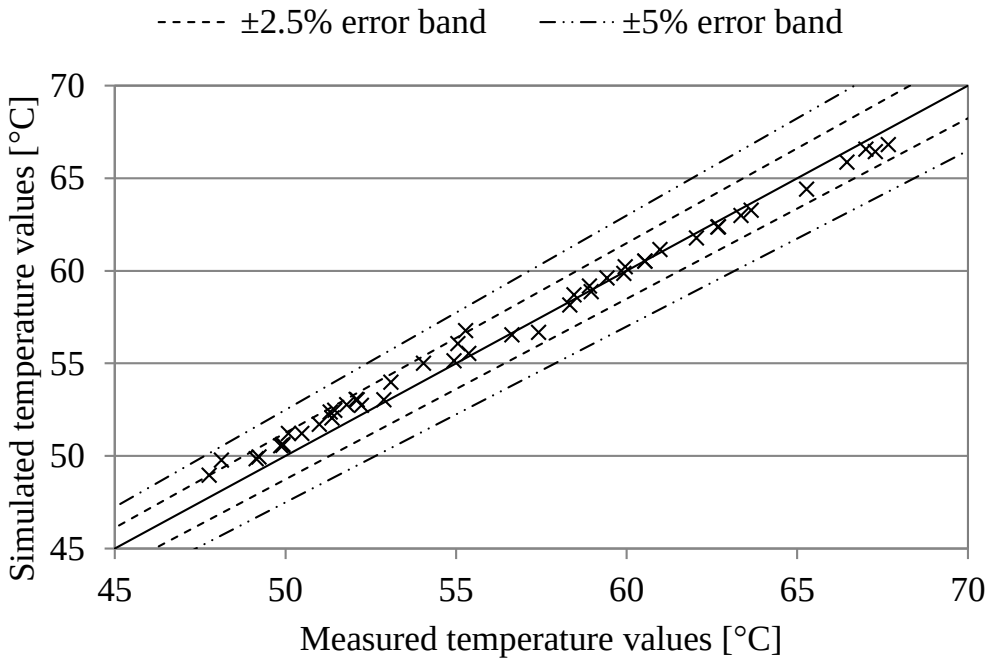

Fig. 74: Measured and simulated values of water temperature at the outlet of the heat exchanger

No values are outside the ±5% error band and only two values are outside the ±2.5% error band. Furthermore, a RMSE of 0.714 °C was obtained.

The validation was also based on an energy balance approach and to this aim a specific test was carried out. It had a duration of 75 minutes, during which the electrical power output of the microcogenerator was increased from 2 to 6 kW with steps of 1 kW. Simultaneously, the temperature of water entering the plate heat exchanger was linearly increased from 40 to 56 °C.

The same forcing functions were also applied in a TRNSYS simulation of the MCHP; the error between measured and simulated values are 4.71% and 3.98%, in terms of overall thermal energy produced and overall primary energy required, respectively.

Results are considered satisfactory, especially considering that the analyzed model does not take into account transient effects.

2.3.7 System Level Models (Technische Universität München, Germany)

One of the object in the field test was a health club equipped with two Senertec Dachs micro-CHP systems (CB_1) [80, 81]. For further analyses a model of this installation has been developed, using TRNSYS as software tool and field testing data for the validation. **Fehler! Verweisquelle konnte nicht gefunden erden.** shows the structure of this model. On top metering components are visible providing data for the output files. In the middle from left to right the supply side, heat distribution and demand side are located. At the bottom the control components are shown.

The supply side consists of the following heat generators:

- 2x micro-CHP unit Senertec Dachs (12.5 kW thermal, 5.5. kW electrical output each),
- 2x peak load boiler (60 kW thermal output each),
- 1x solar thermal system (20 m² absorber area).
- The micro CHP units were modelled using Type 154-ICE-Internal Combustion Engine. This type is one of the micro CHP models developed during Annex 42 [82].
- The heat generators feed heat to the distribution system including the piping as well as several thermal storages:
- 1x 3 000 l buffer storage,
- 2x 500 l DHW storages, operated in parallel,
- 1x 500 l DHW storage to integrate the heat gains of the solar collectors.

The demand side is simulated using load profiles for space heating and hot water consumption derived from the measuring campaign.

Fig. 76 shows results of the model validation. As example the December 28th 2011 has been chosen. For each, the outlet temperatures of both CHP systems and the peak load boiler and the return temperature from the buffer storage towards the heat generators, simulated (solid lines) and measured temperatures (dotted lines) are shown. General behavior of the simulation is good. Especially operation of the peak load boiler shows good correlation.

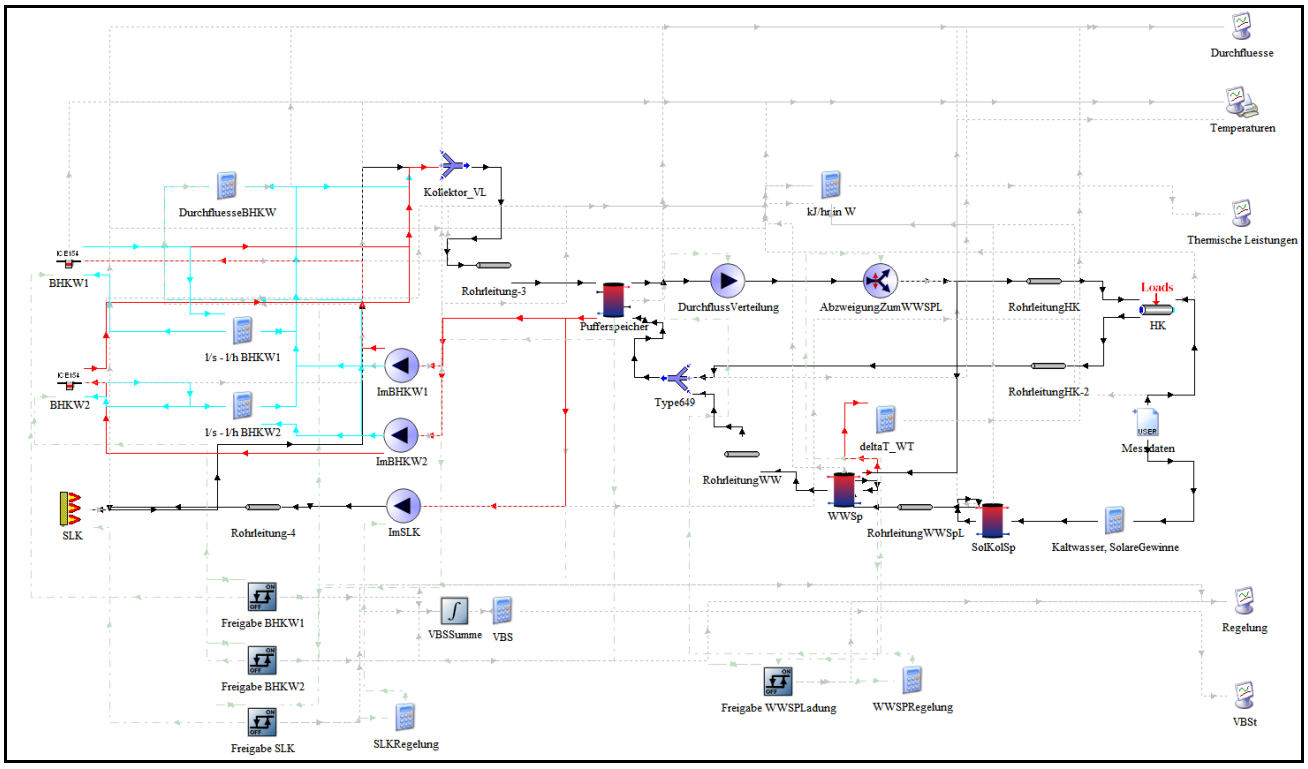

Fig. 75: TRNSYS Model of a health club (CB_1) equipped with two micro CHP systems.

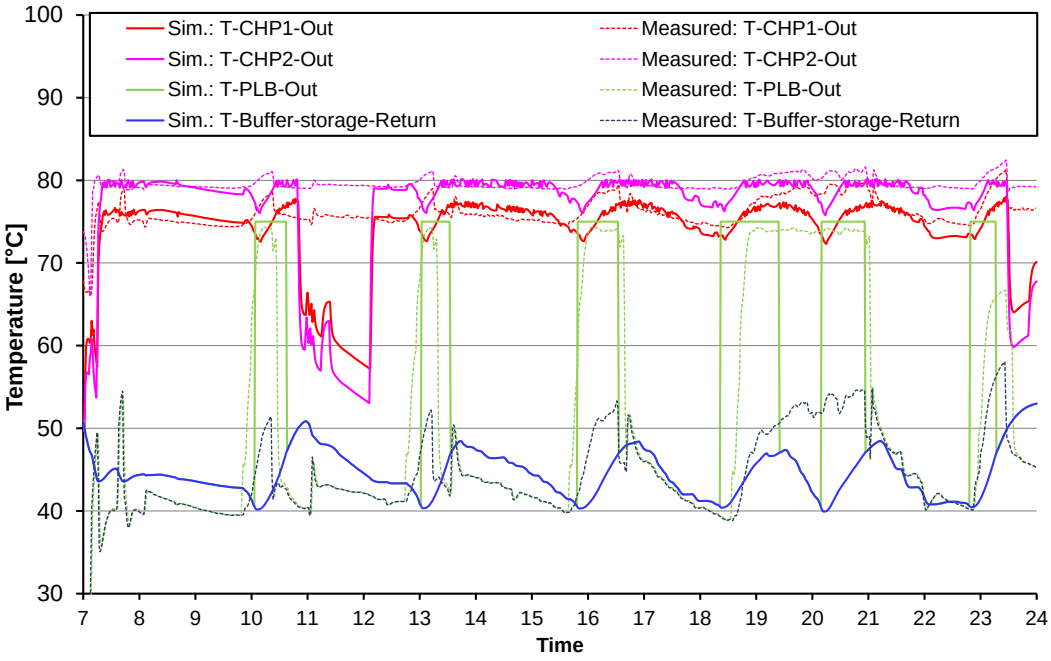

Fig. 76: Validation of the TRNSYS model

A thermal simulation model has also been used to optimize system configuration. The following refers to the building CB_2 of the field test [80], which is a small hotel with an integrated butcher shop.

As the focus is on the integration of the micro CHP unit in the system, only the CHP related part has been modeled in detail. A heat demand profile replaced the building simulation. Out of several configurations realized in TRNSYS the following two will be described more in detail:

- **Status-quo:** Fig. 77 shows the system layout as it has been realized in the supply object. The micro CHP unit (BHKW) delivers heat to a thermal buffer storage (PS) with a volume of 1000 l. The buffer storage is connected in serial with a peak load boiler (SLK) to supply heat to the building. The heating water always circulates through the boiler. The boiler is activated, if the water circulation through it has a temperature below 52°C and stops at temperatures higher than 65°C. A storage Type 4a is included to emulate the heat losses that occur in the boiler.
- **Optimized configuration:** As visible in Fig. 78, now CHP unit (BHKW) and peak load boiler (SLK) both supply heat in parallel to the buffer storage (PS). The boiler is only activated if the outlet temperature of the buffer storage on the demand side is lower than 52°C and stops if the temperature in the middle of the buffer storage reaches 65°C.

The goal of the optimized configuration is to avoid the stand-by heat losses of the peak boiler. This is achieved as heating water only circulates through the boiler if it is in operation. The total efficiency of the boiler increases from 45 % (status-quo) to above 70°% (optimized configuration).

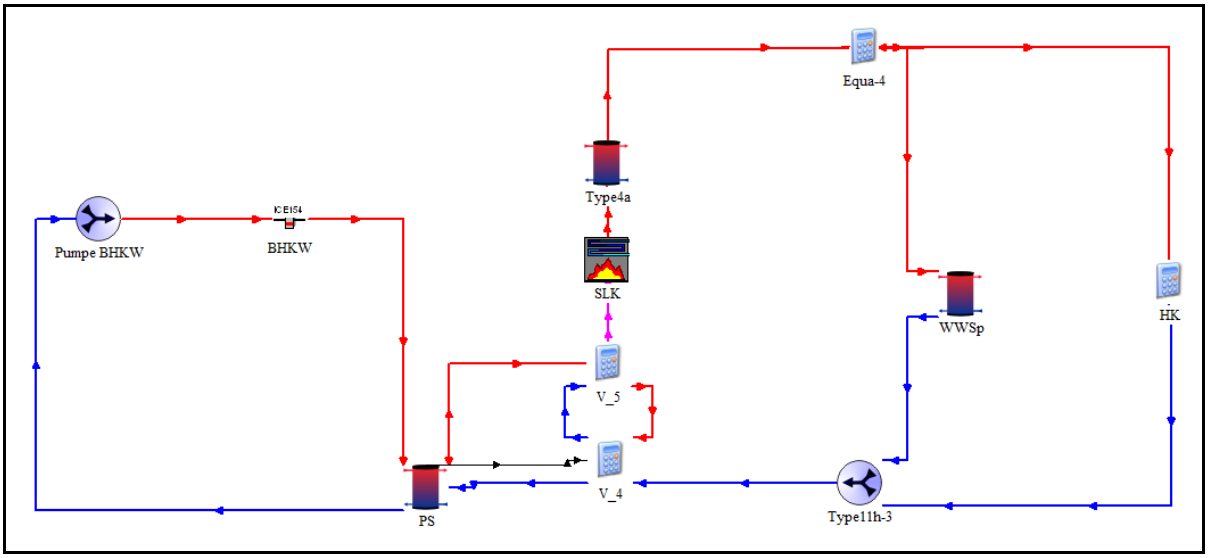

Fig. 77: Simplified TRNSYS model – status-quo

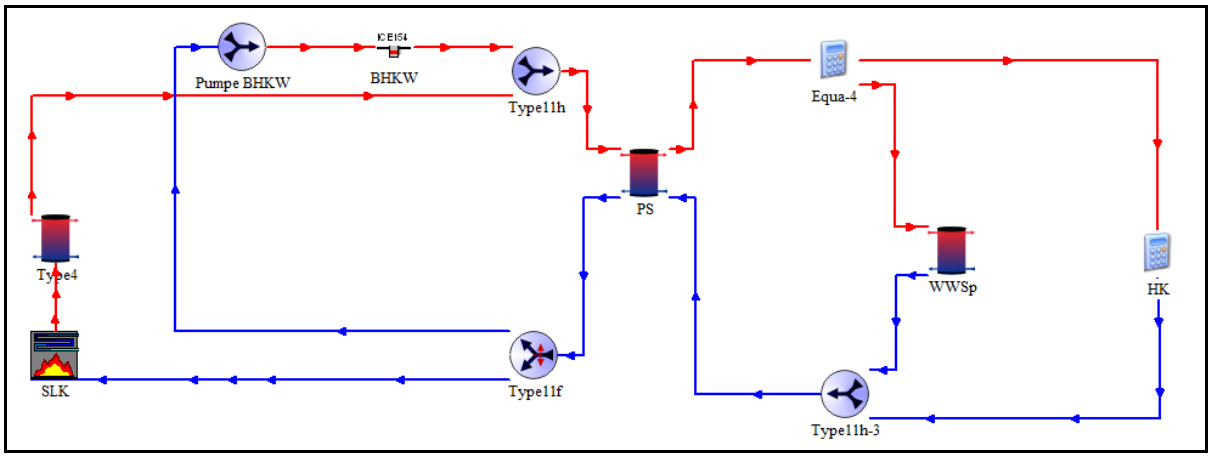

Fig. 78: Simplified TRNSYS model – optimized configuration

Another advantage of the optimized configuration is a significant reduction of the start-stop cycles of the boiler as is shown in Fig. 79.

Based on a load profile of 6 months, the TRNSYS simulation leads to the results of Table 42:

- The fuel consumption of the peak load boiler could be reduced by 6 % while the heat output increased by 40 %
- Due to the lower heat losses, the CHP delivers 15 % less heat and electricity and consumes less fuel. Additional 2.7 MWh electricity have to be purchased from the grid.
- Altogether 5.6 % of primary energy can be saved.

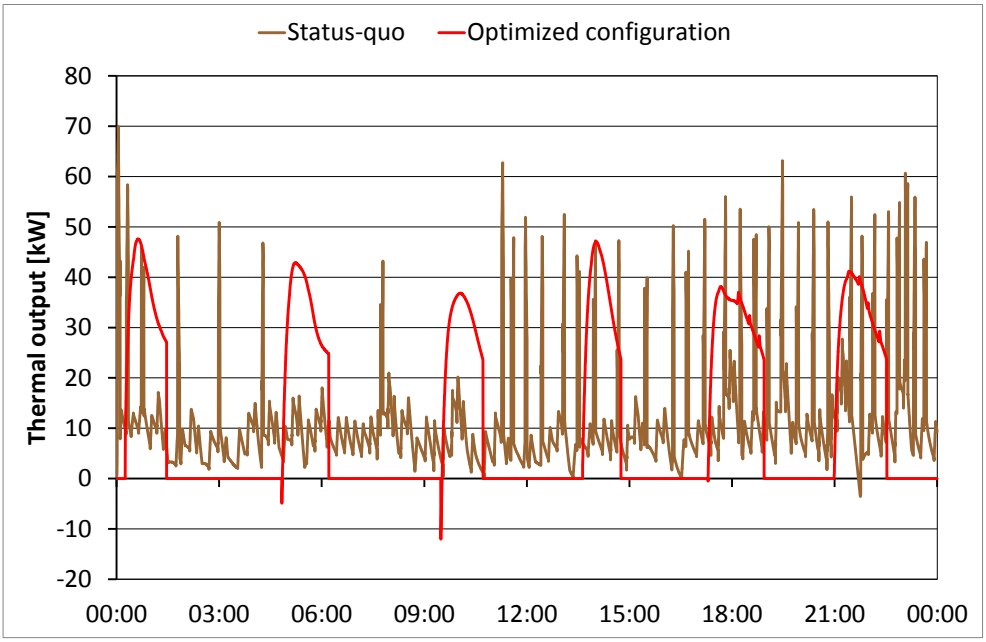

Fig. 79: Peak Load Boiler operation in status quo and optimized configuration

Table 42: Comparison of both configurations

		Status-quo	Optimized configuration
CHP fuel consumption	[MWh]	71.8	61.4
CHP heat output	[MWh]	39.5	33.7
CHP electricity generation	[MWh]	18.7	15.9
PLB fuel consumption	[MWh]	24.0	22.6
PLB heat output	[MWh]	10.9	15.5
Heat demand DHW	[MWh]	18.2	18.2
Space heating demand	[MWh]	30.2	30.2
Electricity grid import	[MWh]	0.0	2.7
Final energy demand	[MWh]	95.8	86.7
Primary energy demand	[MWh]	105.3	99.4
Primary energy savings		---	5,6%

2.3.8 A Cogeneration System for an Apartment Building based on Distributed Heat Storage Technology (Japanese Group)

Introduction

In order for economically viable distributed generation systems for apartment buildings to spread, it is essential to develop an efficient and low-cost heat supply system. We have developed a new cogeneration system ca11ed the Neighboring Cogeneration system (NCG). The key concept of this system is to install a heat accumulator with a hot water supply and a room heating function at each household and to connect different households by a single loop of hot water. We report the results of the NCG system for 7 lived-in households. The controlling system worked efficiently. All of the households were able to use hot water without any difficulties. Further, we report the results of the energy saving effect of the NCG system for 50 lived-in households by means of a simulation based on the experimental results for NEXT21.

By introducing this system into an apartment building of over 20 households, we can assume that the heat load leveling effects are high. To determine the optimal heat supply control and equipment specifications for an apartment building with tens to hundreds of households and various heat load patterns, a heat supply simulation model was created based on the heat supply test results for NEXT21. The heat supply simulation model was created by using Visual Modeler (Omega Simulation Co., Ltd.). This process simulator can take dynamic characteristics into consideration, and it reads heat demand data for every minute and calculates simulation data for every second.

Scope of Model

A model of the heat storage unit was created. Since the temperature distribution in the heat storage tank needed to be reproduced in this model, the tank was divided into 50 segments. A model of perfect mixing of hot water entering a water-filled cooling tank from a bottom inlet was created, and an extrusion flow with temperature stratification up to a segment portion of higher temperature than the tank-bottom inlet flow temperature was created.

The parameters of elements, such as valves, heat exchangers, and pumps were adjusted, and the model was created so that it would be in agreement with the heat supply test results for the heat storage unit.

The model of the heat storage unit was used to connect seven households; a model of the NEXT21 system was then created by combining the models of the newly created heat sources. The control logic for the inverter pump, heat storage unit gas engine, and backup boiler was made the same as that for the NEXT21 system.

Finally, the model of the heat storage unit was used to connect 50 households, and the heat source.

Using the model of 50 connected households, it was considered whether heat supply to 50 households would be possible with a single-loop pipe of 25-mm inner diameter.

Model inputs

The simulation was performed for the heat demand pattern of a single day in winter on the apartment building (50 households).

A gas engine (rated power output: 25kW, hot water output: 38kW) and two backup gas boilers (hot water output: 175kW) were assumed as the heat source. Regarding the heat loss in the single-loop pipe and heat storage units, the heat loss coefficient was calculated from the experimental date for NEXT21 and was included in the model.

Further, the outlet flow rate from the single-loop pipe was inverter-controlled by the return temperature of the single-loop pipe by making the standard flow rate 20L/min. The maximum flow rate was assumed to be 60L/min.

As a method to reduce the heat load on the single-loop pipe and to use the heat storage effectively during the peak heat load hours, heat storage was not used from of 17:00 to 20:00 but corresponding to hot-water supply by the heat supply directly from single-loop pipe. The time from 20:00 to 23:00 was considered to be the peak heat load hours, and heat storage was not performed.

Results

A trial calculation for the energy-saving effects of introducing this system into an apartment building of 50 households was performed.

Heat source equipment, a gas engine (rated power output: 25kW, power generation efficiency: 33.5% (LHV), hot water output: 38kW, total efficiency: 85%) and two backup boilers (87.5kW), were installed in an apartment building of 50 households.

The load survey data for an apartment building (50 households) for a representative day of every month was used for electricity and heat demand. The trial calculation was made for this representative day, and then the energy-saving effects over a year were evaluated.

The heat supply simulation model for 50 households introduced in the previous section was used in the trial calculation. When the peak heat load cutting effect (difference between the heat loads of all the households in the peak heat load time zone and the heat load in the single-loop pipe) by distributed heat storage in each households was calculated, it was approximately 130kWh (including the heat source system). The trial calculation was made with this value as the amount of effective heat storage. Moreover, the control logic that the gas engine used was part of the load in terms of electricity demand, stopping when the amount of effective heat storage was reached, was adopted.

As a noteworthy feature of NCG, the heat storage capacity of the entire system was large as compared with conventional systems, so that the engine operating rate increased and the energy-saving effect was improved. When evaluated over one year, it turned out that NCG can reduce the amount of the primary energy used by 15% and carbon dioxide emission by 23% by compared with the case of a gas boiler installed in each household.

Conclusions

A single-loop pipe of 25-mm inner diameter was able to demonstrate that supplying heat to 50 households was possible by using a heat supply simulation model based on experimental results.

According to the results of evaluation throughout the year, it turned out that NCG can reduce the amount of primary energy used by 15% and that the amount of carbon dioxide emission from it by 23% as compared with the case where a gas boiler is installed in each household.

2.3.9 Water Heater Models for use in City-Level Energy use Simulations (Japanese Group)

Introduction

Simulation models for new types of water heaters (gas engine co-generation, PEFC, SOFC, condensing gas water heater, solar water heater, and heat pump water heater) are developed [83]. These models are merged with the city-level residential energy end-use simulation model [84] which calculates electricity and hot water demand of various types (household member, type of house, etc.) of household in 5 minutes interval. Due to the granularity of the electricity and hot water demand, the model is able to be used to determine the relative efficiency of these water heaters for different household categories from the viewpoint of reductions in cost, energy use, and CO_2 emissions. Based on the results, the optimum distribution of these water heaters in Osaka City (population: 2.6 million, households: 1.2 million) is demonstrated. The CO_2 emission-reduction effect, the energy-saving effect, and the change in the electricity load curve of Osaka City under conditions of optimum distribution of water heater types were evaluated using the model.

Scope of Model

This model can simulate energy performance of micro gas engine co-generation, polymer electrolyte fuel cell cogeneration system, solid oxide fuel cell, condensing gas water heater, solar water heater, and heat pump water heater.

In the city-level residential energy end-use model, the annual energy consumption of one household is calculated iteratively for the 19 household categories, as well as the 12 building-type categories, six of which are classified as detached houses and the other six as apartments according to floor area. In addition, four different thermal insulation levels are considered for each building. In the appliance energy use schedule model, the energy use of each appliance is simulated separately and is based on occupant behaviour. Occupant behaviour for a variety of activities is stochastically determined over 24 hours on weekdays, weekends, and holidays based on attributes of the occupants. In the heating and cooling energy-use model, dynamic heat load simulations are carried out using both building data and weather data. Ventilation and heat conduction between rooms is calculated using a thermal circuit network method. Heating and cooling loads are simulated considering internal heat gain, which is calculated using the appliance energy use model and the behaviour of the occupants. The time interval used for the heat-load and energy-use simulations is five minutes.

Model inputs

Input data are as follows:

1) Census and other statistics for estimating the distribution of household categories.
2) 2005 National time use survey for occupants' behaviour schedule model.
3) Electricity consumption, dissemination ratio and frequency of appliance use.
4) City water temperature estimated from climate data.
5) Weather data (Standard Weather Data of Osaka City)
6) Specifications of walled and windows, plan of house.
7) Heating and cooling operation probability function by room air temperature and hour.
8) Set air temperature
9) Quantity and temperature of hot water for each use and season.

In this study, heat from hot water heater s is utilised for only water heating and surplus electricity generated by cogeneration that cannot be utilized within household cannot be sold to electricity grid.

Results

The difference in the primary energy reduction effect among household categories for the CO2HP(heat pump water heater), PEFC and SOFC systems is large compared to LHB(condensing gas water heater) and MGE(micro gas engine) systems, which are smaller. SOFC systems have the highest primary energy-savings

for households consisting of two members or more, followed by the SOLAR(solar water heater) and CO2HP systems.

For each household category, the optimum water heating system is selected for primary energy reduction. In all household categories with two or more family members, the SOFC system is considered optimal. Performing the analysis again to exclude the SOFC, which is not yet commercially available, reveals that the CO2HP system is better suited for use in apartments while the SOLAR system is better suited for use in detached houses.

Optimal distribution of the various systems for achieving optimal reductions in CO_2 emissions under Japanese electricity grid condition shows different results. For all apartments and most detached houses, the CO2HP system was identified as being optimum. It should be noted that CO_2 emissions are dependent upon the CO_2 emission factor of the electricity grid in the target region. For detached houses with one or two members, SOLAR systems were found to be the most optimum system.

For the cost optimum distribution, the SOFC system is not considered since its initial cost cannot be predicted at present. The LHB system was selected as being optimum for cost in detached houses with one to three members and in apartments with one to four members, probably because the hot water demand of these household types is relatively small, resulting in a longer pay-back time for the other water heating systems. For families with more than four members, the CO2HP and PEFC were selected as being optimum because the larger hot water demand has the effect of decreasing the pay-back time.

In the baseline case, the annual primary energy consumption is 70.2 PJ, 24.7% of which is used for producing hot water. By replacing water heating systems, the total primary energy consumption decreases by 3.8 to 12.7% compared to the baseline case. In the Energy Optimum case, the total primary energy consumption can be decreased by 12.7%. However, if the SOFC system is excluded, the reduction in total primary energy consumption decreases to 8.3%.

Replacement of all of the water heaters with LHB or SOLAR systems reduces the total CO_2 emissions by 4.2% and 4.5%, respectively. Since SOLAR systems are only considered for detached houses in this study, the effect is comparatively small. Replacement of conventional water heaters with CO2HP systems reduces total CO2 emissions by 12.3%. In the CO_2 Optimum case, where the proportion of CO2HP systems is 87.2%, total CO2 emissions decrease by 12.5%. The CO_2 reduction effects of a cogeneration system, such as an MGE or PEFC system, are small or negative because the CO_2 emission factor for the grid electricity in the study is small (0.358 kg-CO2/kWh); approximately half of the electricity that is used to supply Osaka with power is primarily generated by nuclear and hydro power plants.

Large-scale introduction of heat pump water heaters will increase the demand for electricity in the residential sector. On the other hand, introduction of cogeneration systems will decrease the electricity demand. The electricity load curve of the residential sector in Osaka is calculated for the baseline, Energy Optimum, and CO_2 Optimum cases for three days from August 7 to 9; however, this time in the Energy Optimum case we considered using the SOFC systems. In the CO_2 Optimum case, 87.2% of households installed CO2HP systems. The electricity demand due to CO2HP appears two hours before 6 a.m., which is when the night-time rate for power ends according to the current tariff system. This demand due to the CO2HP system at 6 a.m. amounted to approximately 1 GW of electricity, which is higher than the peak demand in the daytime and, except for these hours, the electricity load curve is almost the same as the baseline case. In the case where 96.4% of households install SOFC systems (Energy Optimum case),

electricity demand decreases by 300-500 MW as the SOFC system generates electricity in response to the specific electricity demands of the house.

Conclusions

The energy-saving effects attributable to the water heaters differs with household-type, with the effect being more noticeable in households with more members and in those that consumed more hot water.

Optimal water heating systems exist for each household category. The optimal system for a given household could be identified through selection of the optimum system based on the electricity and hot water demand of each household and application of the end-use demand model developed by authors. The distribution of optimal water heater-types by household category was found to differ for primary energy reduction, CO_2 emission reduction, and cost reduction.

Combined with low-carbon grid electricity, the CO2HP system is associated with the highest CO_2 reduction for most household categories.

Although SOFC systems are not yet commercially available, compared to other residential cogeneration systems, these systems have considerable energy and CO_2 reduction potential.

New water heating systems could potentially reduce CO_2 emissions by the residential sector of Osaka City by a maximum of 12.5%. However, in order to introduce the CO_2 Optimum system into each household, a subsidy is considered necessary to offset the expenses incurred. Highly cost-effective CO_2-reduction through such subsidies could be achieved by subsidizing relatively more cost-effective households only.

Large-scale introduction of heat pumps and cogeneration systems would have the effect of markedly changing the electricity load curve.

2.3.10 High Solar Concentrator Model (Università Politecnica delle Marche, Italy)

The aim of the HCPV technology is to take the advantage of the solar concentration principle and thus reduce the amount of the photovoltaic material. The PV material can be replaced with a cheaper optical system, which can be made by plastic, glass or aluminium. Optical systems for solar concentration work properly only with a fraction of the whole solar radiation: the direct rays' normal irradiation (DNI). This means that HCPV systems require solar tracking and that the technology is really effective only in those countries where the solar radiation is more intense and constant, such as Mediterranean Countries and Middle Est North Africa countries (MENA).

The main components of an HCPV module are: the triple junction photovoltaic cell, the optics and tracking mechanism. The key characteristics of the system lies in its innovative design since it uses a very compact and lightweight chassis, an accurate tracking mechanism and a very small triple junction solar cell (see Fig. 80).

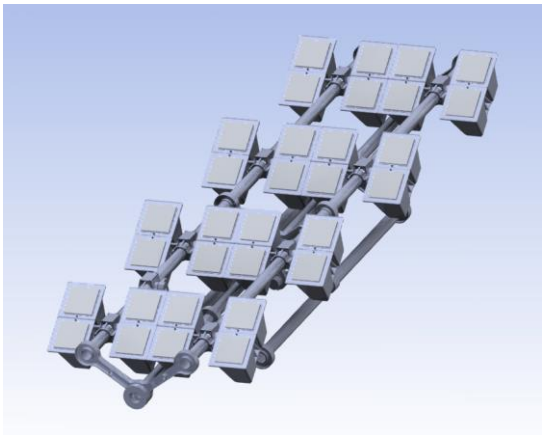

Fig. 80: Model of the HCPV system

In addition, a specific optics was developed to suite the solar cell and to reduce the encumbrance of the module. All of these characteristics make this system suitable for small power generation application and building integration. The HCPV plant can be assembled according to the user need, in terms of electric power requirement and space availability. The Power output of each module is 70W (DNI 900 W/m2, ambient temp. 25°C) with an efficiency of about 30%.

Table 43: Main electric, optics and mechanical parameters of the HCPV system

Parameter	VALUE
Power output (DNI 900 W/m2, ambient temp. 25°C)	70 W
Cell Typology	Monolithic Triple Junction
Cell dimension	Circular, 2.3 mm diam.
Cell efficiency (flash test)	41%
Optics	Fresnel lens and secondary optics
Optics efficiency (on axis)	85 %
Module efficiency	30 %
Dimensions	1.6x0.4x0.4 m

The effectiveness of the whole system depends on the performance of each single component of the HCPV module. An 'ad hoc' model has been developed to simulate the performance of the High Concentrator PhotoVoltaic, HCPV, system [85]. For the simulation of the HCPV module under analysis a simplified approach has been adopted: the profile of the solar radiation spectrum is neglected and only the whole DNI flux is used as an input parameter.

As regards the optics, the system uses a Fresnel lens as first optic and a reflective cone as a secondary optic. The secondary optics has a double aim: first to improve the concentrated solar flux homogeneity on

the cell (which is a requirement to achieve higher cell fill factor and efficiency); secondly, to reduce the optical efficiency losses in case of tracking misalignment (the radiation that is not directed to the cell is reflected by the secondary optics and redirected on the photosensitive material).The optical concentration level has been pushed up to 1000 suns in the modelled prototype. This high concentration ratio can be achieved thanks to the use of a small MJ solar cell that have lower series resistance losses and can spread the extra heat from the concentrated light more easily

The optical efficiency has been defined on the basis of: i) simulations coming from a ray-tracing software and ii) the mechanical accuracy of the dual-axis tracking mechanism defined trough a probability function.

Fig. 81 shows the trend of the relative optical efficiency as a function of the misalignment error of the tracking mechanism.

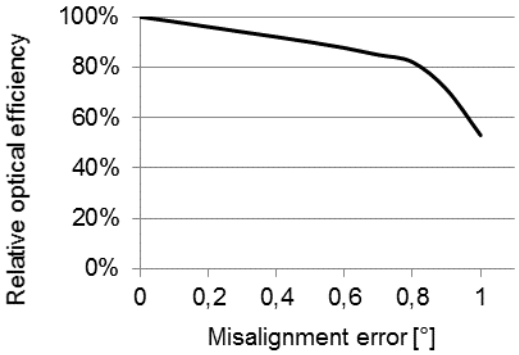

Fig. 81: Relative optical efficiency vs. misalignment error

Once the optics' performance is defined, the triple junction solar cell response can be simulated by means of a semi-empirical diode model. The parameters that are required to define the model are obtained by the I-V performance curve of the cell. The experimental data come from a test bench that can acquire the I-V curve of the cell at various concentration levels and cell temperatures. In the test bench, a continuous xenon lamp source was used with an Air Mass 1.5D filter to control the output spectrum. A diode model is assessed to define the performance of the cell; the parameters in the model are deduced by a regression that minimizes the difference between the experimental I-V curve and the I-V curve from the analytical model. Also the cell temperature is an important parameter that influences its performance; for this reason, a specific model is defined. The cell's temperature depends on the ambient conditions (ambient temperature) and the optical concentration ratio (optical efficiency and DNI). On the basis of the experimental data an accurate model has been defined.

The cells in the flash tests show an efficiency of 41% which drops to 35% in real working conditions (overheating due to the concentrated solar flux). 3J solar cells do not suffer from sensible performance decay at high working temperature as traditional silicon cells and thus they are suitable for the application under high radiation flux. The extra heat can be easily rejected in small cells since the hot spots are smaller and better distributed on the chassis thus no active or passive cooling devices are required.

Fig. 82 shows the comparison between an experimental I-V curve and the I-V curve described by the analytical model; Fig. 83 reports the experimental I-V curves of the cell at four different levels of solar concentration.

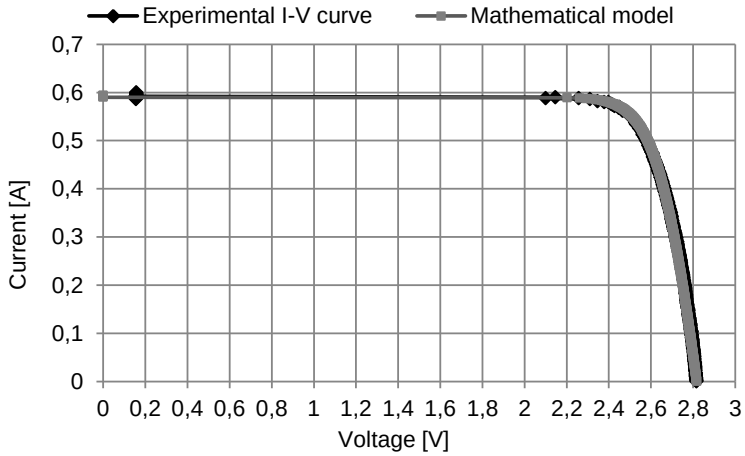

Fig. 82: Comparison between an experimental I-V curve and a modelled I-V curve

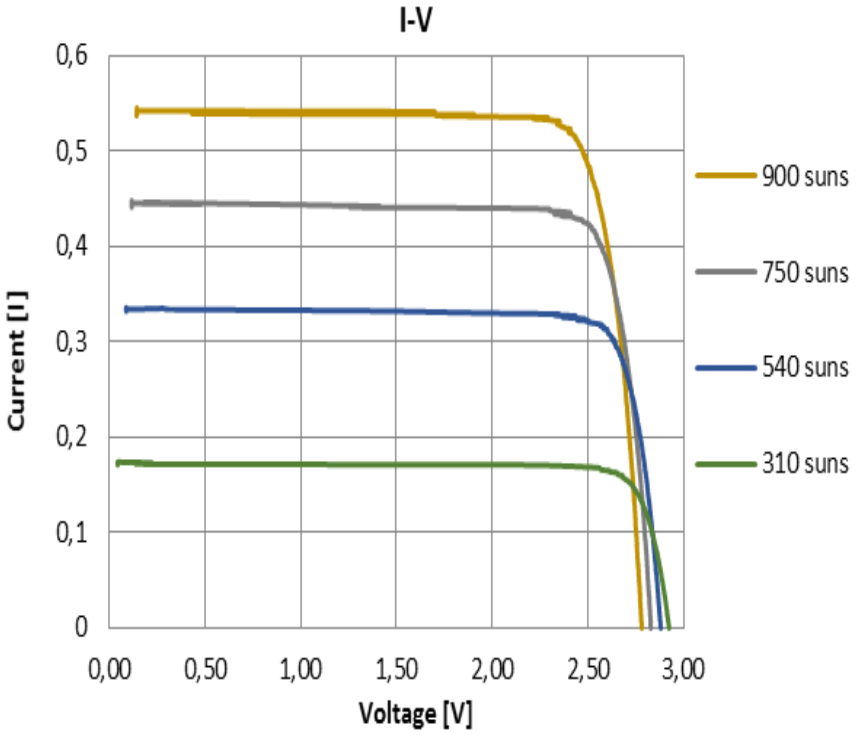

Fig. 83: Experimental I-V curves of the cell at different solar concentration levels

The HCPV system accounts also for a series of other losses; the so-called Balance Of System, BOS, takes into account all the components of a photovoltaic system other than the photovoltaic panels. This includes wiring, switches, support racks, inverters, and batteries in the case of off-grid systems. For this reason, the definition of the BOS losses depends on many parameters; usually, a value of 15% losses is suggested for a small scale system. So finally the output of the cell can be obtained as the combined result of the solar DNI data, the tracking accuracy, the correspondent optical accuracy, the solar cell electrical output and finally the BOS losses.

2.3.11 Optimal Strategies for Hybrid Systems made up of HCPV and Micro-CCHP Devices (Università Politecnica delle Marche, Italy)

The aim of the work was to identify the optimal strategies for the management of a hybrid system made up of a micro-Combined Cooling Heat and Power (CCHP) technology and a High Concentrator Photovoltaic (HCPV) system, suitable for the residential and tertiary sectors in the Mediterranean area. For many times CCHP systems, and especially small units, have been granted fixed electricity prices, but recently, fixed prices have been replaced with variable prices, according to the negotiations on the day-ahead electricity market, providing both new opportunities and the need of identifying new management strategies. A specific algorithm has been developed to assess the operation of the hybrid poly-generation system, in details a multi-objective approach has been followed, considering the minimization of three items: i) operating costs, ii) carbon dioxide emission and iii) primary energy consumption, on the basis of weighting factors defined 'a priori'; thus all the three objectives have been expressed on cost basis. The configuration A of Fig. 84 shows a conceptual layout of the hybrid poly-generation system under analysis, aimed at maximizing plant flexibility. The plant is made up of an ICE, a HCPV unit, modelled by the authours [86], [87], a Thermal Energy Storage (TES), an additional heating boiler, an absorption chiller and a vapour compression chiller. Both micro-CHP and HCPV systems are connected in parallel to the grid and to the end-user; this means that the electrical load of the end-user can be satisfied by both the power devices and by the grid. In the same way, the energy produced by the devices can be either sent to the end-user, or sold to the grid, or used to feed the vapour compression chiller.

The thermal demand can be satisfied either by the additional heating boiler, or by the thermal power recovered from the ICE, or by the thermal power stored in the TES.

The cooling demand can be satisfied either by the vapour compression chiller or by the absorption chiller, driven by the thermal power recovered by the micro-CHP unit or by the thermal power stored in the TES. The inclusion of both the cooling devices increases the lay-out complexity and, in general, it is not feasible in a real installation. Anyway, the complexity of this layout gives the opportunity to understand which of the two cooling systems is the most suitable when a multi-objective optimization criteria is followed.

Results coming from configuration A have been compared to other three configurations, as shown in Fig. 84.

The main findings of the work [88] are the following:

- optimal management of a hybrid system provides advantages (in terms of operating costs, carbon dioxide emissions and primary energy consumption) compared to separate production. Micro-CHP units and HCPVs modules are conveniently used in: i) winter and fall/spring days and ii) for all the three cases analysed. These results suggest the applicability of a hybrid system, in particular for all the areas characterised by a reduced number of 'hot climate periods';
- a reduction ranging from 30% to 50% in the operating costs, in the carbon dioxide emissions and in the primary energy consumption can be achieved adopting an optimal dispatch

algorithm with respect to separate production. This suggests and underlines the advantage of a real-time management strategy;

- the electricity purchase and sell price affects the hybrid system operation only when a higher weight is attributed to the operating costs. This means that the advantages of variable electricity prices can be effectively appreciated only following a minimisation criteria based on the operating costs;
- the application of a HCPV system is beneficial for all the analysed cases, providing a reduction of the primary energy consumption, carbon dioxide emissions and of operating costs compared with SP. This trend is particularly evident in sunny periods and for low thermal demand users, as in the office case;
- as regards the cooling devices, the absorption chiller is never chosen by the multi-objective optimisation strategy, suggesting that the best option is the adoption of a vapour compression chiller.

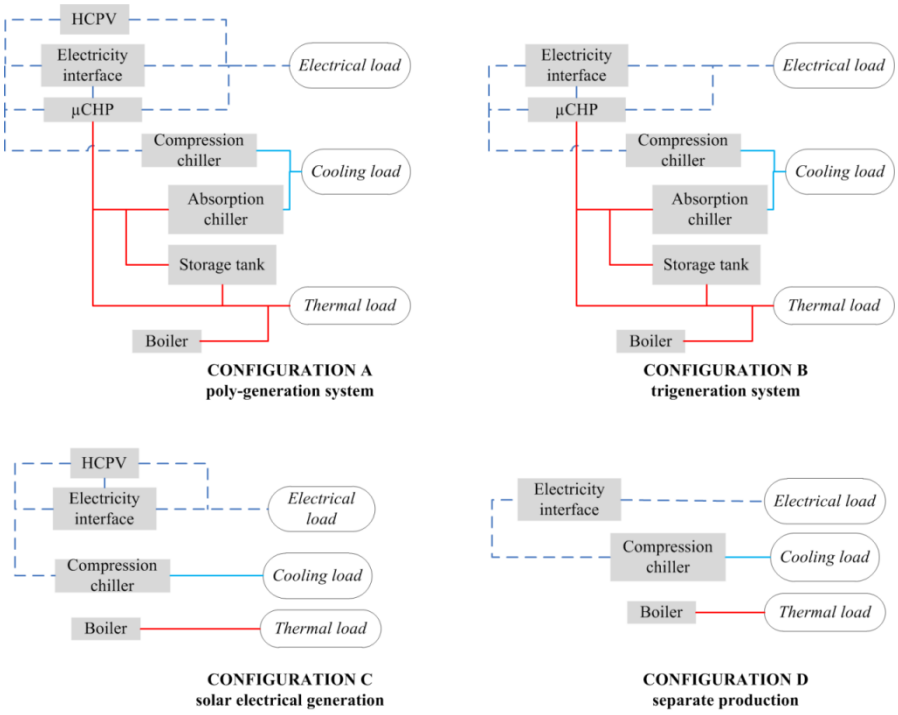

Fig. 84: Configurations considered in the analysis

2.4 Control Systems Linked with Micro-Cogen Operations

2.4.1 Alternative Algorithms for Dispatching a Virtual Power Plant (Research Center for Energy Economy (FfE), Germany)

Combined Heat and Power (CHP) devices devices are basically operated heat tracked; thermal demand determinates electricity production. The integrated thermal storage is only used to reduce the number of start-ups and to increase user comfort. From the grid point of view, the heat tracking operation results in fluctuating electricity feed-in that must be compensated by balance power.

Without lack of comfort, electrical production can be shifted into certain temporal intervals by anticipatory operation of the CHP-device and the thermal storage. This shifting capability can be used to avoid schedule deviations in the balance group or to provide balance power to the transport system operator (TSO).

In practice, this task is organized by a control centre of several linked CHP-devices. This pool of linked devices is called virtual power plant (VPP), as the linked Distributed Energy Resources (DER) can perform tasks, which have usually been performed by larger fossil power plants.

At first sight, dispatching a VPP seems like planning today's conventional power plants. A closer look reveals that the commonly used methods based on Mixed Integer Linear Programming (MILP) do not meet the special needs of a VPP. The mathematical problem differs from that of a conventional dispatch by the high number of individual devices, which are characterized by similar or identical technical and economic parameters. Furthermore, the local thermal load of the CHP devices must be considered.

This chapter describes the development and assessment of different algorithms for day-ahead and intraday dispatching which fulfil the requirement of a virtual power plant consisting of individual CHP devices. This work is carried out within the research project "Pooling of Distributed Energy Resources" which is subsidized by the Federal Ministry for Economy and Technology and supported by the two German utilities "Stadtwerke München" and "EWE AG" from Oldenburg.

Dispatching of conventional and virtual power plants

Conventional dispatching

Usually, power plants are dispatched one or a few days ahead. To that time forecasts of all relevant values are available. For instance, a temperature forecast is used to estimate the end-user electricity demand. Depending on the forecast electricity prices decisions are taken to either run the power plant or to buy electricity from the wholesale market. Special qualified plants may provide additional positive or negative balance power. Commonly, only a limited number of plants are involved into this dispatch. These plants, which do not provide heat simultaneously, predominantly can be planned by the merit order of their electricity production costs.

The planner has knowledge about the characteristics of the plants like the year of construction, technical parameters or upcoming revisions. In many cases, he could do the dispatch without computer aided optimization. Schedule deviations can be faced by increasing or lowering the power of a single plant.

Considering heat production of CHP plants as well can be done easiliy by conventional dispatching methods. If there is a district heating system, the combined heat and power plants are taken into account preferential to cover the heat demand. The thermal heat demand can be forecast appropriately due to the high amount of consumers. Smaller CHP-devices usually receive daytime-independent subsidies by the German government. A fixed feed-in tariff means that there is no incentive to dispatch these devices or shift the production to other times.

Dispatching of VPP

In a virtual power plant schedules are created for every DER to use the trading potential and to make the electricity feed-in more predictable. The planner cannot know all the details of the single devices and must rely on an automated dispatching process.

The manageable devices of a VPP are often CHP devices, which provide heat to small district heatings or to single buildings. Heat supply is at first priority. A heat overrun leads to an emergency stop, a lack of heat may cause the distributed devices to switch to local control. Prediction of the demand of the smaller consumer objects is more difficult and leads to intraday schedule deviation regarding electricity.

As the imperfection of the thermal load forecasts of the single houses may compensate each other, a new balancing and a redispatch for the remaining day considering the new thermal situation is useful. This intraday redispatch should be run in short time intervals to react appropriately to forecast deviations.

Usage of MILP algorithm for virtual power plants

The FfE implementation of a Mixed Integer Linear Programming (MILP) algorithm reveals that dispatching a VPP with that method does not provide the appropriate solution quality. The calculation time depends basically on the occurrence of integer components, as shown in /Stimpfl 2010/. This issue has little influence to an academic analysis of a VPP, however, it is not tolerable for the productive and time sensitive appliance of a pool operation. Additional to the day-ahead dispatching, a rolling intraday planning is necessary to balance the forecast deviations of the distributed thermal demands.

The optimization problem differs from conventional power plant dispatching by the high number of devices with similar production costs (Table 44). Similar costs shrink the difference between alternative operation options and lead to a flat solution tree, which takes long time to work out.

Linear and heuristic algorithms achieve solutions without walking through the solution tree and can provide results in a significantly shorter time. However, the gain of calculation time means disadvantages in the solution quality. For instance, if there are many identical devices linked to a pool and 6 out of the installed 49 devices would be enough to cover the electricity supply in a specific time step, there would be about 14 million options to combine the running devices. Of course, not all combinations are equal due to the heat demand and storage usage, but the differences are slight and may cause problems to standard MILP-approaches. Heuristic and linear algorithms may solve faster by ignoring these small differences and by pre-setting the operation modes of the devices.

If there are plants with wide difference in the installed electric power, inappropriate settings in the simulation tolerances may cause improper results. Too weak relative tolerances may retard an optimization of the small device and probably lead to unnecessary start-ups. Strict tolerances do consider the operation

of the smaller devices but increase calculation time. Heuristic and linear algorithms do not use tolerances to stop the optimization process.

When redispatching the planning of conventional power plants, it is often sufficient to regard the merit order of the production costs only. In case of CHP devices in single buildings ignoring the thermal situation means losing synergetic effects of contrarious thermal forecast deviations.

Table 44: Problems of conventional algorithms used for VPP

Algorithm	Problem	Solution
Mixed Integer Linear Programming (e.g. for day-ahead planning)	Similar devices and market parameters cause similar opportunity cost and a flat solution tree.	Alternative Algorithms, which work without browsing the solution tree, for instance heuristic or linear programming algorithms.
	A high number of devices can be combined to a huge number of variations ("6 out of 49"~14 mio. possibilities) - in every time step.	Pre-allocation of the operation mode through previous solution or heuristic algorithm.
	Linking mixed devices of small and big power output require narrow tolerances to regard the operation of the small devices.	Usage of tight relative tolerance and moderate absolute tolerance. Heuristic and linear algorithms work without tolerances.
Merit-Order of electricity producers (intraday planning)	Ignoring the heat supply disregards the synergetic gain of different heat demand forecasts.	Consideration of heat supply within algorithm. Utilization of alternative algorithms regarding the time limit.

Alternative Dispatching Approaches

This section introduces the conventional MILP based dispatch approach and to two alternative methods, which were developed at the FfE.

The first algorithm MIPR (Mixed Integer Programming Reference) is based on former FfE work and is used as a reference to assess the alternative implementations. The modelling by equations makes this method very flexible. It can be used for day-ahead or intraday planning and for heat led or electricity led operation.

The LPH algorithm combines the linear programming with heuristic aspects. The linear optimization is run several times, while heuristic intermediate steps ensure that non-linear conditions are considered. These methods can be used for all common planning tasks just like the MIPR algorithm.

The heuristic approach is divided into several specific application modes. There is the HHL algorithm for heat led scheduling and HDA for electrical day-ahead planning. HFIX is used for the intraday redispatch, when trading volumes are already fixed. A final MILP step can be executed by the HMIP method that hands over the heuristic results as a initial value. A summary of these developed implementations is presented in Fig. 85.

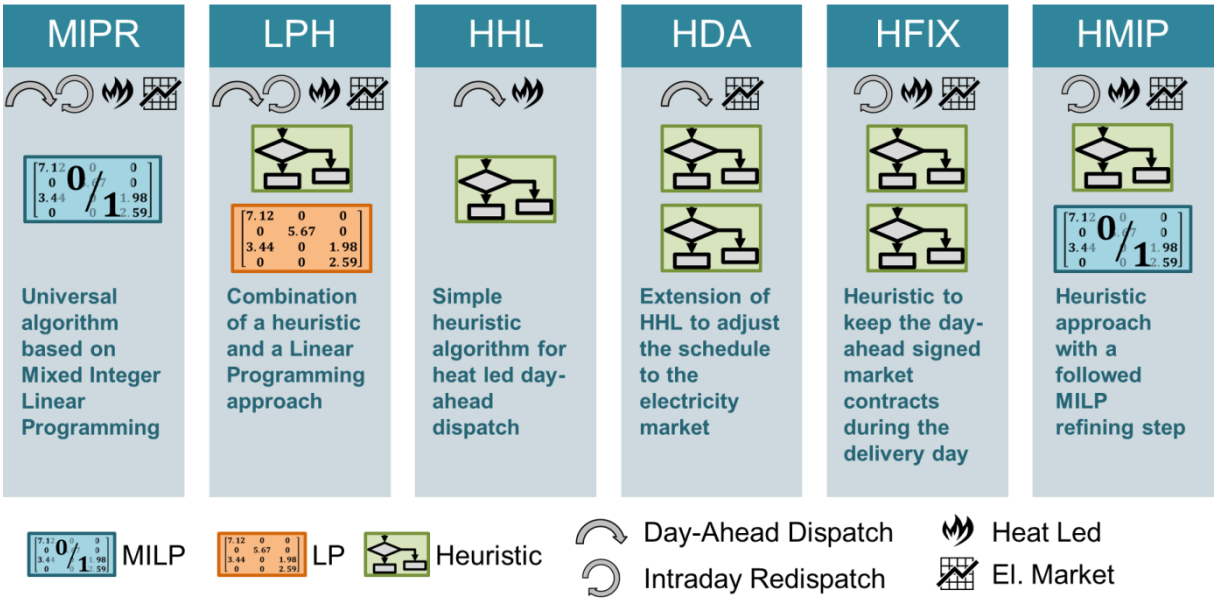

Fig. 85: Implemented and tested algorithms for VPP

MILP approach

Within the project „DER - Distributed Energy Resources“ [89] a power plant dispatch has been developed, which is based on *Mixed Integer Linear Programming* MILP.

The general form of a linear optimization problem can be written like shown in **equation (68)**. The objective must be minimized while regarding the constraints expressed by equations and inequations.

$$\min\{c^T x | Ax \leq b, A_{eq} x = b_{eq}\} \tag{68}$$

$c^T x$ *objective*

$Ax \leq b$ *constraint of inequation*

$A_{eq} x = b_{eq}$ constraint of equation

The objective (**equation (69)**) of a linear model must be expressed as a polynomial of 1st degree. In a power plant dispatch the costs should be minimized. That is why there should only appear cost and revenue terms in the objective.

$$c^T x = c_1 \cdot x_1 + c_2 \cdot x_2 \ldots + c_n \cdot x_n = \\ = c_{EALT}^T x + c_{TALT}^T x + c_{FUEL}^T x + c_{BLR}^T x + c_{START}^T x + c_{GRAD}^T x + c_{ET}^T x + c_{RC}^T x \tag{69}$$

$c^T x$ *objective*

x *variable*

c objective coefficient

The single terms are grouped thematically and cover costs for a fictitious energy source and sink for electric and thermal grids ($c_{EALT}^T x$, $c_{TALT}^T x$), fuel costs ($c_{FUEL}^T x$), costs for boiler operation ($c_{BLR}^T x$), start-up

($c_{START}^{T}x$) and load change costs ($c_{GRAD}^{T}x$) as well as the costs and reveneues of electricity trading ($c_{ET}^{T}x$) and providing balance power ($c_{RC}^{T}x$).

The constraints can be expressed as inequations (equation 3) or equations (equation 4) and are formulated as linear terms like the objective.

$$\mathrm{Ax} \leq \mathrm{b} \tag{70}$$

$$a_{11} \cdot x_1 + a_{12} \cdot x_2 \ldots + a_{1n} \cdot x_n \leq b_1$$

- $\boldsymbol{a}$ *constraint coefficient (inequation)*
- $\boldsymbol{x}$ *variable*
- $\boldsymbol{b}$ *right hand side argument*

$$\mathrm{A}_{eq}\mathrm{x} = \mathrm{b}_{eq} \tag{71}$$

$$a_{eq,1} \cdot x_1 + a_{eq,2} \cdot x_2 \ldots + a_{eq,n} \cdot x_n = b_{eq,1}$$

- $\boldsymbol{a_{eq}}$ *constraint coefficient (equation)*
- $\boldsymbol{x}$ *variable*
- $\boldsymbol{b_{eq}}$ right hand side argument

MILP-characteristics imply that every variable x_i can be defined as a real or integer number. It thereby can take continuous or discrete values.

For power plant dispatching relevant objective terms and constraints are covered extensively in literature [90-94].

Heuristic approach

Heuristic algorithms find solutions by following rules which are set up for a specific problem. This set of rules can be illustrated as a decision tree (Fig. 86). A global mathematic description of the problem is not necessary. The advantage of the heuristic is the velocity to find an appropriate solution. The disadvantage is the none-optimal result and the lack of information about the rate of the solution quality. Both, velocity and solution quality, essentially depend on the implemented set of rules.

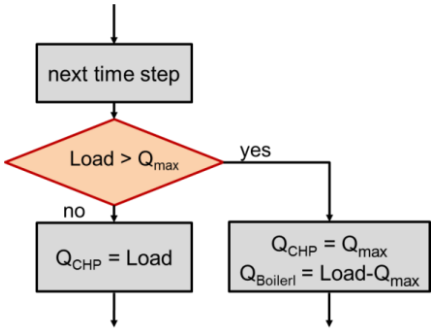

Fig. 86: Illustration of a heuristic decision tree

Basically, the developed heuristic proceeds by improving a given initial value repetitively. The heat led operation can be used as initial value. Based on this schedule the marketing revenues are improved by shifting the CHP production to more profitable time steps. The possible shiftings are grouped according to their purpose (Fig. 87).

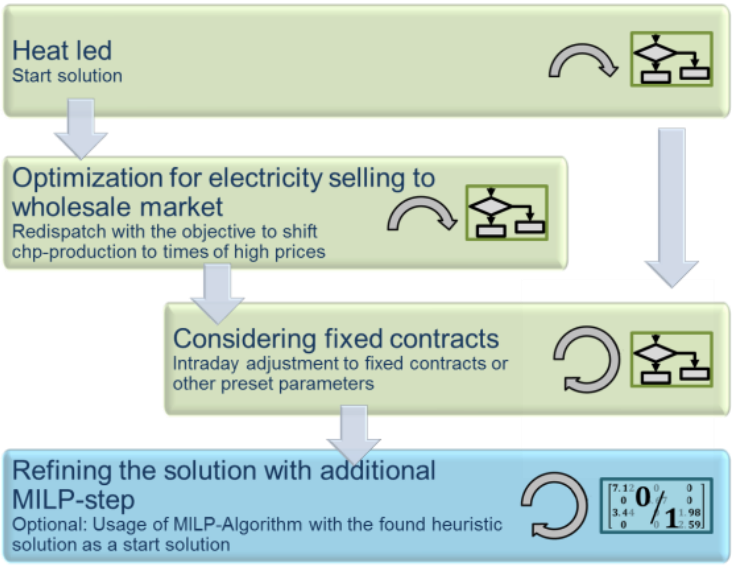

Fig. 87: Steps of the heuristic dispatching

The intraday dispatch tries to correct the forecast deviations and tries to reduce the deviation of the registered electricity schedule as well as a possible failure in the local heat supply. Additionally, it is possible to use the heuristic result as an initial value for a final MILP step in order to refine the solution quality.

As a shifted CHP operation influences the thermal storage or the boiler, all changes are clustered to a so-called shifting scheme. A shifting scheme (Fig. 88) bears a temporal limited impact to the schedule and may be considered isolated, without changing the schedule in other timesteps or other devices. For every scheme the shifted electric energy and the specific revenue are rated. As these schemes are seldom independent, many shifting options are evaluated and only the most profitable ones are executed. For instance, only a limited number of schemes which increase the storage level can be executed. The order of the analyzed and executed schemes thereby influence the solution quality significantly.

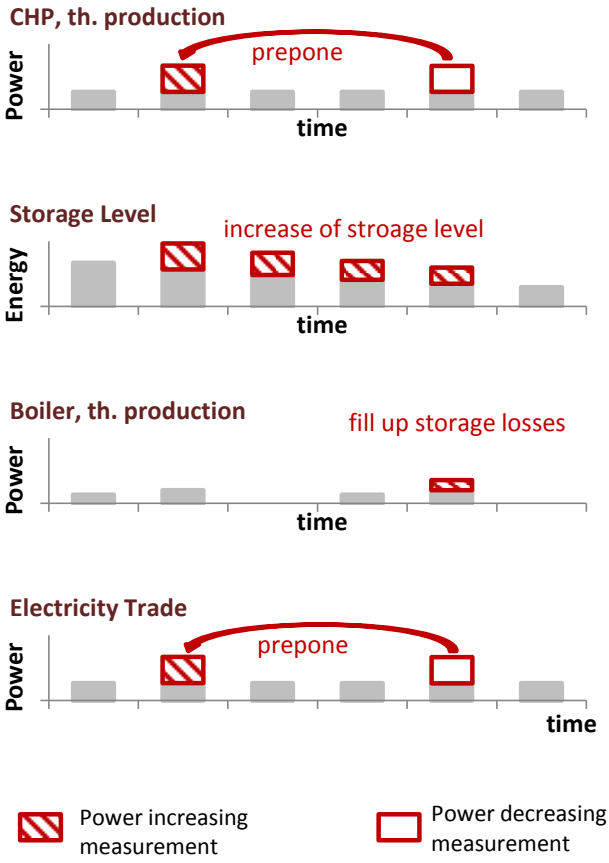

Fig. 88: Illustration of the method of the heuristic algorithm

Linear-Heuristic

This algorithm, which is based on Linear Programming (LP), is used to dispatch non heat producing power plants and considers the minimum load criteria without usage of integer components [95]. The optimization problem of a VPP differs by the additional consideration of the thermal load. The LPH-algorithm provides a schedule after passing through 3 LP optimizations and 2 heuristic intermediate steps (Fig. 89).

Initially, the entire pool is optimized without minimum load criteria. This thus created schedule contains time steps in which the CHP power is lower than technically possible.

The following heuristic (H1) analyzes the heat demand of the connected building and the necessary minimum and maximum operation time of the CHP device. The optimized operation time must be inbetween that range to avoid heat overrun or an inappropriate boiler usage. Preferentially, CHP is planned to operate in time periods in which the LP algorithm has calculated the highest production rate. Furthermore, adjacent time steps are analyzed whether a focused production is profitable. If necessary, further operation time periods are pre-set in the order of the LP result, until the required minimum operation time is reached.

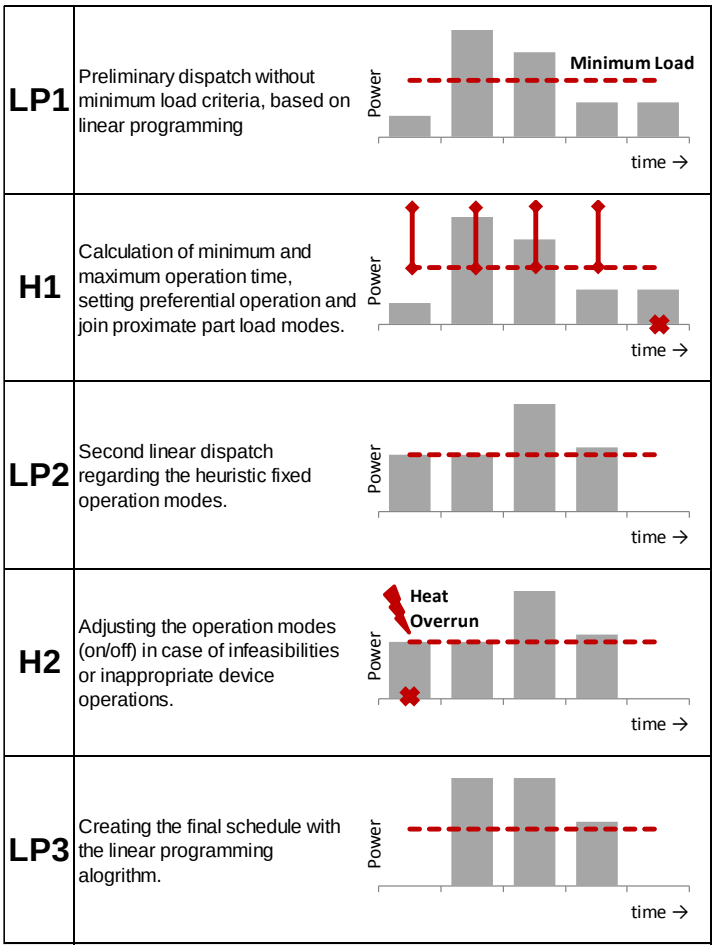

Fig. 89: Illustration of the method of the mixed linear and heuristic approach

The second run of the LP optimization does not hit the minimum load criteria any more, as for all devices and time steps the device is turned off (upper boundary is set to zero for that purpose) or the lower boundary is set to the technical minimum load ("device on").

However, it can happen that in practice, the result of LP2 is not realizable, as the fictitious energy sources and sinks are dispatched in certain time steps. A following heuristic step analyzes these infeasibilities or improper boiler operations and adjusts the operation pre-set. The final LP optimization LP3 then can find solutions, which come without heat over- or underproduction.

The outlined method is suitable both, for heat and electricity led day-ahead planning, as both modes differ only by the used marketing prices of trading electricity – constant prices cause a heat led operation in the simulation.

Additional detail may also be found in [96]

Summary

Dispatching virtual power plants results in special demands regarding the optimization algorithm. The common approach established for conventional power plants is usually based on MILP. The implemented reference algorithm does not perform sufficiently for productive usage of a VPP. A higher number of devices with similar technical and economical parameters slow down the solution process. The developed alternative algorithms lead to a faster solution, but achieve minor power trading revenues. It appears that none of the investigated approaches fits best to all criteria.

The MILP method leads to best solution quality and trading revenues. The disadvantages are the long calculation times and the unsteady operation characteristics. The latter can be reduced by introducing additional constraints such as minimum down time, minimum up time, start-up costs and load changing costs. Without these constraints the schedule shows many start and stop operations, especially in transition times. The calculation time is sensitive to the number of devices with similar producing costs, as they determine the flatness of the solution tree.

Applying the alternative approach based on pure heuristic algorithms yields shorter and model parameter independent calculation times. The VPP is operated steadily without additional constraints. On the other hand; trading results are lower than in the MILP solution. This disadvantage is serious as the profitability of VPPs with today's German electricity market prices is marginal.

The third investigated approach combines a heuristic and a linear programming method. The steady operation schedule and the short calculation time, which is achieved by avoiding integer variables in the linear programming, are the advantages of this concept. The day-ahead results do not reach to MILP level, but the LPH approach is promising as it can be developed towards optimized revenues in further steps.

2.4.2 Control Strategies for Cogeneration Systems with Lithium-Ion Batteries (National Research Council Canada)

Introduction

Lithium ion batteries at ratings around a 2 kW/6 kWh level are expected to play a role for residential power supply and storage. It is envisioned that they can provide some economic benefit under time-of-use (TOU) pricing structures. Storing energy can also reduce peak power demands as well as offset costly infrastructure upgrades to electrical power grid networks. [97]

Micro-cogeneration devices are making inroads for electricity generation at the residential level. These devices include internal combustion engines (ICE), solid oxide fuel cells, proton exchange membrane fuel cells, or Stirling engines. They typically generate less than 15kW of electricity and are located within the household. When producing electricity alone, micro-cogeneration devices yield poor efficiencies, however when configured in systems that recover thermal energy generated in the electrical conversion process, the efficiency can rise to over 80%, referenced to the higher heating value of the fuel. [98]

Annex 42 of the International Energy Agency's Programme on Energy Conservation in Building and Community Systems (IEA/ECBCS) was focussed on reducing residential electric demand using micro-cogeneration devices through study with whole-building computer simulation software. [99]

A residential micro-cogeneration system consisting of a CHP unit, PV panels and a Li-ion storage battery will be simulated here under various scenarios, in order to gain insight and make recommendations for suitable large-scale battery sizes and architecture for overall energy use efficiency.

The quest for higher energy/power density lithium batteries has led to research on higher voltage cathode materials to replace the commonly used $LiMO_2$ (M = Co and Ni) and $LiMn_2O_4$ A common mixed metal spinel, LiNMC is the cathode material in the battery pack prototype developed by Electrovaya, which is modeled in this study.

NRC laboratories have had success in developing materials that improve battery performance and can enhance residential energy storage (RES) units integrated into micro-cogeneration systems. For comparison, a second cathode material will be considered in this paper, lithium nickel cobalt aluminum oxide ($LiNi_{0.8}Co_{0.15}Al_{0.05}O_2$ or NCA). It is a leading candidate for lithium-ion batteries due to its high capacity and durability. The nominal voltage is 3.7 V, and the material capacity is in the 150 to 180 mAh/g range. [100] NCA is less common in the consumer market, but is often found in the automotive industry.

Battery Cell Model

In a lithium-ion battery, lithium is stored or removed from the active cathode and anode materials by diffusing through micron-scale spherical electrode particles. This step is driven by the intercalation current and can be described by a transient spherical diffusion equation:

$$\frac{\partial c_i}{\partial t} = \frac{D_i}{r^2}\frac{\partial}{\partial r}\left(r^2\frac{\partial c_i}{\partial r}\right) \tag{72}$$

$i = (pos,neg)$

where c_i is the concentration of lithium inside the spherical particle, r is the radial position inside the spherical particle and D_i is the solid phase diffusion coefficient in electrode i (either positive or negative). Eq. 1 has boundary conditions:

$$D_i\frac{\partial c_i}{\partial r} = -J_i \tag{73}$$

at $r = Rp$

$$D_i\frac{\partial c_i}{\partial r} = -J_i\frac{\partial c_i}{\partial r} = 0 \tag{74}$$

at $r = 0$

where J_i is the intercalation current density at the surface of the particle, described by Butler-Volmer kinetics:

$$J_i = i_{0,1}\left[\exp\left(\frac{\alpha F}{RT}\eta_i\right) - \exp\left(\frac{-\alpha F}{RT}\eta_i\right)\right] \quad (75)$$

and the exchange current density is,

$$i_{0,1} = Fk_{ct,i}\left(C_{max,i} - \theta_i C_{max,i}\right)^{0.5}\left(\theta_i C_{max,i}\right)^{0.5} C_e^{\,0.5} \quad (76)$$

where k_{ct} is the rate of the electrochemical reaction, C_{max} is the maximum concentration of lithium that can be stored in the active material, θ is the electrode state-of-charge (SOC) and C_e is the lithium salt concentration (mol m-3).

The intercalation current density is related to the applied current and the internal surface area of the electrode,S_i. Thus, $J_i = I_{tot}/S_i$. With this definition, the electrode overpotential, η_i, can be solved in Eq. (75) to calculate the electrode potentials:

$$\phi_{1,i} = \eta_i + \phi_2 + E_{ref,i} + J_i R_{film,i} \quad (77)$$

where $R_{film,i}$ is the film resistance on the electrode particle, and $E_{ref,i}$ is the reference potential of the electrode. Subscript i refers to either the positive or negative electrode.

The cell voltage is then simply defined as the difference between the positive and negative electronic phase potentials:

$$V = \phi_{1,p} - \phi_{1,n} \quad (78)$$

Full detail is given in [101], and further general description of the single particle model is available in [102, 103]. The single particle model assumes that the majority of the cell polarization is attributed to the lithium diffusion in the active material particle and the kinetics of the charge transfer reaction. In such circumstances, the gradient in the electrolyte concentration and ionic phase potential can be assumed to be negligible, allowing for spatial distributions within the cell layer to be treated as uniform.

Battery Energy-Use Model

Battery charge and discharge processes can be represented empirically with a lumped capacitance assumption and state variables [104]. This approach uses a reference curve based on data fit to a polynomial curve for battery depth of discharge (DOD) as a function of open-circuit voltage (OCV). This approach scales the reference curve by factors which depend on the battery current and temperature, and are unique to each battery chemistry. Output from the electrochemical battery cell model is used to characterize this energy-use model.

The voltage during discharging is given by:

$$V(t,DOD, I(t)) = OCV(DOD) - I(t)R_{int}(DOD) \quad (79)$$

where I(t) is the current (amperes) and R_{int} is the internal resistance (ohms). At different currents, there is a shift of the voltage as a function of DOD, equal to the internal resistance multiplied by the current. Simulations in energy use simulation occur at discrete time-steps in a quasi-steady-state manner within the time interval. The battery current is considered constant over the course of a time-step. Under transient load, the current is updated for the next time-step. At a given DOD, an imposed power load P, where P = IV, determines a required current I(t) based on the cell voltage. Applying this current over a time step will cause a small voltage drop, and correspondingly advance the DOD via:

$$\Delta DOD = \frac{-\Delta t\, I(t)}{\alpha\beta\, cap_{rel}} \quad (80)$$

Numerical implementation of the simulations took place as follows. The single-particle model was run to characterize the cells at different discharge currents (beyond what can be done safely with laboratory measurements). Sets of discharge curves are then curve-fit with the Gao model parameters [104] (α, β, reference capacity) to provide an engineering-type model to be used in the energy use scenario simulations. The single-particle model was programmed using Python and the Scipy [105] and Numpy numerical libraries, while the energy scenarios were run with OpenFOAM software [106] .

Ontario Energy Environment

The province of Ontario in Canada has a TOU pricing scheme for electricity. The details of the scheme are shown below in Table 45. [107]

Table 45: Ontario Time-of-use electricity pricing [11]

Time	Summer (May-Oct)	¢/kWh	Winter (Nov-Apr)	¢/kWh
07h-11h	Mid-peak	9.9	On-peak	11.8
11h-17h	On-peak	11.8	Mid-peak	9.9
17h-22h	Mid-peak	9.9	On-peak	11.8
22h-07h	Off-peak	6.3	Off-peak	6.3

In addition to the TOU rates, there are also delivery fees charged to customers of the grid, encompassing transmission, local delivery, low voltage service and regulatory costs, totalling 4.43 ¢/kWh, as well as a $9.42/month fixed charge. [108]

As of April 2012, there is a feed-in tariff for residentially generated PV electricity. For the case considered here of solar rooftop, the rate is 54.9 ¢/kWh. Full details of the program are available in [109]. For the moment, the Ontario PV feed-in is so generous, that the only real sensible action is to sell PV power to grid. It is envisioned however, that in the future, when residential PV becomes more of a standard installation, normal market rates for electricity will apply for smart-metered PV electricity.

In a similar way as with electricity, natural gas is distributed and sold by Ontario utilities. There are gas usage rates as well as delivery and fixed charges for consumers. [110]. As of February 2013, the rates (Enbridge Gas) are \$0.2582 ¢/m^3 and a fixed service charge for customers of \$10/month.

Energy Use Simulations – Components

To demonstrate the capability of the Li-ion model, a detached single-family house located in Ottawa, ON was used. For energy use estimates, it had a floor space of 132 m^2 and a volume of 528 m3. [111]. A weather file of Ottawa, ON from 2008, collected from Environment Canada's Weather Office [112], along with data from [113] were used to produce thermal loads for the house for 10 minute intervals for one year.

A paper presenting new measured data on the electrical consumption of a sample of 12 Canadian houses was used to provide the electrical load profiles. [114] Measurements at 1-min intervals were taken of whole-house electricity draws. These profiles were reintegrated to 10-minute intervals to correspond to the overall data set used in the present paper. The data from house 6 in [114] were used, as the house size corresponded closely to the house size upon which the thermal loads were based.

Photovoltaic data were obtained experimentally on the NRC installation at the Canadian Centre for Housing Technology test house, in Ottawa, Canada. The 2 kW PV system consisted of two strings of 7 amorphous silicon PV laminate, rated 144 W per laminate. The rated efficiency was 6.7%, while the measured efficiency of the installation is 5.3%. The slope of the roof is 34.1°. The system and roof are oriented 13° east of south. Data at 5-minute intervals were taken for a period of more than one year in 2011 and 2012.

The CHP unit included in the model is based on the Aisin Seiki GECC 46 A2, which is rated at an input power of 18.0 kW, with 4.6 kW of electric power output, 11.7 kW of thermal output for efficiencies of ηel of 0.255 and ηth of 0.585. [115] The unit can be operated with natural gas as its fuel.

Table 46: Li-ion battery specifications.

Parameter		***Specifications***
Technology		Lithium Ion SuperPolymer®
Chemistry		MN-Series
Capacity		120 Ah
Energy		6 kWh
Voltage	Max.	56 V
	Nominal	52 V
	Min.	46 V
Charge*	Max.	80 A
Discharge*	Continuous	80 A
	Pulse	130 A (surge)
Operating Temp.		0 to +45 °C
Storage Temp.		-20 to +60 °C
Dimensions		78 x 31 x 44 cm (L x W x H)
Weight		
Shelf Life		> 7 years

* Inverter Limited

The Li-ion battery is based on a prototype residential storage battery made by the Canadian company Electrovaya. It contains LiNMC cells of 37.7 A·h capacity, in a 4-cell parallel, 14-cell series pack architecture. Table 46 outlines the battery specifications.

Plant Configuration

Fig. 90 shows the components included in the MCG simulation, and their connectivity.

The control logic employed in the simulation is straightforward. Scenarios can be considered with the PV and CHP either present or absent. They can also be configured to connect to only the house (electrical load) or to both the house and battery.

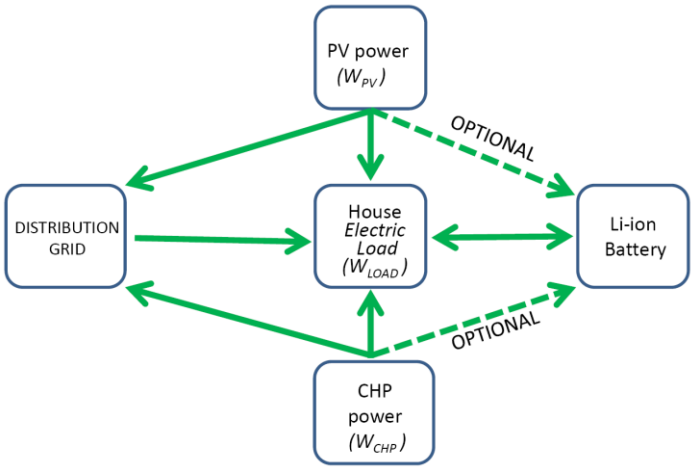

Fig. 90: Components and connections in the energy use simulations.

In general, the battery discharges during the ON-peak TOU period, and will be charged during the MID-peak and OFF-peak periods. If either or both of the PV and CHP produce more power than the house load, during the ON-peak period, the battery could be charged then as well. Fig. 90 depicts the logic flow sheet for this case. The CHP unit is always operated in a thermally led mode. ICE was a suitable CHP technology for Canada, since it can serve a highly variable thermal load, without generating waste heat. Considerable scope exists for developing sophisticated control algorithms for integrated full system optimization.

Results

A number of scenarios were investigated to explore the interplay of the components, and the effects of system configurations and various parameters. In this case, the active components are only the house, grid and battery. For a 6kWh battery in this system, it is sized so that it regularly cycles deeply, which is appropriate. Cost analysis shows that time-shifting with the battery reduces annual electricity costs from $1050 to $1009, requiring the equivalent of 247 battery cycles. When the battery does not simply go from fully charged to discharge, but oscillates in its DOD, the number of equivalent cycles can be defined as:

$$\text{cycles}_{\text{equiv}} = \sum\left(\frac{\Delta DOD}{2}\right) \tag{81}$$

Under the same control scheme Fig. 91 shows the effect of cell capacity on annual cycle requirements, and suggests that cell capacities upwards of 40 A·h will provide the desired 30-year service life. The current LiNMC cells have a capacity of 37.7 A·h.

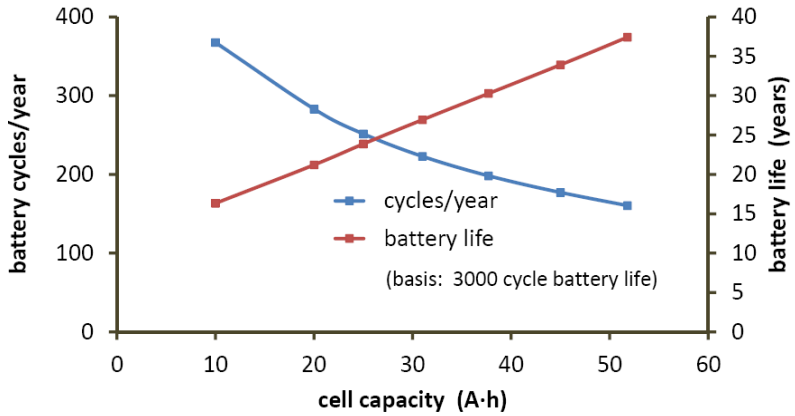

Fig. 91: Annual battery cycles and projected battery life vs. cell capacity.

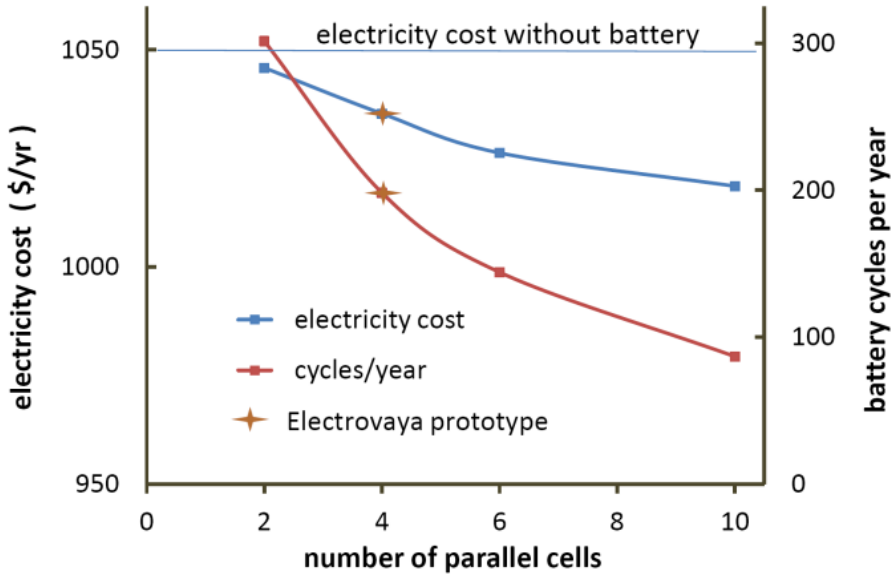

Fig. 92: Annual cost and equivalent cycles vs. number of parallel cells for n ×14 architecture.

Fig. 92 above shows annual costs and the number of equivalent cycles for a battery pack with a varying number of cells in parallel and 14 cells in series. These simulations consider only TOU shifting between the house load, grid and battery. As battery size increases, the cost benefits will level-off and cease to improve.

Many different usage scenarios were simulated with the model described above. This was to provide an overview of the possibilities of configuring a residential system in Ontario with an ICE CHP unit, PV power, a large Li-ion storage battery and interactions with the distribution grid. For cases without CHP, thermal loads were assumed to be handled by a high-efficiency gas-fired furnace, with a 98% thermal efficiency. [116] For the load profiles used for the house in Ottawa, the total annual electricity load was 7328.62 kWh (20.1 kWh/day), and the thermal load was 37487.51 kWh (102.7 kWh/day).

A number of observations can be made upon inspection of these results. In general, the TOU schemes in Ontario only allow for an insignificant cost savings for a system with only a battery. Under 2007 TOU rates, this scenario was more cost effective than now. [97] A more pronounced difference between ON-peak and OFF-peak prices would be necessary to make such operation more viable.

The PV panels at market electricity rates would cover about 27% of the annual household electricity cost. The PV unit would supply about 30% of the required electricity, but the lost 3% cost comes from grid connection and supply fees.

Given the high winter thermal loads in Canada which become much lower at other times of the year, the ICE CHP unit is a suitable choice for its ability to operate at variable output in a thermal-led mode. Despite requiring natural gas to cover the annual thermal load priced at $1730 (compared to $1090 for a conventional gas-fired furnace), the ICE CHP unit significantly offsets this cost by reducing the electricity cost to under $50/year. The largest operating cost savings are obtained with CHP, PV and the Li-ion battery, but of course, with a much larger capital investment. The control strategy for the battery was to discharge is during ON-peak periods. For comparison, the system was run with discharge during both ON and MID-peak periods. Such a strategy gave small cost benefit at the expense of roughly a 60% increase in battery cycling. Noting this, a simulation was tried with the battery+PV+CHP configuration, that did not allow the grid to charge the battery, giving a total annual cost of $1642, about $100 more than allowing grid charging, but with only 29 cycles required, compared to 45 for the case with the grid helping to charge the battery.

Conclusions

A simulation model has been developed using a two-step approach beginning with a fundamental electrochemical cell model to simulate battery operation for anode, separator and cathode layers used in a residential prototype large-size Li-ion battery supplied be the Canadian company, Electrovaya. These cell discharge curves over a range of currents then provided a framework for producing a simplified lumped capacitance engineering model to serve in energy use simulations for a typical detached house in Ottawa, Canada over a one year period. The household energy system consisted of a grid connection, PV panels, an ICE CHP unit and a Li-ion battery.

The principal benefit in terms of economy was to include the CHP unit, operated in a thermally led manner. In the Canadian context, the cogenerated electricity significantly offset the electrical demand and provided a net annual cost reduction of almost $400 when used alone, and about $600 when used together with PV panels and a battery.

It was also found that use of the battery and the PV panels provided cost benefits independently, but to a lesser degree than the CHP unit. Several control strategies were examined for the energy system. A main finding was that operating cost optimization could be achieved with aggressive use of the battery allowing excess PV or CHP power to charge it during ON-peak and MID-peak TOU periods. In the scope of the annual simulation, the cost savings were in the $20 to $50/yr range, but the number of equivalent battery cycles almost doubled in doing so. For the overall conservation of the system, restricting charging in MID-peak and ON-peak periods would be advisable.

For the residential system considered for operation in Ottawa, Canada, the battery pack size of 4 cells in parallel and 14 cells in series with an overall rating of 6 kWh / 2 kW, was found to be good. Simulations

with a hypothetical battery using advanced LiNCA material of higher capacity showed improved performance and less battery cycling.

2.4.3 Optimal Operation of Cogeneration Devices for Imbalance Reduction (KU Leuven, Belgium)

The model performs a mixed integer linear optimization (MILP) that aims to schedule a Virtual power plant (VPP) integrated by several cogeneration devices (CHP). In general, the virtual power plant sales its electricity in the spot market and is part of a balance responsible party (BRP). This entity in Belgium is in charge to keep the balance in its perimeter.

Cogeneration devices

In order to include a cogeneration device in a MILP, it is assumed that the modulation of the cogeneration device is linear and varies between a maximum and minimum operating points. This assumption is valid for most gas engines as shown in Fig. 93. This figure illustrates the steady state characteristics of the Ecopower micro-CHP. which is a gas driven engine that enables full modulation between 1.2 kWe and 4.7 kWe (3.8 to 12.5 kWth) [117]. It shows the linear relationship between electric and primary energy (dashed line) and the electric and thermal energy (full line).

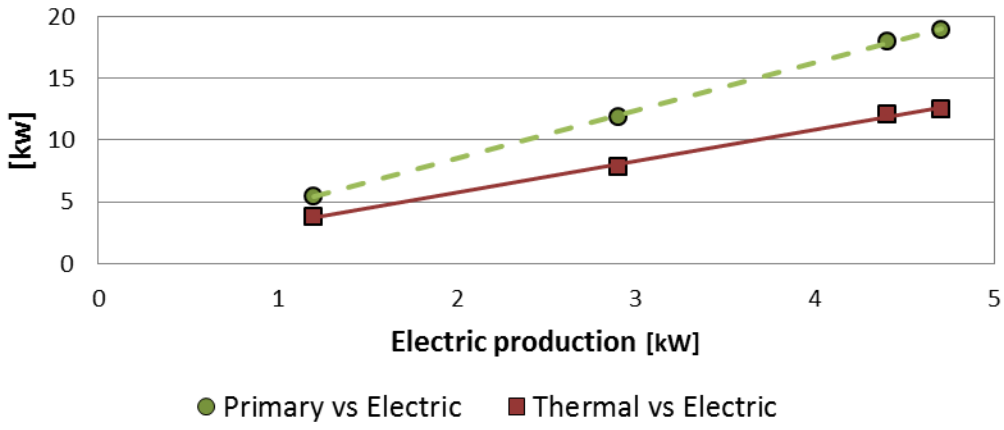

Fig. 93: Technical characteristics of the Micro-CHP Ecopower Plus.

The device exhibits almost linear relationships between the electric and thermal output, as well as between the electric output and the fuel use. These relationships are described in Equations (82) and (83).

$$Q_{prim} = 3.87 \cdot E_{chp} + 0.79 * ON \quad (82)$$

$$Q_{chp} = 2.54 \cdot E_{chp} + 0.68 * ON \quad (83)$$

Where Q_{chp} and E_{chp} denote the heat production and electricity produced by the CHP respectively. Q_{prim} is the primary energy consumption and ON is an integer variable that indicates the on/off status of the device.

Rolling horizon approach

The optimization was performed in a rolling horizon approach. In a first step the making use of the forecasted variables (e.g. solar prediction, spot price forecast etc.) a first optimization is performed to decide the amount of electricity bided in the day-ahead market in the next period (e.g. the next 24 hours). Afterwards, at each time step using the actual values the optimization is repeated and only the first step of the simulation is implemented in order to account for the difference between the forecast and the actual values, depicted in Fig. 94.

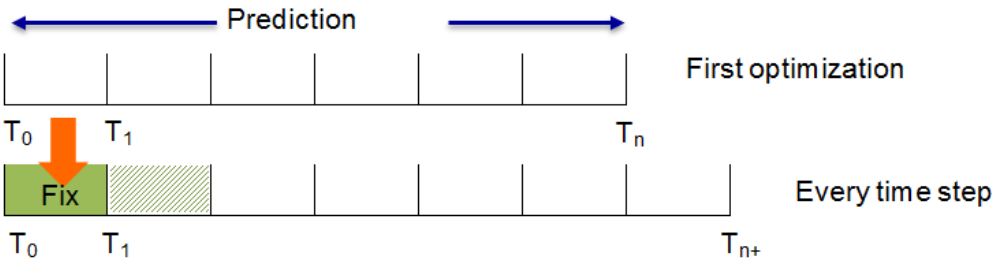

Fig. 94: Rolling horizon approach.

First optimization algorithm - Cost minimization

The objective of the cost optimization algorithm is to minimize the operational cost of the system as expressed in equation (84) and extended in equation (85). The operational cost is the sum of the fuel cost of the CHPs and boilers (CCHP, C_{boiler}).On the other hand, the savings(G) can include the revenues due to the electricity that is sold to the grid and the savings due to the self-consumption of the electricity generated by the CHP (If this last one is considered):

$$min objective\ function = \sum_{t=1}^{T} (Cost(t) - Savings(t)) \quad (84)$$

$$min = \sum_{t=1}^{T} \left(C_{CHP}(t) + C_{boiler}(t) - G(t)\right) \quad (85)$$

The optimization is constrained by several operational and technical conditions. The operational constraints ensure that the heat demand (Q_{demand}) will always be met using the CHP (Q_{chp}), the boiler (Q_{boiler}) or the heat that is (dis)charged from the storage (Q_c). As described in equation 86:

$$Q_{demand}(t) = Q_{chp}(t) + Q_{boiler}(t) + Q_c(t) \quad (86)$$

The state of charge of the storage tank (q_{st}) is calculated using equation (87). The efficiency of the storage tank (η_{st})[1] is assumed to be constant. The analyzed time step (Δt) is 15 minutes:

$$q_{st}(t) = (\eta_{st}) * q_{st}(t-1) - Q_c * \Delta t \quad (87)$$

On the other hand, some technical restrictions prevent to exceed the operational limits of the machines. These are expressed in equations (88) – (91) for the storage, the boiler and the CHP respectively:

$$0 \leq q_{st}(t) \leq q_{st\_max} \quad (88)$$

$$0 \leq Q_{boiler}(t) \leq Q_{boiler\_max} \quad (89)$$

$$Q_{chp\_min} \leq Q_{chp}(t) \leq Q_{chp\_max} \quad (90)$$

$$E_{chp\_min} \leq E_{chp}(t) \leq E_{chp\_max} \quad (91)$$

Other technical constraints control the minimum start up time of the CHP device. This is performed as in [119] and it is important to consider in order to avoid wearing out of the machine.

As no heat connection exist between the houses, each system has to satisfy its individual heat demand; thus, equations (82) – (85) and (88) – (91) apply to every individual CHP. On the contrary, the electric demand is the aggregated electric demand of the houses. Therefore, the electricity generated by the CHP (E_{chp}) is equal to the sum of the individual production of each CHP device:

$$E_{CHP}(t) = \sum_{j} E_{chp}(j,t) \quad (92)$$

Second optimization algorithm- Imbalance reduction

Two different approaches are evaluated at this point. The first concept aims to reduce physical imbalance anytime this implies to attach as much as possible to the schedule proposed the day ahead. The second approach aims to offer a service to a balance responsible party[2] (BRP) to reduce their imbalance.

[1] The efficiency of the storage tank represents the percentage of heat that remains in the storage after it has been stored during one time step.

[2] Balance Responsible party is responsible for keeping the balance between injections and off-takes in its perimeter for each time period meaning.

VPP Physical imbalance reduction

In this case the objective function of the second optimization problem is to minimize the imbalance error. As stated in equation 93, this is the difference between the real output ($P_{el}(t)$) and the forecasted output ($\bar{P}_{el}(t)$). This optimization is performed every time step once the real PV output is obtained.

$$\boldsymbol{objective = min \sum_{t=1}^{T} |P_{el}(t) - \bar{P}_{el}(t)|} \quad (93)$$

Although the objective function is different, the optimization has the same constraints previously explained and described in equations 3-11. Nevertheless, an additional constraint guaranties that the imbalance is always covered either by the actual CHP output (ECHP_Real) or getting the electricity from the balancing market (EImb) as expressed in equation (94)**Fehler! Verweisquelle konnte nicht gefunden werden.**. The variable EImb can be positive or negative depending on the nature of the imbalance error. More information of this approach can be found in [120].

$$\bar{\boldsymbol{P}}_{el}(t) = \boldsymbol{P}_{el}(t) + \boldsymbol{E}_{CHP\_real}(t) + \boldsymbol{E}_{Imb}(t) \quad (94)$$

Imbalance reduction as a service [3]

As explained before this approach assumes that the VPP of aggregated micro-CHPs is used by a BRP to lower the imbalance caused by the BRP and thus lowers the imbalance tariff that Elia applies to this BRP.

Thus an extra profit can be obtained by taking into account the total system imbalance (I_{tot}) and driving the vpp imbalance in the right direction.

$$\Delta P_{el}(t) = P_{el}(t) - \bar{P}_{el}(t) \quad (95)$$

In other words the sum of all CHPs will be regulated in the direction required by the TSO. This means that if there is a deficit in the system balance $\Delta P_{el}(t)$ should be positive (upward regulation), on the other hand if the system has a surplus downward regulation is required. This is guaranteed using equation (96).

$$\boldsymbol{\Delta P_{el}(t) = 0 \; or \; sign(\Delta P_{el}(t)) = -sign(I_{tot}(t))} \quad (96)$$

The objective function is described in equation 97, it aims to maximize the extra-profit obtained which is given by equation where p_{imb} indicates the imbalance price and $\Delta F(t)$ is the extra expenditure or saving in fuel cost of a particular CHP in the aggregator. Note that if supporting policies such as green certificates that are given to CHP producers are taken into account, they should be summed up in this equation

[3] Authored by Ruben Doncel, Jens van Engeland, Juliana Zapata and William D'haeseleer

$$objective = max \sum_{t=1}^{T} (\Delta P_{el}(t) \cdot p_{imb} - \Delta F(t)) \quad (97)$$

This approach guaranties that the imbalance service will be provided only if it is profitable for the VPP to do so this is the main advantage compared to the previous approach.

As well as in the previous cases the technically and operational constraints stated in equations 1-10 are applied. Further information of this model can be found in [121]

2.5 General Model Simplification

In a more general vein, work has been undertaken to simplify the parameter requirements [122] when employing the Annex 42 approach. IEA/ECBCS Annex 42 produced a zero-order model for simulating the performance of combustion-based micro-cogeneration devices within whole-building simulation programs. This model had been previously calibrated by Annex 42 participants to represent the performance of one particular SE micro-cogeneration device and its validity was partially assessed using a limited set of empirical data.

A study was undertaken to critically assess and improve the Annex 42 model for combustion-based micro-cogeneration devices. An extensive experimental data set that was collected specifically for the purposes of improving this model. These experimental data were gathered from a prototype SE micro-cogeneration device with a net electrical output of 750 W and a thermal output of 5 kW. Measurements of parameters that were critical for model calibration and validation were recorded at 10-second intervals. The test matrix, based upon the Annex 42 experimental protocol, included several 30-minute-long experiments under steady-state conditions. These experiments spanned a range of cooling water flow rates and engine inlet temperatures in order to produce a data set suitable for critiquing the functional form of the steady-state efficiency performance equations of the Annex 42 model. The new data set also includes start-up and shut-down modes of operation used to assess the Annex 42 model's treatment of transient states.

Based upon the experimental observations, a new "linear difference" formulation was proposed as a replacement to the steady-state efficiency equations in the Annex 42 model. This is found to be more representative of actual engine behaviour, requires fewer experiments to calibrate, provides transparent results, is less sensitive to erroneous calibration data, and provides greater accuracy between calibration points.

The new experimental data have verified the appropriateness of the Annex 42 model's treatment of the fuel flow during shut-down. However, observations based upon these same data have resulted in proposed changes to the treatment of electrical production during both start-up and shut-down. Specifically, new functional formulations were put forward for these transient modes of the Annex 42 model.

It must be noted that these proposed improvements to the Annex 42 model are based upon data gathered from a single prototype SE micro-cogeneration device. The general applicability of the proposed changes should be tested using experimental data from other SE and ICE micro-cogeneration devices.

These proposed model improvements have been implemented into a developmental version of the ESP-r simulation program. Furthermore, the data sets gathered in this work have been used to calibrate the improved Annex 42 model and to validate its implementation into ESP-r.

3 Overview and Concluding Remarks

The present Annex 54 is the successor of Annex 42, which was focussed on demonstrating the benefits of combined heat and power on a residential scale along with developing standardized models of micro-cogeneration equipment in order to raise the profile of the promising technologies and thereby facilitate its uptake, reputation and regulatory support. Annex 42 ended in 2008 and in the present Annex 54, the focus has visibly shifted to research dealing with a more mature technology, and the attendant challenges in ensuring and enabling its adoption, reliability and versatility. In terms of prime movers, the set of devices has remained the same since Annex 42. What has evolved however is the attention given by the research community to the large range of auxiliary devices that have been incorporated into residential micro-CHP systems. This evolution has been in recognition of the requirements for overall energy-use efficiency for residences, and the understanding that variability in climate, political and energy contexts all play a key role in determining the most cost-effective ways in which to design and implement micro-CHP systems. Since Annex 42, there has been a significant emphasis placed on energy storage, as optimizing efficiency with either a thermally-led or electrically-led system naturally leads to situations where the temporal load demands of one of the forms of energy results in the production of an excess of the second form. Very significant benefits have been shown to arise from incorporating energy storage units into balance-of-plant configurations. Table 47 summarizes the progress in terms of residential energy equipment considered over the course of these two succeeding IEA Annexes.

Given the shift in emphasis from the individual components used in CHP from Annex 42 to system design and configuration in Annex 54, the interplay and compatibility of devices has become an important research topic. In view of this, the subsection 2.4 of section 2 of this report was focussed on control logic and systems for micro-cogeneration. It has also become evident that the scale of the CHP system is critical in determining is economic viability. For example, a study was included here on energy storage with batteries, where sizing the battery pack was a key research objective. Further, it has become evident that single residence applications may restrict the benefits of a broader implementation of micro-cogeneration. In view of this, systems are beginning to be considered on a community or shared level, and the logistics and control of such systems are introduced in this report with work done by the participating group from Japan. Beyond this, the subject of incorporating micro-cogeneration systems into trading schemes via virtual power plants is also being studied.

The evolution towards a higher level view of CHP components as part of energy use systems is also reflected by the accompanying large recent increase in activity in the area of supporting governmental policy instruments being enacted to support adoption of these technologies. Information on developments in this area can be found in the Annex 54 report from Subtask C “A Comparative Review of Microgeneration Policy Instruments in OECD Countries”.

The material covered and presented in this reports reflects the recent research focus of groups active in the micro-cogeneration sector, responding to the current understanding that benefits from adoption of CHP prime movers are best obtained with a measured system design that accounts for local environmental, housing, energy context and political factors. As such, modeling efforts have moved to include modules on the conventional modeling platforms such as ESP-r, Trnsys and Energy Plus reflecting the operation and performance of a large number of additional energy storage, heating and cooling devices.

Table 47. List of equipment modeled in Annex 42 and Annex 54.

Annex 42 prime movers modeled	Annex 54 prime movers modeled	Annex 54 auxiliary devices modeled
Fuel cell	Fuel cell	lithium ion battery
Stirling engine	Stirling engine	absorption chiller
Internal combustion engine	Internal combustion engine	desiccant wheel
		solar cooling
		photovoltaic panels
		ground source heat pump
		air source heat pump
		distributed storage systems
		hybrid system with electric vehicle
		thermal storage
		thermal storage with phase change materials

Appendix

The Results of KIER Air to Air Heat Pump Testing

Table 48: Test results of KIER Heat Pump - heating mode

Condensing Temp. (C)	Evaporating Temp. (C)	Indoor Inlet Temp. (C)	Indoor outlet temp. (C)	Outdoor inlet temp. (C)	Outdoor outlet temp. (C)	P.comp (W)	COPh
33.56	6.25	21.13	29.77	10.06	6.62	0.65	3.31
33.74	6.44	21.28	30.01	10.34	6.89	0.65	3.33
34.19	6.97	21.41	30.35	11.93	7.78	0.66	3.36
34.48	7.62	21.40	30.70	14.10	9.03	0.66	3.47
34.80	8.27	21.33	30.96	15.87	10.12	0.68	3.52
34.98	8.37	21.38	31.06	16.25	10.35	0.68	3.53
35.39	8.93	21.41	31.43	17.45	11.17	0.69	3.62
35.68	9.17	21.67	31.77	17.96	11.46	0.69	3.62
36.08	10.13	21.47	32.13	20.70	12.86	0.69	3.81

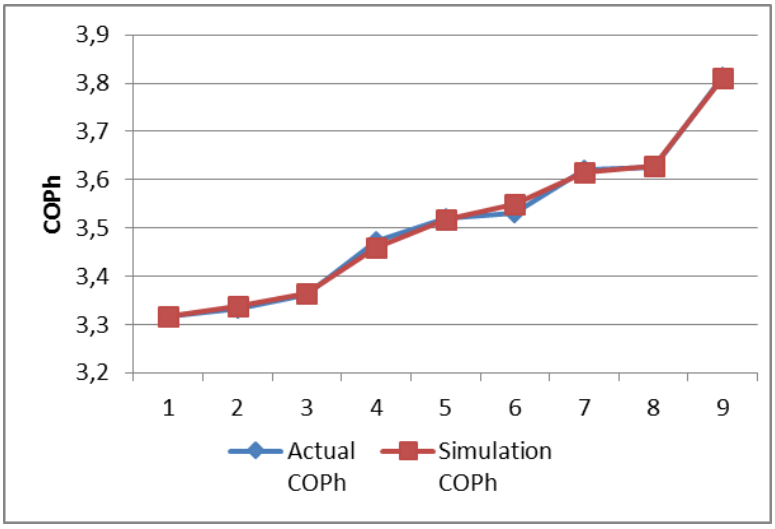

Fig. 95:

Table 49: Test results of KIER Heat Pump - cooling mode

Condensing Temp. (C)	Evaporating Temp. (C)	Indoor Inlet Temp. (C)	Indoor outlet temp. (C)	Outdoor inlet temp. (C)	Outdoor outlet temp (C)	P.comp (W)	COPc
34.49	9.81	19.82	12.42	18.66	29.86	0.68	2.71
38.61	10.68	19.69	12.88	26.13	35.46	0.72	2.34
40.23	11.37	20.16	13.43	28.21	37.52	0.74	2.25
40.12	11.08	20.03	13.24	28.37	37.52	0.74	2.27
41.39	11.71	20.22	13.67	29.69	38.82	0.76	2.14
41.23	11.63	20.27	13.69	29.85	38.85	0.76	2.15
42.47	11.75	20.37	13.87	32.12	40.60	0.77	2.09
43.54	12.06	20.40	14.10	33.90	42.01	0.79	1.98
43.64	12.09	20.39	14.08	34.09	42.14	0.79	1.99
44.58	12.23	20.51	14.22	35.98	43.57	0.80	1.95

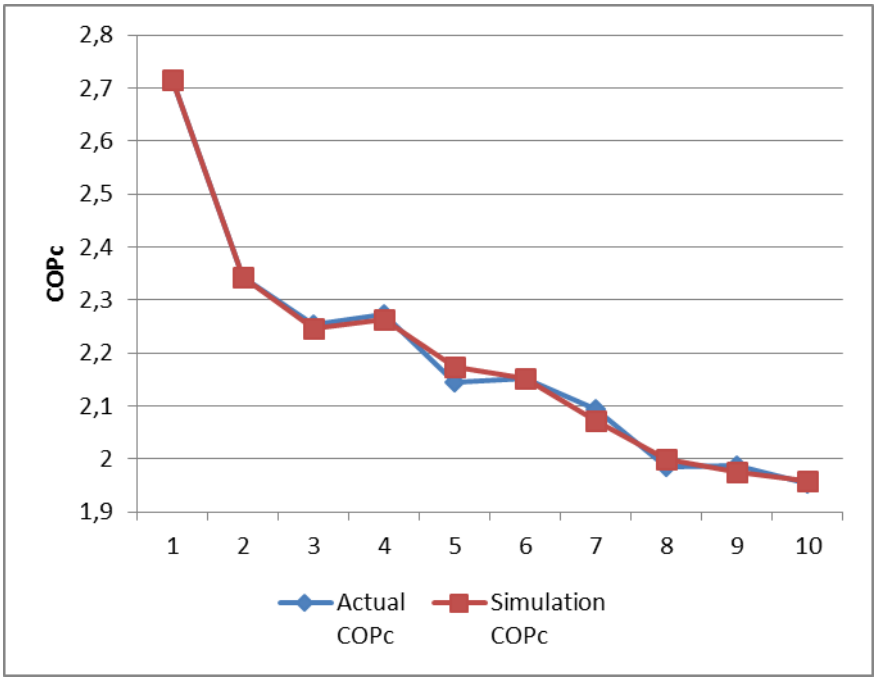

Fig. 96:

References

[1] Kelly N. and Beausoleil-Morrison I., Editors (2007), Specifications for Modelling Fuel Cell and Combustion-Based Residential Cogeneration Devices within Whole-Building Simulation Programs, IEA/ECBCS Annex 42 Report, ISBN No. 978-0-662-47116-5.

[2] A Ferguson, N Kelly, A Weber, B Griffith, Modelling residential-scale combustion-based cogeneration in building simulation, Journal of Building Performance Simulation, 2 [1] (2009) 1-14.

[3] I Beausoleil-Morrison, K Lombardi, The calibration of a model for simulating the thermal and electrical performance of a 2.8 kW_{AC} solid-oxide fuel cell micro-cogeneration device Journal of Power Sources, 186 [1] (2009) 67–79.

[4] http://www.trnsys.com/ (TRNSYS website).

[5] Thorsteinson, E., Performance Testing of a 1kWe PEM Fuel Cell Cogeneration System, MICRoGen'II, 2nd Internation Conference Microgeneration and Related Techenologies, Glascow, April, 2011.

[6] Kelly, N., Beausoleil-Morrison, I. 2007. Specifications for Modelling Fuel Cell and Combustion-Based Residential Cogeneration Devices within Whole-Building Simulation Programs, IEA/ECBCS Annex 42 report [online], ISBN No. 978-0-662-47116-5. Available from: http://www.ecbcs.org/annexes/annex42.htm.

[7] University of Wisconsin-Madison, TRNSYS 17 - Mathematical Reference, Vol. 4.

[8] Kelly, N.J. and Cockroft, J. (2010) Analysis of retrofit air source heat pump performance: Results from detailed simulations and comparison to field trial data. Energy and Buildings . ISSN 0378-7788

[9] Ferguson A, Kelly N J, Weber A, Griffith B, (2009) 'Modelling Residential-Scale Combustion-Based Cogeneration in Building Simulation', Journal of Building Performance Simulation, 2(1), pp1-14.

[10] Clarke, J.A. (2001), 'Energy simulation in building design'. 2nd Edition ed., Oxford: Reed Educational and Professional Publishing Ltd.

[11] Hawkes A, Leach M (2005) 'Impact of Temporal Precision in Optimisation Modelling of Micro-Combined Heat and Power, Energy, 30(10), 1759-1779.

[12] Johnson G, Beausoleil-Morrison I, Strathearn B, Thorsteinson E, and Mackintosh T. "The calibration and validation of a model for simulating the thermal and electrical performance of a 1 kW proton-exchange membrane fuel-cell micro-cogeneration device." Journal of Power Sources, (2013): 435-446.

[13] Kelly N and Beausoleil-Morrison I (Eds.), Specifications for Modelling Fuel Cell and Combustion-Based Residential Cogeneration Devices within Whole-Building Simulation Programs (2007), ISBN 978-0-662-47116-5. IEA/ECBCS Annex 42 Report.

[14] Beausoleil-Morrison I, and Lombardi K. "The calibration of a model for simulating the thermal and electrical performance of a 2.8 kWAC solid-oxide fuel-cell micro-cogeneration device." Journal of Power Sources, (2009): 67-79.

[15] J. P. Holman, Heat tansfer. New York: McGraw-Hill Companies, 1997.

[16] University of Strathclyde, The ESP-r system for building energy simulations: user guide version 9 series, ESRU Manual U00/1, 2000.

[17] K. Darcovich, “Residential electrical power storage scenario simulations with a large-scale lithium ion battery,” Journal of Applied Electrochemistry, vol. 40, no. 4, pp. 749–755, 2010.

[18] H. Ribberink and W. Wang, “Improving ESP-r’s battery model with active battery life control and coverage of vanadium redox flow batteries,” Proceedings eSim2008 Conference, 2008.

[19] P. Pinel, “Immosolars battery model: Battery and thermal management system,”tech. rep., Immosolar ABT, Santa Ponsa, Spain, 2006.

[20] M. W. Verbrugge, “Electrochemical and thermal characterization of battery modules commensurate with electric vehicle integration,” Journal of the Electrochemical Society, vol. 149, no. 1, p. A45, 2002.

[21] B. Y. Liaw, “Modeling of lithium ion cells - a simple equivalent-circuit model approach,” Solid State Ionics, vol. 175, no. 1, pp. 835–9, 2004.

[22] L. Gao, S. Liu, and R. Dougal, “Dynamic lithium-ion battery model for system simulation,” IEEE Transactions on Components and Packaging Technologies,vol. 25, no. 3, pp. 495 – 505, 2002.

[23] Knight I, Ugursal I, Residential cogeneration systems: A review of the current technologies. IEA/ECBCS Annex 42; 2005.

[24] Beausoleil-Morrison I, An Experimental and Simulation-Based Investigation of the Performance of Small-Scale Fuel Cell and Combustion-Based Cogeneration Devices Serving Residential Buildings. IEA/ECBCS Annex 42 Report; 2008.

[25] Scrosati B, Garche J, Lithium batteries: Status, prospects and future. J Power Sources 2010; 195:9 2419-2430.

[26] Saldanha N, Beausoleil-Morrison I, Measured end-use electric load profiles for 12 Canadian houses at high temporal resolution, Energy and Buildings 2012; 49 519-530.

[27] Acquati A, APS to test energy efficient substation in Flagstaff, Northern Arizona News March 20, 2012.

[28] DasGupta R, Substation Installations of Electrovaya's MWh-Scale Lithium-Ion SuperPolymer®. Batteries for Smart Grid Applications. PRiME 2012, 222nd Meeting of the Electrochemical Society, 2012 Oct 7-12; Honolulu, Hawaii.

[29] Duncan H, Abu Lebdeh Y, Davidson IJ, Study of the CathodeElectrolyte Interface of LiMn1:5Ni0:5O4 Synthesized by a Sol-Gel Method for Li-ion Batteries. J Electrochem Soc 2010; 157:4 A528-A535.

[30] Cho Y, Cho J, Signi_cant Improvement of LiNi0:8Co0:15Al0:05O2 Cathodes at 60C by SiO2 Dry Coating for Li-ion Batteries. J Electrochem Soc 2010; 157:6 A625-A629.

[31] Barnett B, Rempel J, Ofer D, Oh B, Sriramulu S, Sinha J, et al, PhEV Battery Cost Assessment. DOE Hydrogen Program and Vehicle Technologies Program Annual Merit Review and Peer Evaluation Meeting, 2010 Jun 7-11; Washington, DC.

[32] Strachan PA, Kokogiannakis G, Macdonald IA, History and development of validation with the ESP-r simulation program. Building and Environment 2008; 43:[4] (2008) 601-609.

[33] Ramadass P, Haran B, White R, Popov BN, Capacity fade of Sony 18650 cells cycled at elevated temperatures: Part I. Cycling performance. J Power Sources 2002; 112:2 606-613.

[34] Natural Resources Canada. Energy use data handbook 1990 to 2007. Ottawa, 2009. Available from: http://oee.nrcan.gc.ca/publications/statistics/handbook09/pdf/handbook09.pdf

[35] A. Ferguson, "Modelling residential-scale combustion-based cogeneration in building simulation," Journal of building performance simulation, vol. 2, no. 1, pp. 1–14, 2009.

[36] Saldanha N, Towards the assessment of a residential electric storage system: analysis of Canadian residential electricity use and the development of a lithium-ion battery model [dissertation]. Ottawa (ON): Carleton U; 2010.

[37] Divya KC, Østergaard J, Battery energy storage technology for power systems An overview. Elec Power Sys Res 2009; 79:4 511-520.

[38] G. Angrisani, A. Capozzoli, F. Minichiello, C. Roselli, M. Sasso, Desiccant wheel regenerated by thermal energy from a microcogenerator: experimental assessment of the performances, Applied Energy 88 (2011) 1354-1365.

[39] G. Angrisani, C. Roselli, M. Sasso, F. Minichiello, Experimental analysis on the dehumidification and thermal performances of a desiccant wheel, Applied Energy 92 (2012) 563–572.

[40] G. Angrisani, C. Roselli, M. Sasso, Effect of rotational speed on the performances of a desiccant wheel, Applied Energy 104 (2013) 268–275.

[41] G. Angrisani, P. Bareschino, C. Roselli, F. Pepe, M. Sasso, Analysis of thermal and dehumidification performances of a silica-gel desiccant wheel regenerated with a low-temperature medium, Microgen III Conference, Proceedings of The 3rd edition of the International Conference on Microgeneration and Related Technologies (Naples, Italy, April 15-17, 2013), ISBN: 9788890848902.

[42] G. Angrisani, C. Roselli, M. Sasso, Experimental validation of constant efficiency models for the subsystems of an unconventional desiccant-based Air Handling Unit and investigation of its performance, Applied Thermal Engineering 33-34 (2012) 100-108.

[43] S.A. Klein, A Design Procedure for Solar Heating Systems, Ph.D. Thesis, Department of Chemical Engineering, University of Wisconsin-Madison, 1976.

[44] B.J. Newton, Modeling of Solar Storage Tanks, M.S. Thesis, Department of Mechanical Engineering, University of Wisconsin-Madison, 1995.

[45] Caresana F., Brandoni C., Feliciotti P., Bartolini C.M.(2011). Energy and economic analysis of an ICE-based variable speed-operated micro-cogenerator; APPLIED ENERGY 88(3); pp. 659-671. ISSN: 0306-2619, doi:10.1016/j.apenergy.2010.08.016

[46] A. Ferguson, N. Kelly, A. Weber, B. Griffith, Modelling residential-scale combustion-based cogeneration in building simulation, J. Build. Perform. Simul. 2 (2009) 1–14.

[47] N. Kelly, I. Beausoleil-Morrison, Specifications for modelling fuel cell and combustion-based residential cogeneration devices within whole-building simulation programs, IEA/ECBCS Annex 42 report, 2007.

[48] A. Rosato, S. Sibilio, Calibration and validation of a model for simulating thermal and electric performance of an internal combustion engine-based micro-cogeneration device, Applied Thermal Engineering 45-46 (2012) 79-98.

[49] A. Rosato, S. Sibilio, Energy performance of a micro-cogeneration device during transient and steady-state operation: experiments and simulations, Applied Thermal Engineering, 52 (2013) 478–491.

[50] AISIN SEIKI, TECNOCASA CLIMATIZZAZIONE, <www.tecno-casa.com/EN/Default.aspx?level0=prodotti&level1=mchp> (retrieved on 13/12/2012).

[51] Solar Energy Laboratory, TRNSYS 16, A transient system simulation program, Tech. rep., University of Wisconsin, Madison, USA, 2004.

[52] G. Angrisani, A. Rosato, C. Roselli, M. Sasso, S. Sibilio, Experimental results of a micro-trigeneration installation, Applied Thermal Engineering 38 (2012) 78-90.

[53] I. Beausoleil-Morrison, Experimental Investigation of Residential Cogeneration Devices and Calibration of Annex 42 Models, IEA/ECBS Annex 42, 2007.

[54] N. Rossi, Manuale del Termotecnico, Second Edition, HOEPLI, 2007.

[55] GenOpt, <http://simulationresearch.lbl.gov/GO/> (retrieved on 13/12/2012).

[56] eERG, MICENE: MIsure dei Consumi di ENergia Elettrica nel settore domestico, 2006 <http://www.eerg.polimi.it/micene.php> (retrieved on 2011-11-23).

[57] I. Bertini, F. Ceravolo, M. De Felice, B. Di Pietra, F. Margiotta, S. Pizzuti, G. Puglisi (2009) Sviluppo dell'ambiente di progettazione Optimal DESign for Smart Energy – ODESSE, RICERCA SISTEMA ELETTRICO (in Italian).

[58] J. A. Duffle, W. A. Beckman (2006), Solar Engineering of Thermal Process, John Wiley & Sons Inc.

[59] M. Badami , A. Portoraro (2011), Micro-trigenerazione nel settore residenziale con l'utilizzo di motori a combustione interna: sviluppo di un modello matematico di un assorbitore a bromuro di litio, RICERCA SISTEMA ELETTRICO (in Italian).

[60] L. Pistocchini, L. Colasuonno, M. Aprile (2009), Modelli Simulink per la simulazione dei moderni impianti di solar cooling: collettori e chiller, RICERCA SISTEMA ELETTRICO (in Italian).

[61] I. Bertini, L. Castellazzi, F. Ceravolo, B. Di Pietra, A. Federici, R. Iannucci, F. Margiotta, A. Pannicelli, G. Puglisi (2011), Integrazione di layout impiantistici nella piattaforma di simulazione ODESSE (Optimal DESignfor Smart Energy), RICERCA SISTEMA ELETTRICO (in Italian).

[62] D. Thevenard, K. Haddad, Development of a stratified tank model with immersed heat exchangers in ESP-r, eSim 2010 Conference, Winnipeg, Canada, May 19-20, 2010

[63] Voller V.R. An Overview of numerical Methods for Solving Phase Change Problems, in Advances in Numerical Heat transfer, W.J. Minkowycz E.M. Sparrow Editors, Taylor & Francis, Washington, DC, 1997, 341-380

[64] Heimrath, H. Haller, M., The Reference Heating System, the Template Solar System, Report A2, of IEA Solar Heating and Cooling programme - Task 32, "Advanced storage concepts for solar and low energy buildings", IEA-SHC, 2008 (http://www.iea-shc.org/task32/publications/index.html)

[65] R. Padovan, M. Manzan, Development of a Stratified Tank Storage Component for ESP-r With Embedded Phase Change Material Modules, Proceedings of the Institution of Mechanical Engineers, Part A: Journal of Power and Energy, 2013, vol. 227 no. 1, 53-61

[66] H Ribberink, K Lombardi, LYang, E Entchev, Investigation of a hybrid renewable– microgeneration energy system for power and thermal generation with reduced emissions Proceedings of the Institution of Mechanical Engineers, Part A: Journal of Power and Energy February 2013 227: 62-72.

[67] K Lombardi, MA Douglas, Integrating a Stirling cogeneration appliance with a forced-air furnace. 2nd International conference on microgeneration and related technologies, Glasgow, UK, 4–6 April 2011.

[68] E. Entchev, L. Yang, F. Szadkowski, M. Armstrong, M. Swinton, Application of hybrid micro-cogeneration system—Thermal and power energy solutions for Canadian residences, Energy and Buildings, 60 (2013) 345–354.

[69] E. Entchev, L. Yang, F. Szadkowski, M. Armstrong, M. Swinton, "Application of Hybrid Micro-cogeneration systems – Total Energy Solution for Canadian Residences", International Journal of Energy and Buildings 60(13), 345-354.

[70] H. Ribberink, E. Entchev, Improving micro-cogeneration economics through overnight electric vehicle charging, MicroGen III, Naples, Italy, April 15-17, 2013.

[71] TRNSYS, The Transient Energy System Simulation Tool. Available from http://www.trnsys.com. 2010.

[72] Natural Resources Canada, The Plug-in Electric Vehicle – Charge Impact Model (PEV-CIM), available from www.canmetenergy.nrcan.gc.ca/software-tools/PHEV-CIM/3049.

[73] Saldanha N, Beausoleil-Morrison I, Measured end-use electric load pro_les for 12 Canadian houses at high temporal resolution, Energy and Buildings 2012; 49 519-530.

[74] Numerical Logics. Canadian Weather for Energy Calculations, Users Manual and CD-ROM. Downsview Ontario: Environment Canada, 1999.

[75] A. Rosato, S. Sibilio, Calibration and Validation of a Model for Simulating Thermal and Electric Performance of an Internal Combustion Engine-Based Micro-Cogeneration Device, Applied Thermal Engineering 45-46 (2012) 79-98.

[76] CEC. 2001. A Guide to Photovoltaic (PV) System Design and Installation, California Energy Commission.

[77] NABCEP. 2012. Photovoltaic (PV) Installer Resource Guide, North American Board of Certified Energy Practitioners.

[78] G. Angrisani, Experimental and simulative analysis of a microtrigeneration system based on an air handling unit with desiccant wheel, Ph.D. thesis, University of Naples, 2012;

[79] P. Gonçalves, G. Angrisani, C. Roselli, A.R. Gaspar, M.G. Silva, Energy and exergy-based modeling and evaluation of a micro-combined heat and power unit for residential applications, Microgen III Conference, Proceedings of The 3rd edition of the International Conference on Microgeneration and Related Technologies (Naples, Italy, April 15-17, 2013), ISBN: 9788890848902.

[80] Sänger F., Lipp J., Tzscheutschler P.: Mikro-KWK-Anlagen im Gewerbe (Micro CHP Systems for Commercial Applications). Final report of Bavarian joint reseach project FORETA; Germany 2012

[81] Darcovich K.,Entchev E., et.al.: An International Survey of Electrical and DHW Load Profiles for Use in Simulating the Performance of Residential Micro-cogeneration Systems. ECB Annex 54 report. Canada 2013

[82] Kelly N., Beausoleil-Morrison I., et.al.: Specifications for Modelling Fuel Cell and Combustion-Based Residential Cogeneration Devices within Whole-Building Simulation Programs. ECBCS Annex 42 report; ISBN 978-0-662-47116-5; Canada 2007

[83] Y Shimoda, T Okamura, Y Yamaguchi, Y Yamaguchi, A Taniguchi, T Morikawa, City-level energy and CO2 reduction effect by introducing new residential water heaters, Energy, 35 [12] (2010) 4880-4891.

[84] Y Shimoda, T Asahi, A Taniguchi, M Mizuno, Evaluation of city-scale impact of residential energy conservation measures using the detailed end-use simulation model, Energy, 32 [9] (2007) 1617-1633

[85] Brandoni C., Renzi M., Hybrid renewable energy systems made up of high concentration PV solar technology and micro-CHP. Proceedings of EuroSun2012, ISES Europe Solar Conference, September 18-20, 2012. Rijeka, Croatia, ISBN 978-953-6886-20-3.

[86] Caresana F., Brandoni C., Feliciotti P., Bartolini C.M.(2011). Energy and economic analysis of an ICE-based variable speed-operated micro-cogenerator; APPLIED ENERGY 88(3); pp. 659-671. ISSN: 0306-2619, doi:10.1016/j.apenergy.2010.08.016

[87] Brandoni C., Renzi M., Hybrid renewable energy systems made up of high concentration PV solar technology and micro-CHP. Proceedings of EuroSun2012, ISES Europe Solar Conference, September 18-20, 2012. Rijeka, Croatia, ISBN 978-953-6886-20-3.

[88] C. Brandoni, M. Renzi, F. Caresana, F.Polonara, Optimization of hybrid micro-CCHP systems in the day-ahead electricity market, Proceedings of the 3rd International Conference on Microgeneration and Related Technologies, Naples, 15-17 April 2013

[89] Steck, Michael (2012): Pooling of distributed energy resources. Munich: Research Center for Energy Economics (FfE)

[90] Hinüber, G.(2007): Intraday optimization of power plant operation at markets for scheduled energy and reservation (In German: Untertägliche Optimierung des Kraftwerksbetriebs an Märkten für Fahrplanenergie und Reserve), in ABEV Contribution to Energy Supply in Aachen, Aachen

[91] Dentcheva, D., Möller, A., Reeh, P., Römisch, W., Schultz, R., Schwarzbach, G., Thomas, J.(2005): Optimized application of modules at power plant operation planning (In German: Optimale Blockauswahl bei der Kraftwerkseinsatzplanung), Humboldt University in Berlin, Institute of Mathematics

[92] Henle, Markus (2009): Exploitation and Commercialization of virtual power plants - Master Thesis. Jacobs University Bremen

[93] Stimpfl, Roman (2010): Modeling Virtual Power Plants (In German: Modellierung virtueller Kraftwerke). München: Lehr¬stuhl für Energiewirtschaft und Anwendungstechnik (IfE), TU München

[94] Steck, Michael (2012b): Development and Assessment of Dispatching Algorithms of Virtual Power Plants - Dissertation. Munich: Technische Universität München (TUM))

[95] Steck, Michael (2008): Power Plants of the 21st Century: Technical Aspects of Future Power Plants in an Energy System of Distributed Production (In German: Kraftwerke des 21. Jahrhunderts: Technische Anforderungen an neue Kraftwerke im Umfeld dezentraler Stromerzeugung). Munich: Research Center for Energy Economics (FfE)

[96] Steck, Michael (2011): Simulation to Quantify the Revenues of Linked CHP-devices Providing Balance Power Under Realistic Conditions. SuperGEN HiDEF Conference "MicrogenII", 4-6th April 2011 at the University of Strathclyde, Glasgow

[97] K. Darcovich, N. Gupta, T. Caroni, I.J. Davidson, Residential electrical power storage scenario simulations with a large-scale lithium ion battery, J. Appl. Electrochem., 40 [4] (2010) 749-755.

[98] I. Knight and I. Ugursal, Residential cogeneration systems: A review of the current technologies. IEA/ECBCS Annex 42, (2005) 92 pp.

[99] I. Beausoleil-Morrison, (Ed.), An Experimental and Simulation-Based Investigation of the Performance of Small-Scale Fuel Cell and Combustion-Based Cogeneration Devices Serving Residential Buildings. IEA/ECBCS Annex 42 Report, (2008), 58 pp.

[100] Y. Cho, J. Cho, Significant Improvement of LiNi0.8Co0.15Al0.05O2 Cathodes at 60C by SiO2 Dry Coating for Li-ion Batteries, J. Electrochem. Soc., 157 [6] (2010) A625-A629.

[101] B. Kenney, K. Darcovich, D. MacNeil, I.J. Davidson, Modeling the Impact of Variations in Electrode Manufacturing on Lithium-Ion Battery Modules, Journal of Power Sources, 213 (2012) 391-401.

[102] G. Ning, B.N. Popov, Cycle life modeling of lithium-ion batteries, J. Electrochem. Soc., 151 (2004) A1584-A1591.

[103] S.K. Rahimian, S.C. Rayman, R.E. White, Maximizing the life of a lithium-ion cell by optimization of charging rates, J. Electrochem. Soc.,157 (2010) A1302.

[104] L. Gao, S. Liu and R. Dougal, Dynamic Lithium-Ion Battery Model for System Simulation, IEEE Trans. Components and Packaging Technologies, 25 [3] (2002) 495-505.

[105] E. Jones, T. Oliphant, P. Peterson, et al., SciPy: Open Source Scientific Tools for Python (2001).http://www.scipy.org.

[106] A.C. Powell IV, R. Arroyave, Open source software for materials and process modeling, JOM, 60 [5] (2008) 32-39.

[107] http://www.ontario-hydro.com/index.php?page=current_rates

[108] http://www.hydroottawa.com/resources/documents/publications/rates/rates_residential_e.pdf

[109] http://microfit.powerauthority.on.ca/sites/default/files/news/FIT-FITPriceScheduleV2.0.pdf

[110] http://www.ontarioenergyboard.ca/OEB/Consumers/Natural+Gas/Natural+Gas+Rates

[111] "Energy use data handbook 1990 to 2007," tech. rep., Natural Resources Canada, 2009. http://oee.nrcan.gc.ca/publications/statistics/handbook08/index.cfm?attr=0.

[112] Environment Canada, 2010. Daily data report Ottawa, Ontario, tech. rep., Weather Office, http://climate.weathero_ce.gc.ca/

[113] A. Muralidhar, L. Hughes, Integrating wind generated electricity with space heating and storage batteries, International Green Energy Conference, Waterloo, Canada, June 2010, paper ERG/201004, 16 pp.

[114] N. Saldanha, I. Beausoleil-Morrison, Measured end-use electric load profiles for 12 Canadian houses at high temporal resolution, Energy and Buildings 49 (2012) 519–530.

[115] C. Roselli, M. Sasso, S. Sibilio, P. Tzscheutschler, Experimental analysis of microcogenerators based on different prime movers, Energy and Buildings, 43 (2011) 796-804.

[116] http://oee.nrcan.gc.ca/pml-lmp/index.cfm?action=app.formHandler&operation=sort&nr=1 &validate=no&sd=1&appliance= FURNACES_G

[117] C. Roselli, M. Sasso, S. Sibilio, and P. Tzscheutschler, "Experimental analysis of microcogenerators based on different prime movers," Energy and Buildings, vol. 43, no. 4, pp. 796–804, Apr. 2011.

[118] W. D. J. Zapata Riveros, J. Vandewalle, "Assessment of different distributed generation technologies for a virtual power plant," IAEE European Energy Conference 2012, no. Venice, 2012.

[119] E. D. Mehleri, H. Sarimveis, L. G. Papageorgiou, and N. C. Markatos, "Model Predictive Control of distributed energy resources," Control & Automation (MED), 2012 20th Mediterranean Conference on. pp. 672–678, 2012.

[120] W. D. J. Zapata Riveros, J. Vandewalle, "Reducing Imbalance with virtual power plant operation," To be presented MICROGEN III conference, Naples , 2013.

[121] R. Donceel and J. Van Engeland, "Opportunities for micro-CHPs in the Belgian balancing mechanism: imbalance reduction versus reserve power supply" Master thesis University of Leuven, 2013.

[122] K Lombardi, VI Ugursal, I Beausoleil-Morrison, Proposed improvements to a model for characterizing the electrical and thermal energy performance of Stirling engine micro-cogeneration devices based upon experimental observations, Applied Energy 87 (2010) 3271–3282.

Background

International Energy Agency

The International Energy Agency (IEA) was established in 1974 within the framework of the Organisation for Economic Co-operation and Development (OECD) to implement an international energy programme. A basic aim of the IEA is to foster co-operation among the twenty-eight IEA participating countries and to increase energy security through energy conservation, development of alternative energy sources and energy research, development and demonstration (RD&D).

Energy in Buildings and Communities

The IEA co-ordinates research and development in a number of areas related to energy. The mission of one of those areas, the EBC - Energy in Buildings and Communities Programme, is to develop and facilitate the integration of technologies and processes for energy efficiency and conservation into healthy, low emission, and sustainable buildings and communities, through innovation and research. (Until March 2013, the EBC Programme was known as the Energy in Buildings and Community Systems Programme, ECBCS.)

The research and development strategies of the EBC Programme are derived from research drivers, national programmes within IEA countries, and the IEA Future Buildings Forum Think Tank Workshop, held in April 2013. The R&D strategies represent a collective input of the Executive Committee members to exploit technological opportunities to save energy in the buildings sector, and to remove technical obstacles to market penetration of new energy conservation technologies. The R&D strategies apply to residential, commercial, office buildings and community systems, and will impact the building industry in five focus areas of R&D activities:

- Integrated planning and building design
- Building energy systems
- Building envelope
- Community scale methods
- Real building energy use

The Executive Committee

Overall control of the program is maintained by an Executive Committee, which not only monitors existing projects but also identifies new areas where collaborative effort may be beneficial. To date the following projects have been initiated by the Executive Committee on Energy in Buildings and Communities (completed projects are identified by (*)):

Annex 1: Load Energy Determination of Buildings (*)
Annex 2: Ekistics and Advanced Community Energy Systems (*)
Annex 3: Energy Conservation in Residential Buildings (*)
Annex 4: Glasgow Commercial Building Monitoring (*)
Annex 5: Air Infiltration and Ventilation Centre

Annex 6: Energy Systems and Design of Communities (*)
Annex 7: Local Government Energy Planning (*)
Annex 8: Inhabitants Behaviour with Regard to Ventilation (*)
Annex 9: Minimum Ventilation Rates (*)
Annex 10: Building HVAC System Simulation (*)
Annex 11: Energy Auditing (*)
Annex 12: Windows and Fenestration (*)
Annex 13: Energy Management in Hospitals (*)
Annex 14: Condensation and Energy (*)
Annex 15: Energy Efficiency in Schools (*)
Annex 16: BEMS 1- User Interfaces and System Integration (*)
Annex 17: BEMS 2- Evaluation and Emulation Techniques (*)
Annex 18: Demand Controlled Ventilation Systems (*)
Annex 19: Low Slope Roof Systems (*)
Annex 20: Air Flow Patterns within Buildings (*)
Annex 21: Thermal Modelling (*)
Annex 22: Energy Efficient Communities (*)
Annex 23: Multi Zone Air Flow Modelling (COMIS) (*)
Annex 24: Heat, Air and Moisture Transfer in Envelopes (*)
Annex 25: Real time HVAC Simulation (*)
Annex 26: Energy Efficient Ventilation of Large Enclosures (*)
Annex 27: Evaluation and Demonstration of Domestic Ventilation Systems (*)
Annex 28: Low Energy Cooling Systems (*)
Annex 29: Daylight in Buildings (*)
Annex 30: Bringing Simulation to Application (*)
Annex 31: Energy-Related Environmental Impact of Buildings (*)
Annex 32: Integral Building Envelope Performance Assessment (*)
Annex 33: Advanced Local Energy Planning (*)
Annex 34: Computer-Aided Evaluation of HVAC System Performance (*)
Annex 35: Design of Energy Efficient Hybrid Ventilation (HYBVENT) (*)
Annex 36: Retrofitting of Educational Buildings (*)
Annex 37: Low Exergy Systems for Heating and Cooling of Buildings (LowEx) (*)
Annex 38: Solar Sustainable Housing (*)
Annex 39: High Performance Insulation Systems (*)
Annex 40: Building Commissioning to Improve Energy Performance (*)
Annex 41: Whole Building Heat, Air and Moisture Response (MOIST-ENG) (*)
Annex 42: The Simulation of Building-Integrated Fuel Cell and Other Cogeneration Systems (FC+COGEN-SIM) (*)
Annex 43: Testing and Validation of Building Energy Simulation Tools (*)
Annex 44: Integrating Environmentally Responsive Elements in Buildings (*)
Annex 45: Energy Efficient Electric Lighting for Buildings (*)
Annex 46: Holistic Assessment Tool-kit on Energy Efficient Retrofit Measures for Government Buildings (EnERGo) (*)

Annex 47: Cost-Effective Commissioning for Existing and Low Energy Buildings (*)
Annex 48: Heat Pumping and Reversible Air Conditioning (*)
Annex 49: Low Exergy Systems for High Performance Buildings and Communities (*)
Annex 50: Prefabricated Systems for Low Energy Renovation of Residential Buildings (*)
Annex 51: Energy Efficient Communities (*)
Annex 52: Towards Net Zero Energy Solar Buildings (*)
Annex 53: Total Energy Use in Buildings: Analysis & Evaluation Methods (*)
Annex 54: Integration of Micro-Generation & Related Energy Technologies in Buildings (*)
Annex 55: Reliability of Energy Efficient Building Retrofitting - Probability Assessment of Performance & Cost (RAP-RETRO)
Annex 56: Cost Effective Energy & CO2 Emissions Optimization in Building Renovation
Annex 57: Evaluation of Embodied Energy & CO2 Emissions for Building Construction
Annex 58: Reliable Building Energy Performance Characterisation Based on Full Scale Dynamic Measurements
Annex 59: High Temperature Cooling & Low Temperature Heating in Buildings
Annex 60: New Generation Computational Tools for Building & Community Energy Systems Based on the Modelica & Functional Mockup Unit Standards
Annex 61: Development & Demonstration of Financial & Technical Concepts for Deep Energy Retrofits of Government / Public Buildings & Building Clusters
Annex 62: Ventilative Cooling
Annex 63: Implementation of Energy Strategies in Communities
Annex 64: LowEx Communities - Optimised Performance of Energy Supply Systems with Exergy Principles
Annex 65: Long-Term Performance of Super-Insulation in Building Components and Systems

Working Group - Energy Efficiency in Educational Buildings (*)
Working Group - Indicators of Energy Efficiency in Cold Climate Buildings (*)
Working Group - Annex 36 Extension: The Energy Concept Adviser (*)

(*) – Completed

Annex 54

The **Annex 54 "Integration of Micro-Generation and Related Energy Technologies in Buildings"** undertook an in depth analysis of micro-generation and associated other energy technologies.

Scope of activities

- multi-source micro-cogeneration systems, polygeneration systems (i.e. integrated heating / cooling / power generation systems) and renewable hybrid systems;
- the integration of micro-generation, energy storage and demand side management technologies at a local level (integrated systems);
- customised and optimum control strategies for integrated systems;
- the analysis of integrated and hybrid systems performance when serving single and multiple residences along with small commercial premises; and
- the analysis of the wider impact of micro-generation on the power distribution system. To broaden the impact of the Annex's output there will be significant effort to disseminate its deliverables to non-technical stakeholders working in related areas such as housing, product commercialisation and regulatory development.

Outcomes

- An update on occupant related DHW and electric load profiles.
- Component models and their implementation in building simulation tools.
- Review of best practice in the operation and control of integrated micro-generation systems.
- Predictive control algorithms to maximize the performance and value of micro-generation.
- Experimental data sets for the calibration and validation of device models.
- Performance assessment methodologies.
- Country-specific studies on the performance of a range of micro-generation systems.
- Studies of the viability of micro-generation systems in different operational contexts and of the impacts of micro-generation on the wider community and the potential benefits, in particular for the electricity network.
- An investigation of interactions between technical performance and comercialization/ regulatory approaches for micro-generation.
- Compilation of case studies of the introduction of microgeneration technologies.

Annex 54 was built upon the results of Annex 42 "The Simulation of Building-Integrated Fuel Cell and Other Cogeneration Systems".

To accomplish its objectives Annex 54 conducted research and development in the framework of the following three Subtasks:

Subtask A - Technical Development

The subtask contains a broad range of activities related to models and load profiles development, data collection and micro-generation systems predictive controls development and optimization.

Subtask B - Performance Assessment

The subtask uses simulations to develop an extensive library of performance studies and synthesis techniques to identify generic performance trends and “rules of thumb” regarding the appropriate deployment of micro-generation technologies.

Subtask C - Technically Robust Mechanisms for Diffusion

The subtask contains work related to the interaction between technical performance, economic instruments and commercialization strategies and provision of this information to the relevant decision makers. Given the importance of micro-generation in meeting many countries’ climate change targets the subtask assesses the ability of micro-generation to enter the market and deliver on national and international energy policy objectives.

Research Partners of Annex 54

Belgium	Catholic University of Leuven
Canada	Natural Resources Canada
	National Research Council
	Carleton University
Denmark	Dantherm Power A/S
Germany	Research Center for Energy Economics (FfE)
	Technische Universität München (TUM)
	University of Applied Science of Cologne
Italy	Università degli Studi del Sannio
	Seconda Università di Napoli (SUN)
	National Agency for New Technologies, Energy and Sustainable Economic Development (ENEA)
	Università Politecnica delle Marche
Japan	Tokyo University of Agriculture and Technology
	Osaka University
	Nagoya University
	Tokyo Gas
	Osaka Gas
	Toho Gas
	Saibu Gas
	Mitsubishi Heavy Industry Ltd
	Yanmar Energy Systems Ltd
Korea	Korean Institute for Energy Research (KIER)
Netherlands	Technische Universiteit Eindhoven (TU/E)
United Kingdom	University of Strathclyde, Scotland
	Imperial College London, England
	University of Bath, England
United States	National Institute for Standards and Technology (NIST)